

POLITECNICO DI MILANO

Department of Physics

Doctoral Program in Physics



**Epitaxial growth and
characterization of $\text{Si}_{1-x}\text{Ge}_x$ and GaN
crystals on micrometer-sized silicon
pillars**

Doctoral Dissertation of:

Fabio Isa

Supervisor:

Dr. Giovanni Isella

Tutor:

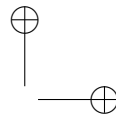
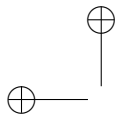
Prof. Franco Ciccacci

The Chair of the Doctoral Program:

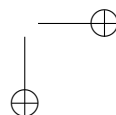
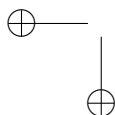
Prof. Paola Taroni

2014 - XXVI Doctoral Cycle

19th February 2014



To my Family



Contents

Introduction	1
Abbreviation List	7
1 Heteroepitaxy	11
1.1 Plastic relaxation of $\text{Si}_{1-x}\text{Ge}_x/\text{Si}$	12
1.1.1 Thermodynamic models for plastic relaxation in $\text{Si}_{1-x}\text{Ge}_x/\text{Si}$	17
1.1.2 Kinetic model for plastic relaxation in $\text{Si}_{1-x}\text{Ge}_x/\text{Si}$	24
1.2 Nucleation of misfit dislocations in $\text{Si}_{1-x}\text{Ge}_x/\text{Si}$	27
1.3 Thermal strain induced problems	39
1.4 Gallium nitride: physical properties	42
1.5 GaN epitaxial growth	46
2 Experimental	57

2.1	Epitaxial growth techniques	57
2.1.1	LEPECVD	57
2.1.2	PA-MBE	61
2.2	Preparation of patterned silicon substrates . .	65
2.3	Characterization techniques	69
3	3D heteroepitaxy of $\text{Si}_{1-x}\text{Ge}_x/\text{Si}$ crystals	77
3.1	Morphology of $\text{Si}_{1-x}\text{Ge}_x/\text{Si}$ crystals	78
3.2	Impact of patterning conditions on Ge crystal morphology	95
3.2.1	Role of patterning geometry	95
3.2.2	Role of lateral Si sidewalls passivation	103
3.2.3	Role of Si substrate orientation	107
3.3	Growth modeling of $\text{Si}_{1-x}\text{Ge}_x/\text{Si}$ crystals . . .	109
3.3.1	Crystalline facet growth and flux modeling	109
3.3.2	Kinetic parameters	123
3.3.3	Diffusion and growth temperature effects	130
3.4	Thermal strain relaxation	140
4	Dislocation Engineering in $\text{Si}_{1-x}\text{Ge}_x/\text{Si}$	145
4.1	Threading dislocation analysis and elimina- tion in pure Ge crystals	146

<i>Contents</i>	iii
4.2 Onset of vertical threading dislocation formation in $\text{Si}_{1-x}\text{Ge}_x/\text{Si}$	170
5 Nanofocused HR-XRD analysis of Ge/Si crystals	187
5.0.1 Lattice bending at the Ge/Si interface	192
5.0.2 Random net tilt of Ge/Si crystals induced by misfit dislocations	197
5.0.3 High quality Ge crystals from dislocated Ge/Si interface	200
6 Optical properties of Ge/Si crystals	205
6.1 PL intensity <i>vs</i> TDD	206
6.2 Inter-band PL intensity enhancement via band gap engineering	217
6.3 PL properties of Ge quantum wells crystals	224
7 GaN/Si crystals by PA-MBE	233
7.1 Growth and morphology	234
7.2 Optical properties	249
Conclusions	257

Cover Gallery	263
Acknowledgements	269
Bibliography	271
Publications	311

Introduction

The stacking of different semiconductor layers has been widely investigated in the last decades both from the point of view of fundamental research [1] and for the development of novel semiconductor devices [2]. While most of the early works were focused on the integration of lattice-matched heterostructures, thus limiting the degrees of freedom to tailor the semiconductor device properties, more recently, many efforts have been devoted to grow epitaxially mismatched heterostructures. Indeed, strained silicon represents nowadays one of the most important building blocks in microprocessor technology [3]. On the other hand, several devices, e.g. multiple-junction solar cells, photo-detectors, high-brightness light-emitting diodes etc., require several micrometer thick epitaxial crystals. In particular, the integration of dissimilar semiconductors on Si has a fundamental

role in modern technology, it would enable the combination of semiconductor heterostructures with the well established CMOS technology. The heteroepitaxial growth of semiconductors on Si substrates paves a possible way in this direction [4–7].

Whatever epitaxial growth technique is used, due to the misfit between the substrate and the epilayer lattice parameter, the system relaxes plastically at the growth temperature by introducing dislocations. According to the pioneering studies of Frank and van der Merwe [8, 9], the deposited material, after a certain critical thickness, relaxes the accumulated lattice stress by introducing misfit dislocations at the epilayer/substrate interface. Unfortunately, misfit dislocations are terminated by threading dislocations which run through the whole crystal volume ending at its free surfaces [10]. Since threading dislocations strongly affect the performances of opto-electronic devices [11], many strategies have been proposed in the last years to reduce their density. These approaches are based on the deposition of thick graded buffers [12], selective area deposition into dielectric windows [13], use of compliant nano-structured substrates [14, 15], annealing treatments [16] etc.. The aforementioned

strategies are not completely effective in reducing the density of vertical threading dislocations, which are typically created in high misfit systems [17], since they evolve parallel to the [001] growth direction [18]. Indeed, they can be eliminated only by depositing thick 3D crystals with slanted top facets, attracting and expelling the defects at the free lateral sidewalls [19].

Despite the lattice stress is completely relaxed by means of misfit dislocations during the epitaxial growth, the crystal can be still strained at room temperature if its thermal expansion coefficient differ from that one of the substrate [20]. The accumulated thermal stress can be deleterious, especially for thick epitaxial layers. Indeed, the thermal stress is relaxed by wafer bowing or by formation of cracks, thus strongly compromising any possibility of further sample processing.

Structure of the Thesis

This Ph.D. thesis will report on the epitaxial growth, the structural and optical characterization of $\text{Si}_{1-x}\text{Ge}_x$ and GaN 3D crystals epitaxially grown on patterned silicon substrates

consisting of arrays of micrometer-sized pillars. The deposition of $\text{Si}_{1-x}\text{Ge}_x$ and GaN 3D crystals, has been respectively performed by low energy plasma enhanced chemical vapor deposition (LEPECVD) and by plasma assisted molecular beam epitaxy (PA-MBE). The structural characterization has been carried out by atomic force microscopy, high resolution X-ray diffraction, scanning electron microscopy and transmission electron microscopy, while the optical characterization by photoluminescence and cathodoluminescence measurements.

Chapter 1 discusses the problems related to heteroepitaxy. In particular the issues related to the formation and nucleation mechanisms of dislocations in $\text{Si}_{1-x}\text{Ge}_x$ alloys deposited on Si, the thermal strain due to different thermal expansion coefficients, the physical properties and epitaxial growth of GaN are addressed.

Chapter 2 describes the experimental setups which have been used for the epitaxial growth and for the characterization of $\text{Si}_{1-x}\text{Ge}_x$ and GaN crystals.

Chapter 3 presents the results about the morphology of 3D $\text{Si}_{1-x}\text{Ge}_x$ crystals deposited on micrometer-sized Si pillars together with a growth model, explaining the peculiar self-

limited lateral growth mechanism.

Chapter 4 describes the critical growth conditions for the formation of vertical threading dislocations in $\text{Si}_{1-x}\text{Ge}_x$ alloys on (001)Si and their character. A mechanism to get rid of threading dislocations is also presented.

Chapter 5 presents the high resolution X-ray diffraction analysis performed at the ESRF synchrotron in Grenoble of 3D Ge crystals, in particular focusing on the impact of misfit dislocations and thermal strain on the crystal quality and lattice tilt.

Chapter 6 is devoted to the study of the optical properties of 3D Ge and multiple quantum wells crystals with controlled threading dislocation density.

Finally, chapter 7 describes the epitaxial growth by PAMBE of GaN crystals on (001) patterned Si substrates with faceted pillars and their optical properties.

Abbreviation List

- Atomic Force Microscope (AFM)
- Bright Field (BF)
- Cathodoluminescence (CL)
- Dark Field (DF)
- Deep Reactive Ion Etching (DRIE)
- Electron Back Scattered Diffraction (EBSD)
- Electron Beam Lithography (EBL)
- Full Width Half Maximum (FWHM)
- High Resolution X-Ray Diffraction (HR-XRD)
- Kinetic Crystal Shape (KCS)
- Inter Band (IB)

- Large Angle Convergent-Beam Electron Diffraction (LACBED)
- Low Energy Plasma Enhanced Chemical Vapor Deposition (LEPECVD)
- Misfit Dislocation (MD)
- Mono Layer (ML)
- Multiple Quantum Wells (MQWs)
- Plasma Assisted Molecular Beam Epitaxy (PA-MBE)
- Photoluminescence (PL)
- Reciprocal Space Map (RSM)
- Room temperature (RT)
- Root Mean Square (RMS)
- Scanning Electron Microscope (SEM)
- Scanning Transmission Electron Microscope (STEM)
- Threading Dislocation (TD)
- Threading Dislocation Density (TDD)

Abbreviation List

9

- Three Dimensional (3D)
- Transmission Electron Microscope (TEM)
- Two Dimensional (2D)
- Vertical Threading Dislocation (VD)

Chapter 1

Heteroepitaxy

In this chapter we will focus on the problems regarding the plastic relaxation of the epitaxial stress due to the lattice parameter mismatch between the epilayer and the substrate, and the thermal strain induced by the difference in thermal expansion coefficients.

1.1 Plastic relaxation of $\text{Si}_{1-x}\text{Ge}_x/\text{Si}$

Silicon and germanium share the same diamond crystal structure: the Bravais lattice is *face centered cubic (fcc)* containing two unit atoms: one in the $(0,0,0)$ and the second one in the $(\frac{a}{4}, \frac{a}{4}, \frac{a}{4})$ position where a is the lattice parameter. Within one cubic unit cell, 8 atoms are present, each one surrounded by 4 nearest neighbours disposed at the corners of a tetrahedron. Germanium has a 4.2% larger lattice pa-

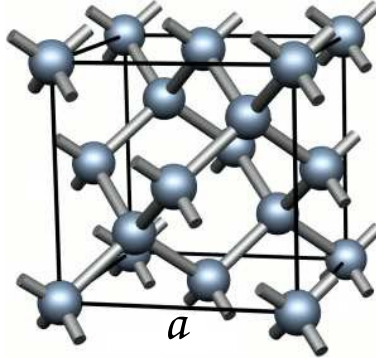


Figure 1.1: 3D diamond crystal structure for silicon. a represents the lattice parameter.

rameter than Si, thus increasing the concentration of Ge in a $\text{Si}_{1-x}\text{Ge}_x$ alloy, the relaxed lattice parameter $a_{\text{Si}_{1-x}\text{Ge}_x}$ is almost linearly changing according to equation 1.1 [21].

$$a_{\text{Si}_{1-x}\text{Ge}_x} = 0.5431 + 0.01992x + 0.0002733x^2(\text{nm}) \quad (1.1)$$

During the very first stages of the epitaxial deposition, the epilayer crystal is perfectly registered with respect to the substrate, accumulating elastic strain due to the lattice mismatch. Let us consider the deposition of a $\text{Si}_{1-x}\text{Ge}_x$ alloy on a fully relaxed $\text{Si}_{1-y}\text{Ge}_y$ buffer layer ($0 \leq x, y \leq 1$). If $x > y$ the top pseudomorphic epilayer is compressively strained, while if $y > x$ the strain is tensile (see Figure 1.2 b), d) respectively). Both in the tensile and compressive strain case, the epilayer crystal experiences an in plane biaxial strain $\varepsilon_{xx} = \varepsilon_{yy} = \varepsilon_{\parallel} = \frac{a_{\parallel} - a_B}{a_B}$, producing a tetragonal distortion deforming the cubic lattice cell in the out of plane direction. The out of plane strain $\varepsilon_{\perp} = \frac{a_{\perp} - a_B}{a_B}$, according to the isotropic elasticity theory [22], is related to ε_{\parallel} through the Poisson ratio ν by the expression reported in equation 1.2. For more details about the Poisson ratio dependence on crystallographic orientations see [23].

$$\varepsilon_{\perp} = \frac{-2\nu}{1 - \nu} \varepsilon_{\parallel} \quad (1.2)$$

If we call respectively a_A and h_A the relaxed lattice parameter and the thickness of the $\text{Si}_{1-x}\text{Ge}_x$ epilayer, a_B and h_B the same ones for the $\text{Si}_{1-y}\text{Ge}_y$ substrate and assuming $a_A < a_B$

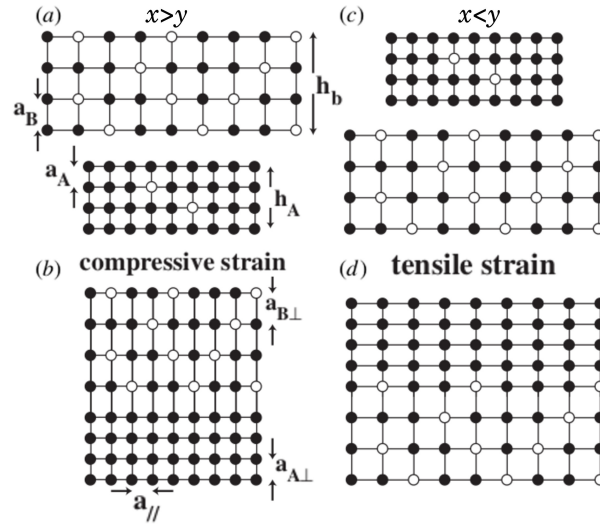


Figure 1.2: a) drawing of the lattice crystal structure of relaxed $\text{Si}_{1-x}\text{Ge}_x$ (TOP) and $\text{Si}_{1-y}\text{Ge}_y$ (BOTTOM) alloys with $x > y$. b) drawing of the two crystals lattices perfectly matching reported in a). c), d), same of a), b), respectively, for $x < y$. a_A, h_A (a_B, h_B) are respectively the lattice parameter and the layer thickness of the $\text{Si}_{1-x}\text{Ge}_x$ epilayer ($\text{Si}_{1-y}\text{Ge}_y$ substrate) [7].

(see Figure 1.2a)), the in plane lattice constant a_{\parallel} due to the tetragonal distortion (see Figure 1.2b)) is expressed by equation 1.3, [24].

$$a_{\parallel} = a_A \left[1 + \frac{f}{1 + \frac{G_A h_A}{G_B h_B}} \right] \quad (1.3)$$

Where G_A , G_B are respectively the shear modulus of the epilayer and of the substrate, f is the lattice misfit between the two crystals which is defined according to equation 1.4.

$$f = \frac{a_B - a_A}{a_A} \quad (1.4)$$

The in-plane strain $\varepsilon_{\parallel A}$ in layer A is expressed by $\frac{f}{1 + \frac{G_A h_A}{G_B h_B}}$, thus in equilibrium conditions, the in-plane strain $\varepsilon_{\parallel B}$ in layer B is related to the one in layer A through the equation 1.5.

$$\varepsilon_{\parallel A} = -\frac{G_B h_B}{G_A h_A} \varepsilon_{\parallel B} \quad (1.5)$$

If the lattice misfit between the epitaxial layer and the substrate is sufficiently small, the first deposited monolayers are

perfectly matched with the substrate crystal lattice. In this conditions the epitaxial layer is fully strained and called pseudomorphic. The in plane epilayer lattice constant is forced to be the same one of the substrate ($a_{\parallel A} = a_{\parallel B}$) and tetragonal distortion occurs according to equation 1.2. Increasing the thickness of the epilayer, the elastic strain energy stored increases proportionally, thus the fully strained layer on the substrate is no more energetically stable and relaxation takes place. Depending on the lattice misfit between the epilayer and the substrate and on the growth conditions (thickness, growth temperature, growth rate, concentration of pre-existing defects or impurities, adsorbates, etc..) [25–28] different relaxation processes occur. In this section we will focus on plastic relaxation of the epilayer through the formation of misfit dislocations (MDs) at the heterointerface examining different models.

1.1.1 Thermodynamic models for plastic relaxation in $\text{Si}_{1-x}\text{Ge}_x/\text{Si}$

The plastic relaxation of epitaxial layers on substrates with different lattice constants, has been largely investigated by several thermodynamic models [10, 29–34]. In these models the critical epilayer thickness h_c for the onset of the MD formation has been calculated based only on mechanical equilibrium considerations, i.e. the interfacial energy between the epilayer and the substrates coincides with the areal strain energy (Van der Merwe’s model) [29, 30] or the force exerted on the dislocation line by the misfit stress equals its line tension (Matthews’ model) [10, 31, 32].

In the Van der Merwe’s model, the critical thickness h_c for the formation of MDs at the heterointerface has been evaluated considering the thickness h of the epilayer at which its areal strain density ϵ_H is equivalent to the interfacial energy ϵ_I between the substrate and the epilayer. In case of moderate misfits ($f \lesssim 4\%$), the expressions for the interfacial energy ϵ_I and the strain energy ϵ_H are reported respectively

in equation 1.6 and 1.7.

$$\epsilon_I \simeq 9.5f \left(\frac{Gb}{4\pi^2} \right) \quad (1.6)$$

$$\epsilon_H = 2G \frac{1+\nu}{1-\nu} hf^2 \quad (1.7)$$

Where G is the shear modulus of the epilayer and b the Burger's vector. It is worth to underline that ϵ_I doesn't depend on the film thickness h , while ϵ_H linearly depends on it. If we impose the equilibrium between the strain and interface energies ($\epsilon_H = \epsilon_I$) and set $h = h_c$ we get the critical thickness expression (see equation 1.8) as a function of misfit f and relaxed lattice parameter (a_0).

$$h_c \simeq \left(\frac{1}{8\pi^2} \right) \left(\frac{1-\nu}{1+\nu} \right) \frac{a_0}{f} \simeq 0.1 \left(\frac{a_0}{f} \right) \quad (1.8)$$

The calculated values of h_c , according to equation 1.8, for different $Si_{1-x}Ge_x$ alloys on Si, is reported in Figure 1.3 by the dashed line marked by a). It is clear that the calculated h_c values are rather reliable, compared with the experimental data of [34], only for $f \gtrsim 3.4\%$.

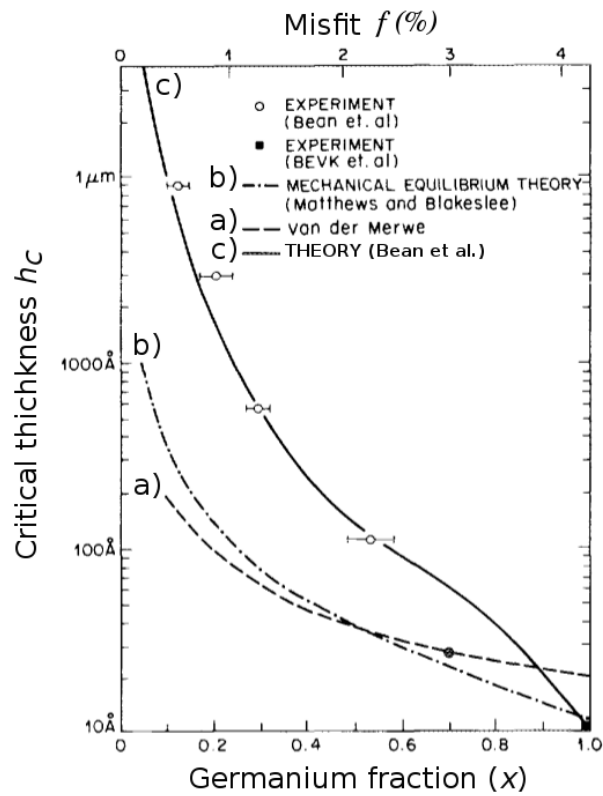


Figure 1.3: Calculated critical thickness h_c according to different models: a) dashed line (Van der Merwe), b) dashed dotted line (Matthews), c) black line (People). Open circles and black squares are experimental data respectively from [33] and [35]

The Matthews relaxation model considers the mechanical equilibrium between the line tension to create a MD from an already existing defects coming from the substrate (threading dislocations (TDs)) and the force related to the misfit stress, as illustrated in Figure 1.4. If the elastic constants

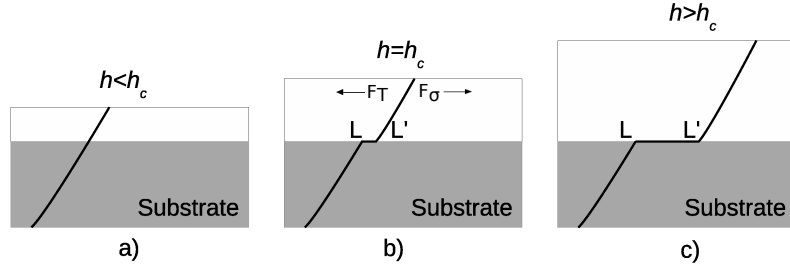


Figure 1.4: Schematic of the formation of a MD (segment LL') at the epilayer/substrate interface for different epilayer thickness h from a TD coming from the substrate. a) $h < h_c$. b) $h = h_c$. c) $h > h_c$. F_T and F_σ are respectively the tension line and the misfit stress force acting on the dislocation.

of the epilayer and of the substrate are the same, we can define the tension line F_T and the misfit stress force F_σ by the equations 1.9 and 1.10 [31].

$$F_T \simeq \frac{Gb^2}{4\pi(1-\nu)} \left(\ln \left(\frac{h}{b} \right) + 1 \right) \quad (1.9)$$

$$F_\sigma \simeq \left(\frac{1+\nu}{1-\nu} \right) Gbh\varepsilon \quad (1.10)$$

The equilibrium condition at the critical thickness h_c is given by $F_T = F_\sigma$. For an epilayer thickness $h < h_c$ (see Figure 1.4 a)) the tension line is larger than the misfit stress force, impeding the formation of a MD at the heterointerface. At the critical thickness the two forces are balanced, thus the TD coming from the substrate starts to move at the heterointerface creating a short MD segment LL' (see Figure 1.4 b)). For $h > h_c$ the misfit stress becomes predominant over the line tension, creating long MD segment LL' (see Figure 1.4 c)) to release plastically the accumulated strain. The expression for the critical thickness, reported in equation 1.11, is obtained imposing $F_T = F_\sigma$ and $f = \varepsilon$. From the dashed dotted line b) of Figure 1.3 it is clear that the Matthews model predicts larger critical thickness than the Van de Merwe's one for low Ge content alloys.

$$h_c \simeq \left(\frac{b}{f}\right) \left(\frac{1}{4\pi(1+\nu)}\right) \left(\ln\left(\frac{h_c}{b}\right) + 1\right) \quad (1.11)$$

The People and Bean approach [33, 34], assumes that the generation of misfit dislocations is driven only by the energy balance between the strain areal energy reported in equation 1.7 and the energy to create a single dislocation

(screw or edge in type). A relevant difference with respect to the Matthews' model is that the substrate is assumed to be completely free from pre-existing defects or TDs, thus the MD is nucleated in the epilayer when the film thickness is larger than the calculated h_c . Nabarro has calculated the self energy of screw and edge dislocations [36], finding that screw dislocations have a self energy lower by a factor $\frac{1}{1-\nu} \simeq 1.4$, thus in the Pele approach the areal energy density ϵ_D of an isolated screw dislocation with distance h from the film surface has been considered (see equation 1.12).

$$\epsilon_D \simeq \frac{Gb^2}{8\pi\sqrt{2}a_x} \ln\left(\frac{h}{b}\right) \quad (1.12)$$

Where a_x is the lattice parameter of the $Si_{1-x}Ge_x$ alloy on Si. Imposing $\epsilon_D = \epsilon_H$ and setting $h=h_c$ it is possible to get the expression for the critical thickness, as shown in equation 1.13. The solid black line c) in Figure 1.3 represents the calculated h_c from equation 1.13 for a $Si_{0.5}Ge_{0.5}$ alloy considering $b=0.4\text{nm}$. Especially in the case of low Ge content alloys, the calculated critical thickness fits very well with the

experimental data (open circles and solid black squares).

$$h_c \simeq \frac{1 - \nu}{1 + \nu} \frac{b^2}{a_x 16\pi\sqrt{2}} \left[\frac{1}{f^2} \ln \left(\frac{h_c}{b} \right) \right] \quad (1.13)$$

1.1.2 Kinetic model for plastic relaxation in $\text{Si}_{1-x}\text{Ge}_x/\text{Si}$

The critical thickness calculated according to the thermodynamic models is most of the times an underestimation of that one experimentally measured. The main reason for this discrepancy is because the processes of nucleation and propagation of dislocations are not taken into account [7, 37]. Here the kinetic model for the critical thickness calculation by Dodson and Tsao [38] is presented, based on the previous works about plastic flow and dislocation dynamics in diamond semiconductors by Alexander and Haasen [39]. The glide velocity v of a dislocation in a strained semiconductor layer is thermally activated and linearly dependent on the excess stress $\sigma_{excess} = F_\sigma - F_T$, as reported in equation 1.14.

$$v = v_0 \sigma_{excess} e^{-E_v/KT} \quad (1.14)$$

Where v_0 is a constant, T the absolute temperature, K the Boltzmann's constant and E_v the activation energy barrier (2.2 and 1.6 eV respectively for pure Si and Ge). The rate for the dislocation multiplication process (e.g. Hagen and

Strunk [40]) can be expressed by equation 1.15.

$$\frac{d\rho_m}{dt} = K\rho_m v \sigma_{excess} \quad (1.15)$$

Where K is a phenomenological parameter and ρ_m is the density of mobile dislocations. The strain state $\gamma(t)$ of the epilayer with thickness h is proportional to the density ρ of MDs at the heterointerface, so that :

$$\frac{d\gamma(t)}{dt} = b \frac{d\rho}{dt} \quad (1.16)$$

The excess stress σ_{excess} , which promotes the motion of dislocations, is also depending on the density of misfit dislocation formed at the heterointerface, in particular it is reduced during the relaxation process, as shown by equation 1.17.

$$\sigma_{excess} = 2 \frac{(1 + \nu)}{1 - \nu} G [f - \gamma(t) - r(h)] \quad (1.17)$$

Where f is the initial misfit between the epilayer and the substrate and $r(h)$ is the residual strain of the film with thickness h . Combining the expressions from equations 1.14, 1.15, 1.16, 1.17 and considering γ_0 as the initial dislocation source density from the substrate, it is possible to get a single

non-linear differential equation to describe the time dependent strain relaxation:

$$\frac{d\gamma(t)}{dt} = CG^2[f - \gamma(t) - r(h)]^2[\gamma(t) + \gamma_0] \quad (1.18)$$

The calculated relieved strain, for a $Si_{0.5}Ge_{0.5}$ alloy on Si (001) with different epilayer thickness, is presented and compared with experimental data in Figure 1.5 showing good agreement between them.

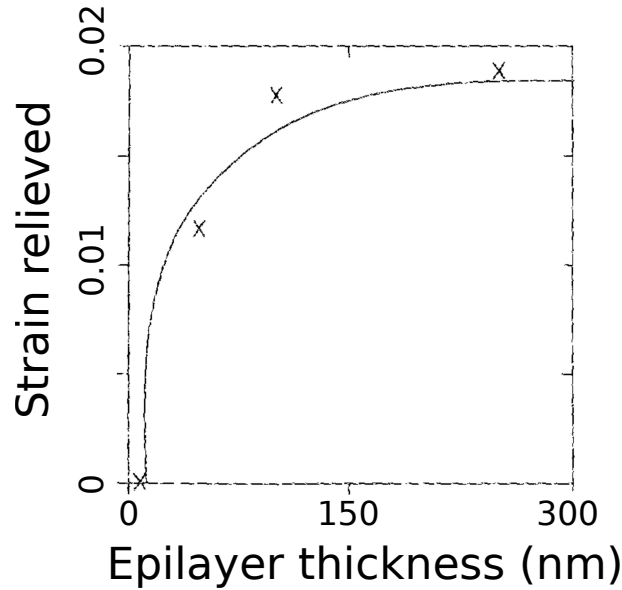


Figure 1.5: Strain relaxation of $Si_{0.5}Ge_{0.5}/Si(001)$ films with different thickness. The black curve is the calculated behaviour according to the Dodson and Tsao model, the crosses are the experimental data (see [38]).

1.2 Nucleation of misfit dislocations in $\text{Si}_{1-x}\text{Ge}_x/\text{Si}$

After the discussion in section 1.1, about the plastic relaxation of the epitaxial layer, here the nucleation mechanisms of MDs, as a function of the Ge content in the alloy and of the crystalline quality of the substrate will be illustrated. The nucleation sources of dislocations in the epitaxial layer can be divided in the following categories [41, 42]:

1. Fixed sources (TDs and imperfections of the substrate)
2. Heterogeneous nucleation of half-loops at the epilayer surface
3. Dislocation interactions and multiplication
4. Homogeneous nucleation of half-loop at the epilayer surface

The fixed sources are those imperfections of the substrate with a certain areal density: TDs, surface imperfections or precipitates. Here the nucleation of a MD is favoured as shown in Figure 1.6 since TDs can be bent according to the Matthews model reported in section 1.1, or impurities

clusters on the substrate surface can favor the nucleation of surface half-loops. The heterogeneous nucleation of surface

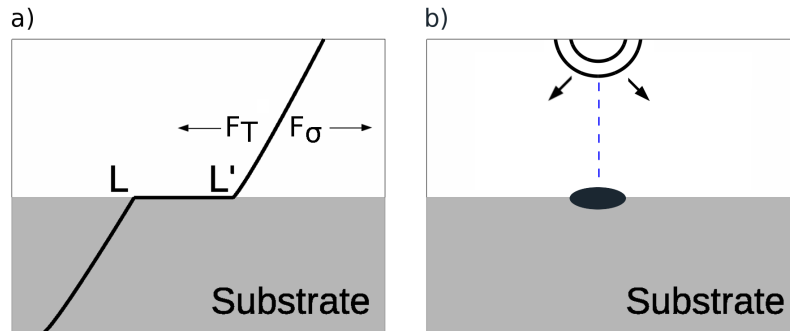


Figure 1.6: Nucleation's schematic of MDs from fixed sources: a) from a substrate TD, b) from a substrate impurity.

half-loops takes place when on the surface of the epilayer are present impurities or defects such as precipitates or contaminations from the growth chamber or very high surface roughness which lower the activation energy barriers to nucleate dislocations (see Figure 1.7).

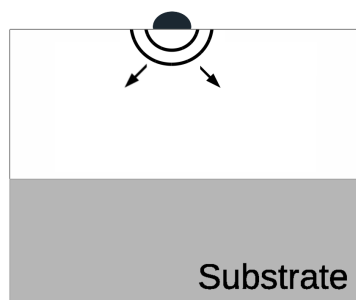


Figure 1.7: Schematic of heterogeneous nucleation of surface half-loops from impurity on the epilayer surface.

In the dislocation interaction and multiplication mechanism, once the epitaxial layer starts to relax introducing an high density of MDs and TDs their probability to react is strongly increased. According to the Hagen-Strunk model [40, 43] when two 60° perpendicular MDs, running along the $[110]$ and $[\bar{1}10]$ directions, with the same Burger’s vector, are crossing in the (001) interface plane, they experience a repulsive force [44]. One dislocation forms a right-angle segment in the (001) interface plane, the other one a rounded right-angle segment laying in the $\{111\}$ plane above the interface pointing towards the epilayer surface (it experiences the image force, especially for epitaxial layers thickness $\lesssim 500$ nm). The segment laying in the $\{111\}$ planes can separate in 2 dislocation segments which can glide under the elastic driving

force, thus creating a new dislocation. The Hagen-Strunk dislocation multiplication mechanism is schematically represented in Figure 1.8.

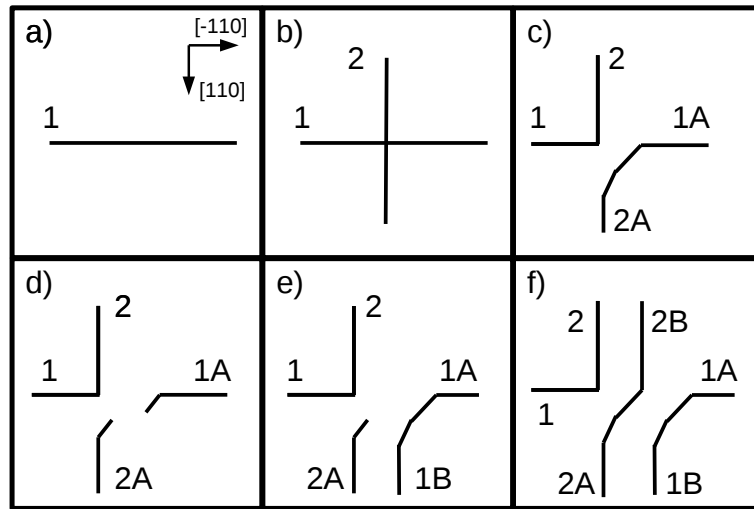


Figure 1.8: Schematic of the Hagen-Strunk dislocation multiplication mechanism. a), b) Two perpendicular 60° MDs with the same Burger's vector, are crossing in the (001) interface plane. c) Annihilation reaction forming two asymmetric angular dislocations: 1-2 in the (001) interface plane and 1A-2A in the $\{111\}$ planes. d) The 1A-2A dislocation dissociate in two segments ending on the epilayer surface. e), f) The two segments 1A and 2A elongate by gliding.

The last nucleation mechanism of dislocation is the homogeneous nucleation of half-loop at the epilayer surface. In this case dislocations half-loops are directly nucleated at the

strained epilayer surface, without any external nucleation source. According to [45] it is possible to calculate the half-loop self energy according to the equation 1.19.

$$\begin{aligned}
 E_{loop} = & \frac{\mu b^2 R}{4 - 4\nu} \left[\frac{b_z^2}{b^2} + (1 - \nu/2) \left(1 - \frac{b_z^2}{b^2} \right) \right] \\
 & \left[\ln \left(\frac{\pi R \alpha}{b} \right) - 1.758 \right] + \\
 & + \frac{\mu b^2 R}{32(1 - 2\nu)^2 \left[(6 - 4\nu) \left(\frac{b_z^2}{b^2} \right) - (1 - 2\nu) \left(1 - \frac{b_z^2}{b^2} \right) \right]}
 \end{aligned} \tag{1.19}$$

where b_z is the Burger’s vector component perpendicular to the half-loop, R is the half-loop radius and $\alpha \sim 2$ is the dislocation core energy parameter [44]. The energy to create a dislocation half-loop is counter balanced by the elastic energy E_{strain} released by the MD according to equation 1.20.

$$E_{strain} = \frac{\pi R^2 \mu (1 + \nu) \varepsilon}{1 - \nu} (b_g \cos \chi \cos \psi + b_e \cos^2 \chi) \tag{1.20}$$

where ε is the lattice strain between the (001) Si substrate and the $Si_{1-x}Ge_x$ epilayer, b_e and b_g are respectively the climbing and gliding components of the Burger’s vector. ψ is the angle between b_g and the segment at the epilayer surface

which is perpendicular to the intersection of the half-loop with the heterointerface. χ is the angle between the free epilayer surface and the half-loop normal. The nucleation of a dislocation non-edge in character, requires the formation or removal of a surface step, producing an extra energy E_{step} . E_{step} depends on the epilayer surface energy γ_s and the angle β between b and the free surface according to the equation 1.21.

$$E_{step} = 2Rb\sin\beta\gamma_s \quad (1.21)$$

Finally, the total energy E_{tot} related to the homogeneous nucleation of dislocation half-loops, is expressed by equation 1.22 [46].

$$E_{tot} = E_{loop} - E_{strain} \pm E_{step} \quad (1.22)$$

where the step energy is positive for creation and negative for the removal of a step on the free surface. In Figure 1.9 E_{tot} , E_{strain} , E_{loop} and E_{step} are reported for 60° dislocation nucleation in a $\text{Si}_{0.7}\text{Ge}_{0.3}/\text{Si}$ as a function of R . It is worth to note that E_{tot} presents a maximum, with barrier height δE at the critical radius R_c . In Figure 1.10 it is clearly shown

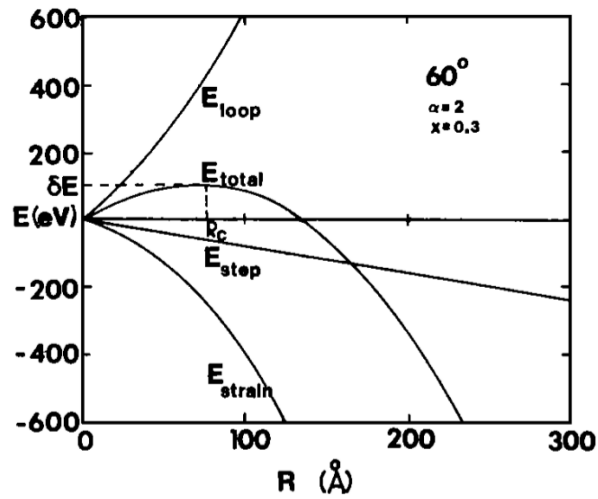


Figure 1.9: Energy variation as a function of dislocation half-loop radius R for $\text{Si}_{0.7}\text{Ge}_{0.3}/\text{Si}$ [46].

that both δE and R_c are strongly dependent on the lattice strain ε , i.e. increasing the Ge content in the epilayer the homogeneous nucleations of half-loops is favoured.

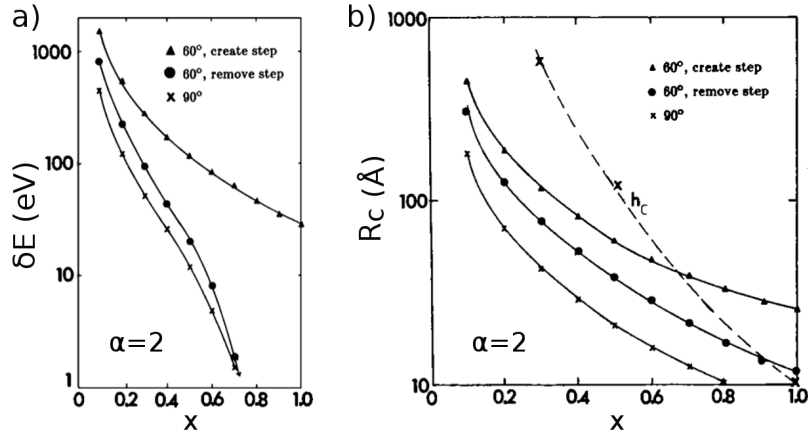


Figure 1.10: a), b) Barrier energy δE and critical radius R_c respectively, as a function of Ge content in the epilayer [46]

The above mentioned nucleation mechanisms of dislocations have different activation energy, thus a hierarchy, as a function of growth temperature and lattice strain is expected [41]. In Figure 1.11 a sketch representing the hierarchical order of the different nucleation mechanism is presented. The y axis qualitatively shows the activation energy of the nucleation mechanism, which is depending mostly on the growth temperature T and the lattice strain ε . In case of low growth temperature and low lattice strain, only the fixed sources of dislocation are active, which have the lowest activation energy barrier. After the formation of the first dislocations,

their interaction and multiplication become possible, thus increasing the relaxation of the epilayer. For higher strain and growth temperature, other nucleation sources, like heterogeneous or homogeneous surface half-loop, starts to be active. If these sources are predominant, they form a multitude of dislocation half-loops starting from the epilayer surface reaching the heterointerface, hence the interaction a multiplication probability is largely increased, developing an high threading an misfit dislocation density.

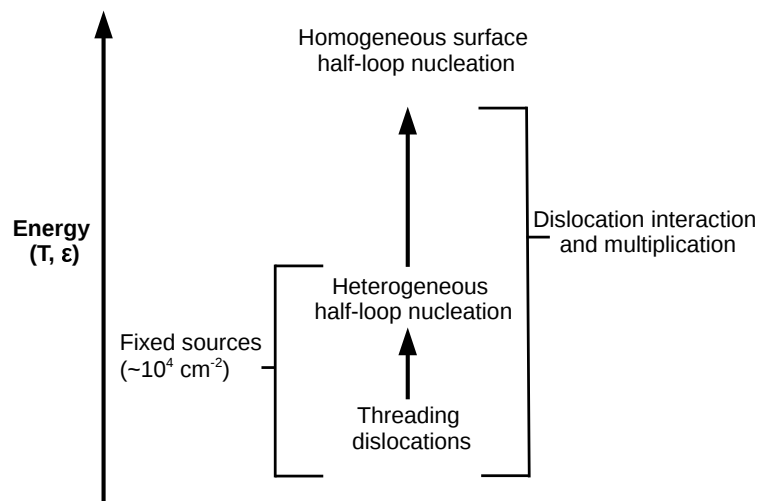


Figure 1.11: Schematic illustrating the hierarchy of the different nucleation processes of misfit dislocations [41].

The increase of the lattice misfit between the $\text{Si}_{1-x}\text{Ge}_x$ epilayer and the $\text{Si}(001)$ substrate strongly affects the nature of MDs [42, 46–50]. In the case of low misfit (Ge content $\lesssim 0.25$ -0.4, depending on the growth conditions) mostly only standard 60° dislocations are present. 60° dislocations belong to the primary slip system in diamond structure, they are characterized by Burger's vector $\mathbf{b} = a/2\langle 110 \rangle$, forming an angle of 60° with the MDs at the heterointerface running along the $\langle 110 \rangle$ directions and glide planes $\{111\}$, as shown in Figure 1.12.

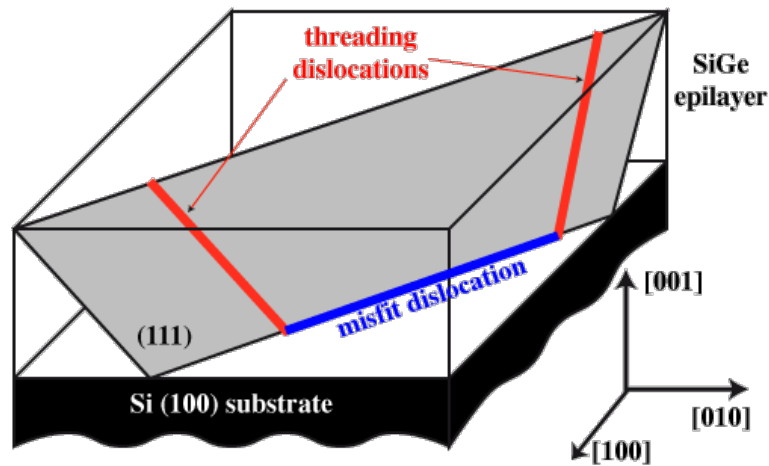


Figure 1.12: Schematic of 60° MD (blue) running along the $[110]$ direction. The (111) glide plane is shown in grey colour and TDs in red (courtesy from Prof. D. J. Paul).

The Burger’s vector of 60° MD is able to release only 50 % of the misfit released by a pure edge 90° dislocation since it isn’t laying in the (001) interface plane. Nevertheless, 60° dislocations move by pure gliding, while 90° edge dislocations (called also Lomer dislocations) are sessile, thus their formation is not favoured in a stressed epitaxial layer under relaxation. It has been reported and calculated [42, 48] that in case of high lattice misfit (Ge content $\gtrsim 0.4-0.5$) the population of MDs moves from predominantly 60° to 90° , especially in case of thermal annealing treatments [51]. Thus the population of 90° dislocation increases with both the temperature and the lattice misfit. Indeed in these conditions, thanks to high mobility and large number of dislocations loops, respectively given by the temperature and the lattice mismatch, the interaction and reaction between dislocations are favoured. Bolkhovityanov *et al.* [52] have demonstrated that the formation of Lomer dislocations can be attributed to the interaction of two 60° dislocations followed by a climbing process. The reported mechanisms are listed below.

- Random meeting of two complementary 60° MDs. In this case two complementary (e.g. $\mathbf{b}_1 = a/2[10\bar{1}]$ and $\mathbf{b}_2 = a/2[011]$) 60° dislocations gliding in two mirror like

{111} planes are crossing at the heterointerface followed by a climbing process.

- Crossing of two complementary 60° MDs on misoriented substrate.
- Cross-slipping of a secondary 60° MD. This process requires the interaction of a pre-existing 60° MD with another complementary one which is perpendicular.
- Induced nucleation of a secondary complementary 60° MD. In this case the nucleation of a complementary 60° dislocation loop is favoured by the strain field of a pre-existing 60° MD, thus enhancing their interaction probability.

1.3 Thermal strain induced problems

The epitaxial integration of dissimilar semiconductors suffers also from the difference in thermal expansion coefficients. Indeed in the Ge/Si case, the lattice mismatch is plastically relaxed by MDs at the growth temperature (typically $\sim 400 - 600^\circ\text{C}$ for LEPECVD). Subsequently during the cooling of the sample from the growth temperature (T_H) to room temperature ($T_L = 300\text{K}$), the substrate and epitaxial layer lattices contracts differently [53]. In particular, the lattice shrinkage of Ge is larger than the one of Si, according to the respective thermal expansion coefficients reported in equations 1.23, 1.24 [54, 55].

$$\alpha_{Ge}(T) = 6.05 \times 10^{-6} + 3.6 \times 10^{-9}T + 0.35 \times 10^{-12}T^2 \quad (K^{-1}) \quad (1.23)$$

$$\alpha_{Si}(T) = 3.725 \times 10^{-6} \left[1 - e^{-5.88 \times 10^{-3}(T-124)} \right] + 5.548 \times 10^{-10}T \quad (K^{-1}) \quad (1.24)$$

Where α_{Ge} and α_{Si} are respectively the thermal expansion coefficients of Ge and Si as a function of temperature T. The difference between α_{Ge} and α_{Si} , as a function of temperature,

results in the accumulation of tensile strain ε_{\parallel} in the Ge layer [20] according to equations 1.25 and 1.26.

$$\varepsilon_{\parallel} = (1/r) \frac{Y_{Ge}t_{Ge}^3 + Y_{Si}t_{Si}^3}{6Y_{Ge}t_{Ge}(t_{Ge} + t_{Si})} \quad (1.25)$$

$$1/r = \frac{6Y_{Ge}Y_{Si}t_{Ge}t_{Si}(t_{Si} + t_{Ge}) \int [\alpha_{Si}(T) - \alpha_{Ge}(T)] dT}{3Y_{Ge}Y_{Si}t_{Ge}t_{Si}(t_{Si} + t_{Ge})^2 + (Y_{Ge}t_{Ge} + Y_{Si}t_{Si})(Y_{Ge}t_{Ge}^3 + Y_{Si}t_{Si}^3)} \quad (1.26)$$

Where r is the curvature radius of the wafer (see Figure 1.13 a)), Y_{Ge} , Y_{Si} the Young's moduli and t_{Ge} and t_{Si} the thickness respectively of the Ge layer and the Si substrate. Capellini *et al.* [56] showed that ε_{\parallel} accumulated during the cooling from T_H to T_L cannot be completely plastically relaxed due to the hardening of the material caused by the blocking of MDs gliding. Thus the epitaxial layer tends to relax the tensile ε_{\parallel} inducing bowing or generating cracks [57]. Both mechanisms are strongly affecting the possibility to further process the wafer due to the increase of the brittleness and the difficulty to perform any lithographic step [58].

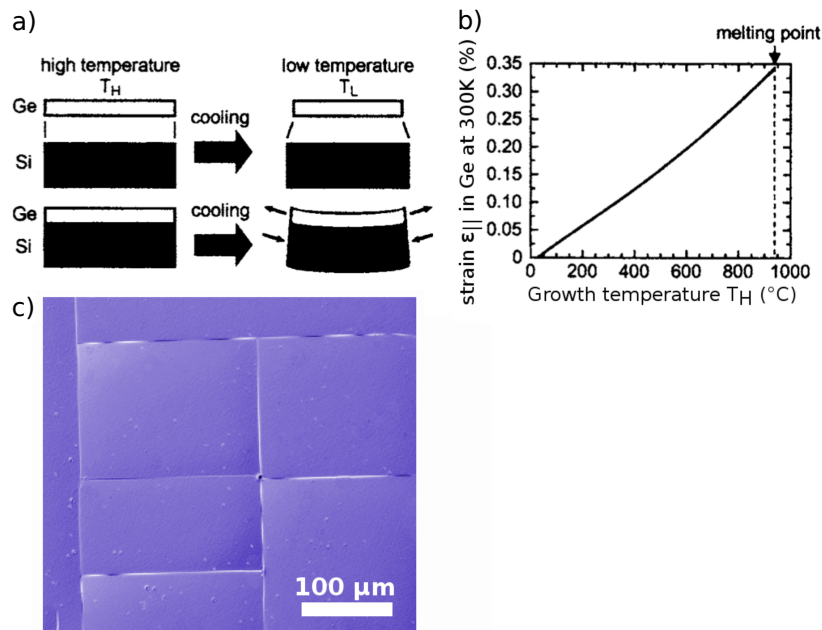


Figure 1.13: a) Sketch of the Si substrate and Ge epilayer thermal contraction from the growth temperature T_H to room temperature T_L in case of separated (upper case) and bounded crystals (lower case) [20]. b) Calculated thermal strain $\epsilon_{||}$ at room temperature as a function of the growth temperature T_H for 1 μm thick Ge layer on 500 μm thick (001) Si substrate [20]. c) Nomarski microscope image of 50 μm thick Ge layer (grown at 500°C) on (001) Si substrate, thermal cracks are clearly visible as lines running in the $\langle 110 \rangle$ directions.

1.4 Gallium nitride: physical properties

III-nitrides, such as GaN, AlN and InN have three different crystal structures: wurtzite, zinc blende and rock salt [59]. The rock salt structure can be obtained only in conditions of very high pressure, thus it isn't discussed here. The zinc blende structure has a cubic unit cell where the two *face centered cubic (fcc)* sub-lattices of metal (Ga, Al or In) and N are interpenetrated along the body diagonal with $a_0/4$ offset, where a_0 is the relaxed lattice parameter. The group space of zinc blende structure is $F\bar{4}3m$. Each atom is surrounded by 4 different atoms situated in the corners of a tetrahedron and the stacking sequence of the (111) close-packed planes in the zinc blende structure is ABC (see Figure 1.14 c)). The wurtzite structure, which has group space $P6_3mc$, consists of an hexagonal unit cell characterized by two lattice constants: c_0 and a_0 . a_0 is the basal edge of the relaxed hexagonal cell, while c_0 is the height, in the unit cell 6 atoms of each type are present. The wurtzite structure is made by two interpenetrating *hexagonal closed packed (hcp)* sublattices one for N and one for the metal, which are displaced by $5c/8$ along the

[0001] direction. Also in this case each metal atom is surrounded by 4 N placed at the corners of a tetrahedron, but differently from the zinc blende case, the stacking sequence of closest-packed (0001) planes is ABAB in the [0001] direction, called also *c*-axis (see Figure 1.14 b)).

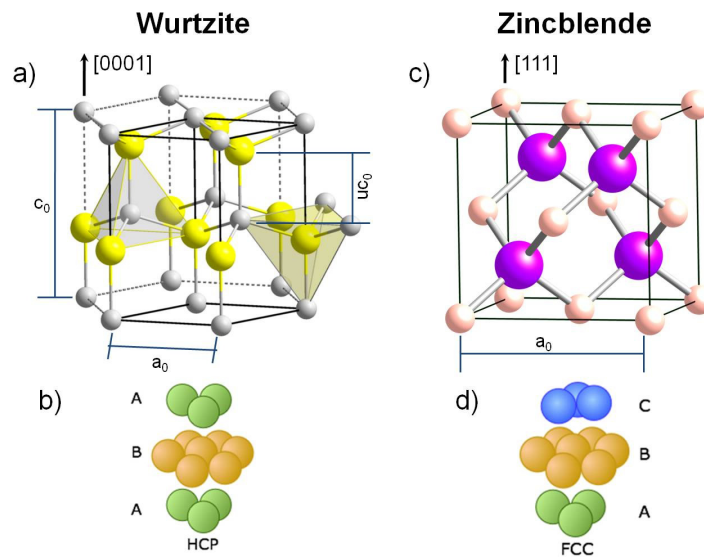


Figure 1.14: a) Balls and sticks crystal structure of wurtzite GaN. Metal atoms are drawn in yellow, while N in grey. b) stacking sequence of (0001) planes along the *c*-axis. c) Balls and sticks crystal structure of zinc blend GaN. Metal atoms are drawn in violet, while N in grey. d) stacking sequence of (111) planes along the [111] direction [60].

Since in the wurtzite structure, there is no inversion plane

perpendicular to the $[0001]$ direction, the crystal surface could have either both a metal element (Ga, Al or In) polarity (called Ga-polarity) or N-polarity. The Ga-polarity surface plane is also called (0001) or $(0001)A$ and the N-polarity one $(000\bar{1})$ or $(0001)B$ as reported in Figure 1.15. The different polarity of III-N strongly influences the polarization field within the crystal and the surface properties [61].

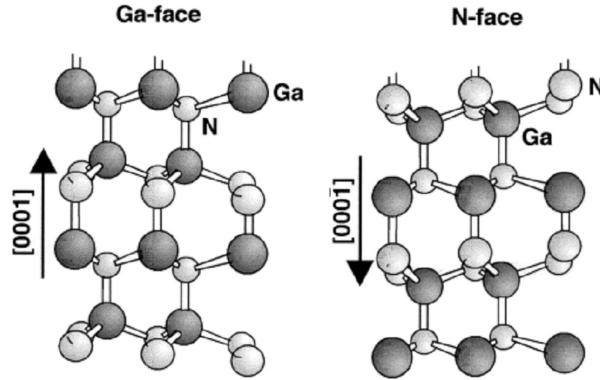


Figure 1.15: Different polarities of GaN: Ga-polarity labeled as Ga-face and N-polarity labeled as N-face [62].

The most relevant crystalline family planes and directions for wurtzite GaN are respectively: (0001) - c , $(1\bar{1}00)$ - m and $(11\bar{2}0)$ - a (see Figure 1.16). The basal (0001) plane is typically the most used for epitaxial growth, while the high

symmetry $\langle 1\bar{1}00 \rangle$ and $\langle 11\bar{2}0 \rangle$ directions are employed during the deposition to check by reflection high-energy electron diffraction (RHEED) the morphology of the crystal. In the

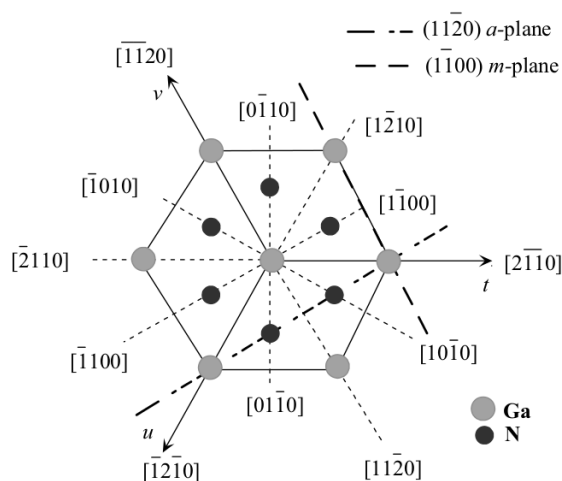


Figure 1.16: Most important crystalline direction in GaN projected on the (0001) basal plane [59].

wurtzite structure, the metal-N bond length normalized by the c constant is called the internal u parameter, the values of u and axial ratio are respectively $u=3/8=0.375$ and $c/a=\sqrt{8/3}=1.633$.

1.5 GaN epitaxial growth

Here we describe the different growth conditions to deposit epitaxial GaN by *plasma assisted molecular beam epitaxy* (PA-MBE), more details about this technique are given in section 2.1.2. Let us consider all the surface processes which are involved in the epitaxial growth of the GaN crystal:

1. adsorption
2. desorption
3. surface diffusion
4. incorporation
5. decomposition

All the processes listed above and schematically shown in Figure 1.17, are competing with each other during PA-MBE epitaxial deposition and can influence differently the morphology and quality of the deposited crystal. Adsorption represents the process in which atoms impinging on the substrate surface are physisorbed overcoming an activation barrier E_a . If we consider an uniform solid surface exposed to a

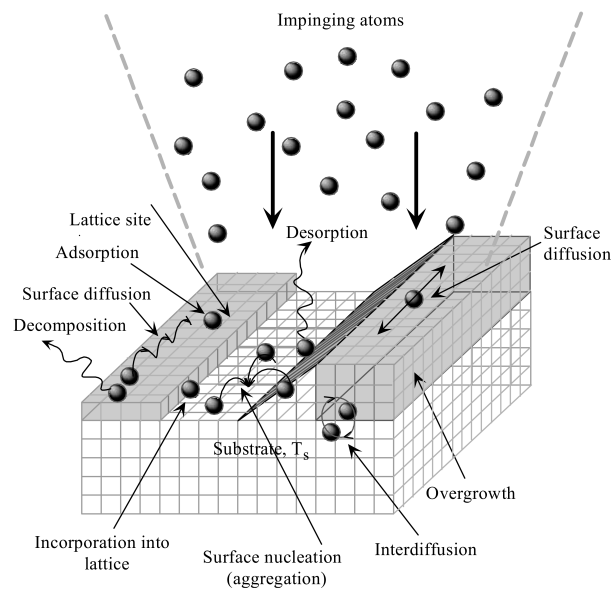


Figure 1.17: Schematic of the kinetic growth processes during the epitaxial deposition by PA-MBE: adsorption, desorption, surface diffusion, incorporation and decomposition [59].

gas, the adsorption rate r_a could be defined as follows:

$$r_a = \sigma f(\Theta) \exp(-E_a/k_B T_s) \frac{p}{\sqrt{2\pi m k_B T_s}} \quad (1.27)$$

where σ is the condensation coefficient which takes in to account the accommodation energy of the adsorbed species, $f(\Theta)$ is a function depending on the surface coverage which describes the probability to find a free adsorption site, $\exp(-E_a/k_B T_s)$ is the activation Boltzmann term for the adsorption process, being k_B and T_s respectively the Boltzmann constant and the substrate temperature, and p is the partial pressure of the adsorbing species. It has been found that only a maximum of 2.5 ± 0.2 MLs of Ga are stable on the GaN surface, larger coverages turn to form liquid Ga droplets [63–65].

Desorption is the process in which the adsorbing atoms, thanks to their thermal energy, can leave the crystal surface overcoming an activation energy barrier E_{des} . The desorption rate r_{des} thus strongly depends on the binding energy of the adsorbed atoms with the crystal surface and it can be

expressed by the following equation.

$$r_{des} = \sigma^* f^*(\Theta) \exp(-E_{des}/k_B T_s) \quad (1.28)$$

where σ^* is the desorption coefficient, $f^*(\Theta)$ is the function describing the desorption probability as a function of surface coverage and $\exp(-E_{des}/k_B T_s)$ represents the Boltzmann term for desorption. The desorption energy E_{des} , eventually, takes into account the chemical binding energy with the surface: $E_{des} = E_{ads} + E_{binding}$. The lifetime τ of the adsorbed species, defined as the average time they spend on the crystal surface after the adsorption process, is used to estimate the desorption energy. τ can be expressed by the following Arrhenius expression and measured by RHEED and mass spectroscopy [66]

$$\tau = \tau_0 \exp\left(\frac{E_{des}}{k_B T_s}\right). \quad (1.29)$$

Surface diffusion is the process describing the motion of the adsorbed species on the crystal surface due to the finite substrate temperature. From the microscopic point of view, it is a thermal activated process since atoms, to diffuse towards the next neighboring crystalline site, have to

overcome the lattice barrier potential. The diffusion length λ of the adsorbed species exponentially depends on the substrate temperature: $\lambda = 2\sqrt{D\tau}$ where D is the diffusivity ($D = D_0 \exp(-E_{diff}/k_B T_s)$). At high T_s , λ can be larger than the average width of atomic terraces on the crystal surface, thus ensuring a step-flow growth where atoms move by surface diffusion from the terrace to the step edge where they crystallize. In this way a smooth crystal surface is obtained. For shorter values of λ (e.g. lower T_s), atoms interact and crystallize on the terraces before reaching a step edge or the border of a pre-existing island. These conditions lead to the formation of rough surfaces and 3D growth mode. In the case of GaN, the diffusivity difference of the 2 atomic species is large. Zywietz *et al.* [67] calculated the surface potential energy for N and Ga on the Ga-polar (0001) crystal surface, finding two transition sites. As shown in Figure 1.18, in the case of Ga diffusion, the highest energy site is the *on-top* position (>3 eV), while the lowest energy site is the *bridge* (0.4 eV). On the other hand, for N the barrier energy for *on-top* position is similar to Ga, while the *bridge* one is 1.4 eV. Thus, at the typical growth temperatures ($T_s \sim 700^\circ\text{C}$) the surface diffusivity of N atoms is much smaller than the

one of Ga. Moreover the excess of N atoms on the crystal surface can reduce the Ga diffusion increasing its diffusion barrier from 0.4 to 1.8 eV.

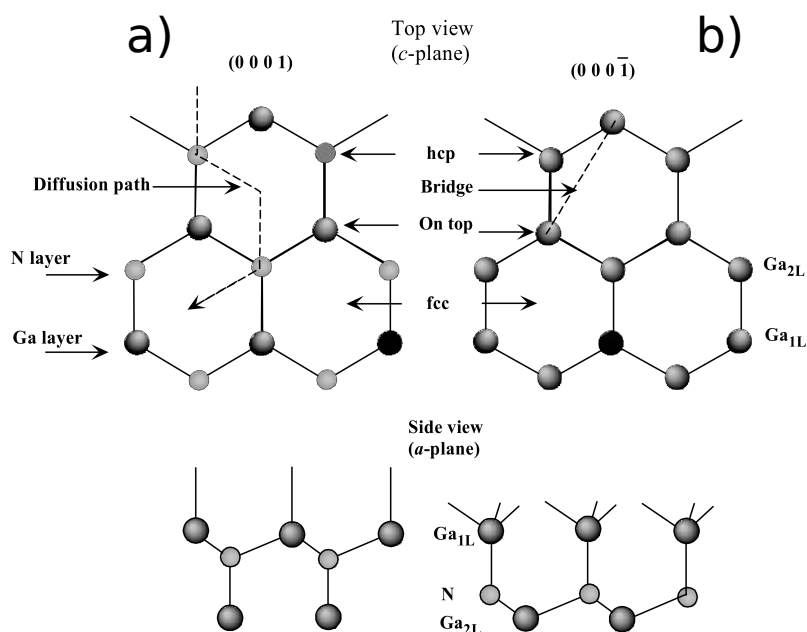


Figure 1.18: a), b) schematic drawing of the diffusion paths for atoms on the GaN surface, respectively Ga-polar and N-polar. In the lower part side views are also reported [67].

During the incorporation process Ga and N atoms bond on the crystal surface, this process strongly depends on the interplay between the growth kinetics and thermodynamic. The GaN growth rate (v_g) depends on the Ga and active

nitrogen atoms $N_{(g)}^*$ fluxes impinging on the substrate, called respectively Φ_{Ga} and Φ_N [68]. The morphology of the GaN layer strongly depends on the ratio between Φ_{Ga}/Φ_N . Indeed at the growth temperature, Ga atom desorb with a flux Φ_{des}^{Ga} , thus influencing the real III/V ratio on the crystal surface (see Figure 1.19). Thus, at a fixed growth temperature, it is possible to define three different growth regimes depending on the Ga/N surface ratio.

1. *N-rich regime* if $\Phi_N > \Phi_{Ga}$
2. *intermediate regime* if $\Phi_{Ga} - \Phi_N < \Phi_{des}^{Ga}$
3. *droplet or Ga-rich regime* if $\Phi_{Ga} - \Phi_N > \Phi_{des}^{Ga}$

As reported in Figure 1.20, depending on the growth regime, the morphology and quality of the GaN layer can be different. In the *N-rich regime* ($\Phi_N > \Phi_{Ga}$), the deposition rate is limited by the Ga flux and the N excess desorb from the surface. In this condition, the mobility of the Ga atoms is hindered by the large amount of reactive N atoms leading to the so called 3D growth where smooth plateaus, separated by steep valleys are formed. In this condition the growth of GaN nano-wires is possible [70]. In the case of *intermediate-regime* ($\Phi_{Ga} - \Phi_N < \Phi_{des}^{Ga}$), the excess of Ga desorbs from the

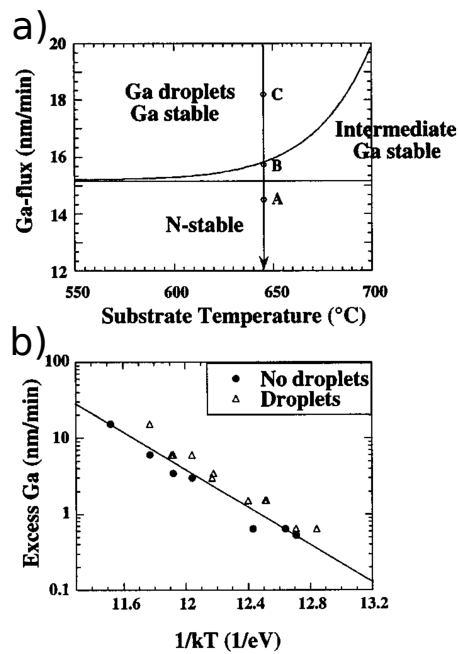


Figure 1.19: a) diagram of the GaN surface structure describing the three different *droplet*, *intermediate* and *N-rich regimes* as a function of Φ_{Ga} and T_s with $\Phi_N=15.2$ nm/min. b) excess of Ga as a function of $1/k_B T_s$ [69].

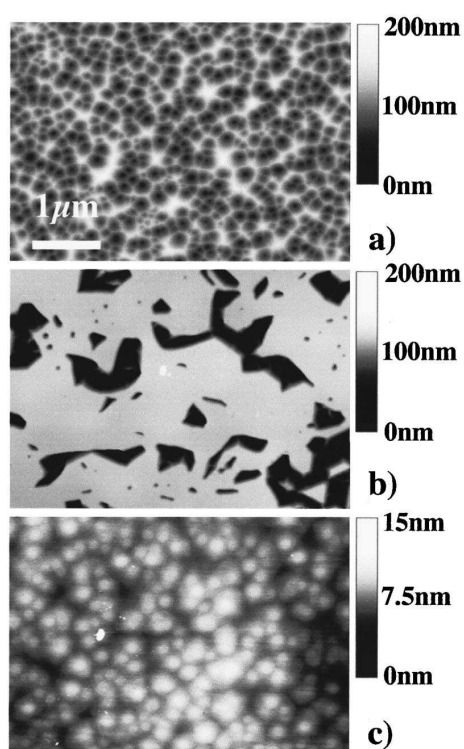


Figure 1.20: AFM images of GaN crystals grown in different conditions: a) *N-rich regime*, b) *bilayer* or *Ga-stable regime*, c) *droplet* or *Ga-rich regime* [69].

GaN surface [71]. Under steady-state conditions, it has been shown that a stable Ga-layer ranging from 0 to 2.5 MLs is formed on the Ga-polar GaN surface [72]. The liquid Ga layer promotes the diffusivity of the adatoms enabling the deposition of 2D-smooth films [69, 73]. In the *Ga-rich regime*, the high Φ_{Ga} or low T_s , generate large accumulations of liquid Ga on the crystal surface, leading to the formation of micrometer-sized Ga droplets. Also in this condition the resulting GaN crystal morphology is characterized by rougher surface as compared to the *intermediate regime* case.

Depending on the substrate temperature T_s and pressure, GaN decompose i.e. Ga-N bondings are broken and the atomic species leave the crystal surface instead of melting. Guha *et al.* [63] found that the decomposition rate is between 3-4 MLs/minute at $T_s \sim 830^\circ\text{C}$ while Grandjean *et al.* [74] reported a negligible decomposition rate decomposition below 750°C and a rapid increase up to $1\mu\text{m/h}$ at 850°C . Thus, the epitaxial growth of GaN by PA-MBE (typical chamber pressure $\sim 5 \times 10^{-5}\text{torr}$) is limited to a maximum $T_s \sim 850^\circ\text{C}$. Different mechanisms have been proposed to describe the decomposition process which consider the formation of gaseous Ga and N, liquid Ga and gaseous N or the

sublimation of GaN [75].

Chapter 2

Experimental

In this chapter the growth techniques, the fabrication process of the Si substrates and the characterizations tools which have been used to assess the morphology and quality of 3D $\text{Si}_{1-x}\text{Ge}_x$ and GaN micro-crystals will be discussed.

2.1 Epitaxial growth techniques

2.1.1 LEPECVD

The epitaxial deposition of $\text{Si}_{1-x}\text{Ge}_x/\text{Si}$ here considered has been performed by low-energy plasma-enhanced chemical vapour deposition (LEPECVD) [76, 77]. LEPECVD has

been demonstrated to be a suitable technique to grow several high quality Ge based electro-optical devices on Si [78–81]. The schematic of the LEPECVD reactor is reported in Figure 2.1.

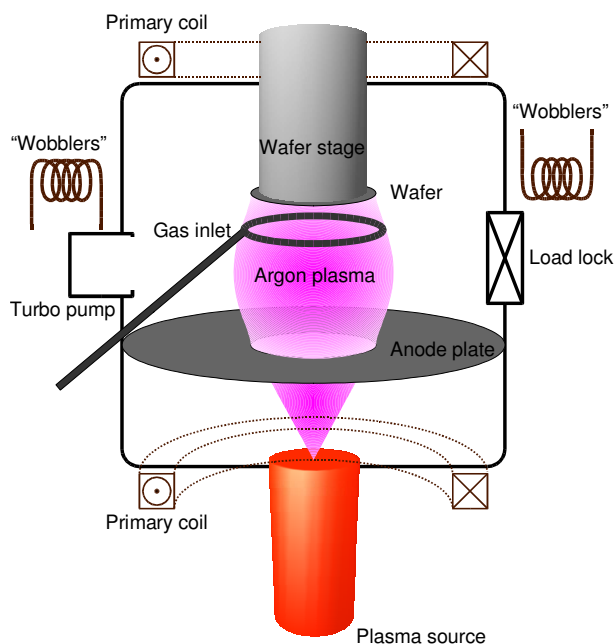


Figure 2.1: Schematic of the LEPECVD reactor.

The LEPECVD technique has been invented and developed in the late '90s by Prof. Hans von Känel at ETH Zürich [82, 83] to grow fastly (up to 10nm/s) and epitaxially high quality pure Ge and $\text{Si}_{1-x}\text{Ge}_x$ alloys on Si. In LEPECVD, the activation energy to break the precursor molecules in

the gaseous phase is supplied by a DC Ar plasma, guaranteeing the decoupling between the substrate temperature and the chemical processes occurring at the epilayer surface. In this approach the Ge content of the epilayer is determined almost completely by the reactive gases mixture and the plasma conditions, being independent from the substrate temperature. A typical problem of thermal-CVD which can be circumvented by LEPECVD, is the possibility to tune the $\text{Si}_{1-x}\text{Ge}_x$ deposition rate independently from the temperature of the Si substrate. This fact avoids several drawbacks related especially to the deposition of epilayers at high temperature, such as intermixing, island formation and surface roughening. Indeed, thanks to the large out-of-equilibrium growth conditions (high growth rate and low growth temperature) of LEPECVD, thick, high quality (TD density $\sim 5 \times 10^6 \text{cm}^{-2}$) and smooth (RMS $\lesssim 1 \text{ nm}$) Ge-rich buffers have been achieved [84–86]. The working principles of LEPECVD are described below. The DC Ar plasma discharge is generated by a Balzers ULS 400 plasma source directly attached to the lower part of the growth chamber. The plasma source consists in a hot tantalum filament (130 A DC) positioned in a cylindrical metallic chamber with a

1cm wide orifice in the upper part. The Ar gas is directly injected in this chamber. The thermionic emitted electrons from the filament are extracted setting a potential difference of about 30 V between the filament itself and the grounded sample holder and chamber walls which act as anode. Typical arc discharge currents are in the range 30-50 A. Moreover, an additional ring-shaped anode plate positioned just below the sample holder is present to further control the geometry of the Ar plasma. The reactive gases: SiH₄ and GeH₄ for growing Si_{1-x}Ge_x alloys, PH₃ and B₂H₆ for doping, H₂ for cleaning or as a surfactant, are injected through a ring placed a few centimeters from the substrate to ensure an homogeneous distribution of the feeding precursors. The substrate is inserted from the load-lock chamber (pressure $\sim 5 \times 10^{-7}$ mbar) in the top part of the reactor. Its potential during the growth is controlled and maintained to $V_{sub} = -11$ V to reduce the energy of the impinging ions, preventing the damage of the epitaxial surface by high energy bombardments. The Si_{1-x}Ge_x growth rate can be finely tuned in a broad range, from 10 nm/s to 0.01 nm/s, changing both the gaseous fluxes and the plasma intensity or geometry. The gaseous fluxes are controlled by mass flow controllers with

maximum flux of 25 sccm for pure GeH_4 and SiH_4 and 10 sccm for PH_3 and B_2H_6 (respectively 5 % and 1 % diluted in Ar). A precise control (1 s of delay) for the switching of the gas lines is performed by pneumatic valves. The plasma intensity and geometry can be respectively changed by regulating the emitted current from the Ta filament and changing the intensity of the current passing through the external magnetic confining coils generating a field $B \sim 1\text{-}10$ mT. More details about the plasma characteristics of LEPECVD can be found in [87, 88]. The substrate heater consists in a graphite susceptor embedded in two boron nitride disks, which allows to reach about 800°C for 4" Si substrates. The temperature is read by a C-type thermocouple positioned at the back of the heater. The thermocouple reading is calibrated by measuring with a pyrometer the temperature of a dummy Si wafer. The LEPECVD chamber is pumped by a turbomolecular pump to a base pressure of $\sim 3 \times 10^{-9}$ mbar, while during the growth it is $\sim 3 \times 10^{-2}$ mbar.

2.1.2 PA-MBE

The epitaxial deposition of GaN crystals on patterned Si(001) substrates has been performed using the M1 plasma-

assisted molecular beam epitaxy (PA-MBE) reactor at the Paul-Drude-Institut in Berlin during my Ph.D. internship under the guidance of Dr. R. Calarco.

A picture showing the M1 PA-MBE reactor is reported in Figure 2.2.

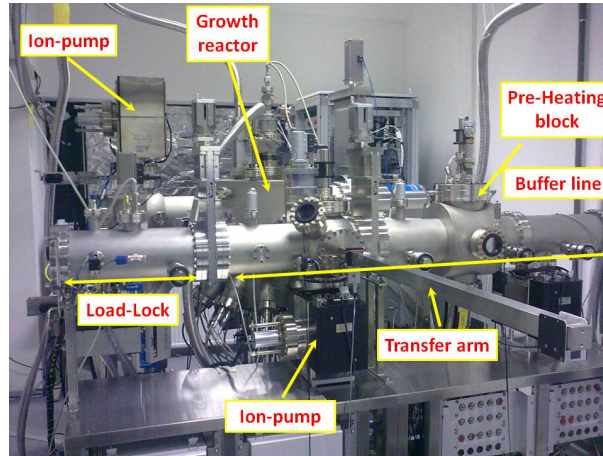


Figure 2.2: Picture of the PA-MBE M1 reactor at Paul Drude Institut in Berlin [60].

The M1 reactor consists in a commercial P600 MBE system for nitrides constructed by DCA instruments. As reported in Figure 2.2, it comprises i) a load-lock chamber, ii) a buffer-chamber, and iii) the growth chamber. The clean substrates are introduced into the load-lock chamber where they are heated up to $\sim 130^\circ\text{C}$ and transferred into the buffer-

chamber when the pressure is 3×10^{-8} torr. In the buffer-chamber the pressure is typically $\sim 3 \times 10^{-10}$ torr (a 240 l/s Gamma Vacuum 300L ion pump is installed), substrates can be mounted on a 3" manipulator and heated up to 1000°C for further degassing. Typically the substrates are stored here. The growth chamber is equipped with 12 ports for effusion Knudsen cells and other devices such as nitrogen ADDON water-cooled RF plasma source, a Pfeiffer Vacuum quadrupole mass spectrometer and pyrometer. A schematic of a MBE plasma source is reported in Figure 2.3.

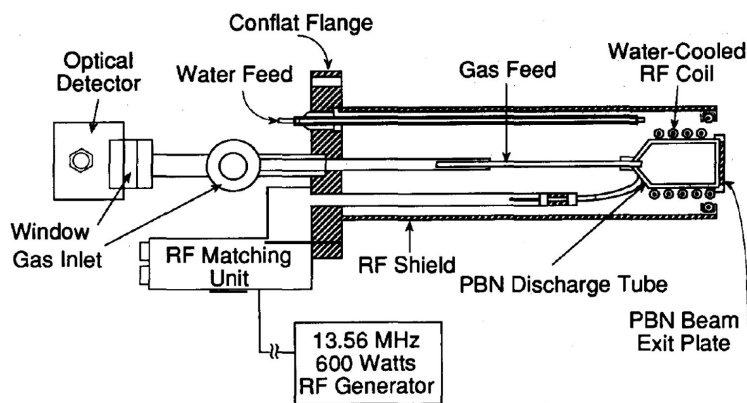


Figure 2.3: Schematic of MBE nitrogen plasma source [89].

The nitrogen gas injected into the plasma source is 6.0 grade, further purified to 5 ppb by a getter filter. The ni-

nitrogen flux is controlled by a MKS Instruments PR 4000B-F mass flow controller, and the typical flux that has been used is 3 ml/minute. Into the nitrogen plasma source, a 13.56 MHz radio frequency voltage is fed by means of an Advanced Energy Cesar RF power supply unit (maximum power 600 W) to generate the nitrogen plasma within an hollow pyrolytic boron nitride (PBN) cylinder pointing towards the sample. The efficiency of the plasma generated into the PBN cylinder, is controlled by a coupled matching unit which enables to minimize the RF reflected power. The ignition and stability of the nitrogen plasma is constantly controlled by an optical photo-diode measuring the emitted light intensity. The typical growth conditions: nitrogen flux 3ml/min and plasma power=400 W, guarantee a GaN growth rate (in Ga-rich conditions) of 2.34 nm/min.

The substrate is mounted on a 3" manipulator which can heat up the patterned silicon $1 \times 1 \text{ cm}^2$ substrate up to $\sim 810^\circ\text{C}$. The substrate temperature is controlled by a pyrometer, placed in the bottom part of the chamber and pointing perpendicular to the sample surface, and by a W-Re thermocouple located on the back side of the substrate. Additionally, in situ RHEED and laser reflectometry [90] system are

mounted in the growth chamber to check the surface quality of the GaN crystals during the epitaxial deposition.

2.2 Preparation of patterned silicon substrates

The patterning of the (001) silicon substrates (100 mm, n-type 3-7 Ωcm) has been performed by standard optical lithography and Bosch process by Dr. P. Niedermann at the CSEM in Neuchâtel. The Bosch process consists in the repetition for several times of a deep reactive ion etching step by SF_6 plasma, followed by the deposition of a protective C_4F_8 layer on the lateral sidewalls. Thanks to the fast and high anisotropic etching, this process is widely used for the fabrication of Si-based micro systems [91]. The repetition of etching/passivation cycles, leads to the formation of typical scallops on the lateral sidewalls of the Si structures, which are not critical for the epitaxial deposition of $\text{Si}_{1-x}\text{Ge}_x$ crystals. Eventually, the wavy sidewalls of the Si structures could be passivated by 100 nm thick thermal oxide, thus favoring the epitaxial deposition only on the top (001) surface. The silicon patterned substrates contain several 8×8

mm^2 areas consisting in dense arrays of $8 \mu\text{m}$ tall pillars. In each patterned area, squared Si pillars aligned along the $\langle 110 \rangle$ directions, with different side d and separation are present. Moreover some patterned areas contain ridge structures aligned along both the $\langle 110 \rangle$ and $\langle 100 \rangle$ directions. The lateral size of the Si pillars is: 2, 5, 9 and $15 \mu\text{m}$, while the trench width is: 1, 2, 3, 4, 5 and $50 \mu\text{m}$. Figure 2.4 and 2.5 report respectively SEM images of Si pillars with and without lateral passivation.

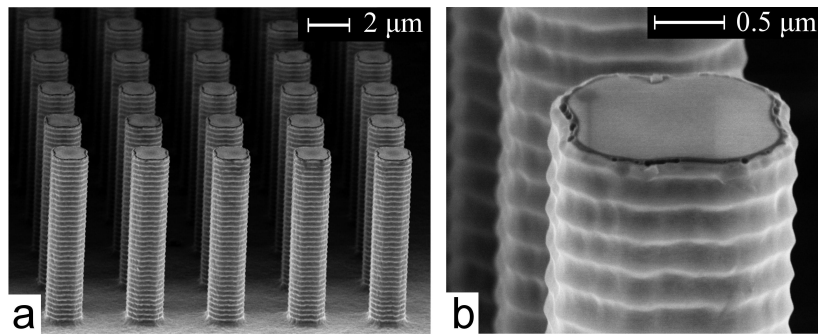


Figure 2.4: SEM micrograph of $2 \times 2 \mu\text{m}^2$ Si pillars, separated by $2 \mu\text{m}$ wide trenches with lateral oxide passivation. a) Perspective view, b) magnification of the top (001) surface of a single pillar.

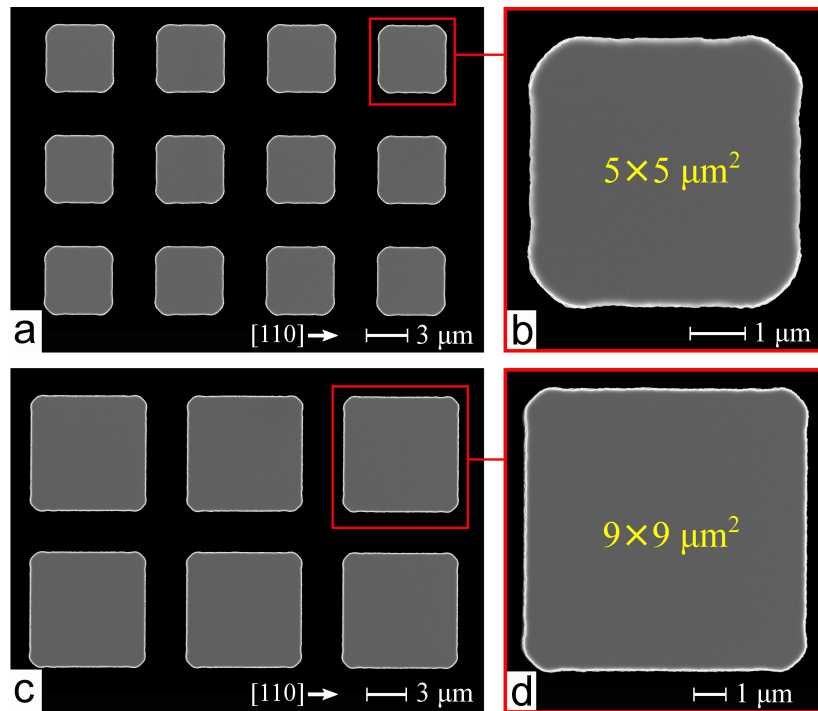


Figure 2.5: Top view SEM images of Si pillars with different lateral size without oxide passivation. a) $5 \times 5 \mu\text{m}^2$ with $3 \mu\text{m}$ wide trenches, b) magnification of the top (001) surface of one pillar shown in a). c), d) same of a) and b) for $9 \times 9 \mu\text{m}^2$ Si pillars with $3 \mu\text{m}$ wide trenches.

Each patterned area is surrounded by a 2 mm wide un-patterned frame, thus in one single deposition, it is possible to compare the morphology of crystals deposited on Si pillars with different characteristics and with that one of the planar epilayers.

Sub-micrometer sized Si pillars have also been patterned by means of electron beam lithography (EBL) and cryogenic deep reactive ion etching (DRIE) [92], resulting in smooth lateral sidewalls without scallops typical of the Bosch process. The patterning of these substrates has been performed by D. Colombo at PGT Photonics in Milano. In this case, a 640 nm thick DUV-5 positive resist has been spun on the Si (001) substrate and the EBL writing process has been performed by VISTEC VB6UHR with an acceleration voltage of 100kV and a dose of $30 \mu\text{C cm}^{-2}$ to avoid proximity effects. The anisotropic etching of the Si (001) substrates has been performed using the inductive coupled plasma DRIE Plasmalab System 100 with the operating parameters reported in Table 2.1 In this way, arrays of square Si pillars, 1.8 μm tall, with lateral side $d = 0.8, 1.3$ and $1.7 \mu\text{m}$, and separated by 200 nm wide trenches have been fabricated. The feature size of these sub-micrometer pillars is $\sim 1/10$ of the Bosch processed ones.

The patterned Si substrates have been cleaned by RCA standard procedure and before the epitaxial deposition, they have been dipped in a 5% diluted HF solution for 30s and rinsed in deionized water for 3 minutes to remove the silicon-

Table 2.1

Etching parameters used in the DRIE Plasmalab System 100 to obtain sub-micrometre patterned Si substrates with smooth lateral sidewalls.

	Substrate temperature (°C)	Gas pressure (mTorr)	ICP power (W)	Bias power (W)	SF ₆ /O ₂ flux ratio
Step 1	-100	10	2000	100	30/15
Step 2	-100	10	2000	100	100/15

oxide from the surface. Afterwards, the substrates are loaded into the LEPECVD reactor and kept for 10 minutes at 300° for degassing. Finally they are heated up to the growth temperature with a grading rate of 60°C/minute. SEM inspection after the cleaning procedure, revealed neither impurities or contamination on an area of at least 500 × 500 μm².

2.3 Characterization techniques

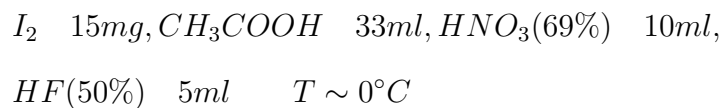
After the epitaxial growth, Si_{1-x}Ge_x and GaN crystals have been characterized by several techniques. The first analysis concerns the morphology and the structural properties of the epitaxial crystals by the following techniques:

- Nomarski microscope Nikon Eclipse 200D to analyze on a large scale the presence of defects, impurities and

thermal cracks.

- Scanning electron microscopy (SEM) to study the morphology of the crystals in terms of facet distribution, facet expansion and homogeneity. The SEMs which have been used are a Zeiss ULTRA 55 digital field emission and Philips xl30 FEG.
- Atomic force microscope (AFM), Veeco Innova model, to precisely measure the morphology of the crystals, the angles between different facets and their roughness.
- Laboratory high-resolution X-Ray diffraction (HR-XRD) to measure the composition and strain of the deposited crystals. The used laboratory diffractometer is a PANalytical X'Pert Pro-MRD, equipped with a 4-bounce Ge(220) crystal monochromator on the incident beam. For particular Ge crystals deposited on Si pillars, a detailed analysis on the crystal properties and quality has been performed at the european synchrotron radiation facility (ESRF) beamline ID-01 during the experiments HS-4674 and HS-4277. More details will be discussed in section 3.4 and chapter 5.

Moreover, the crystalline quality of the samples has been studied analyzing the density and character of dislocations. This analysis, for $\text{Si}_{1-x}\text{Ge}_x/\text{Si}$, has been performed by selective defect etching and counting of TDs by Nomarski microscope, AFM and SEM on an area of at least $200 \times 200 \mu\text{m}^2$. The character of dislocations has been investigated by transmission electron microscope (TEM) performing $\mathbf{g} \cdot \mathbf{b}$ analysis. TEM measurements have been performed by E. Müller at ETH Zürich and by H. Groiss at JKU in Linz. The TEM setups they have used are a JEOL JEM-2011 FasTEM and a Tecnai F30ST, respectively. Two different defect etching solutions have been used to reveal the TD density (TDD) depending on the Ge content: *Iodine* for $x \geq 0.9$ or *Secco* for Si richer alloys [93]. The chemical composition of the *Iodine* solution is the following:



While for the Secco solution:



The structural quality and the impact of TDD on the optical properties both of Ge and GaN crystals, have also been investigated by photoluminescence (PL) and cathodoluminescence (CL) spectroscopy, see respectively chapter 6 and 7 for further details.

The PL measurements of GaN crystals have been performed by C. Hauswald using the micro-PL setup *Horiba Jobin Yvon Labram HR 800 UV* at the Paul-Drude-Institut in Berlin, its schematic is reported in Figure 2.6. The excitation laser has

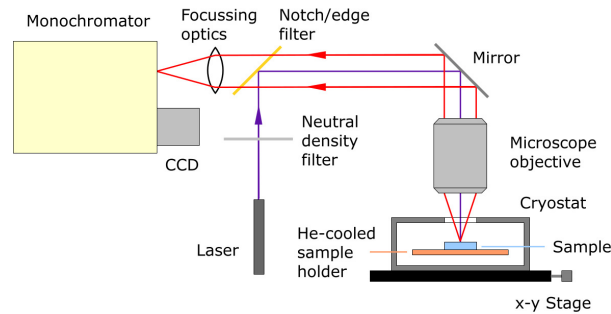


Figure 2.6: Schematic of micro-PL setup *Horiba Jobin Yvon Labram HR 800 UV* [94].

been performed using a 325 nm *Kimmon IK 3552R-G HeCd* laser with a maximum emitted power of 30 mW. The laser light is focused on the sample surface by a 40x objective to a spot size of $\sim 1.5 \mu\text{m}$. The emitted light is also collected by the same objective (confocal design). The monochromator is

equipped with a diffraction grating of 2400 lines/mm and it has a focal length of 80 cm. The detector is a liquid nitrogen cooled ISA Spectrum One CCD with 1024×256 pixels. The micro-PL measurements at 10 K have been performed using a Kriovac cryostat mounted on x-y moving stage which allows to map the micro-PL with a spatial resolution of about $0.25 \mu\text{m}$.

GaN/Si crystals have also been analyzed by CL spectroscopy by Dr. J. Lähnemann at the Paul-Drude-Institut in Berlin. The CL setup is a Gatan MonoCL 3 system attached to the Zeiss Ultra 55 field-emission SEM, its schematic is reported in Figure 2.7.

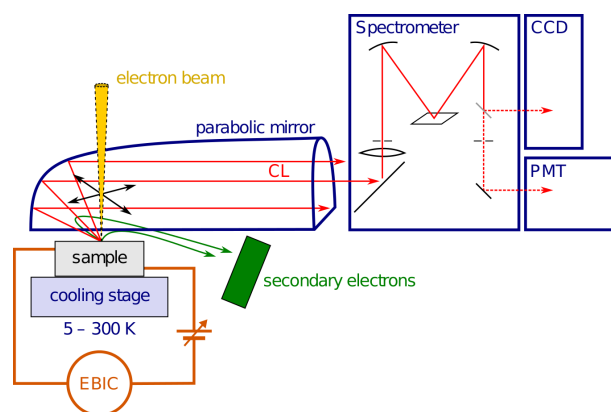


Figure 2.7: Schematic of CL setup used by Dr. J. Lähnemann at Paul Drude Institut (Berlin) [95].

The PL measurements of Ge/Si crystals have been performed under the supervision of Dr. F. Pezzoli at the Università degli studi di Milano Bicocca. The PL setup is sketched in Figure 2.8. The optical excitation is performed by a

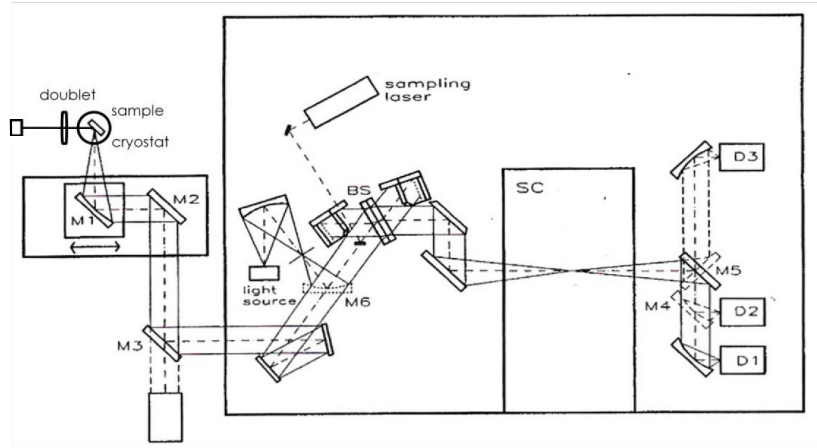


Figure 2.8: Schematic of the continuous wave laser PL setup used by Dr. F. Pezzoli at the Università degli studi di Milano Bicocca [96].

continuous-wave 1064 nm (1.165 eV) Nd:YVO laser with maximum excitation power up to 5 kW/cm^2 . The light which is emitted by the sample, after the mirrors M1, M2 and M3 is analyzed by a Fourier transform spectrometer Jasco FT-IR 800. Two different photodetector are mounted on the spectrometer: InGaAs for the spectral range between 1.38 and 0.73 eV and a Peltier cooled PbS photoresistance to

reach 0.4 eV. The sample is mounted in a Oxford Optistat AC-V12 cold finger closed circle cryostat which enables to measure the PL from 5 K to room temperature.

Chapter 3

3D heteroepitaxy of $\text{Si}_{1-x}\text{Ge}_x/\text{Si}$ crystals

In this chapter, the morphology, the growth conditions and modeling of $\text{Si}_{1-x}\text{Ge}_x/\text{Si}$ crystals, deposited in a mask-less process on patterned Si substrates will be treated [97, 98]. The deposition of a non-conformal epitaxial film can be achieved by growing strongly in out-of-equilibrium conditions onto Si substrates with high aspect ratios. Indeed, a uniform space-filling array of three-dimensional (3D) $\text{Si}_{1-x}\text{Ge}_x$ epitaxial crystals, separated by nanometric gaps thanks to self-limited lateral expansion, has been obtained. The shape, crystalline facets, size and height of the $\text{Si}_{1-x}\text{Ge}_x$ crystals can

be finely tuned over a wide range by growth and substrate parameters. The vertical piling-up of crystalline material parallel to the growth direction, which is dictated by kinetical and geometrical constrains, mimics the 3D growth of bulk ingots on a micrometer scale.

3.1 Morphology of Si_{1-x}Ge_x/Si crystals

The epitaxial deposition of Si_{1-x}Ge_x alloys has been performed by LEPECVD on the Si patterned substrates described in section 2.2 (for further details on the LEPECVD deposition technique see section 2.1.1).

A typical array of 8 μm tall, non conformal Ge crystals deposited on Si pillars is reported in Figure 3.1. The SEM images reported in Figure 3.1, show that the deposition of 8 μm thick Ge layer at 415°C and 4.2 nm/s on top of Si pillars, results in the formation of closely spaced crystals, tessellating the sample surface with a filling factor higher than 90 % in the 1 μm wide trenches case. Indeed, it is clear that an highly non conformal growth has been obtained: the in-plane expansion is eventually suppressed, turning to

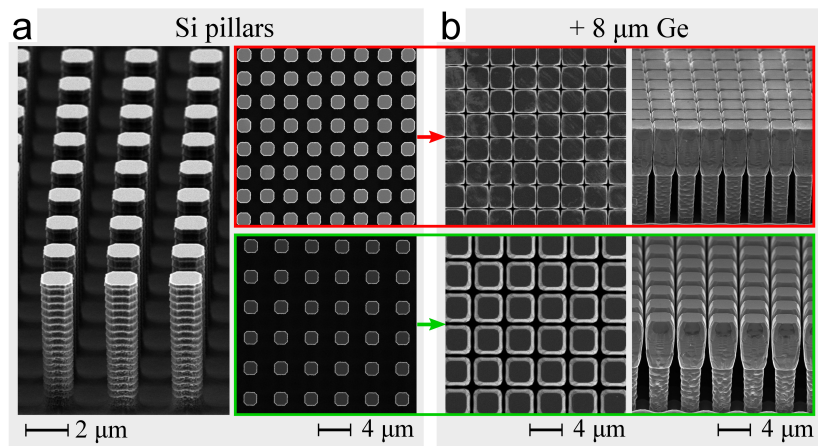


Figure 3.1: Perspective and top-view SEM images of: a) patterned Si substrate with pillar side $d = 2 \mu\text{m}$, separated by $1 \mu\text{m}$ (red box) and $2 \mu\text{m}$ (green box) wide trenches. b) $8 \mu\text{m}$ tall Ge crystals deposited at 415°C and 4.2 nm/s on top of the Si pillars reported in a) [98].

3D micrometer-sized crystals elongated in the [001] growth direction.

The key mechanisms to obtain self-limited lateral expansion growth, which are: reduced diffusion length of the adatoms compared to the structure size, and mutual gas shielding between adjacent crystals, will be described in section 3.3.

The top surface of the Ge crystals is characterized by regular facets. For the growth conditions reported in Figure 3.1 a large central (001) facet is surrounded by steeper {113} and {111} facets.

In order to prove that the peculiar non-conformal 3D growth modality is not related to any strain effect nor to a particular surface chemistry of Ge, pure Si and Si_{0.5}Ge_{0.5} have been deposited on Si pillars. The SEM images of the resulting Si and Si_{0.5}Ge_{0.5}/Si crystals are reported in Figure 3.2, they all show 3D non-conformal growth with similar surface morphologies. A broader example, in terms of Ge content x , of 3D non-conformal growth modality of Si_{1-x}Ge_x crystals on Si pillars is reported in Figure 4.15. The growth parameters for Si_{1-x}Ge_x crystals have been chosen by optimizing the surface roughness (RMS < 3 nm) and crystalline

quality for planar layers [99].

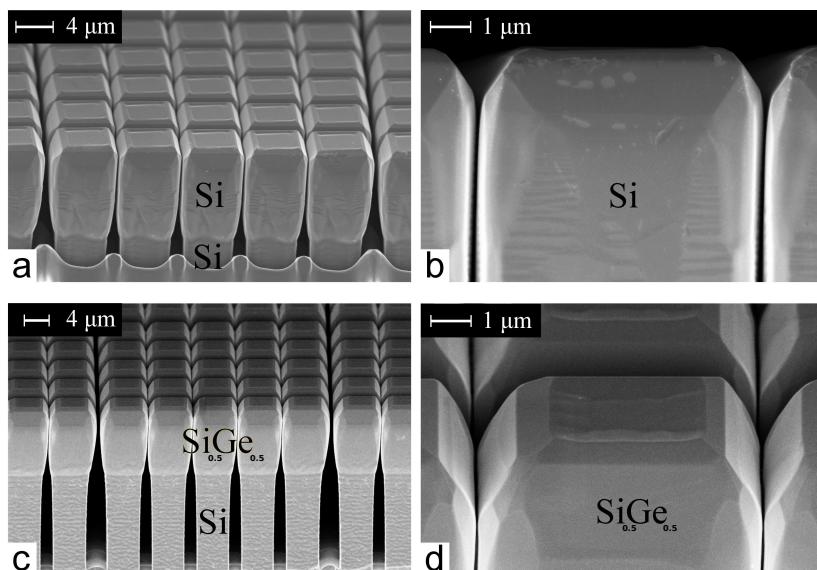


Figure 3.2: Perspective view SEM images of: a), b) Si/Si crystals grown at 750°C and 4.9nm/s. c), d) $Si_{0.5}Ge_{0.5}/Si$ crystals grown at 660°C and 7.4nm/s. Both Si and $Si_{0.5}Ge_{0.5}$ crystals, are deposited on Si pillars with side $d = 5 \mu\text{m}$ and separated by $2 \mu\text{m}$ wide trenches [98].

The top surface morphologies, measured by AFM scans, of $8 \mu\text{m}$ tall Ge and Si crystals, respectively deposited at 515°C and 750°C on Si pillars with side $d = 2$ and $5 \mu\text{m}$, are reported in Figure 3.4, 3.5 and 3.6. Here, the crystalline facets distribution is analyzed by producing a stereographic map to address the inclination of each facet. A schematic sketch reporting the measured angles is presented in Figure

3.3.

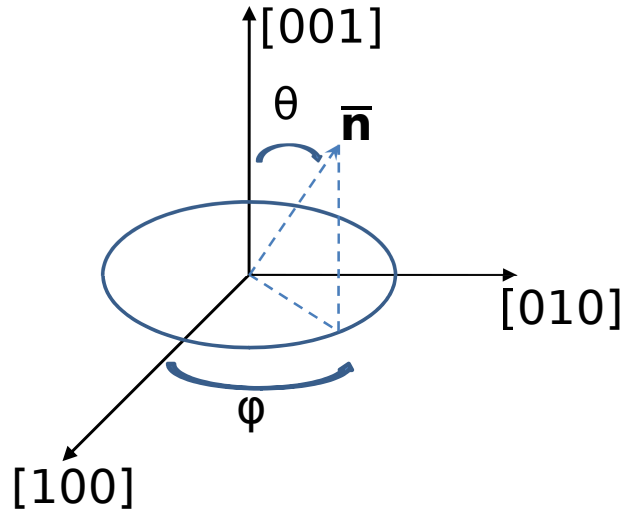


Figure 3.3: Schematic sketch of the angles θ and φ between the basal (001) plane and an arbitrary plane with normal \bar{n} .

Each set of crystalline facet family is addressed by the angle θ , while φ depends on the in-plane rotational symmetry. Indeed, for example, in Figure 3.4, there are 8 symmetric maxima for the $\{15\ 3\ 23\}$ facets (marked by a green circle) and 4 symmetric maxima for the $\{113\}$ facets. In the stereographic maps reported in panels b) of Figure 3.4, 3.5 and 3.6, the radial distance from the (001) central peak is proportional to the angle θ , while the angle φ varies counter clockwise from 0° to 360° . The color of the peaks is propor-

tional to the number of points with a certain (θ, φ) coordinate [100].

From the AFM scans and stereographic maps reported in Figure 3.4, 3.5 and 3.6, it is evident that the crystalline facets formed on the top surface of pure Si and pure Ge crystals are identical. Indeed, they always present a central (001) area (its extension increases with the lateral side d of the Si pillar), surrounded by steeper $\{113\}$ and $\{111\}$ facets along the sides of the crystal and $\{15\ 3\ 23\}$ facets at the corners.

Despite the high accuracy of the AFM scans, this technique presents problems to measure the steeper facets close to the crystal borders, especially for very narrow distance between adjacent pillars (see for example panel e) of Figure 3.5). Therefore, the top and side view SEM images of Figure 3.7 are useful to address the prototypical crystalline facets of Ge crystals. Indeed, (001), $\{113\}$, $\{111\}$, $\{15\ 3\ 23\}$, $\{20\ 4\ 23\}$ facets and vertical $\{110\}$ sidewalls are visible and indicated with different symbols. The crystalline facets are indeed the same ones exposed by Ge domes and barns at thermodynamical equilibrium [100], apart from the lack of $\{105\}$ facets which are favored by the compressive epitaxial strain in pseudomorphic layers [101]. The facet morphol-

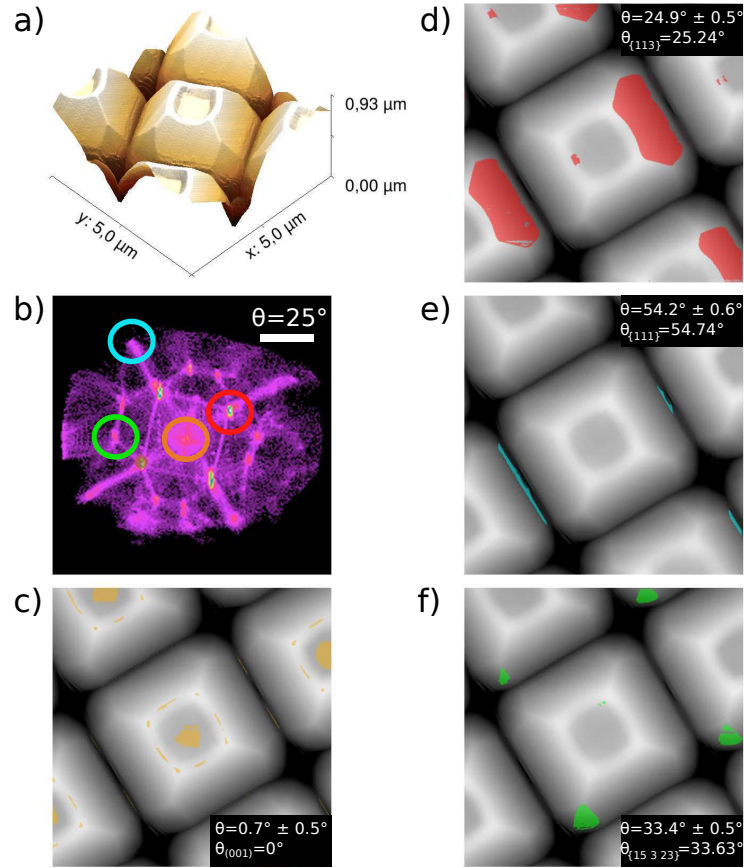


Figure 3.4: Facet analysis of 8 μm tall Ge crystals deposited at 515°C and 4.2 nm/s on Si pillars with side $d = 2\text{ }\mu\text{m}$ and separated by $2\text{ }\mu\text{m}$ wide trenches. a) 3D AFM scan. b) stereographic map of the facet distribution. The colored circles indicate different crystalline facets. c), d), e) and f) depict the extension of respectively (001), {113}, {111} and {15 3 23} facets (marked by the same circle color of b)). In each panel is reported the measured value of θ and the respective theoretical value. The lateral size of c), d), e) and f) is $5\text{ }\mu\text{m}$.

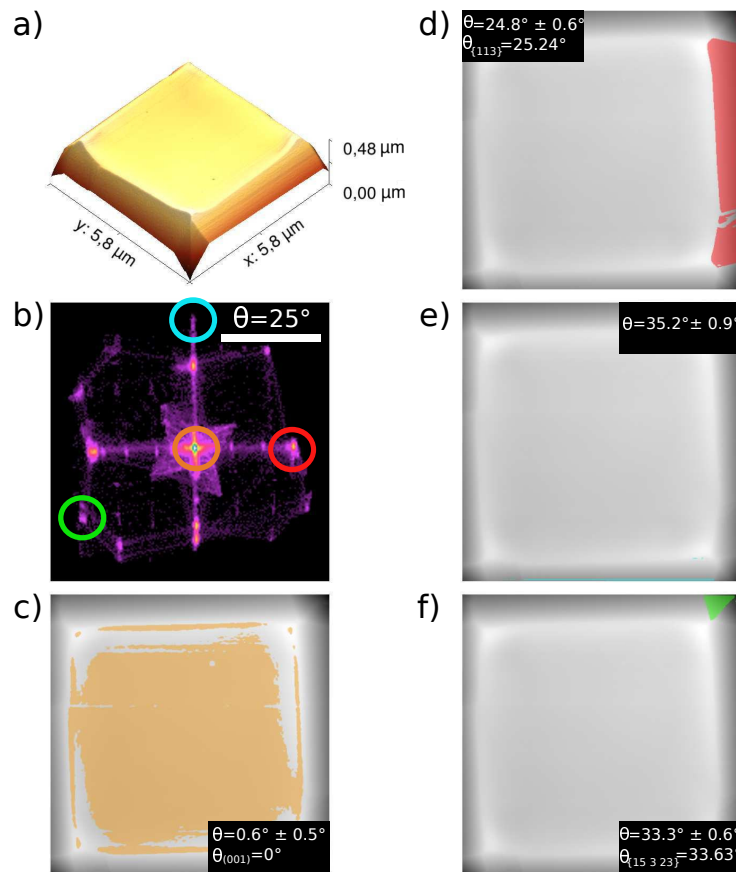


Figure 3.5: Facet analysis of 8 μm tall Ge crystals deposited at 515°C and 4.2 nm/s on Si pillars with side $d = 5\text{ }\mu\text{m}$ and separated by $2\text{ }\mu\text{m}$ wide trenches. a) 3D AFM scan. b) stereographic map of the facet distribution. The colored circles indicate different crystalline facets. c), d), e) and f) depict the extension of respectively (001), {113}, {111} and {15 3 23} facets (marked by the same circle color of b)). In each panel is reported the measured value of θ and the respective theoretical value. The lateral size of c), d), e) and f) is $5.8\text{ }\mu\text{m}$.

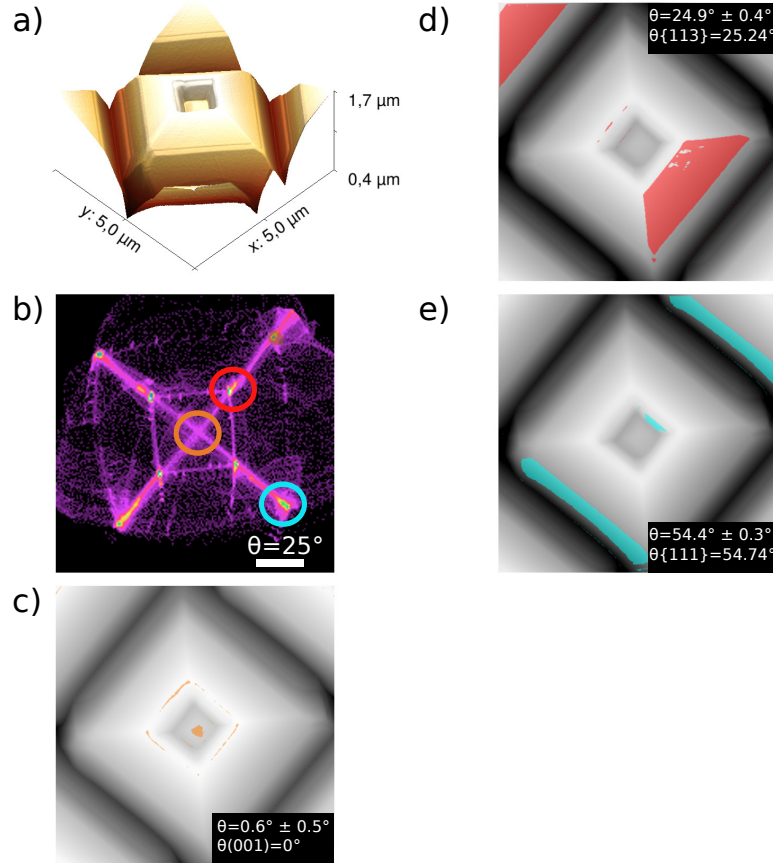


Figure 3.6: Facet analysis of 8 μm tall Si crystals deposited at 750°C and 4.9 nm/s on Si pillars with side $d = 2\text{ }\mu\text{m}$ and separated by $2\text{ }\mu\text{m}$ wide trenches. a) 3D AFM scan. b) stereographic map of the facet distribution. The colored circles indicate different crystalline facets. c), d) and e) depict the extension of respectively (001), {113} and {111} facets (marked by the same circle color of b)). In each panel is reported the measured value of θ and the respective theoretical value. The lateral size of c), d) and e) is $5\text{ }\mu\text{m}$.

ogy on the top surface of the Ge crystals is not determined by equilibrium conditions predicted by the Wulff construction. This has been confirmed by analyzing the morphological evolution with the increase of the growth temperature up to 585°C (see discussion below). Indeed it is rather determined by the balance in the growth rate between competing crystalline facets (see section 3.3).

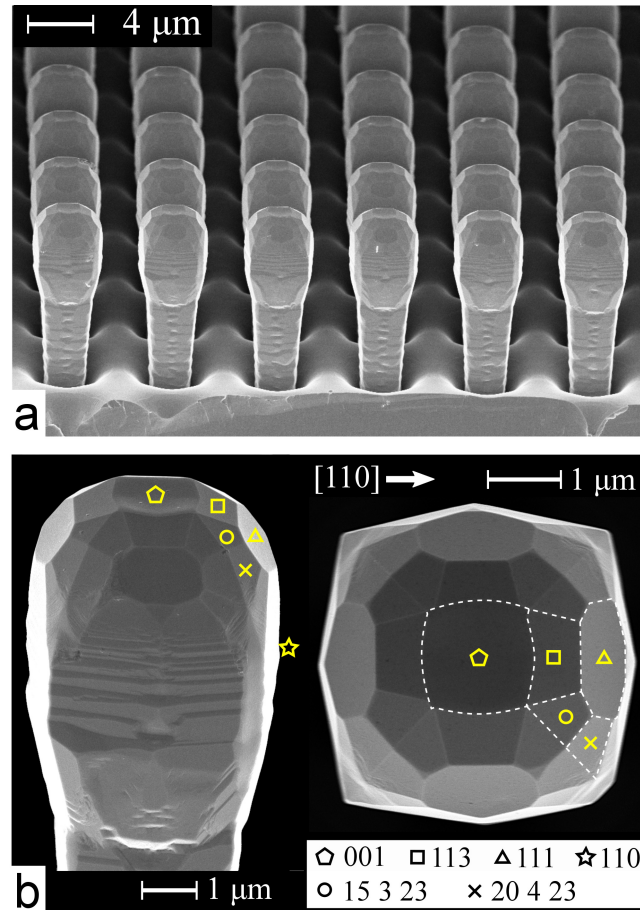


Figure 3.7: SEM analysis of Ge crystals deposited at 490°C and 4.2 nm/s on Si pillars with side $d = 2\ \mu\text{m}$ and separated by $4\ \mu\text{m}$ wide trenches. a) perspective view of the Ge crystals array. b) side and top-view SEM magnification of one Ge crystal shown in a). Each crystalline facet is marked by a different symbol (unmarked facets can be simply addressed by symmetry). Dashed lines highlight the borders between different crystalline facets [98].

The excellent uniformity of the surface morphology across any crystal array indicates that the silicon Bosch fabrication process and the LEPECVD deposition are reliable and reproducible. Indeed, the size fluctuation of the (001) top surface between different crystals is $\leq 5\%$ on an area of $100 \times 100 \mu\text{m}^2$.

The shape and morphology evolution of Ge crystals by increasing the amount of deposited material, has been studied growing several samples with height h ranging between 1 to $30 \mu\text{m}$ on Si pillars with side $d = 2 \mu\text{m}$ separated by $2 \mu\text{m}$ wide trenches. In particular, as reported in Figure 3.8, Ge crystals with height $h = 1, 4, 8$ and $30 \mu\text{m}$ have been investigated by SEM analysis.

The SEM analysis reported in Figure 3.8 shows that increasing the Ge crystal height from 1 to $8 \mu\text{m}$, they tend to expand laterally extending the edges facets, but once they get closer, the lateral in-plane growth is suppressed with respect to the vertical one along the [001] growth direction, and the top surface morphology doesn't change anymore. This mechanism of self-limited lateral growth is related to the reduced diffusion length of adatoms compared to the micrometric size of the Si pillars, and to the mutual shielding

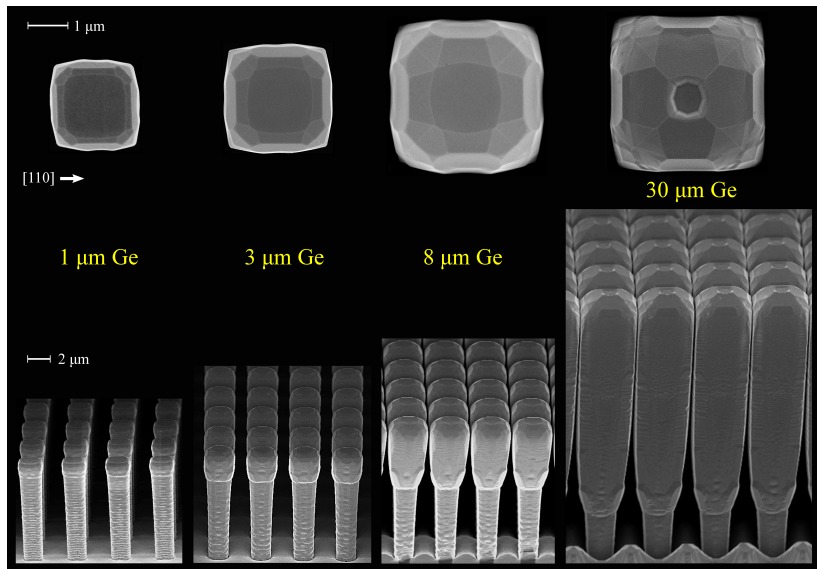


Figure 3.8: Perspective and top-view SEM images of Ge crystals with different heights (written in yellow) deposited at 490°C and 4.2 nm/s on Si pillars with side $d = 2 \mu\text{m}$ separated by $2 \mu\text{m}$ wide trenches [98].

of the feeding gas between adjacent pillars [97, 98]. It will be described with more details in section 3.3.

The lateral in-plane expansion of Ge crystals deposited at 440°C and 4.2 nm/s on Si pillars with side $d = 2 \mu\text{m}$ separated by $2 \mu\text{m}$ wide trenches has been measured in dark field scanning-TEM (DF STEM), see Figure 3.9 a). Figure 3.9 b), reports the distance between two adjacent Ge crystals as a function of the Ge crystal height, confirming that in the first stages of the epitaxial deposition the Ge crystals laterally expands, while after $\sim 3 \mu\text{m}$ their inter-distance remains stable to 55 nm. The SEM image of panel c) confirms that a purely vertical growth has been achieved, indeed Ge crystals with height up to $50 \mu\text{m}$ don't merge remaining separated by few tens of nm, demonstrating that a stationary growth-regime has been established.

In order to study the morphological evolution of a single Ge crystal, excluding the gas shielding effect of the neighboring ones, Ge crystals with height ranging from 1 to $30 \mu\text{m}$, deposited on Si pillars with side $d = 2 \mu\text{m}$ separated by $50 \mu\text{m}$ wide trenches, have been analyzed by SEM (see Figure 3.10).

In this condition, the shape and morphology evolution of

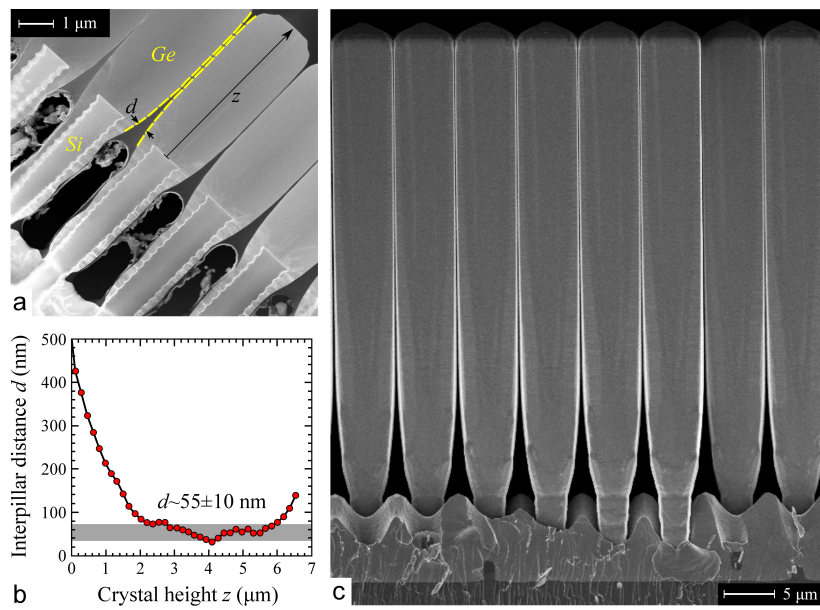


Figure 3.9: a) DF STEM image of 7 μm tall Ge crystals deposited 440°C and 4.2 nm/s on Si pillars with side of 2 μm separated by 2 μm wide trenches. b) graph reporting the inter-crystals distance versus their height extracted from a). c) cross-sectional SEM image of 50 μm tall Ge crystals deposited 490°C and 4.2 nm/s on Si pillars with side $d = 2 \mu\text{m}$ separated by 4 μm wide trenches [98].

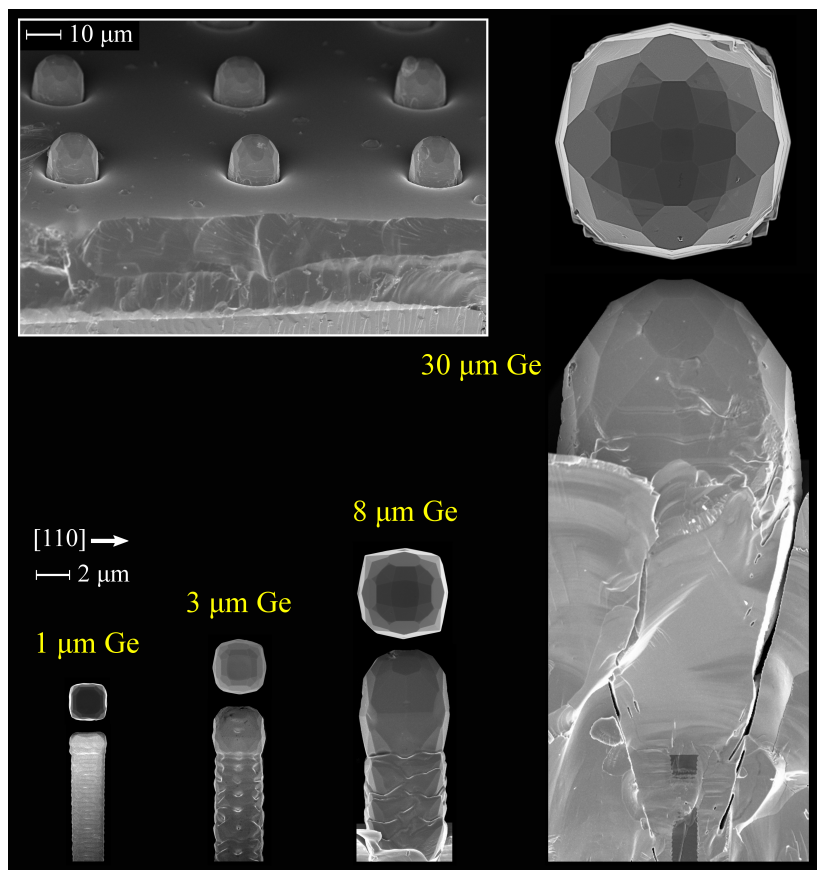


Figure 3.10: Top and side SEM view of isolated Ge crystals with different height (indicated in yellow) deposited at 490°C and 4.2 nm/s on Si pillars with side $d = 2 \mu\text{m}$ separated by 50 μm wide trenches. The inset shows a perspective SEM overview of an array of 30 μm tall Ge crystals [98].

the Ge crystals is only determined by the angular distribution of the impinging flux from the gaseous phase. Increasing the material deposition from 1 to 30 μm , more Ge accumulates on the lateral crystal sidewalls, always to a smaller extent than on the top surface, eventually leading to an "ice cream" crystal shape in the case of 30 μm deposition. Moreover, a certain amount of material is also deposited in the large trenches between the Si pillars, eventually covering their bottom part (see inset of Figure 3.10).

3.2 Impact of patterning conditions on Ge crystal morphology

In this section it will be discussed the role of patterning geometry, crystalline orientation and lateral sidewall silicon oxide passivation on the Ge crystal morphology.

3.2.1 Role of patterning geometry

Ge crystals have been epitaxially grown on patterned Si (001) substrates displaying pillars with different lateral size d (2, 5, 9 and 15 μm) and trench width (1, 2, 3, 4, 5 and 50 μm) as already described in section 2.2. The SEM images of 8 μm tall Ge crystals deposited at 490°C or 510°C and 4.2 nm/s on the aforementioned different Si pillars geometries are reported in Figure 3.11, 3.13 and 3.14.

The impact of the lateral size d of the square Si pillars, for a certain trench width (2 μm in this case), on the morphology of the deposited Ge crystals is illustrated by the SEM images reported in Figure 3.11. Here, different Si pillar sizes have been considered: $d = 2, 5, 9$ and 15 μm . The only remarkable effect of increasing the Si pillar size from $d = 2 \mu\text{m}$ to $d = 15 \mu\text{m}$ on the Ge crystal morphology, is to expand the central

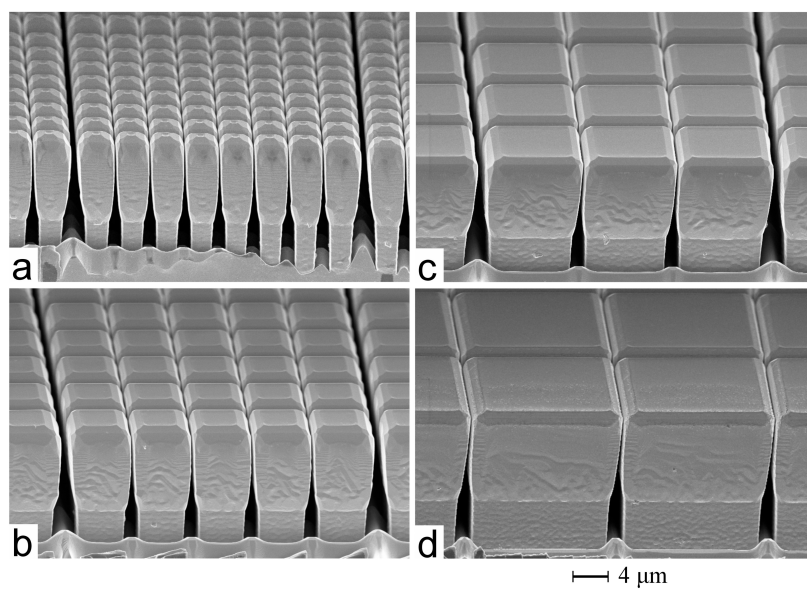


Figure 3.11: SEM perspective images of 8 μm tall Ge crystals deposited at 510°C and 4.2 nm/s on Si pillars separated by 2 μm wide trenches and different lateral size d . a) $d = 2 \mu\text{m}$, b) $d = 5 \mu\text{m}$, c) $d = 9 \mu\text{m}$ and d) $d = 15 \mu\text{m}$ [98].

Impact of patterning conditions on Ge crystal morphology 97

(001) facet. Indeed, the extension of the slanted {113} and {111} facets doesn't essentially vary, while the central (001) facet becomes dominant (see Figure 3.12).

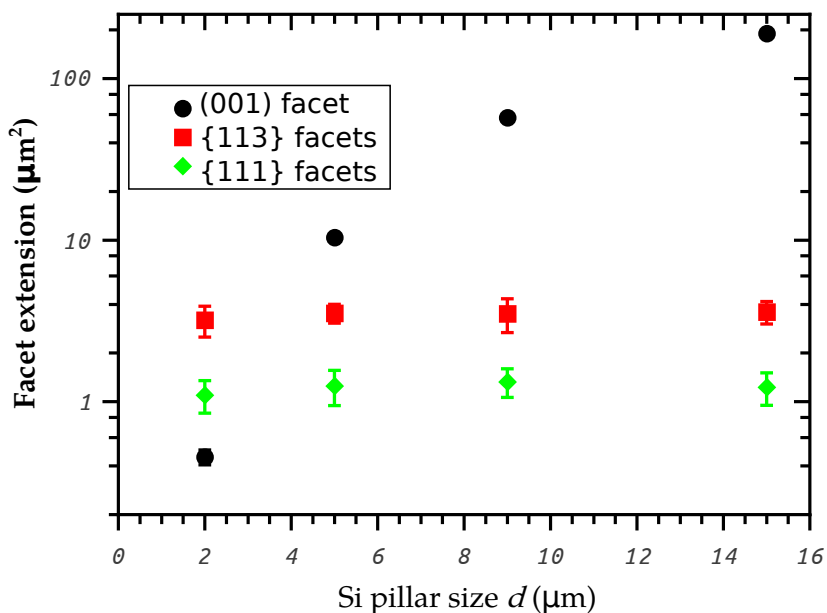


Figure 3.12: Graph reporting the (001), {113} and {111} facets extension of the Ge crystals shown in Figure 3.11. The extension of the {113} and {111} facets is projected onto the (001) interface plane.

The influence of the trench width between adjacent Si pillars on the morphology of Ge crystals, is depicted by the SEM images reported in Figure 3.13 and 3.14.

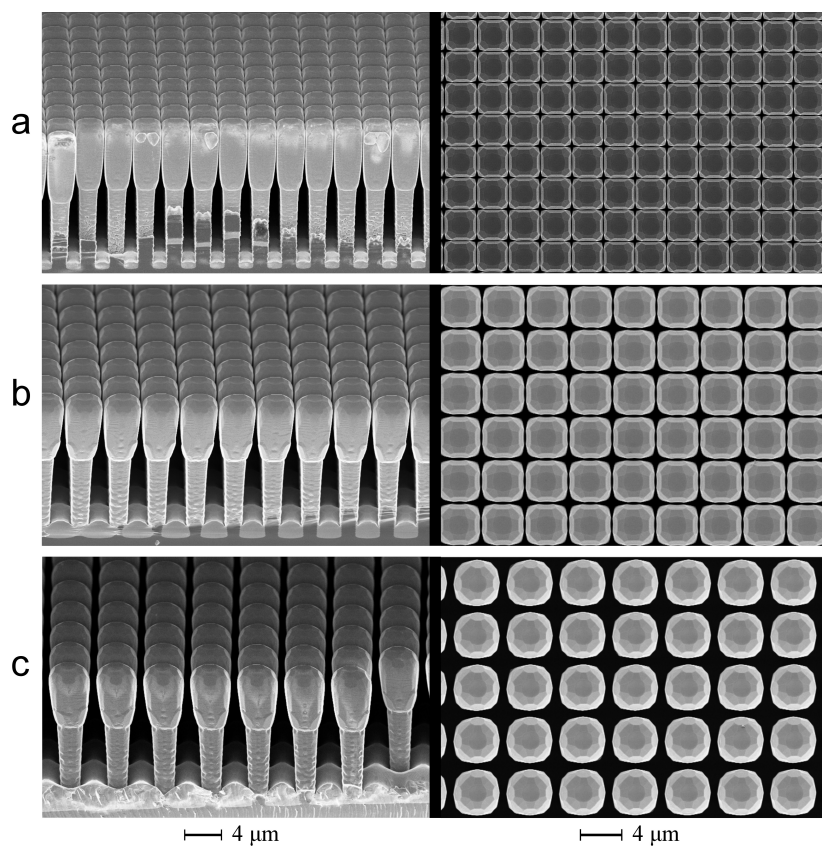


Figure 3.13: Perspective (left) and top (right) view SEM images of $8 \mu\text{m}$ tall Ge crystals deposited at 490°C and 4.2 nm/s on Si pillars with side $d = 2 \mu\text{m}$ and separated by a) $1 \mu\text{m}$, b) $2 \mu\text{m}$ and c) $3 \mu\text{m}$ wide trenches [98].

*Impact of patterning conditions on Ge crystal morphology*99

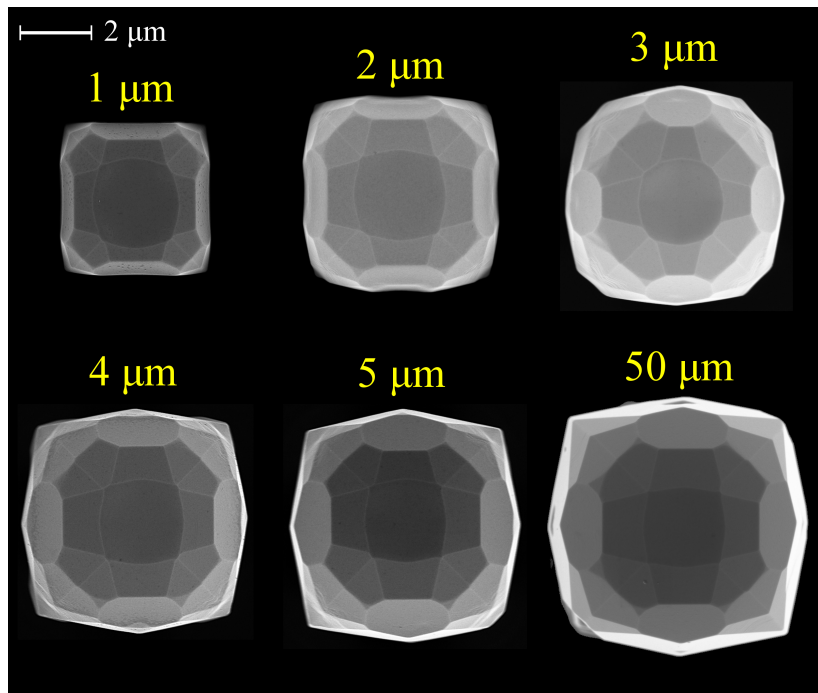


Figure 3.14: Top-view SEM image of 8 μm tall Ge crystals deposited at 490°C and 4.2 nm/s on Si pillars with side $d = 2 \mu\text{m}$ and separated by different trench width, indicated in yellow [98].

Here 8 μm tall Ge crystals, deposited at 490°C and 4.2 nm/s on Si pillars with side $d = 2 \mu\text{m}$ and separated by 1, 2, 4, 5 and 50 μm wide trenches have been analyzed by SEM both in perspective and top-view. It is possible to observe that increasing the trench width from 1 to 50 μm, the central (001) doesn't significantly expands, while the total top area

is increased by $\sim 160\%$ (see Figure 3.15). Thus the lateral expansion of Ge crystals separated by large trench width is mostly due to extension of slanted $\{113\}$ and $\{111\}$ facets.

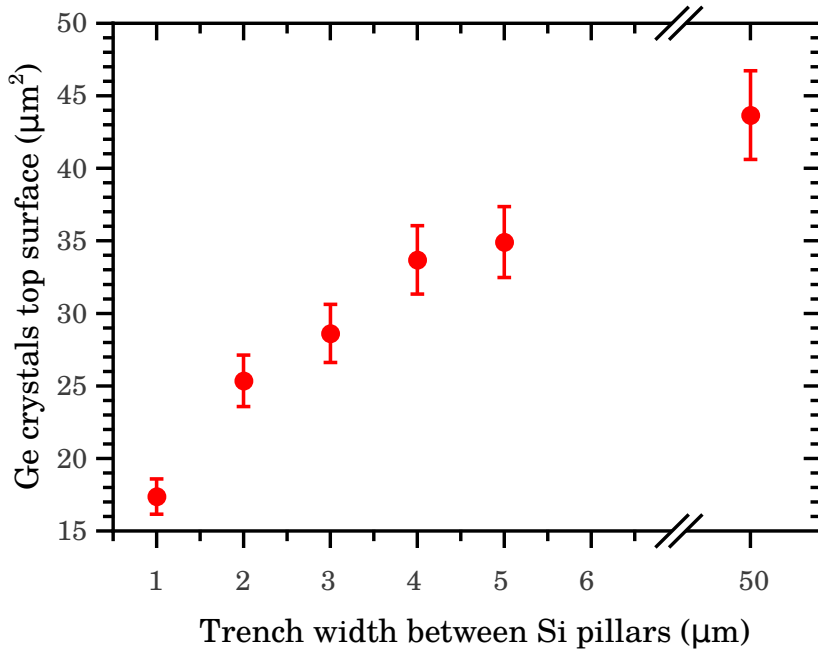


Figure 3.15: Graph reporting the total top surface of the Ge crystals shown in Figure 3.14. The extension of the $\{113\}$ and $\{111\}$ facets is projected onto the (001) interface plane.

Moreover, increasing the trench width from 1 to 50 μm , the thickness of the accumulated Ge in the trenches also increases due to reduced gas shielding effects between adjacent crystals. Indeed, for trench width of 2 and 3 μm , the

Impact of patterning conditions on Ge crystal morphology

Ge thickness increases respectively by a factor 65 % and 140 % with respect to the 1 μm case.

In order to test that the self-limited lateral expansion growth modality also works for smaller Si pillars, i.e. slightly larger than the typical Ge diffusion length (see section 3.3), Ge crystals have been deposited on sub-micrometer sized Si pillars. These sub-micrometer sized Si pillars have been obtained by electron beam lithography (EBL) and cryogenic deep reactive ion etching [92], resulting in smooth lateral sidewalls avoiding the lateral scallops obtained by standard Bosch process (see section 2.2). The SEM images of Figure 3.16 show that despite the smaller size of the Si pillars ($\sim 1/10$ of the ones fabricated by Bosch process) the self-limited lateral expansion growth mechanism is still valid. Indeed, 500 nm tall Ge crystals deposited at 460°C and 4.2 nm/s on Si pillars with side $d = 0.8, 1.3$ and $1.8 \mu\text{m}$ and 200 nm wide trenches are still separated by nanometric gaps (see inset of Figure 3.16 a).

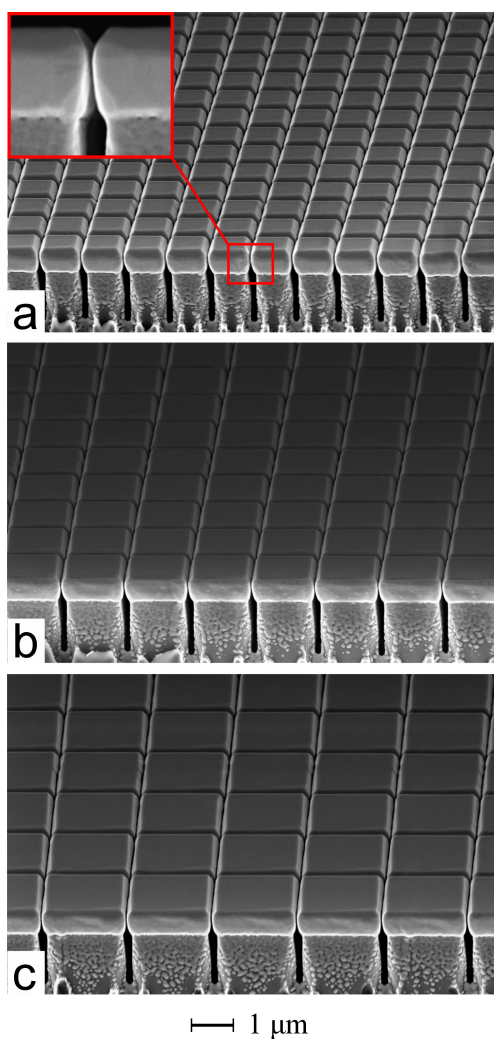


Figure 3.16: Perspective SEM images of 500 nm tall Ge crystals deposited at 460°C and 4.2 nm/s on Si pillars with 200 nm wide trenches and side: a) $d = 0.8 \mu\text{m}$, b) $d = 1.3 \mu\text{m}$ and c) $d = 1.8 \mu\text{m}$. The red inset in a) displays a magnification of the nanometric gap between two adjacent Ge crystals [98].

3.2.2 Role of lateral Si sidewalls passivation

Ge crystals have been also deposited on patterned Si(001) substrates with lateral scalloped {110} sidewalls covered by ~ 100 nm thick silicon oxide layer (see section 2.2). The lateral silicon oxide passivation layer has an important role in the design of vertical electrical devices to prevent short circuits between the highly defected material deposited laterally and in the trenches with the crystals grown on the top (001) surface. Moreover passivated Si sidewalls are useful to prevent Ge diffusion towards the trenches, preserving the non conformal growth conditions, in other deposition techniques, e.g. thermal CVD.

The SEM images of Figure 3.17 compare the morphology of $8 \mu\text{m}$ tall Ge crystals deposited at 560°C and 4.2 nm/s on Si pillars (side $d = 2 \mu\text{m}$ and separated by $2 \mu\text{m}$ wide trenches) with (panels a) and b)) and without (panels c) and d)) oxide passivation layer on the lateral {110} sidewalls.

The morphology of Ge crystals deposited on the top (001) surface of Si pillars with and without lateral silicon oxide passivation is fully comparable, while on the other hand, the material which has been deposited on lateral sidewalls has very poor crystalline quality in the latter case. Indeed poly-

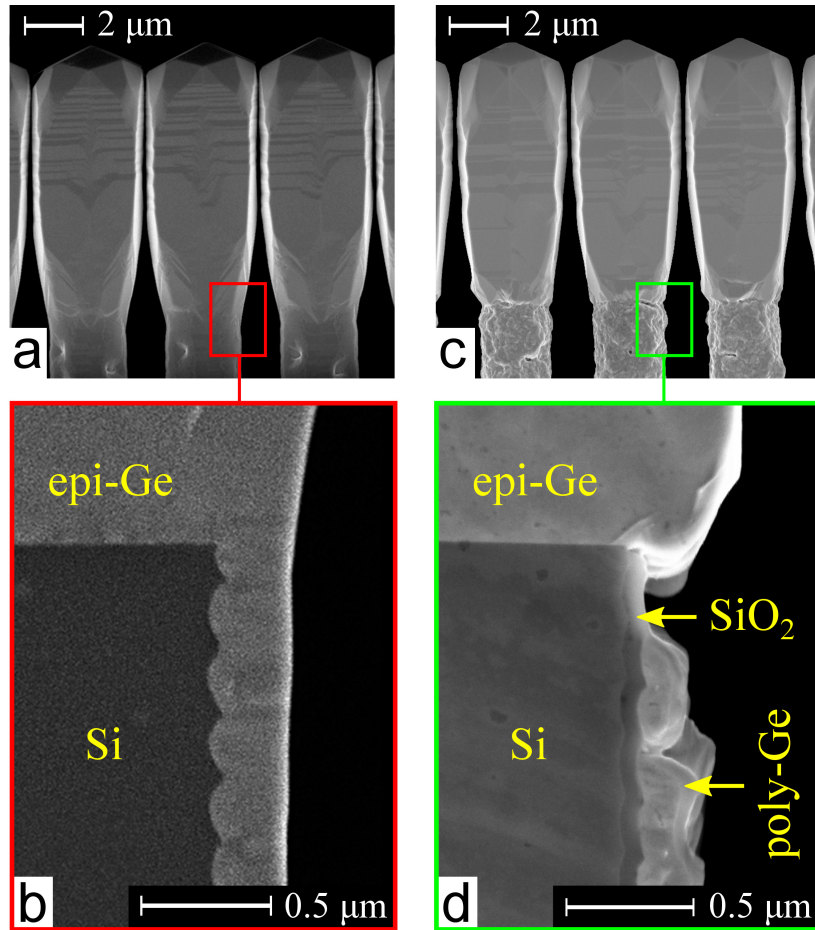


Figure 3.17: SEM images of $8 \mu\text{m}$ tall Ge crystals deposited at 560°C and 4.2 nm/s on Si pillars (side $d = 2 \mu\text{m}$ and separated by $2 \mu\text{m}$ wide trenches) with (a, b) and without (c, d) 100 nm thick oxide passivation layer on the lateral $\{110\}$ sidewalls. b) and d) are respectively magnifications of the Ge/oxide and Ge/Si $\{110\}$ interfaces, clearly showing a lower Ge quality in the former case [98].

Impact of patterning conditions on Ge crystal morphology 105

crystalline grains of Ge are visible on the lateral sidewalls. A similar behavior has been also observed for Ge crystals deposited on passivated Si pillars with larger lateral side $d = 5$ and $9 \mu\text{m}$, as reported in Figure 3.18.

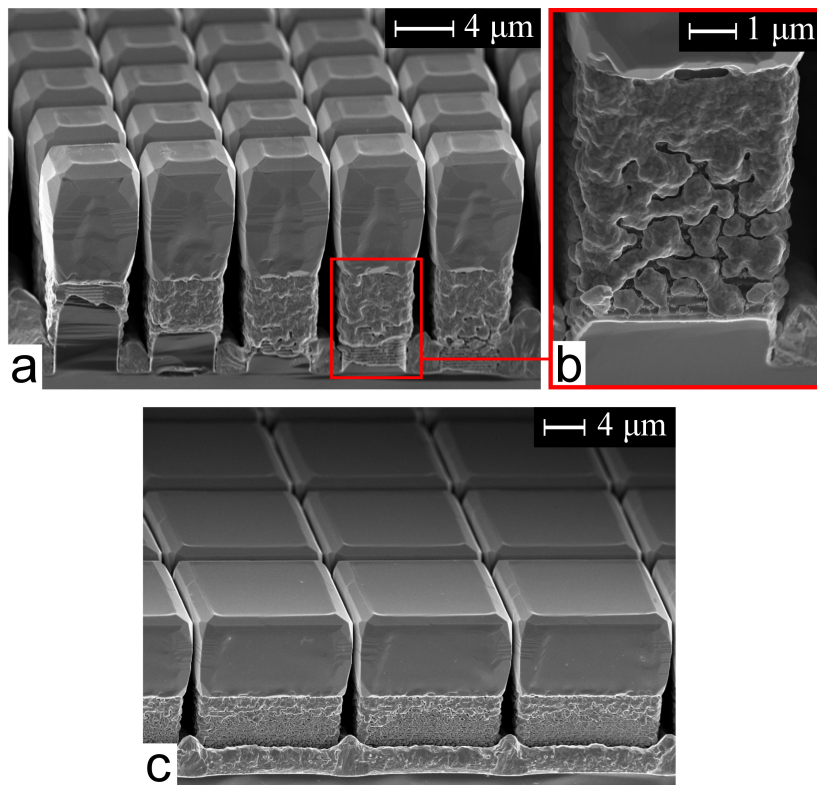


Figure 3.18: SEM images of 8 μm tall Ge crystals deposited at 560°C and 4.2 nm/s on Si pillars with sidewalls passivated by 100 nm thick silicon oxide layer. The Si pillar side is $d = 5 \mu\text{m}$ in a) and b), $d = 9 \mu\text{m}$ in c). b) is a magnification of the Ge/oxide interface in a).

3.2.3 Role of Si substrate orientation

So far, all the patterned Si substrates which have been considered for the Ge deposition, are (001) on axis oriented, with an accuracy of $\pm 0.5^\circ$. Here, the deposition of $8 \mu\text{m}$ tall Ge crystals at 440°C and 4.2 nm/s on Si pillars, realized on (001) substrates with 6° miscut along the [110] direction, is analyzed.

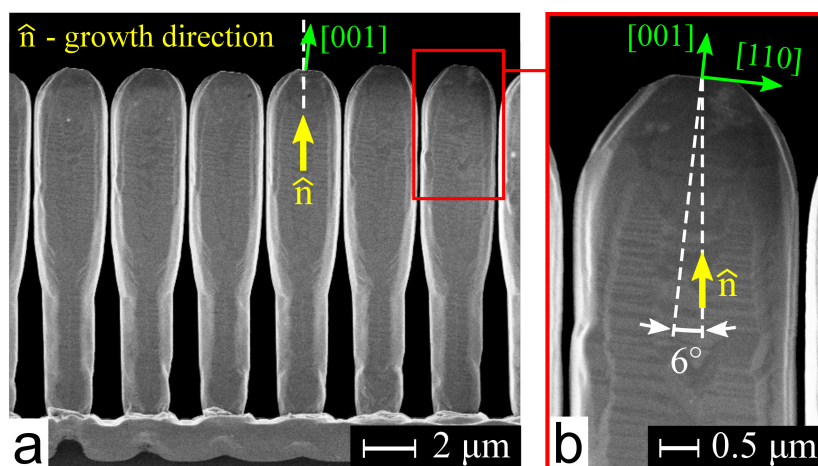


Figure 3.19: a) SEM image of $8 \mu\text{m}$ tall Ge crystals deposited at 440°C and 4.2 nm/s on Si pillars fabricated on (001) substrate with 6° miscut along the [110] direction. The Si pillars have side $d = 2 \mu\text{m}$ and trench width of $2 \mu\text{m}$. b) shows a SEM magnification of the top part of a Ge crystal displayed in a). The growth direction is labeled by \hat{n} , which is normal to the miscut Si substrate surface [98].

The SEM images reported in Figure 3.19 show that despite the mis-orientation of the Si pillars, still the self-limited growth modality is preserved: fully faceted Ge crystals, separated by nanometric gaps are obtained. The morphology of these crystals is fully comparable with the one of Ge crystals deposited on on-axis (001) patterned Si substrates: central (001) facet, surrounded by $\{113\}$ and $\{111\}$ facets along the sides and $\{1\bar{5}323\}$ facets at the corners. It is worth to notice that the final (001) surface is on-axis, nevertheless the original one was 6° miscut towards the $[110]$ direction. This orientation change process is due to step flow Ge diffusion on a finite area. This progressive process requires thicker epitaxial crystals for larger Si pillars, so that a suitable miscut can be achieved for the integration of other materials on top of the Ge crystals.

3.3 Growth modeling of $\text{Si}_{1-x}\text{Ge}_x/\text{Si}$ crystals

In this section will be presented a model, developed by Dr. R. Bergamaschini and Prof. L. Miglio from the Università degli studi di Milano Bicocca, based on rate equations for the adatom phase, in order to interpret the influence of the growth conditions on the $\text{Si}_{1-x}\text{Ge}_x$ crystal morphology [97, 98, 102].

3.3.1 Crystalline facet growth and flux modeling

The morphology and facet distribution of $\text{Si}_{1-x}\text{Ge}_x$ crystals deposited on Si pillars, depend on the competition between kinetic and thermodynamic driving forces. Indeed, thermodynamics drives the system to minimize its free energy, thus it depends on the intrinsic properties of the material (e.g. alloy composition, strain, surface energy..). Several growth models based on thermodynamic driving forces can be found in references [103–108].

On the other hand, kinetics is strongly dependent on the

growth parameters (deposition rate, growth temperature,...) which can be easily tuned in order to drive the system to different morphologies. In LEPECVD growth conditions the deposition is performed out-from equilibrium due to the reduced growth temperature (between 410° and 610° for pure Ge) and high growth rate >4 nm/s, thus in a low diffusion length regime.

Our growth model, based on kinetics, is formulated via rate equations for the adatom phase. It considers only one chemical specie and it doesn't take into account any strain related phenomena which can influence the growth modality [108]. In this framework the growth process can be described by considering the evolution of the adatom phase applying the rate equation models described in references [109–115].

If the crystal is in equilibrium, adatoms are continuously evaporated and re-absorbed on the surface and their local density in the surface site \mathbf{x} is $N_{eq}(\mathbf{x})$. Considering R_g the intrinsic rate of adatom generation, determined by the local properties of the surface (orientation, chemical species,...) and R_c the rate of adatom incorporation into the crystal,

the equilibrium condition is reported in equation 3.1.

$$R_g = R_c = \frac{N_{eq}}{\tau_c} \quad (3.1)$$

where τ_c is the crystallization time, i.e. the average lifetime of an adatom before crystallization. The equilibrium condition is broken by the feeding gas during the epitaxial deposition, indeed the local adatom density becomes $N_{tot}(\mathbf{x}) = N(\mathbf{x}) + N_{eq}(\mathbf{x})$ where the excess value $N(\mathbf{x})$ unbalances the incorporation rate contribution, which ensures the crystallization of the deposited material. The crystal growth rate $v(\mathbf{x}) = v\hat{\mathbf{n}}$ perpendicular to the growth front is expressed by equation 3.2.

$$v(\mathbf{x}) = R_c - R_g = \frac{N(\mathbf{x})}{\tau_c} \quad (3.2)$$

The crystal profile evolution can be determined by knowing the local variation of N during the epitaxial deposition time. As reported in Figure 3.20, at each position \mathbf{x} on the surface, adatoms tends to accumulate due to the deposition flux Φ , they diffuse and get incorporated into the crystal or desorb/etch away [87].

Considering the aforementioned mechanisms, a simple

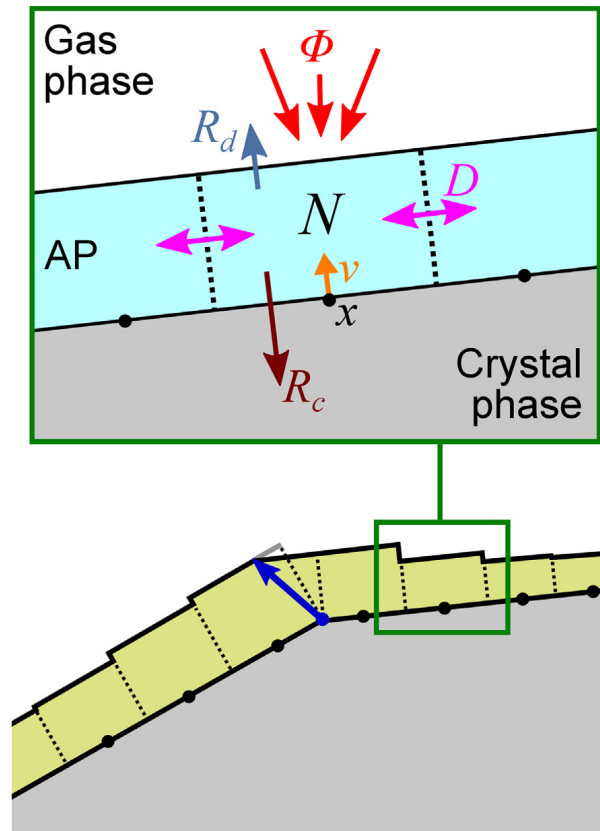


Figure 3.20: Schematic evolution of the discretized profile of the growing crystal. Each segment takes into account the non-uniform conditions along the facets and it expands normally to the crystalline facet depending on the local growth rate v . The green inset shows the different contribution considered in the rate equation model for material transport through the adatom phase (AP) [98].

rate equation for the temporal evolution of N can be written according to equation 3.3.

$$\begin{aligned} \frac{\partial N}{\partial t} = \Phi - \frac{N}{\tau_c} - \frac{N}{\tau_d} + \nabla_s \cdot [D \nabla_s N] = \\ \Phi - v - R_d + \nabla_s \cdot [D \nabla_s N] \end{aligned} \quad (3.3)$$

where $R_d(\mathbf{x}) = N(\mathbf{x})/\tau_d$ is the desorption/etching rate which is the inverse of the average adatom lifetime before desorption τ_d and the last term is related to the diffusion Fick's law. The subscript s means that the derivatives are performed according to the surface coordinates. We can thus define the diffusion length as the average distance of the adatoms before desorption $L_d \sim \sqrt{D\tau_d}$, or crystallization $L_c \sim \sqrt{D\tau_c}$. It is possible to get a complete description of the growth dynamics by coupling the equations 3.3 and 3.2:

$$\begin{aligned} \frac{\partial N}{\partial t} = \Phi - \frac{N}{\tau} + \nabla_s \cdot [D \nabla_s N] \\ v = \frac{N}{\tau_c} \end{aligned} \quad (3.4)$$

where $\tau^{-1} = \tau_c^{-1} + \tau_d^{-1}$ is the inverse of the actual time of the adatoms on the crystal surface. Thus according to equation 3.4, the growth results from the interplay between the ex-

ternal deposition flux Φ , creating the out-of-equilibrium distribution of the adatoms, and the adatom surface processes which depend on the local properties.

So far we have considered a generic crystal surface, but the Ge/Si crystal studied in this work present well defined different crystalline facets. Due to the out-of-equilibrium growth conditions, the resulting crystal morphology is expected to differ from the thermodynamic Wulff reconstruction, indeed the growth velocity $v(\hat{n})$ for each crystalline facet is different. For a certain $v(\hat{n})$, the so called kinetic crystal shape (KCS) is the steady-state crystal shape which maximize the overall growth rate on a convex surface or minimize it on a concave one [116–118]. Thus the KCS is dominated by the fastest growing crystalline facets in a concave region and by the slowest ones in a convex configuration.

The Ge crystals deposited on Si pillars have a concave shape geometry, with well defined crystalline facets (e.g. see Figure 3.7) from the very first stages of deposition. In this case, the morphology of the Ge crystals can be obtained by intersecting the expanding growth facets, which have different growth rates, at different deposition stages and taking the final convolution. This procedure is named Borgstrom

construction [116] and is a prescription to minimize edges and steps between two adjacent crystalline facets. Figure 3.21 a), b) illustrate the Borgstrom construction for two different facets on a convex region, respectively with similar and different growth rates. Panels c), d) are analogous to a) and b) but for a convex region. Depending on the ratio between the growth rates, adjacent facets can coexist during the deposition (Figure 3.21 a) and c)) or one totally consumes the other one (Figure 3.21 b) and d)). Thus, from cross-section SEM images of a Ge crystal deposited on a Si pillar, is it possible to extract the growth rate ratio of 2 adjacent facets by analyzing the displacement evolution of their edge during the deposition.

By considering two crystalline facets A and B, with angles α and β with respect to the (001) plane, the angle θ along which their edge moves during the epitaxial deposition is expressed by equation 3.5.

$$\tan\theta = \tan\alpha + \frac{\tan\beta - \tan\alpha}{1 - \frac{v_B \cos\alpha}{v_A \cos\beta}} \quad (3.5)$$

As reported in Figure 3.21 e) (central part), the coexistence of both A and B facets is obtained for small variations of

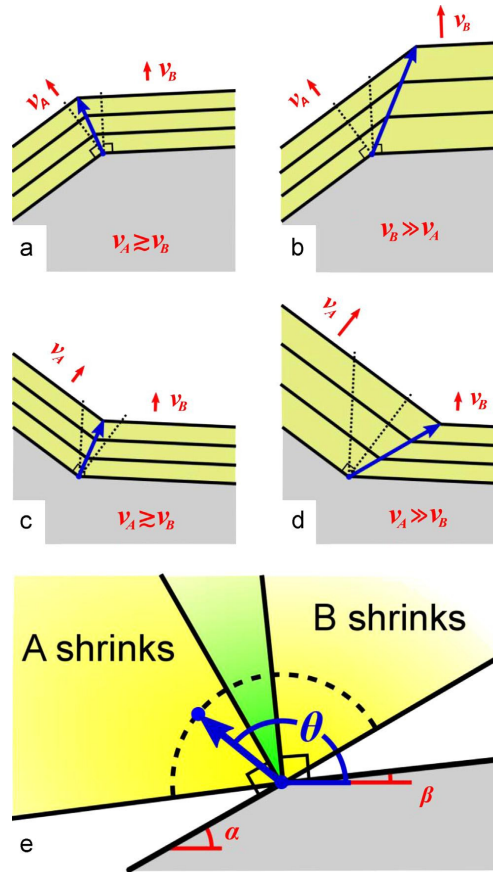


Figure 3.21: Borgstrom construction for two different crystalline facets A and B with different growth rates, respectively named v_A and v_B . In panels a) and b) the profile is convex and the growth rates are respectively similar and very different. c) and d) are respectively analogous to a) and b) but for a concave profile. e) map of the different growth regimes for a convex crystal profile depending on the angle θ which describes the trajectory of the border between A and B facets during growth [98].

growth rates and it implies $\theta \in [\beta + \pi/2, \alpha + \pi/2]$. On the contrary, if the facets A and B have very different growth rates (lateral regions of Figure 3.21 panel e), the slowest facet expands consuming the other one. In particular, for $\theta \in [\alpha, \beta + \pi/2]$ facet A expands, while for $\theta \in [\alpha + \pi/2, \beta + \pi]$ facet B expands because of smaller growth rate.

In order to take into account local variations of the incoming flux, each crystalline facet has been partitioned in line segments, which expand according to the local growth velocity, as reported in Figure 3.20. Thus a stepped crystal profile is obtained and the facet edges proceed according to the Borgstrom construction.

The diffusion length of Ge during LEPECVD deposition is considered to be $\sim 100 - 200$ nm [97, 119, 120] (high deposition rate of 4.2 nm/s), which is much smaller than the typical lateral size of the Si pillars and of the crystalline facets. Indeed, as a first approximation, it is reasonable to neglect the diffusion term in the rate equation 3.4, which can be re-written in the simplified form of equation 3.6.

$$\begin{aligned} \frac{\partial N}{\partial t} &= \Phi - \frac{N}{\tau} \\ v &= \frac{N}{\tau_c} \end{aligned} \tag{3.6}$$

Assuming as initial condition the equilibrium condition $N(t=0)=0$ and a constant deposition flux Φ , the density of adatoms is expected to reach a stationary value $N_{st} = \tau\Phi$ with a transient dependence $N(t)=N_{st} [1 - e^{(-t/\tau)}]$. From equation 3.6 it is possible to write the stationary growth rate according to equation 3.7.

$$v_{st} = \frac{N_{st}}{\tau_c} = \frac{1}{1 + \tau_c/\tau_d} \Phi = \chi\Phi \quad (3.7)$$

where χ is the incorporation factor, defined as $\chi = [1 + \tau_c/\tau_d]^{-1}$. The incorporation factor represents the fraction of the incoming flux which is crystallized, and for a given temperature it depends only on the facet orientation.

The reactive gas flux Φ impinging on the crystal surface at a given \mathbf{x} point can be described in a spherical coordinate system where θ and φ are respectively the polar and azimuthal angles. Integrating all the flux contributions coming from every direction $\hat{\mathbf{r}}(\theta, \varphi)$, projected along the local surface normal $\hat{\mathbf{n}}_s(\mathbf{x})$, it is possible to write equation 3.8.

$$\Phi(\mathbf{x}) = \int_W \phi(\theta, \varphi, \mathbf{x}) \hat{\mathbf{r}}(\theta, \varphi) \cdot \hat{\mathbf{n}}_s(\mathbf{x}) dW \quad (3.8)$$

where $\phi(\theta, \varphi, \mathbf{x})$ is the angular distribution of the incoming

flux at the point \boldsymbol{x} , which depends on the spatial distribution and velocity of the reactive gas in the LEPECVD reactor (see Figure 3.22 b)). A detailed study of the plasma and reactive gas distribution in LEPECVD has been published in references [87, 88]. The integration domain W defines all the accessible directions $\hat{\boldsymbol{r}}(\theta, \varphi)$ to collect the flux at a certain \boldsymbol{x} point. At the typical growth pressure of LEPECVD, which is $\sim 10^{-2}$ mbar, the mean free path of gaseous molecules is in the order of few cm, much larger than the micrometer-sized Ge/Si crystals and smaller than the distance between the substrate and the plasma source. The reactive GeH_3 and GeH_2 radicals, formed in the Ar plasma, reach the substrate surface after several collisions. Indeed, the impinging species can be considered to arrive isotropically on the substrate surface. However, a certain directionality of the flux should be taken into account especially for ionized molecules (e.g. GeH_3^+) due to the accelerating electric field and confining magnetic coils. In Figure 3.22 a), it is represented the flux geometry: a vertical component Φ_V is superimposed on the isotropic one Φ_I .

The isotropic flux has been estimated to be 70 % of the total by systematic fittings of the ratio between the Ge de-

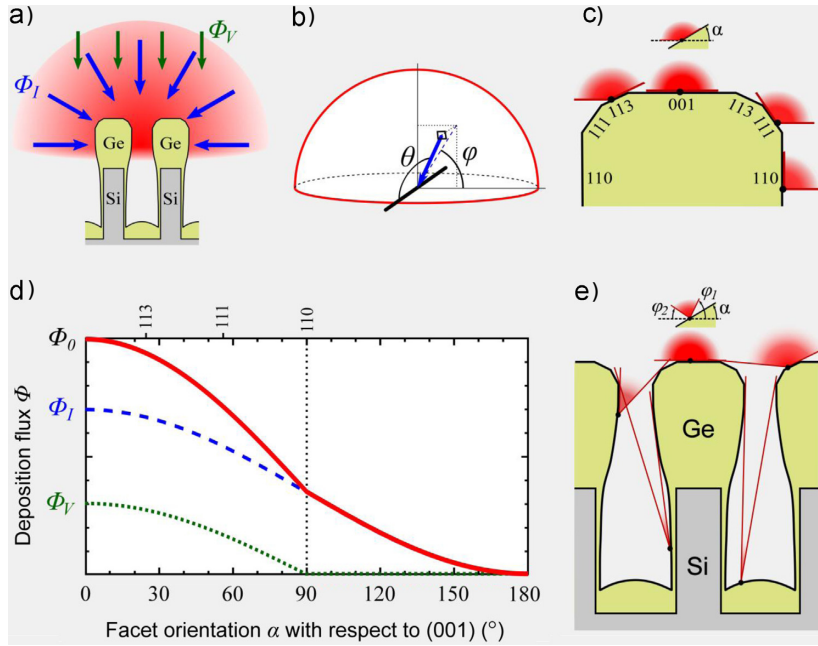


Figure 3.22: a) schematic representation of the reactive gas flux geometry. Φ_V is the vertical flux contribution which is superimposed to the isotropic one Φ_I forming an hemisphere above the sample. b) geometrical definition of the angles θ and φ used in the equation 3.8. c) schematic representation of the flux reduction due to the inclination of the crystalline facets. d) Variation of the net flux, labeled Φ_0 as a function of the angle between the normal to a crystalline facet and the (001) plane. The contributions of Φ_I and Φ_V are also reported. e) schematic representation showing the flux reduction due to shielding effects between adjacent crystals [98].

posited on the top of the Si pillars and in the trenches, which has been measured experimentally by cross-section SEM images.

Since each crystalline facet is inclined by an angle α with respect to the (001) interface plane, the actual impinging flux is reduced, as reported in Figure 3.22 c). Indeed the actual flux $\Phi(\alpha)$, can be calculated for each α angle, directly from equation 3.8 and considering the integration domain $W = \{\theta \in [0, \pi], \varphi \in [\alpha, \pi]\}$:

$$\Phi(\alpha) = \Phi_I \frac{1 + \cos\alpha}{2} + \Phi_V \cos\alpha \Theta(\pi/2 - \alpha) \quad (3.9)$$

where the Heaviside function Θ cuts the contribution of the vertical flux Φ_V for angles $\alpha > \pi/2$. The function $\Phi(\alpha)$, together with the vertical and isotropic contributions Φ_V and Φ_I , for different crystalline facet orientation, are reported in Figure 3.22. The total flux, labeled as $\Phi_0 = \Phi_V + \Phi_I$, is maximum for (001) crystalline facet and decreases monotonically for larger angles.

Equation 3.9 works in the case of isolated crystals, where the reduction of the actual impinging flux only depends on the facet inclination. On the other hand, Ge crystals are ar-

ranged in dense arrays, separated by micro-metric or even nano-metric gaps. In this configuration, the actual isotropic flux Φ_I impinging on one crystal is reduced by a shielding effect of the neighbors. This shielding effect depends on the position \boldsymbol{x} on the crystal surface and it is particularly marked on the lateral sidewalls.

Indeed, by considering a ballistic regime in the nearby of the crystal surface, the shielding effect can be easily calculated by simple geometric considerations and its effect is schematically depicted in Figure 3.22 e). By considering a 2D system, the net flux $\Phi(\alpha, \varphi_1, \varphi_2)$ impinging on a facet inclined by an angle α respect to the interface (001) plane can be calculated from equation 3.8 by imposing the integration domain $W = \{\theta \in [0, \pi], \varphi \in [\varphi_1, \pi - \varphi_2]\}$, where φ_1 and φ_2 define the angular sector to collect the gas flux and depend on the surface position, as sketched in Figure 3.22 e).

$$\begin{aligned} \Phi(\alpha, \varphi_1, \varphi_2) = \Phi_I \frac{\cos(\varphi_1 - \alpha) + \cos(\pi - \varphi_2 - \alpha)}{2} + \\ + \Phi_V \cos\alpha \Theta(\pi/2 - \varphi_1) \Theta(\varphi_2 - \pi/2) \end{aligned} \quad (3.10)$$

3.3.2 Kinetic parameters

Despite a lot of efforts spent in studying the SiGe system, most of the kinetic parameters, necessary to model the epitaxial growth of Ge crystals on Si pillars, are far from being known. Particularly, τ_c , τ_d and D are expected to strongly depend on the growth conditions (temperature and rate) and on local properties of crystalline facets, such as surface reconstruction, step density and crystallographic orientation. As a first approximation we have neglected the diffusion term, indeed the typical Ge diffusion length for LEPECVD at the growth rate of 4.2 nm/s and growth temperature of 400 - 600°C is $L \sim \sqrt{\tau D_0 e^{-E_a/k_B T}} \sim 100 - 200$ nm [97, 119, 120] where τ is the time to deposit one Ge monolayer and E_a is the activation barrier [121]. L is thus smaller than the Ge crystal facets and it corresponds to the size of the discretization elements in which the crystalline facets are considered (see Figure 3.20).

It has been reported [110, 122–125] that $Si_{1-x}Ge_x$ crystals tend to expose (001), {111}, {113} and {011} facets (see also Figure 3.7). Qualitatively, it is assessed that the (001) has the fastest growth velocity and the largest surface energy. Since establishing a growth rate order for the different

crystalline facets largely depends on the specific growth conditions, and no general agreement is found both for Si and Ge, we extracted the relative facet growth velocity by fitting the crystal morphology evolution with experimental profiles of isolated Ge crystals, i.e. negligible shadowing effects.

Indeed, as described in section 3.3.1 the kinetic crystal shape depends on the growth velocity of each crystalline facet, according to the Borgstrom construction. Therefore, in order to extract the relative growth rate of each facet, cross-section SEM images of Ge crystals deposited on isolated Si pillars (trench width of 50 μm) at different deposition stages have been analyzed. The growth sequence, obtained by superimposing the SEM cross-section images for different deposited Ge thicknesses, reported in Figure 3.23 a), allows to measure the relative growth rate of each crystalline facet in comparison to that one of the (001) surface. This assessment is performed by measuring the slope of the lines connecting the edges between different crystalline facets (dashed lines in Figure 3.23 a)) and using equation 3.5.

Since the flux of reacting species is constant (stationary conditions) and known from equation 3.9, it is possible to calculate the incorporating factors χ for each crystalline facet

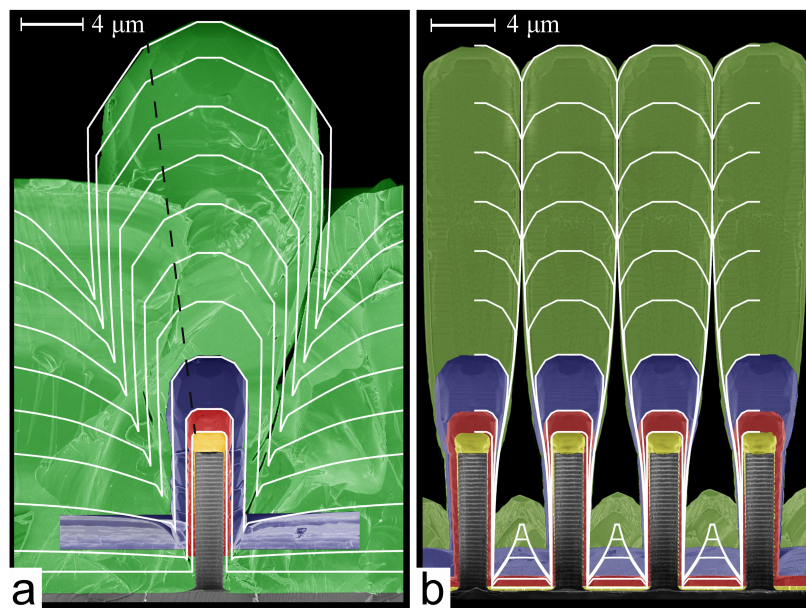


Figure 3.23: Comparison between Ge cross-section images of Ge crystals with different thickness (colored images) and simulated profiles (white lines) in the case of an isolated crystal a) and for an array of Si pillars separated by $4 \mu\text{m}$ wide trenches b). In a) the black dashed line traces the evolution of the border between $\{111\}$ and $\{113\}$ facets. Si pillars have lateral side $d = 2 \mu\text{m}$ and the Ge growth temperature is 490°C [98].

by using equation 3.7 (see Table 3.1).

Table 3.1 Model parameters for each crystalline facet. The growth velocities with respect to the (001) surface are obtained from the experimental profiles. The desorption/ etching time is set $\tau_a = 0.1s$ for all facets.

Facet	$v/v(001)$	$\Phi/\Phi(001)$	χ	τ_c (s)	N_{st}
(001)	1	1	0.91	0.010	0.31
{113}	0.91	0.94	0.87	0.014	0.40
{111}	0.65	0.74	0.80	0.024	0.48
{110}	0.28	0.38	0.67	0.049	0.42

The consistency between the simulated (indicated by white lines) and measured growth profiles (colored crystals) is verified in Figure 3.23 both for isolated and dense arrays of Ge crystals. The profile simulations, for isolated Si pillars, work finely to reproduce the Ge crystal morphology up to a thickness of $\sim 10 \mu m$. For taller crystals, deviations appear mostly on the lateral sidewalls, where the growth velocity is probably reduced by long range shielding effects of other crystals. In the case of dense array of Ge crystals, the profiles have been calculated taking into account the flux shielding due to neighboring pillars and using the same kinetic parameters considered for the isolated crystal case.

The very good agreement between the simulated and measured profiles of the dense array of Ge crystals reported

in 3.23 b), allows to explain the origin of the self-limited lateral expansion growth as a consequence of mutual shielding of the reactive gas between adjacent pillars. Indeed, the shielding effect, limits the amount of adatoms flux which can deposit on the $\{110\}$ sidewalls, thus reducing their growth velocity as the gap width between adjacent pillars shrinks. This shielding effect, combined with the small ratio between the Ge diffusion length and the Si features size, are the two key mechanisms ensuring the 3D epitaxial growth modality preferentially along the $[001]$ direction.

The evolution of the crystalline Ge facets can be traced during the deposition by inserting 10 nm thick, $Si_{0.1}Ge_{0.9}$ fully strained markers every 90 nm of Ge. Cross-section SEM images of 8 μm tall Ge crystals, with embedded 72 $Si_{0.1}Ge_{0.9}$ markers are reported in Figure 3.24. It is worth to notice that the simulated profiles displayed in Figure 3.25, for analogous pillars geometry, perfectly resemble the facet evolution shown by the markers in Figure 3.24.

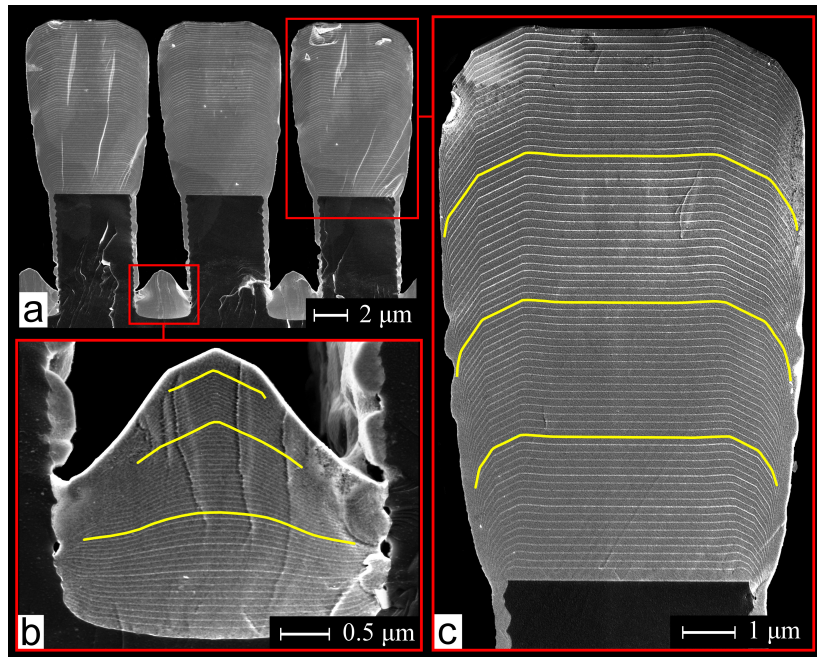


Figure 3.24: a) cross-section SEM image of $8 \mu\text{m}$ tall Ge crystals (deposited at 615°C and 4.2 nm/s) with 72 nm thick, $Si_{0.1}Ge_{0.9}$ fully strained markers every 90 nm of Ge. The Si pillar size is $d = 5 \mu\text{m}$ and are separated by $3 \mu\text{m}$ wide trenches. b) magnification of the material deposited in one trench, c) magnification of one crystal reported in a). The yellow lines remark 3 different $Si_{0.1}Ge_{0.9}$ marker positioned respectively $2, 4$ and $6 \mu\text{m}$ far from the Ge/Si interface [98].

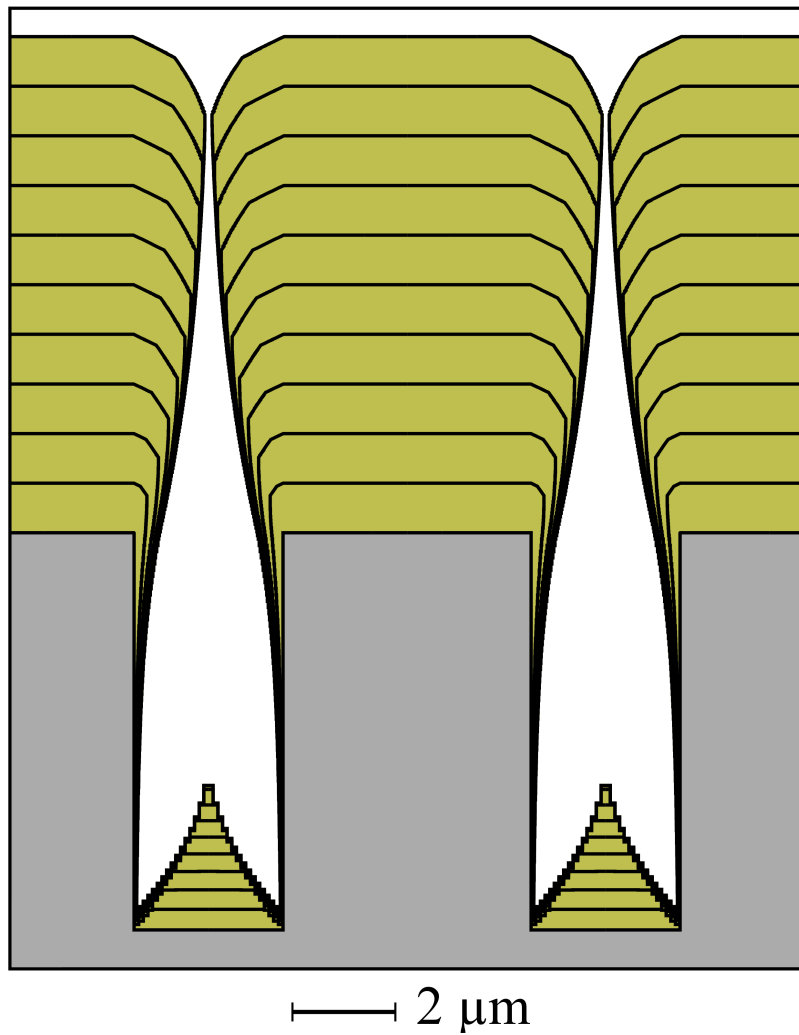


Figure 3.25: Profile simulation of 10 μm tall Ge crystals deposited on Si pillars with side $d = 5 \mu\text{m}$ and separated by 3 μm wide trenches. The growth front is displayed every 1 μm [98].

3.3.3 Diffusion and growth temperature effects

Due to the reduced Ge diffusion length scale ($\sim 100 - 200$ nm) compared to the typical Si pillar and crystal facet size, the role of adatoms diffusion has been so far neglected into the profile model. The only aspect taking into account the diffusion length, is the size (100 nm) of the linear elements in which the crystal surface has been discretized.

Particularly, by inspecting carefully the Ge surface morphology, both by SEM and AFM, it is possible to see traces of material diffusion at the borders between different crystalline facets, especially for high growth temperatures. Figure 3.26 a), b) confirms this observation by analyzing the top surface profile of 8 μm tall Ge crystal deposited at 535°C and 4.2 nm/s on Si pillars with lateral side $d = 5 \mu\text{m}$ and separated by 2 μm wide trenches.

The AFM line scan along the [110] direction through the middle of a Ge crystal, reported in Figure 3.26 b), clearly indicates the presence of a ridge (~ 60 nm tall) following the entire perimeter of the $\{113\}/(001)$ border, generated by local Ge accumulation between the two different crystalline

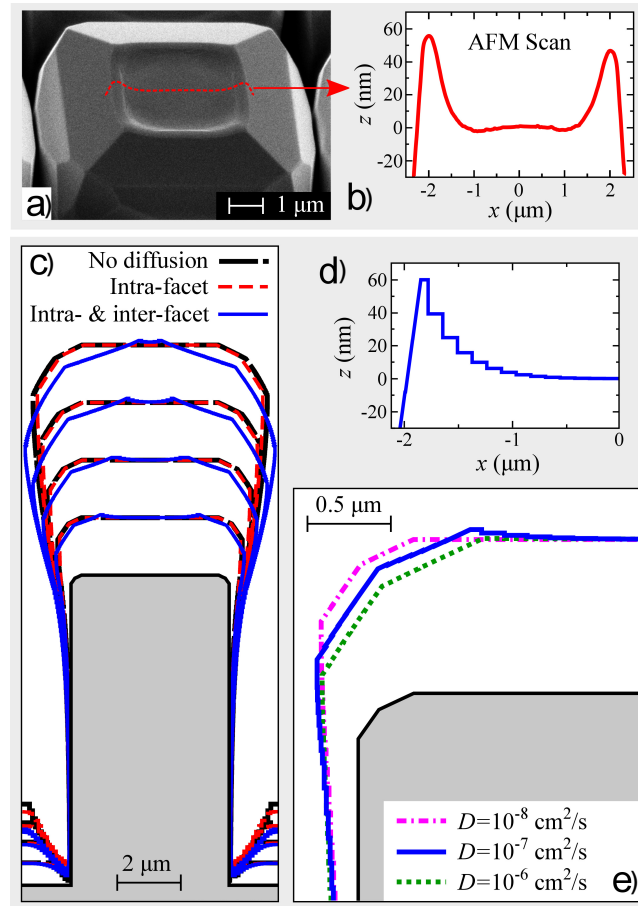


Figure 3.26: a) perspective SEM image and b) AFM scan profile along the $[110]$ direction through the middle of the top surface of a $8 \mu\text{m}$ tall Ge crystal deposited at 535°C and 4.2 nm/s on Si pillars with lateral side $d = 5 \mu\text{m}$ and separated by $2 \mu\text{m}$ wide trenches. c) Comparison of the simulated crystal profile evolution (every $1 \mu\text{m}$ up to $4 \mu\text{m}$) with no diffusion effects, intra-facet transport only and both intra- and inter-facet diffusion ($d = 10^{-7} \text{ cm}^2/\text{s}$). d) magnification of the simulated crystal profile at the border between $\{113\}$ and (001) facets after $1 \mu\text{m}$ of deposition with $d = 10^{-7} \text{ cm}^2/\text{s}$. e) Simulated crystal profiles after $1 \mu\text{m}$ of deposition with different adatom diffusivity D [98].

facets. More precisely, the profile of the Ge accumulated at the $\{113\}/(001)$ border decays exponentially within a length scale of 500 nm. This accumulation of material, can be explained by considering a short-range diffusion process at the border of different crystalline facets, from $\{113\}$ to (001) surface and it can be taken into account in the profile model by restoring the Fick diffusion term $\nabla_s \cdot [D\nabla_s N]$ in equation 3.4 [112–115, 126]. Different diffusion coefficients should be expected for diffusion process within the same crystal facet (intra-facet) and between different ones (inter-facet), indeed the latter process is eventually limited by higher kinetic barriers [111, 127, 128]. Moreover, additional energy barriers for diffusion are expected for highly stepped facets (Erich-Schwoebel barriers [129]). However we don't have sufficient quantitative data to estimate the intra- and inter-facet diffusivity difference, thus in the simulation the same value of D has been used for both mechanisms.

The simulation of Ge crystal profiles are reported in Figure 3.26 c), superimposing the profiles calculated without and with diffusion mechanisms choosing $d = 10^{-7}$ cm²/s. The morphology profiles calculated allowing only the intra-facet diffusion processes are very similar to the ones with

no diffusion. Indeed, the main effect of intra-facet diffusion, consists in moving the material in order to make the adatom density smoother within each facet. On the other hand, when both intra and inter-facet diffusion processes are taken into account, the crystal profile substantially changes respect to the no diffusion case. In particular, some material diffuses from $\{113\}$ and $\{111\}$ facets respectively towards (001) and $\{110\}$ facets. This process is determined by the different density of adatoms on each crystalline facet. A net flow of Ge atoms is produced from $\{113\}$ to (001) facet, creating the ridge at their border as evidenced experimentally by the AFM scan reported in 3.26 b). In 3.26 d) it is reported a magnification of the simulated crystal profile at the $\{113\}/(001)$ border with intra and inter-facet diffusivity $d = 10^{-7}$ cm²/s, clearly revealing the material accumulation in good agreement with panel b). An analogous situations is found at the $\{111\}/\{110\}$ facets border, where material diffuses towards the lateral $\{110\}$ sidewalls. This diffusion mechanism increases the lateral growth at the top of the $\{110\}$ sidewalls, thus increasing the narrowing of the inter-crystals distance faster.

Figure 3.26 e) reports the Ge crystal profile for different

values of Ge diffusivity. It is possible to distinguish three different diffusion regimes, as listed below.

1. Low diffusivity regime: $d = 10^{-8}$ cm²/s. In this condition, diffusion processes are negligible, the deposited material is frozen, the surface evolution is determined only by the flux distribution and no remarkable difference in the crystal profile is found respect to the no diffusion case.
2. Intermediate diffusivity regime: $d = 10^{-7}$ cm²/s. In this case, the diffusion effects become relevant and material accumulates at the border between different crystalline facets.
3. High diffusivity regime: $d = 10^{-6}$ cm²/s. In this case the diffusion processes are very effective, a more homogeneous redistribution of the material is reached, enabling to smear out the accumulation at the facets borders.

The impact of material diffusion between different crystalline facets on the morphology of the crystals consists in altering the relative growth rates and thus, as described in section 3.3.1, the resulting kinetic crystal shape. Indeed,

as shown in Figure 3.26, the net flux of atoms from $\{113\}$ and $\{111\}$ facets towards respectively (001) and $\{110\}$ surfaces, increases the growth rate of the latter ones and reduces the growth rate of the former ones because they are limited by the material supply from the gaseous phase. In particular, the inter-facet diffusion mechanisms, reduces the growth velocity ratio $v\{113\}/v(001)$, thus modifying the morphology of the crystal surface favoring the expansion of $\{113\}$ facets consuming the central (001) plateau which can eventually disappear for high growth temperatures and deposition thickness.

Actually, relative variations of growth rates can be more complicated to describe than considering only diffusion processes, since also incorporation dynamics may change with temperature through the temperature dependence of τ_c , τ_d and different surface reconstructions [128]. In order to analyze the variation of crystal morphology with the growth temperature (T_G), Ge crystals, 8 μm tall, have been grown at different temperatures, ranging from 415°C to 585°C, on Si pillars with side $d = 2 \mu\text{m}$ and separated by 2 μm wide trenches. Their top-view SEM images are reported in Figure 3.27.

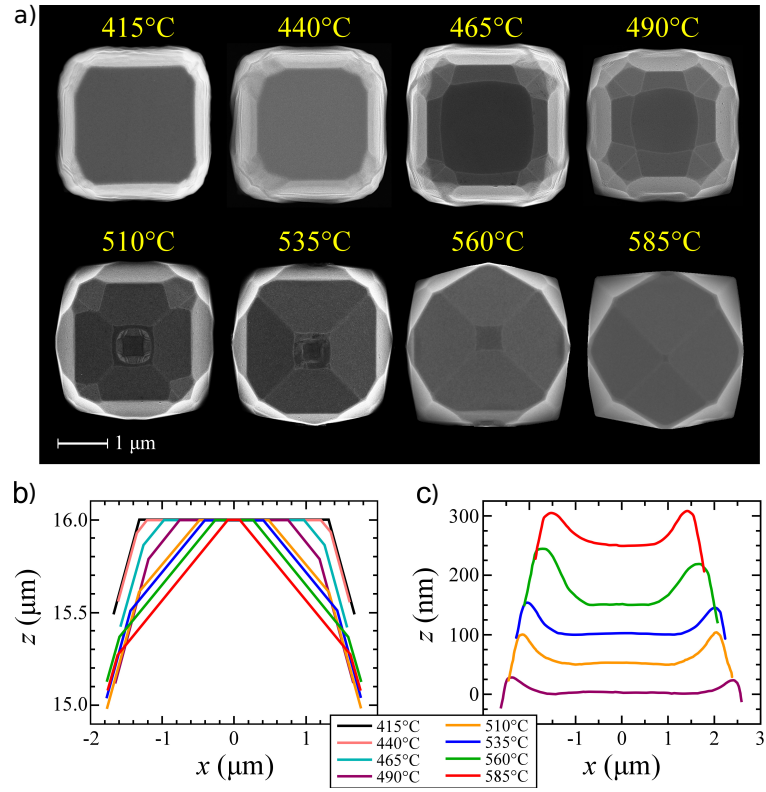


Figure 3.27: a) top-view SEM images of $8 \mu\text{m}$ tall Ge crystals grown at different temperatures (marked in yellow), ranging from 415°C to 585°C , on Si pillars with side $d = 2 \mu\text{m}$ and separated by $2 \mu\text{m}$ wide trenches. Profiles extracted from SEM images of the same Ge crystals reported in a). c) AFM profiles extracted from the top Ge surface of crystals deposited on Si pillars with side $d = 5 \mu\text{m}$ and separated by $2 \mu\text{m}$ wide trenches. In b) and c) the profiles are extracted along the $[110]$ direction through the middle of the crystal and the growth temperatures are labeled with different colors [98].

From the SEM and AFM images displayed in Figure 3.27, it is evident that the crystal morphology strongly depends on the growth temperature. Indeed, the top crystal shape, changes from a large (001) plateau almost covering the whole surface at $T_G=415^\circ\text{C}$, to a truncated pyramid at $T_G=515^\circ\text{C}$, and finally a full {113} facets bounded pyramid at $T_G=585^\circ\text{C}$. Considering that the facet with lower growth rate expands consuming the neighboring ones, the shrinking of the (001) surface increasing T_G , indicates that the $v\{113\}/v(001)$ ratio decreases for higher growth temperatures. Particularly, from the SEM images of Figure 3.27 b), the $v\{113\}/v(001)$ ratio is estimated to be 0.93 at $T_G=415^\circ\text{C}$, 0.89 at $T_G=515^\circ\text{C}$ and 0.96 at $T_G=585^\circ\text{C}$.

Thus tiny variations in the relative growth facet velocity lead to a large variation of Ge crystal morphology. The two main explanations for the change in the $v\{113\}/v(001)$ ratio with the growth temperature are diffusion mechanisms, as described before, which redistribute material between adjacent facets, and a decrease of the $\chi_{\{113\}}$ value for high growth temperatures. The latter case implies a reduction of the crystallization efficiency or higher etching/evaporation rate, which reduces the growth rate of {113} facets, thus

favoring their expansion.

A comparison between the experimental results and profile simulations for Ge crystals deposited at three different growth temperatures are reported respectively in Figure 3.28 a) and b). The simulated profiles reproduce the experimental data with very good agreement, showing the shrinking of the central (001) facet increasing the growth temperature. Panel c) reports cross-section SEM images of Ge crystals, grown at slightly different growth temperatures, with embedded 72 fully strained, 10 nm thick Si_{0.1}Ge_{0.9} markers every 90 nm of Ge. Still, the simulated growth fronts, at each deposition temperature, resemble the crystals shape evolution evidenced by the Si_{0.1}Ge_{0.9} markers.

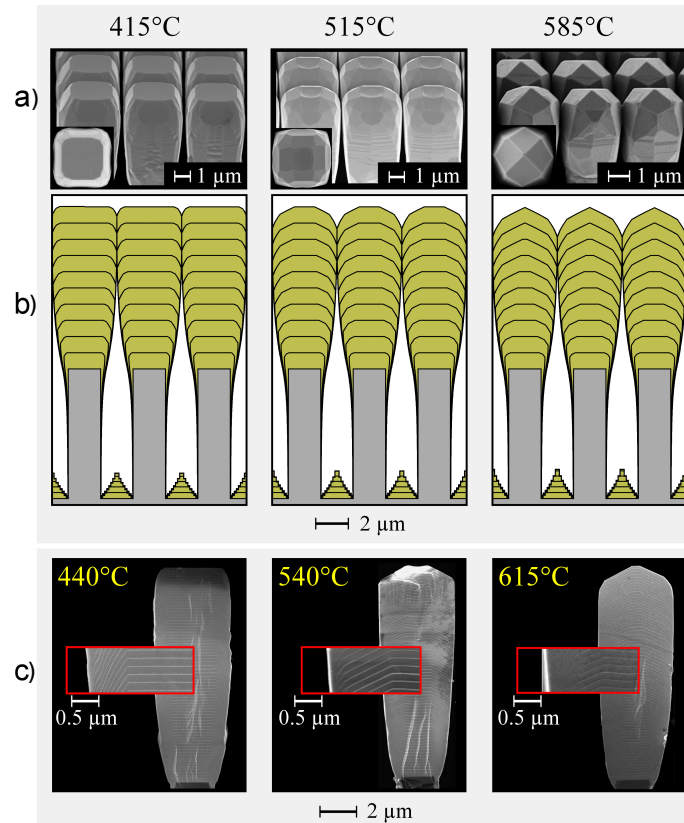


Figure 3.28: a) perspective and top-view SEM images of 8 μm tall Ge crystals grown at different temperatures (marked in black), on Si pillars with side $d = 2 \mu\text{m}$ and separated by 2 μm wide trenches. b) simulations showing the crystal evolution profile during growth. c) cross-section SEM images of 8 μm tall Ge crystals grown at different temperatures (marked in yellow), with embedded 72 fully strained, 10 nm thick $Si_{0.1}Ge_{0.9}$ markers every 90 nm of Ge, on Si pillars with side $d = 2 \mu\text{m}$ and separated by 2 μm wide trenches [98].

3.4 Thermal strain relaxation

The self-limited lateral expansion growth modality, as reported in section 3.1, allows to obtain several micrometers tall Ge crystals, separated by nanometric gaps, fully tessellating the sample surface with a filling factor up to 90%. Each isolated Ge crystal, deposited onto a Si pillar, can expand elastically to relax the thermal tensile strain accumulated during the cooling of the sample from the growth temperature (in the range 400°C - 600°C) to room temperature [97, 98, 102]. As already described in section 1.3, the thermal induced tensile strain in thick Ge/Si planar layers generates several problems, such as wafer bowing and cracks formation.

The Nomarski images reported in Figure 3.29 show that for 8 μm thick Ge layers, deposited at 490°C and 4.2 nm/s, thermal cracks running along the $\langle 110 \rangle$ directions are generated in the planar layer region, while they stop and don't propagate in the pillar patterned region.

The elastic relaxation of the thermal tensile strain in Ge crystals deposited on Si pillars has been confirmed by HR-XRD reciprocal space maps performed around Si(004) and

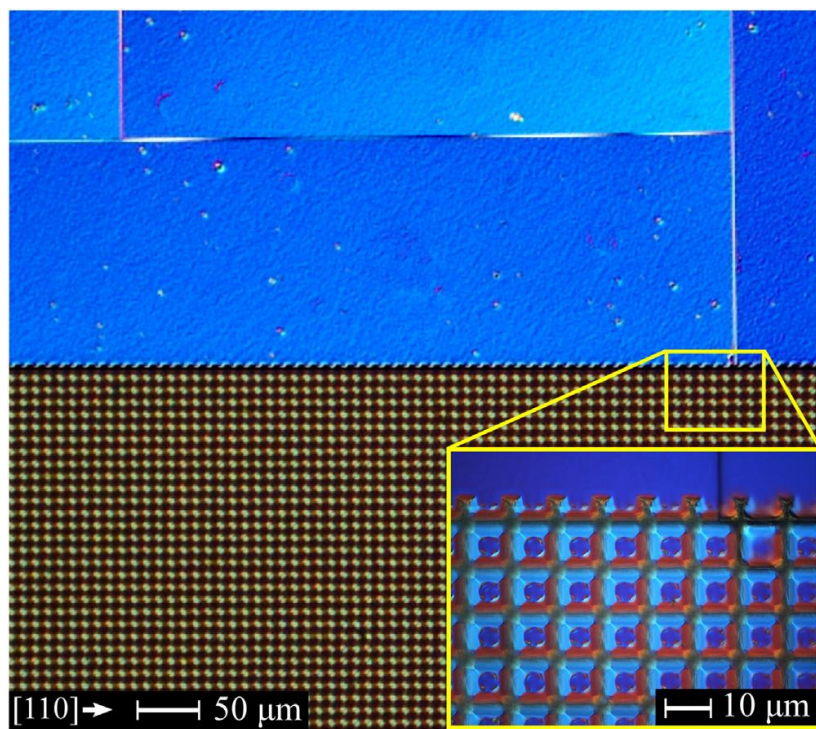


Figure 3.29: Nomarski images of the border between the unpatterned planar region and the patterned one with Si pillars (side $d = 5 \mu\text{m}$, separated by $8 \mu\text{m}$ wide trenches). Ge has been deposited with a thickness of $50 \mu\text{m}$ at 490°C and 4.2 nm/s [98].

(224) Bragg reflections and FEM simulations reported in Figure 3.30.

HR-XRD data, displayed in Figure 3.30 b), show that (004) Bragg reflection for Ge crystals deposited on Si pillars (region I and II, red line) is positioned exactly at the same Q_z position of a Ge bulk wafer (black line), thus confirming full relaxation of the tensile strain. Moreover, the FWHM of peaks I, II is extremely sharp, as sharp as the Ge bulk reference, thus confirming the high crystalline quality of the Ge crystals. Region II, labels the Ge crystals which are at the borders of the 10×10 pillars blocks, presenting an asymmetric crystal expansion, turning in minor tilting of the crystal lattice, not affecting the relaxation process [102]. More details about HR-XRD analysis on Ge/Si crystals can be found in chapter 5 and in reference [130]. The right side peak of the Ge crystals (region III, red line) shifted at higher Q_z values, with in plane strain $\varepsilon_{xx} = 0.09\%$ is related to the partially strained material deposited in the trenches between adjacent pillars (see panel a) to identify the different regions). Its intensity, compared to that one of region I and II, is only 0.013%. On the other hand, the (004) Bragg reflection peak of the planar Ge layer, is shifted to higher Q_z values, revealing

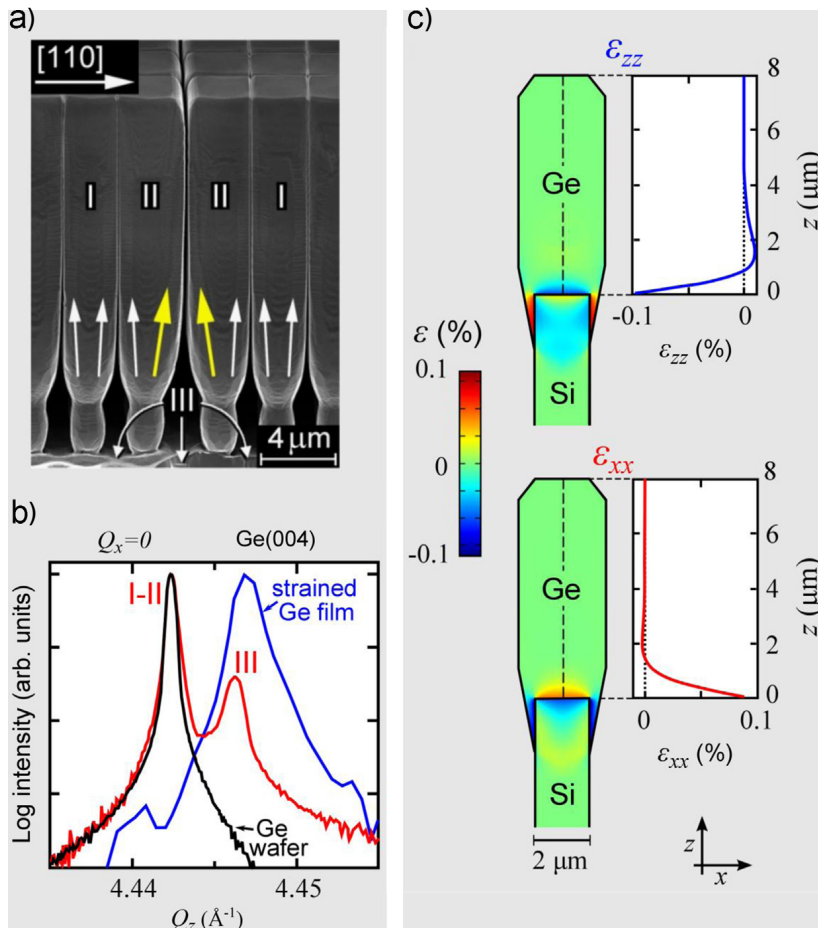


Figure 3.30: a) SEM image of 16 μm tall Ge crystals, deposited at 440°C and 4.2 nm/s on Si pillars with side $d = 2$ μm, separated by 1 μm wide trenches and arranged in 10×10 pillars blocks. b) HR-XRD scan along the Q_z direction ($Q_x=0$) for the (004) Bragg reflection of the Ge crystals depicted in a) (red line), of the tensile strained Ge planar layer (blue line) and a bulk Ge wafer (black line). The roman numbers I, II and III refer to different Ge positions labeled in a). FEM simulations of the strain components ϵ_{xx} and ϵ_{zz} for 8 μm tall Ge/Si crystals on Si pillars with side $d = 2$ μm. Both strain components are also extracted along the [001] z direction through the middle of the crystal [98, 102].

a tensile in plane strain $\varepsilon_{xx} = 0.11\%$, thus introducing wafer bowing and cracks formation. Indeed, FEM simulations, reported in Figure 3.30 c), show that the thermal tensile strain in high aspect ratio Ge crystals is completely elastically relaxed after $\sim 2 - 3\mu\text{m}$ from the Ge/Si interface.

Chapter 4

Dislocation Engineering in $\text{Si}_{1-x}\text{Ge}_x/\text{Si}$

The scope of integrating a mismatched epitaxial layer on a Si substrate points to two different targets [41]: i) the heterostructure acts as the active layer in a device, or ii) the epitaxial layer is used as a template, often called *virtual substrate* to deposit another semiconductor film with interesting electro-optical properties (typically a III-V crystal). In the first approach, the performances of the device are mostly limited by the nucleation of MDs at the hetero-interface to relax plastically the lattice mismatch [131]. In the second approach, the main requirement is getting an high quality

virtual substrate, which enables the integration of an high quality active layer, are the following [132]:

1. relaxed lattice parameter to avoid strain-related problems (see section 1.3)
2. low threading dislocation density
3. low surface roughness
4. reduced thickness

Therefore, the analysis of threading dislocation density, nature and orientation is fundamental in order to develop a deposition approach which fulfills all the listed requirements ensuring an high quality *virtual substrate*. In this chapter we will focus on the study of TDs character in Si_{1-x}Ge_x [133], describing also a viable approach to get fully relaxed, TD-free Ge crystals on patterned Si substrates [19].

4.1 Threading dislocation analysis and elimination in pure Ge crystals

A pure Ge epitaxial layer, 8 μ m thick has been deposited by LEPECVD on a Si patterned substrate (see sections 2.1.1

Threading dislocation analysis and elimination in pure Ge crystals 147

and 2.2) at 490°C and 4.2 nm/s. In Figure 4.1 an AFM scan of the Ge layer surface, deposited in the unpatterned planar region, is reported, showing no crosshatch pattern and a surface roughness with $\text{RMS}=0.68 \pm 0.05 \text{ nm}$ on a surface area of $400 \mu\text{m}^2$.

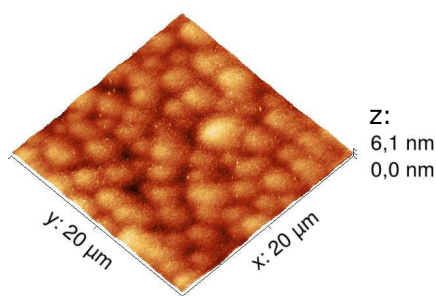


Figure 4.1: AFM scan of the surface of $8\mu\text{m}$ thick Ge layer deposited at 490°C and 4.2 nm/s.

The absence of the crosshatch pattern is typical in high-misfit heteroepitaxial systems where an high number of short dislocation loops are homogeneously nucleated [134, 135]. Indeed, a TDD of $9.0 \times 10^8 \text{ cm}^{-2} \pm 2.3 \times 10^8 \text{ cm}^{-2}$ has been measured counting by AFM dislocation etch pits after defect etching in *Iodine* solution (see section 2.3) on an area of

$1000 \mu\text{m}^2$. Figure 4.2 shows the surface of the Ge layer after defect etching in *Iodine* solution, emerging TDs are clearly revealed as conical shaped valleys [136].

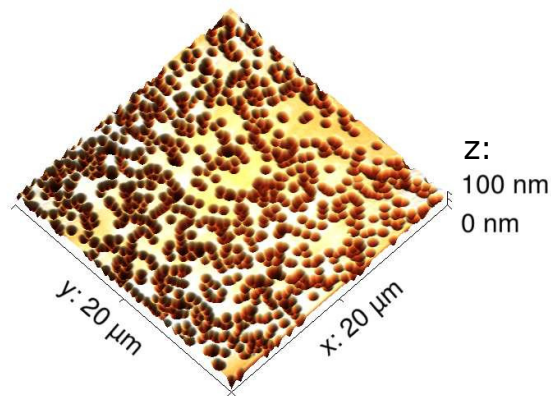


Figure 4.2: AFM image of the surface of $8\mu\text{m}$ thick Ge layer grown at 490°C and 4.2 nm/s by LEPECVD after defect etching in *Iodine* solution. Emerging TDs are clearly visible as dark valleys.

From the TDD value of the Ge film in the unpatterned region alone, it is impossible to extract any information about the nature (screw, edge or mixed) and orientation of the TDs. Indeed, in order to shed light on the characteristics of the

Threading dislocation analysis and elimination in pure Ge crystals 149

TDs, TEM, dark-field (DF) $\mathbf{g} \cdot \mathbf{b}$ and large angle convergent-beam electron diffraction (LACBED) [137, 138] $\mathbf{g} \cdot \mathbf{b}$ analysis have been performed.

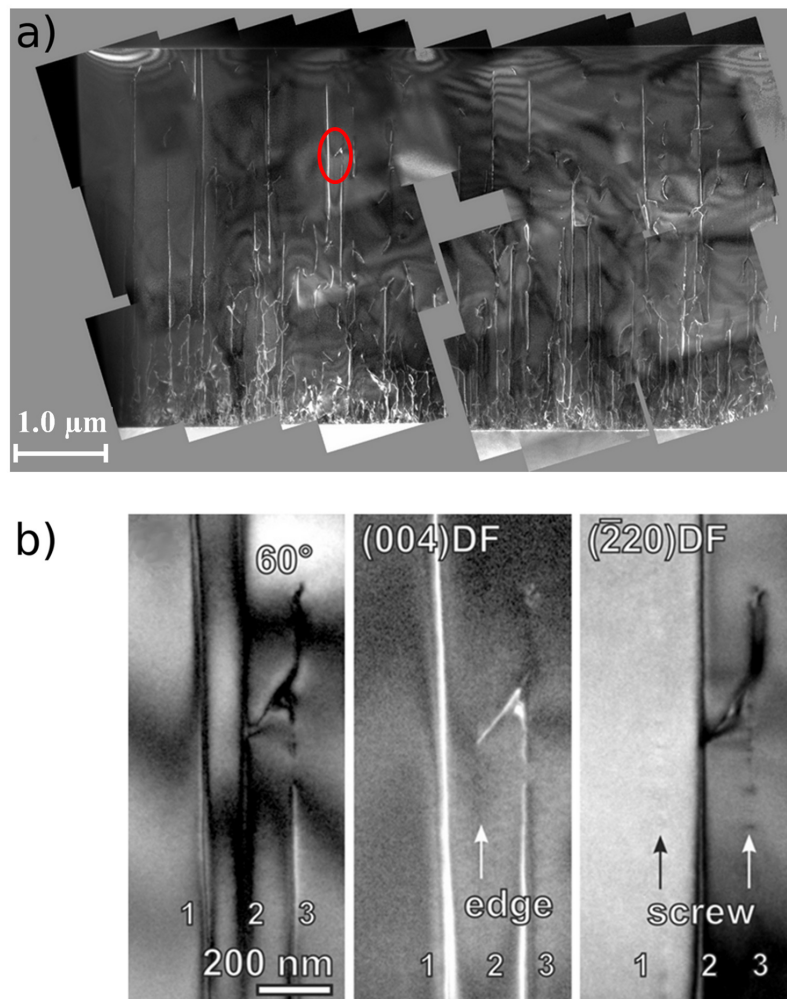


Figure 4.3: TEM analysis of an $8\mu\text{m}$ thick Ge layer grown at 490°C and 4.2 nm/s by LEPECVD on a (001) Si substrate. a) compilation of (004)-DF-TEM images of the unpatterned planar region. b) $g \cdot b$ analysis of 3 different vertical TDs marked by the red circle in a) [19].

Threading dislocation analysis and elimination in pure Ge crystals 151

In Figure 4.3 a), it is shown the cross-section (004)-DF-TEM image of an $8\mu\text{m}$ thick Ge layer grown at 490°C and 4.2 nm/s . Clearly, the majority of TDs is vertical (VDs), i.e. aligned along the $[001]$ direction [19]. The $\mathbf{g} \cdot \mathbf{b}$ analysis reported in Figure 4.3 panel b), clarifies the nature of the VDs. Indeed, here a bright field (BF) image is compared with two DF images taken with two different scattering vector geometries: $\mathbf{g} = [004]$ and $\mathbf{g} = [\bar{2}20]$. The invisibility criterion, states that a dislocation is invisible if the scalar product $\mathbf{g} \cdot \mathbf{b} = 0$, where \mathbf{b} is the Burger’s vector and \mathbf{g} is the scattering vector. The vertical threading dislocation #2 is invisible for $\mathbf{g} = [004]$, which means that is an edge-type TD (dislocation line $\mathbf{l} = [001]$) with Burger’s vector $\langle 110 \rangle$ oriented. Dislocations #1 and #3 are invisible with $\mathbf{g} = [\bar{2}20]$, thus are screw-type VDs with Burger’s vector \mathbf{b} parallel to the dislocation line $\mathbf{l} = [001]$. Dislocation #3 is dissociated, ending with two 60° TDs at the side faces of the TEM lamella. The DF $\mathbf{g} \cdot \mathbf{b}$ analysis reported in Figure 4.3 b) have been completed by LACBED measurements (see Figure 4.4), confirming edge-type Burger’s vector $\mathbf{b} = \frac{a}{2}[\bar{1}10]$ for TD #2 and screw-type Burger’s vector $\mathbf{b} = a[001]$ for TD #1 and for TD #3 [139]. S. Harada *et al.* [17], have already observed the presence of

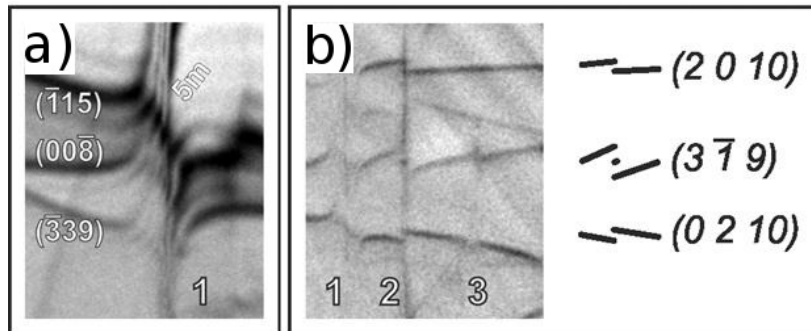


Figure 4.4: a) LACBED analysis of dislocation #1 confirming the screw nature of the VD by the presence of 5 minima in the $\mathbf{g} = (\bar{1}15)$ Bragg line, which is possible only for $\mathbf{b} = [001]$. b) LACBED analysis fully confirms the edge character of dislocation #2 ($\mathbf{b} = \frac{1}{2}a[\bar{1}10]$) thanks to the -1m, 2m and 1m minima for the $\mathbf{g} = (2010)$, $(3\bar{7}9)$ and (0210) Bragg lines respectively [139].

Threading dislocation analysis and elimination in pure Ge crystals 153

screw VDs in Ge/Si(001) crystals grown at $T = 450^\circ\text{C}$ by CVD. Here, the authors present a possible model to explain the formation of screw VDs, which is fully consistent with our findings. Two complementary 60° TDs, gliding in $\{111\}$ planes, respectively with Burger’s vectors $\mathbf{b}_1 = \pm\frac{a}{2}[\bar{1}10]$ and $\mathbf{b}_2 = \pm\frac{a}{2}[110]$ or $\mathbf{b}_1 = \pm\frac{a}{2}[011]$ and $\mathbf{b}_2 = \pm\frac{a}{2}[0\bar{1}1]$ reacts and after a climb process they align along the $[001]$ direction. Edge VDs, belonging to the secondary slip system of the diamond structure $\frac{a}{2}\langle 110 \rangle\{110\}$, can be related to the formation of edge Lomer dislocations ($\mathbf{b} = \pm\frac{a}{2}[110]$ or $\mathbf{b} = \pm\frac{a}{2}[1\bar{1}0]$) at the heterointerface due to the reaction of 60° MDs [52, 140]. The residual TD arms of the two interacting MDs, can join creating an edge VD via a climb process. Climb processes are mediated by the presence of vacancies [44], their concentration is expected to be several orders of magnitude larger than the thermodynamic value [141] due to the large out-of-equilibrium conditions of LEPECVD (for further details see section 4.2). In order to have a better statistic confirming that the majority of TDs is vertical, defect etching and TDs counting have been performed on Ge crystals $8\mu\text{m}$ thick grown at 490°C and 4.2 nm/s (same sample of the planar region reported in Figure 4.3) deposited on

square Si pillars with side d 5, 9 and 15 μm . Since slanted 60° TDs lay in $\{111\}$ glide planes, above a critical aspect ratio (height/width) of the deposited Ge crystals, 60° TDs are filtered out at the lateral sidewalls, while VD's reach the top (001) surface. Indeed, if the Ge crystal height h satisfies the dislocation expulsion condition $h > d \times \tan(\alpha)$, where $\alpha = 54.74^\circ$ is the angle between the $\{111\}$ glide planes and the (001) interface plane, the TDs reaching the top (001) surface are VD's aligned along the [001] direction. A sketch of the slanted TDs mechanism expulsion is reported in Figure 4.5.

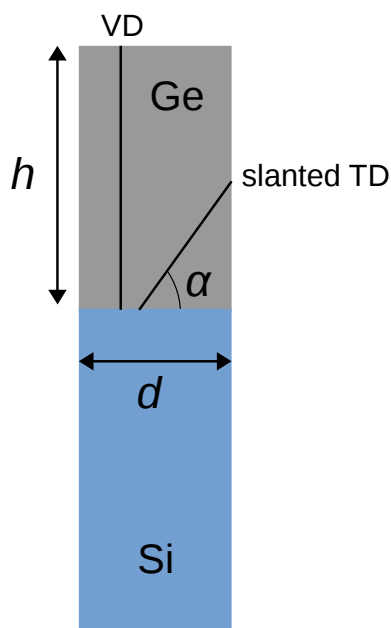


Figure 4.5: Sketch showing the slanted TDs expulsion at the Ge crystal sidewalls for $h > d \times \tan(\alpha)$. VDs reach the top (001) surface.

After defect etching in *Iodine* solution, the measured TDD on the top (001) surface of the Ge crystals with side d 5, 9 and 15 μm is respectively $9.5 \times 10^8 \text{cm}^{-2} \pm 2.1 \times 10^8 \text{cm}^{-2}$, $9.3 \times 10^8 \text{cm}^{-2} \pm 2.0 \times 10^8 \text{cm}^{-2}$ and $9.4 \times 10^8 \text{cm}^{-2} \pm 2.1 \times 10^8 \text{cm}^{-2}$ (see Figure 4.6). In Figure 4.7 are reported an SEM image of the 8 μm tall Ge crystals array deposited on Si pillars with side $d = 5 \mu\text{m}$ and an AFM scan after defect etching on the top (001) surface of a single Ge crystal.

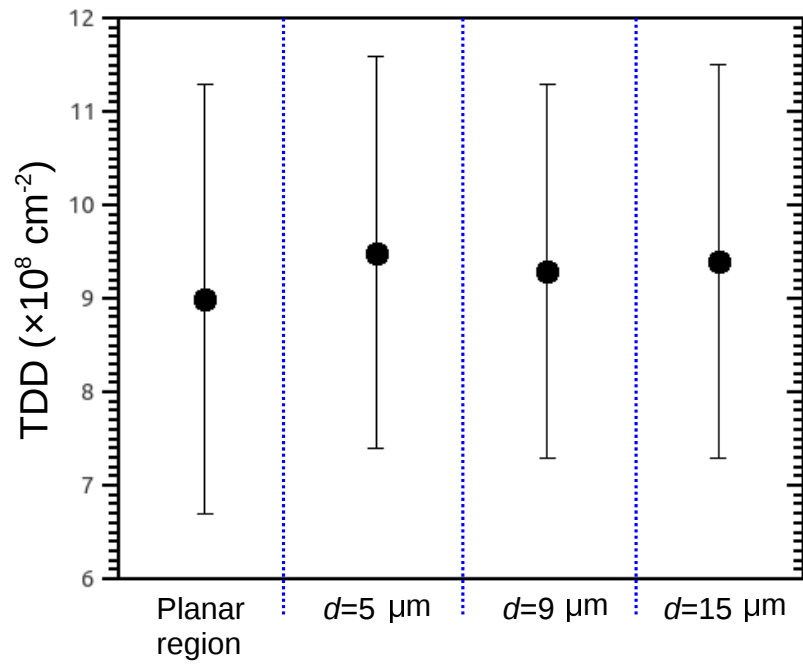


Figure 4.6: TDD of $8.0\mu\text{m}$ Ge deposited at 490°C and 4.2 nm/s on the planar region and on Si pillars with side $d = 5, 9$ and $15 \mu\text{m}$.

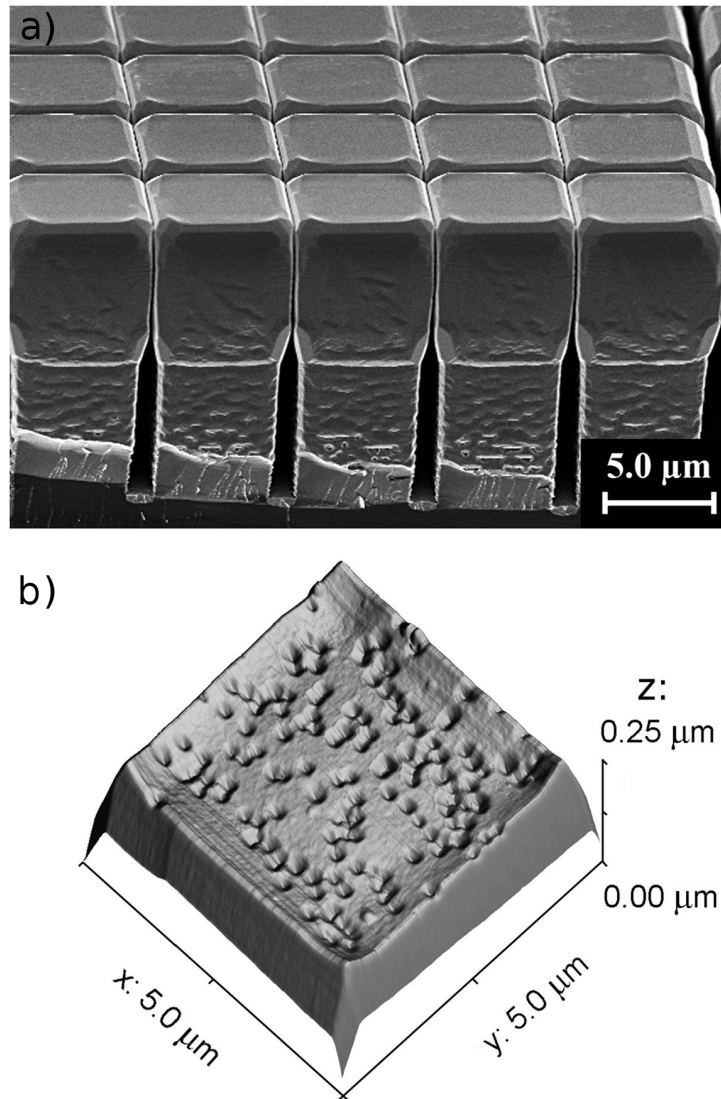


Figure 4.7: a) SEM image of array of Ge crystals $8 \mu\text{m}$ tall deposited at 490°C and 4.2 nm/s on Si pillars with side $d = 5 \mu\text{m}$ separated by $2 \mu\text{m}$ wide trenches. b) AFM scan after defect etching in *Iodine* solution of the top (001) surface of a Ge crystal reported in a) [19].

The TDD values of Ge crystals grown on Si pillars and on planar Si (001) are fully comparable within the experimental error, clearly demonstrating that the majority of TDs are vertical. Moreover, since the TDD in Ge crystals on Si pillars is remarkably independent on the Si pillar size d , it indicates that nucleation of dislocations is not influenced by finite-size effects. The dominance of VDs in Ge/Si (001) is further corroborated by the TDDs values reported in Figure 4.8. Here the TDD on the top (001) surface of Ge crystals with h ranging from 1 to 30 μm , deposited at 500°C and 4.2 nm/s on Si pillars with side $d = 5 \mu m$ is reported. Indeed, the TDD values shown in Figure 4.8 are independent on the Ge crystal height h , thus confirming the dominance of VDs.

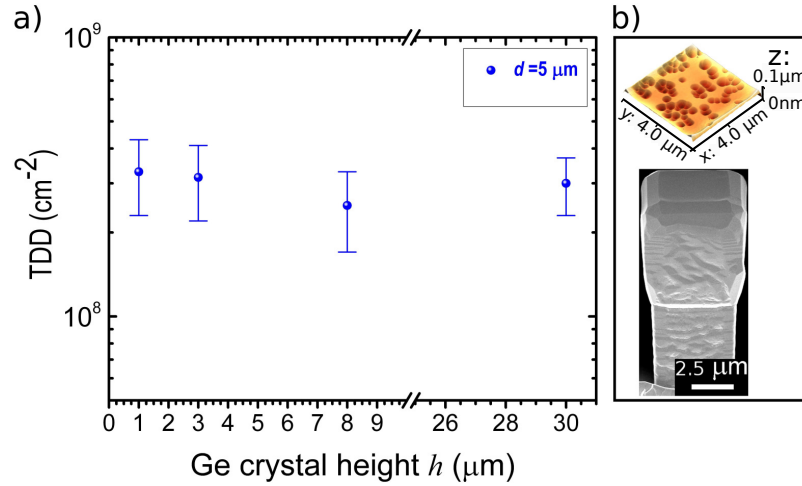


Figure 4.8: a) TDD on the top (001) surface of Ge crystals with different heights h , grown at 500°C and 4.2 nm/s on Si pillars with side $d = 5 \mu\text{m}$ and separated by 3μ wide trenches. b) (BOTTOM) SEM image of a Ge crystal ($h=8 \mu\text{m}$, $d = 5 \mu\text{m}$) before defect etching and (TOP) AFM scan of the top Ge (001) surface after defect etching in *Iodine* solution [133].

According to the limited statistic of TEM analysis, we found a larger fraction (by a factor of 2-3 in the Ge layer reported in Figure 4.3) of screw VDs with respect to edge VDs. For screw VDs, the dissociation of the Burger’s vector into equal sum $\mathbf{b} = \frac{a}{2} \langle 011 \rangle$ vectors is expected. This dissociation mechanism has already been reported in Ref. [17] after Ge annealing. Edge dislocation, are on the other hand sessile. Indeed, the dislocation mobility in the secondary slip system

$\langle 110 \rangle \{100\}$ is expected to be *per se* reduced compared to the primary slip system case [44]; moreover the biaxial stress, induced by the different expansion coefficients of the epilayer and substrate during annealing, has zero resolved shear stress. In order to study the stability, the different behavior and the density reduction of screw and edge VDs, annealing cycles have been performed. Annealing cycles increase the mobility of dislocations, providing a driving force for gliding due to the difference in thermal expansion coefficients of the epilayer and substrate. The enhancement of the dislocation mobility increases the annihilation/reaction between TDs [142], thus reducing their density [143, 144]. Due to the large aspect ratio of the Ge crystals deposited on Si pillars, finite element method (FEM) calculations (reported in Figure 4.9) show that the thermal strain is released elastically after $\sim 2 \mu\text{m}$ from the Ge/Si interface [97, 130]. Therefore, in order to induce a comparable thermal strain in the planar and patterned region during the annealing cycles, they have been performed *in situ* after $1 \mu\text{m}$ Ge deposition, then Ge has been deposited up to the final thickness of $8 \mu\text{m}$ in the same conditions. The annealing cycles consist in ramping the substrate temperature from 600°C to 800°C

with a set-point rate of $2^{\circ}\text{C}/\text{s}$ at 5×10^{-7} mbar in the LEP-ECVD reactor.

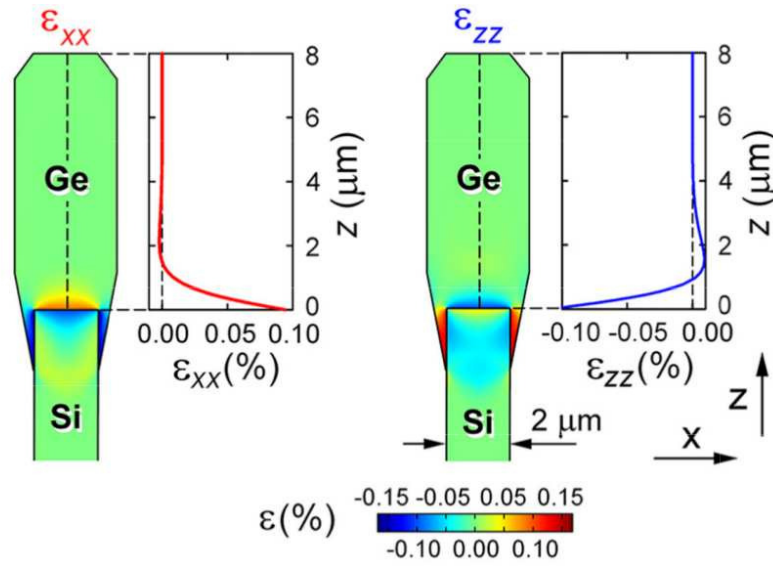


Figure 4.9: FEM calculations of the thermal strain Z-distribution within a $8 \mu\text{m}$ tall Ge crystal deposited on $2 \mu\text{m}$ large Si pillar. The graphs with the red and blue curves show respectively the strain components ϵ_{xx} and ϵ_{zz} in the center of the crystal ($x=0$) [102].

The TDDs of the annealed Ge layer, both on the planar unpatterned region and on the patterned area with Si pillars with side d 5, 9 and $15 \mu\text{m}$ have been measured ($3.9 \times 10^7 \pm 1.2 \times 10^7 \text{cm}^{-2}$, $5.3 \times 10^7 \pm 2.7 \times 10^7 \text{cm}^{-2}$, $2.5 \times 10^7 \pm 0.8 \times 10^7 \text{cm}^{-2}$ and $4.2 \times 10^7 \pm 0.7 \times 10^7 \text{cm}^{-2}$ respectively), showing a reduction by a factor ~ 30 with respect to the as

grown case. The TDD in the patterned area is fully comparable (within the experimental error which has been evaluated on a $500 \mu\text{m}^2$ wide area) with the one in the planar region. Therefore we can affirm that the reduction in TDD is mostly related to the mutual interaction between TDs, rather than gliding to the lateral sidewalls of the crystals. This effect is probably due to the large initial TDD which suppresses the TDs gliding favoring their interaction.

In order to analyze the different behavior of edge and screw TDs under annealing cycles, $\mathbf{g} \cdot \mathbf{b}$ analysis has been performed on $8 \mu\text{m}$ tall, annealed Ge crystals deposited on Si pillars with side $d = 2 \mu\text{m}$, as reported in Figure 4.10.

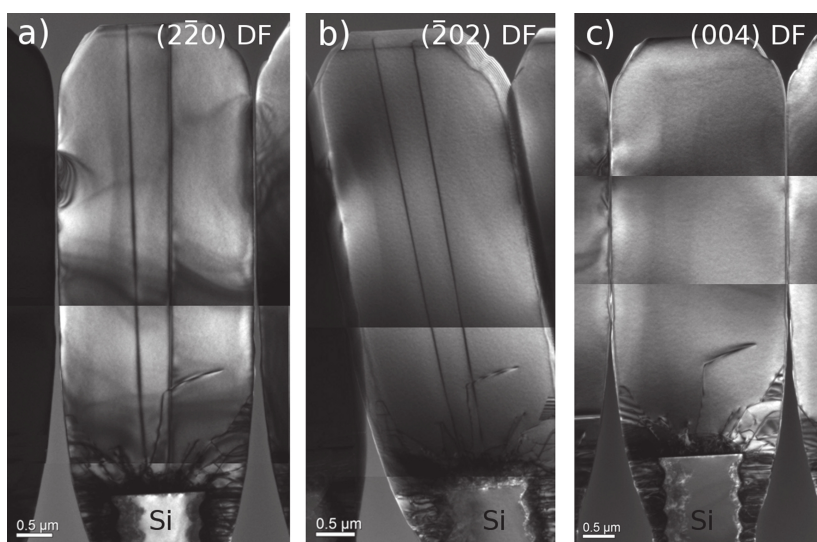


Figure 4.10: $g \cdot b$ analysis of a 8 μm tall, annealed Ge crystal deposited on Si pillars with side $d = 2 \mu\text{m}$. a) DF image with $g = [2\bar{2}0]$ close to the $[110]$ zone axis orientation. b) DF image with $g = [\bar{2}02]$ close to the $[112]$ zone axis orientation. c) DF image with $g = [004]$ close to the $[110]$ zone axis orientation [19].

According to the DF TEM images reported in Figure 4.10, two VDs are present, they are visible in panels a) ($g = (2\bar{2}0)$) and b) ($g = (\bar{2}02)$) while they disappear in c) ($g = (004)$) thus confirming the edge nature of these VDs with Burger’s vector $\mathbf{b} = \pm\frac{a}{2}[\bar{1}10]$ or $\mathbf{b} = \pm\frac{a}{2}[110]$. The same conclusion has been also found for other 3 Ge crystals (not shown here). Despite the relatively low statistic of TEM analysis, it is clearly evident that after annealing cycles the

only remaining VDs are sessile edge dislocations. Vertical screw dislocations have been dissociated into 60° gliding dislocations and annihilated. Since the ratio between screw and edge VDs density is $\sim 2-3$ in the as grown Ge case, and the TDD reduction after annealing cycles is \sim a factor of 30, a certain fraction of edge VDs have been also annihilated interacting with 60° dislocations. This conclusion is also confirmed by the work of Luan [145].

Despite the annealing cycles, for Ge/Si, the TDD cannot be lowered below $\sim 10^6 \text{ cm}^{-2}$, as reported also in other works [7, 143, 146, 147]. Here we present an innovative strategy for reducing to zero the TDD of Ge/Si layers with any annealing treatment (low thermal budget) based on the epitaxial deposition of faceted Ge crystals on patterned Si substrates.

Indeed, it has been demonstrated that if a TD is close to the crystal surface, it bends within the glide plane, towards the direction perpendicular to the growth front in order to reduce its length and therefore its self-energy [18, 142, 148]. C.V. Falub *et al.* [97], have demonstrated that this bending mechanism works also in the case of VDs in pure Ge crystals deposited on patterned substrates. Indeed, in the case of fully faceted $\{113\}$ Ge crystals, VDs are bent and expelled

laterally on the Ge sidewalls leaving the upper part of the crystal completely free of TDs, while in the case of (001) terminated Ge crystals the TDD is not reduced. This TDs expulsion mechanism is better schematically illustrated in Figure 4.11.

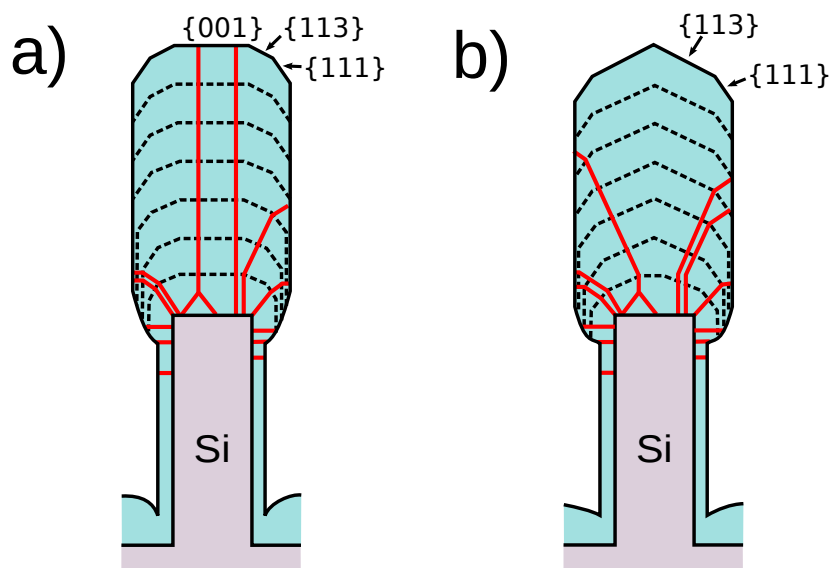


Figure 4.11: Schematic sketch of the VDs bending and expulsion mechanism in Ge/Si crystals. a) VDs reach the top (001) facet. b) all VDs are expelled laterally thanks to the fully {113} faceted crystal, leaving the upper part completely free of TDs [149].

As already reported in section 3.3.3 and in references [97, 98], depending on the Si pillar size d and the growth temperature it is possible to tune the Ge crystal faceting.

Indeed in Figure 4.12, SEM images and AFM scans after defect etching of 8 μm tall Ge crystals deposited at 610°C and 4.2 nm/s on Si pillars with side $d = 2$ and 5 μm , are reported, showing different morphology, i.e. (001) facet extension.

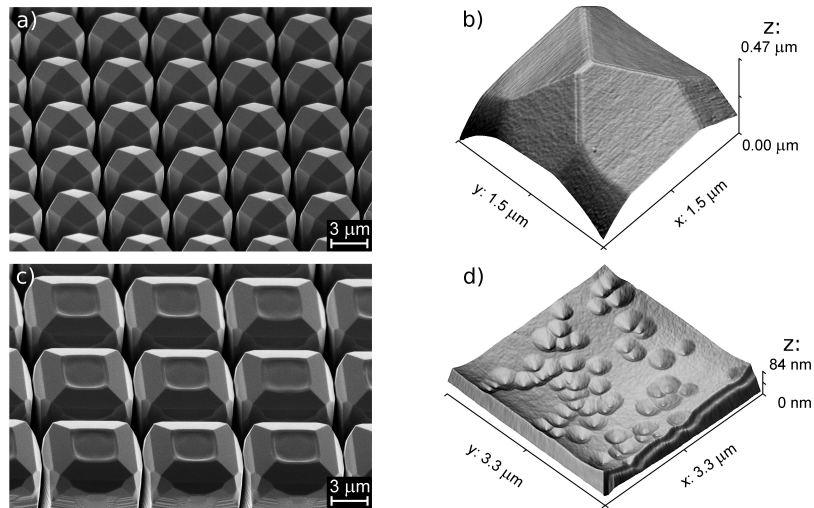


Figure 4.12: 8 μm tall Ge crystals deposited at 610°C and 4.2 nm/s on Si pillars with different sides. a) perspective SEM image of Ge crystals deposited on Si pillars with side $d = 2 \mu\text{m}$. b) AFM scan of the top Ge surface after defect etching in *Iodine* solution of a crystal reported in a). c), d) same of a), b) respectively, but for $d = 5 \mu\text{m}$ [19].

From the SEM and AFM scans after defect etching on Ge crystals reported in Figure 4.12, it is clearly evident the impact of the Ge (001) extension on the TDD. Indeed, in the

Threading dislocation analysis and elimination in pure Ge crystals 167

case of fully {113} faceted Ge crystals ($d = 5 \mu\text{m}$, panels a), b)) the TDD on the top Ge surface is 0, while in the case of larger Si pillars ($d = 5 \mu\text{m}$, panels c), d)), the TDD in the (001) surface remains in the 10^8 cm^{-2} range. In order to study the VDs bending and expulsion mechanisms, $8 \mu\text{m}$ tall Ge crystals with inserted 72 fully strained $\text{Si}_{0.1}\text{Ge}_{0.9}$, 10 nm thick markers, have been deposited at 610°C and 4.2 nm/s on Si pillars with side $d = 2 \mu\text{m}$.

From the cross-section SEM image of a Ge crystal with 72 embedded markers, reported in Figure 4.13, it is possible to trace the growth front evolution during the epitaxial growth. The growth front evolution evidences that {113} facets are already formed after few hundreds of nms from the Ge/Si interface, thus confirming that the VDs bending process starts from the very beginning of the epitaxial growth. From the technological point of view, would be more attractive to have flat topped (001) Ge crystals with $\text{TDD} = 0$. Indeed, this achievement has been fulfilled by depositing firstly $8 \mu\text{m}$ tall, fully {113} faceted Ge crystals at 610°C and 4.2 nm/s on Si pillars with $d = 2 \mu\text{m}$, to expel all VDs, then in a second step the growth temperature has been lowered to 415°C and additional $16 \mu\text{m}$ of Ge have been epitaxially grown. SEM

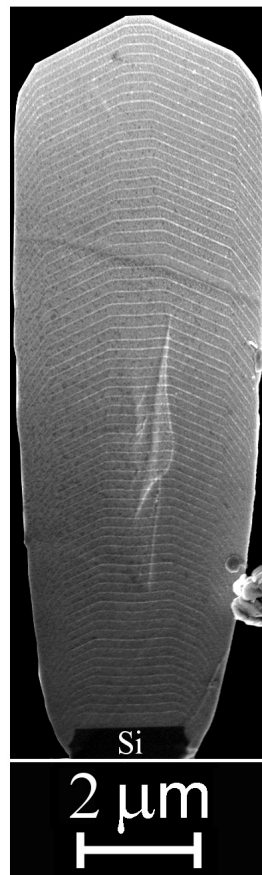


Figure 4.13: Cross-section SEM image of a 8 μm tall Ge crystals with inserted 72 fully strained $\text{Si}_{0.1}\text{Ge}_{0.9}$, 10 nm thick markers, deposited at 610°C and 4.2 nm/s on Si pillars with side $d = 2 \mu\text{m}$ [19]. The spacing between two adjacent markers is 90nm.

images and AFM scans after defect etching are reported in Figure 4.14.

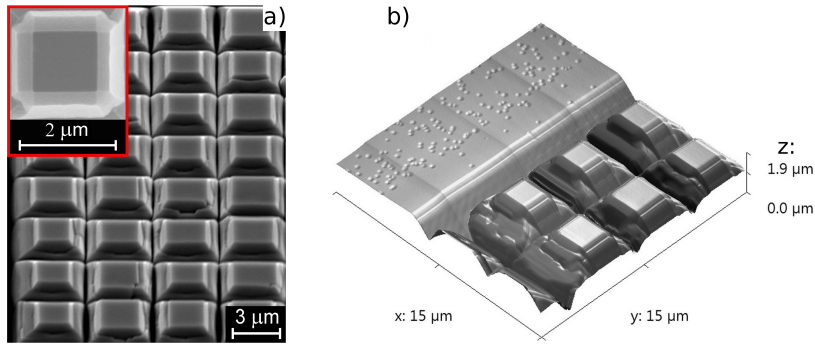


Figure 4.14: a) SEM image of Ge crystals grown in two temperature steps on Si pillars with side $d = 2 \mu\text{m}$ and separated by $2 \mu\text{m}$ wide trenches. First step: Ge $8 \mu\text{m}$ grown at 610°C and 4.2 nm/s . Second step: Ge $16 \mu\text{m}$ grown at 415°C and 4.2 nm/s . The red inset shows a magnification of the (001) top surface of a crystal. b) AFM scan of the border between the Ge crystals reported in a) and the planar region after defect etching in *Iodine* solution. TDs etch pits are present only in the planar region [19].

From the SEM images and AFM scans after defect etching, reported in Figure 4.14, it has been demonstrated the (001) terminated Ge crystals with $\text{TDD} = 0$ can be obtained. The first high temperature step, in which $8 \mu\text{m}$ tall Ge crystals have been deposited at 610°C and 4.2 nm/s , ensures the complete elimination of VDs, while the second low temper-

ature step: 16 μm tall Ge crystals deposited at 415°C and 4.2 nm/s allows to obtain (001) topped crystals. On the other hand, the TDD in the planar region, where the VDs expulsion mechanism is not effective, is $8.5 \times 10^8 \text{ cm}^{-2}$.

4.2 Onset of vertical threading dislocation formation in Si_{1-x}Ge_x/Si

In the previous section 4.1, the attention has been focused on the nature and stability of VDs in pure Ge crystals, while in this section the critical conditions, in terms of Ge concentration, misfit strain and growth parameters, for their formation will be treated. In particular, here we will demonstrate that above a critical Ge concentration $x \sim 0.25$, VDs dominate over the standard slanted threading dislocations. The dominance of VDs is explained in terms of activation of a climb mechanism favoring their formation [133].

In order to study the critical conditions for the formation of VDs in Si_{1-x}Ge_x alloys ($0.05 \leq x \leq 1.00$), several samples have been deposited on patterned Si (001) substrates. The list of Si_{1-x}Ge_x alloy samples and their respective growth parameters are reported in Table 4.1.

Onset of vertical threading dislocation formation in $\text{Si}_{1-x}\text{Ge}_x/\text{Si}$ 171

TABLE 4.1 List of $\text{Si}_{1-x}\text{Ge}_x$ samples and their respective growth parameters.

Ge content x	Crystal height h (μm)	Growth temperature ($^\circ\text{C}$)	Growth rate (nm/s)
0.05	15	740	5.2
0.20	8	715	6.2
0.25	15	705	6.5
0.30	8	690	6.9
0.40	8	645	7.3
0.50	8	600	7.4
1.00	8	500	4.2

The reported growth parameters in Table 4.1, ensure the depositions of $\text{Si}_{1-x}\text{Ge}_x$ epilayers with low surface roughness ($\text{RMS} < 3$ nm) for any Ge content x . Indeed, the large out-of-equilibrium growth conditions of LEPECVD (growth rate ranging between 4.2 to 7.4 nm/s) ensure to avoid island formation, particularly for the Ge-rich alloys on Si [147, 150].

Moreover, the morphology of the $\text{Si}_{1-x}\text{Ge}_x$ deposited on Si pillars is also comparable independently of the Ge content x , i.e. (001) facet extension, thus ensuring a fair comparison of TDD between different crystals. The SEM images reported in Figure 4.15 do confirm this observation.

The morphology of $\text{Si}_{1-x}\text{Ge}_x/\text{Si}$ pillars is illustrated by the SEM images reported in Figure 4.15. The $\text{Si}_{1-x}\text{Ge}_x$ crystals are characterized by slanted $\{113\}$ and $\{111\}$ facets close to

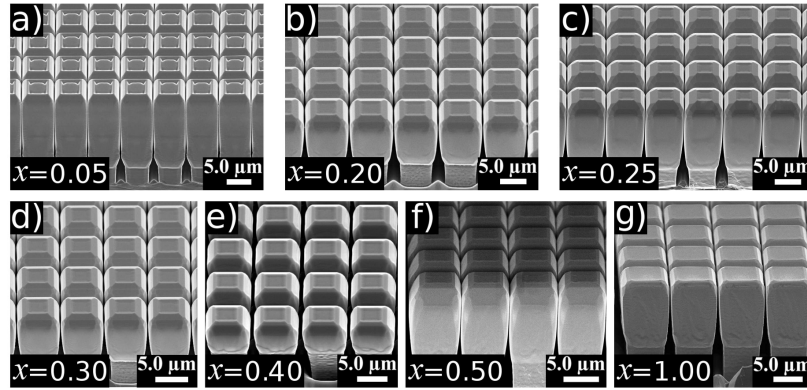


Figure 4.15: Perspective view SEM images of $\text{Si}_{1-x}\text{Ge}_x$ crystals, with different Ge content x , deposited on Si pillars with lateral side $d = 5 \mu\text{m}$. (a) $x = 0.05$, (b) $x = 0.20$, (c) $x = 0.25$, (d) $x = 0.30$, (e) $x = 0.40$, (f) $x = 0.50$, (g) $x = 1.00$ [133].

the edges and a large central (001) area. $\text{Si}_{1-x}\text{Ge}_x$ crystals deposited on Si pillars with larger lateral size $d = 9$ and $15 \mu\text{m}$ are characterized by a comparable morphology, in particular, as reported in Figure 4.16 for the $x = 1.0$ case, the central (001) area gets larger while the $\{113\}$ and $\{111\}$ facets remain unchanged with respect to the $d = 5 \mu\text{m}$ case.

As already described in the section 4.1, the deposition of [001] elongated $\text{Si}_{1-x}\text{Ge}_x$ crystals on Si pillars, enables the discrimination of the presence of VDs. Indeed, if the height h of the crystal satisfies the expulsion condition for slanted

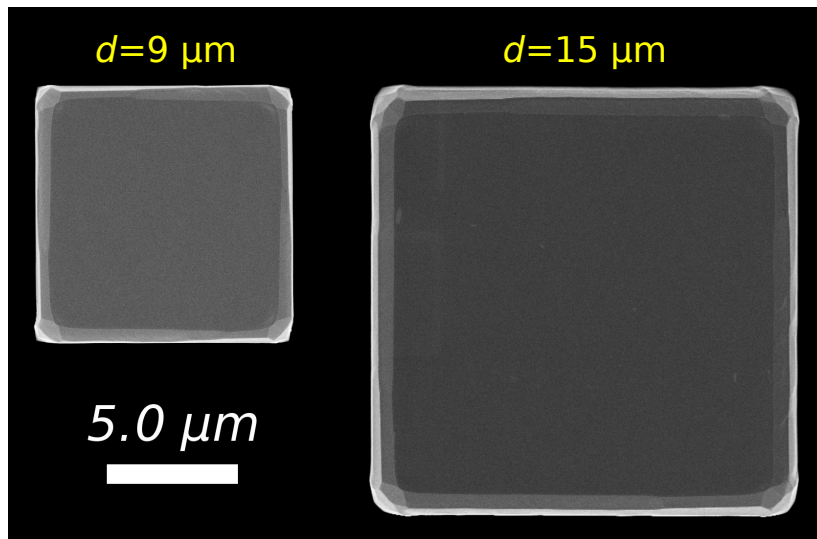


Figure 4.16: Top view SEM images of $8 \mu\text{m}$ tall Ge crystals deposited at 500°C and 4.2 nm/s on Si pillars with side $d = 9$ and $15 \mu\text{m}$ (indicated in yellow).

TDs laying in $\{111\}$ glide planes: $h > d \times \tan(\alpha)$, where $\alpha=54.74^\circ$ is the angle between (001) and $\{111\}$ planes, and after the defect etching some etch pits are revealed on the top crystal surface, the presence of VDs is confirmed (see the schematic sketch of Figure 4.5). The TDDs of the Si_{1-x}Ge_x alloys reported in Table 4.1 have been evaluated firstly dipping the samples in different etching solutions: *Iodine* for $x = 1.0$ or *Secco* for $x \leq 0.50$ (see section 2.3 and [93]), secondly by counting the etch pits formed at the emerging TDs by AFM, Nomarski microscope and SEM on an area of at least $200 \times 200 \mu\text{m}^2$. The TDDs measured for Si_{1-x}Ge_x alloys deposited both on Si pillars with different sides ($d = 5, 9$ and $15 \mu\text{m}$) and on the planar unpatterned Si (001) region are reported in Figure 4.17.

For what concerns the Si_{1-x}Ge_x planar layers, as expected, Figure 4.17 shows that increasing the Ge content x , i.e. increasing the lattice mismatch with respect to the Si substrate, the TDD raises since a larger number of dislocation loops is required to relax the stress. However, the etch-pit density counting in planar layers cannot give any information about the character (slanted or vertical) of TDs which have nucleated during the lattice relaxation process.

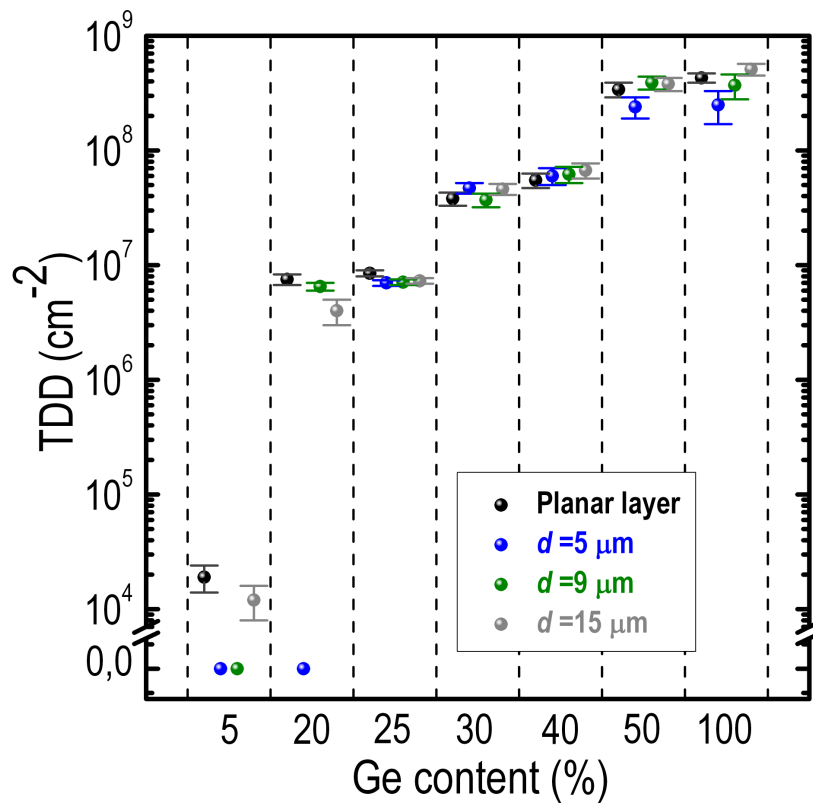


Figure 4.17: TDDs of $\text{Si}_{1-x}\text{Ge}_x$ alloys grown both on Si pillars with different sides ($d = 5, 9$ and $15 \mu\text{m}$) and on planar substrate as a function of the Ge content x . The height h of the crystals with $x = 0.25$ and $x = 0.05$ is $15 \mu\text{m}$, in the other cases is $8 \mu\text{m}$ [133].

On the other hand, the TDD of Si_{1-x}Ge_x crystals deposited on Si pillars, for a certain Ge content x , strongly depends on d . Indeed, for a Ge content $x < 0.25$, if the Si pillar size satisfy the slanted TDs expulsion condition $h > d \times \tan(\alpha)$, the measured TDD on the top surface of the Si_{1-x}Ge_x crystals is zero (within the experimental accuracy), thus all TDs are expelled laterally on the crystal sidewalls. Therefore, it is possible to conclude that in the case of Si_{1-x}Ge_x alloys with $x < 0.25$, all TDs are slanted in character, laying in $\{111\}$ glide planes.

On the contrary, for a Ge content $x \geq 0.25$, the TDDs on the top Si_{1-x}Ge_x crystals surface, independently on d , are always non zero and comparable (within the experimental accuracy) to the ones measured on the planar regions. Therefore, VDs dominate, with no remarkable dislocation expulsion effect on the lateral sidewalls. In Figure 4.18 are reported two key example of Si_{1-x}Ge_x alloys: $x = 0.20$ and $x = 0.30$, which are respectively below and beyond the threshold of the VDs dominance.

The effect of the VDs dominance on the surface properties of Si_{1-x}Ge_x alloys is illustrated in Figure 4.18. Indeed, panels a) and b) report AFM scans respectively of Si_{0.8}Ge_{0.2}

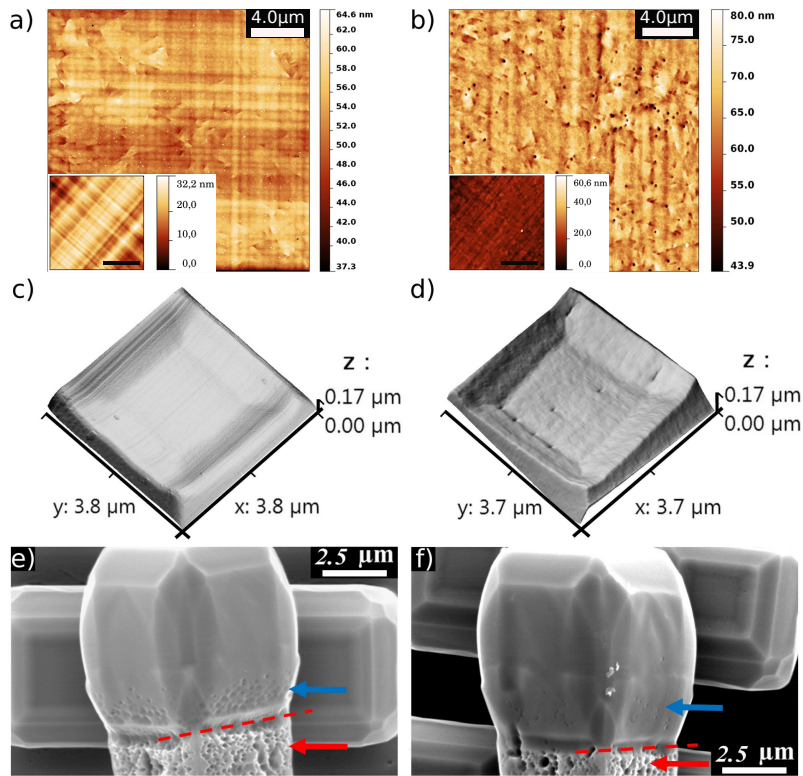


Figure 4.18: (a) and (b) are respectively AFM scans of $Si_{0.8}Ge_{0.2}$ and $Si_{0.7}Ge_{0.3}$ planar layers after defect etching in *Secco* solution. Emerging TDs are clearly visible as dark spots. The insets show the surface of planar layers before defect etching. The black size bar is $10\ \mu\text{m}$. (c) and (d) are respectively AFM scans of the top surface of $Si_{0.8}Ge_{0.2}$ and $Si_{0.7}Ge_{0.3}$ crystals deposited on Si pillars with $d = 5\ \mu\text{m}$ after defect etching in *Secco* solution. Etch pits are absent for $x = 0.20$ while abundant for the $x = 0.30$ case. (e) and (f) are respectively SEM images of the same crystals reported in (b) and (c) showing the distribution of TDs on the lateral sidewalls (marked by a blue arrow). The high number of defects present on the Si sidewalls (marked by a red arrow) is related to the scalloped Si surface due to the Bosch fabrication process of the pillars (see section 2.2). The dashed red line represents the $Si_{1-x}Ge_x/Si$ (001) interface [133].

and $Si_{0.7}Ge_{0.3}$ planar layers before (insets) and after defect etching. In the $Si_{0.8}Ge_{0.2}$ planar layer, the crosshatch pattern is very pronounced and visible, as expected in the case of a low misfit heterointerface (see section 1.2) where the plastic relaxation is driven by dislocation multiplication and piling up via $\{111\}$ glide planes. On the other hand, for the $Si_{0.7}Ge_{0.3}$ planar layer, the AFM scans of panel b) reveal a less remarkable crosshatch pattern. This behavior is in good agreement with the fact that the crosshatch pattern is known to disappear for rich Ge alloys on Si, because the large misfit at the heterointerface promotes the homonucleation of a large number of dislocation loops with an high interacting probability. This effect has been observed also for growth conditions closer to equilibrium than the LEPECVD case [134].

Figure 4.18 c) and d) show the AFM scans, after defect etching, of the top surfaces of a $Si_{0.8}Ge_{0.2}$ and $Si_{0.7}Ge_{0.3}$ crystals both satisfying the slanted TDs expulsion condition $h > d \times \tan(\alpha)$, being $d = 5 \mu\text{m}$ and $h = 8 \mu\text{m}$ in both cases. The $Si_{0.8}Ge_{0.2}$ crystal shows no TD etch-pit on the top (001) surface, while on the $Si_{0.7}Ge_{0.3}$ crystal they are abundant, confirming the dominance of VDs. The SEM images of pan-

Onset of vertical threading dislocation formation in
Si_{1-x}Ge_x/Si 179

els e) and f), which show the lateral sidewalls of respectively the crystals reported in c) and d), confirm that in Si_{0.8}Ge_{0.2} case, all slanted TDs have been expelled laterally close to the heterointerface. Indeed, a larger number of TD etch-pits is found on the lateral sidewalls of the Si_{0.8}Ge_{0.2} crystal compared to that one of the Si_{0.7}Ge_{0.3} crystal.

The TDDs reported in 4.17, show an abrupt transition between slanted 60° and vertical threading dislocations in Si_{1-x}Ge_x alloys for a Ge content larger than $x \sim 0.25$. In section 4.1, it has been shown that VDs can have both edge ($\mathbf{b} = \pm \frac{a}{2}[\bar{1}10]$ or $\mathbf{b} = \pm \frac{a}{2}[110]$) or screw ($\mathbf{b} = a[001]$) character, with two different formation mechanisms. Edge VDs are related to the reaction at the heterointerface of 60° misfit dislocations to form Lomer MDs [140, 151]; the residual TDs of the interacting 60° MDs can join and form an edge VDs via a climb mechanism which aligns the new threading arm along the [001] direction. On the other hand, screw VDs are formed by the reaction of two TDs gliding in {111} planes, with Burger’s vectors $\mathbf{b}_1 = \pm \frac{a}{2}[011]$, $\mathbf{b}_2 = \pm \frac{a}{2}[0\bar{1}1]$ or $\mathbf{b}_1 = \pm \frac{a}{2}[\bar{1}01]$, $\mathbf{b}_2 = \pm \frac{a}{2}[101]$ succeeded by a climb process [17].

Therefore, both an high interaction probability and climb processes are required in order to form VDs. The first re-

quirement, is fulfilled by increasing the Ge content in the Si_{1-x}Ge_x/Si alloys, since a larger lattice mismatch induces a larger number of MDs and TDs, as also confirmed by Figure 4.17 and [152]. The out-of-equilibrium LEPECVD growth conditions (very high growth rates, see Table 4.1) which have been used to grow the Si_{1-x}Ge_x/Si alloys, ensure a vacancy concentration several orders of magnitude higher than close to the thermodynamic equilibrium for any Ge content x , as already reported for other growth techniques [141]. The super-saturation and diffusivity of vacancy are known to promote climbing of dislocations [44], both at the heterointerface and within the epitaxial film, out from the {111} glide planes, thus favoring the alignment of TDs parallel to the [001] growth direction to reduce their length and self-energy [42, 153].

However, the abrupt $x \sim 0.25$ threshold for the formation of VDs, suggests that a critical value in the vacancy mobility D has been achieved. Indeed, according to Ref. [154], the vacancy diffusivity D can be described as the product of three exponential terms, as reported in equation 4.1.

$$D \propto e^{\alpha x} \times e^{\frac{\beta \varepsilon}{0.042}} \times e^{\frac{-E}{k_B T}} \quad (4.1)$$

*Onset of vertical threading dislocation formation in
Si_{1-x}Ge_x/Si* 181

where α and β are positive parameters, E is the diffusion activation energy, x the Ge concentration, ε the misfit strain and T is the growth temperature. The first exponential depends only on the chemical composition of the Si_{1-x}Ge_x alloy, while the second one on strain. However, in the TDD analysis reported in Figure 4.17, by comparing two different Si_{1-x}Ge_x alloys, both terms are changed since both terms linearly depends on x ($\varepsilon = 0.042x$, according to the Vegard’s law). Equation 4.1 gives a vacancy diffusivity D increasing monotonically with the Ge content x in the whole range of composition ($0.05 \leq x \leq 1.0$) analyzed in Figure 4.17 (for activation energies $E < 3.5$ eV), even considering the different growth temperatures reported in Table 4.1. In reference [154], an activation energy of 4.66 eV has been proposed, but due to the large out-of-equilibrium LEPECVD growth conditions, where a supersaturation of vacancies is expected to be generated during the deposition, lower values of E are expected [155]. Thus, the TDD values reported in Figure 4.17, which show an abrupt transition to VDs dominance, is therefore explained by assuming that a critical value in vacancy diffusivity D has been reached at a Ge content $x \sim 0.25$.

In order to shed light on the individual role played by the chemical composition of the Si_{1-x}Ge_x alloy and on strain, two additional *ad hoc* experiments have been performed. In these additional experiments, a two-step growth procedure has been adopted, where the Ge content is changed abruptly after a suitable height of the Si_{1-x}Ge_x/Si crystals. In the first case, Si_{0.8}Ge_{0.2} crystals with height $h_1 = 8 \mu\text{m}$ (analogously to those ones reported in Figure 4.17), followed by other $h_2 = 8 \mu\text{m}$ with $x = 0.40$ have been deposited, the growth conditions for both alloys are the ones reported in Table 4.1. The morphology of a crystal deposited on a Si pillar with side $d = 5 \mu\text{m}$ is reported in Figure 4.19.

The expulsion condition ($h > d \times \tan(\alpha)$) for slanted TDs in $\{111\}$ glide planes is satisfied in both steps. Indeed, the second Si_{0.6}Ge_{0.4} step, is deposited on TD-free Si_{0.8}Ge_{0.2} crystals, as shown by the TDD values reported in Figure 4.17. Surprisingly, despite the misfit strain at the Si_{0.6}Ge_{0.4}/Si_{0.8}Ge_{0.2} interface is the same one of the Si_{0.8}Ge_{0.2}/Si interface, VDs turn to be dominant, as reported by the SEM image after defect etching in *Secco* solution reported in Figure 4.20 with a TDD = $3 \pm 1 \times 10^7 \text{ cm}^{-2}$.

Another similar sample has been grown, where the first

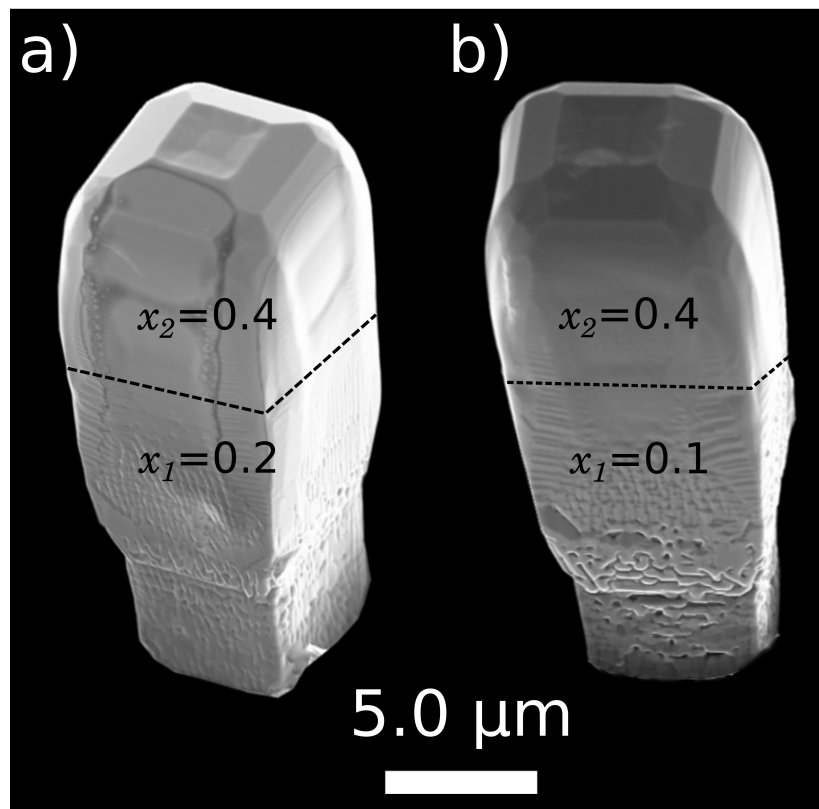


Figure 4.19: SEM image of the two-step experiment crystals deposited on Si pillars with side $d = 5 \mu\text{m}$. a) first step: Ge content $x_1 = 0.20$ and height $h_1 = 8 \mu\text{m}$, second step: Ge content $x_2 = 0.40$ and height $h_2 = 8 \mu\text{m}$. b) first step: Ge content $x_1 = 0.10$ and height $h_1 = 8 \mu\text{m}$, second step: Ge content $x_2 = 0.40$ and height $h_2 = 8 \mu\text{m}$.

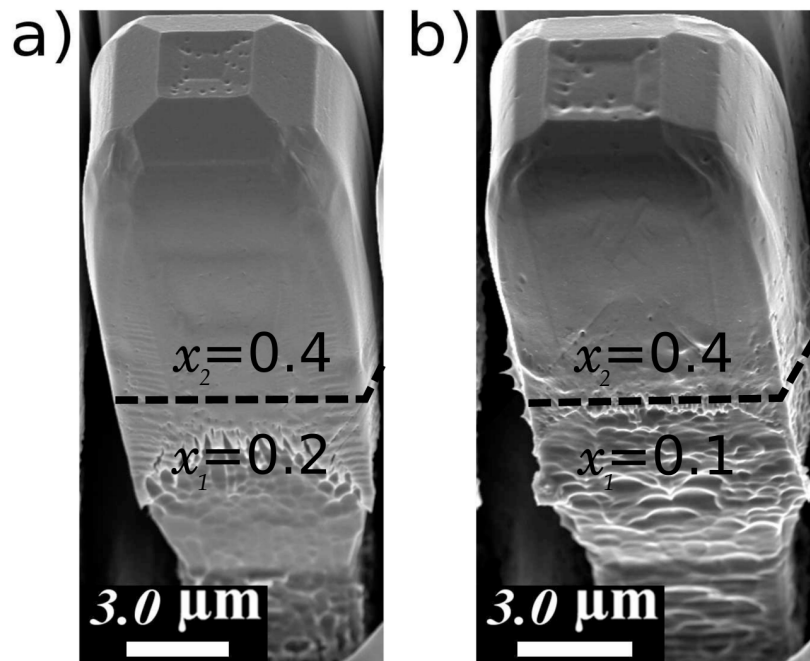


Figure 4.20: SEM image of the two-step experiment crystals deposited on Si pillars with side $d = 5 \mu\text{m}$ after defect etching in *Secco* solution, emerging VDs are clearly visible as pits on the top surface [133]. a) first step: Ge content $x_1 = 0.20$ and height $h_1 = 8 \mu\text{m}$, second step: Ge content $x_2 = 0.40$ and height $h_2 = 8 \mu\text{m}$. b) first step: Ge content $x_1 = 0.10$ and height $h_1 = 8 \mu\text{m}$, second step: Ge content $x_2 = 0.40$ and height $h_2 = 8 \mu\text{m}$.

Onset of vertical threading dislocation formation in
Si_{1-x}Ge_x/Si 185

step consists in Si_{0.9}Ge_{0.1} crystals with height $h_1 = 8 \mu\text{m}$ and the second one still with $x_2 = 0.40$ for $h_2 = 8 \mu\text{m}$. Despite the slanted TDs espulsion condition is still satisfied and the Si_{0.6}Ge_{0.4} alloy is deposited on TD-free Si_{0.9}Ge_{0.1} buffer, VDs are present with a TDD = $3.2 \pm 1 \times 10^7 \text{ cm}^{-2}$, fully comparable, within the experimental accuracy, to that one found in the former Si_{0.6}Ge_{0.4}/Si_{0.8}Ge_{0.2}/Si case.

The dependence of the vacancy diffusivity D on the misfit strain and on the Ge content in the alloy can be separately addressed by comparing the TDD results reported in Figure 4.17 with those of the two-step samples. Indeed, in the latter case, the threshold for the VDs dominance has been observed in samples with strain $\varepsilon = 0.0084$ and Ge content $x = 0.40$, while in the former case it has been found for strain $\varepsilon = 0.0105$ and Ge content $x = 0.25$. Equation 4.1 allows to state that in the two-step experiment, a vacancy diffusivity D overcompensation between the reduction in the misfit strain value and the increase in the Ge content, has been reached with respect to the TDD data reported in Figure 4.17. It is worth noticing that the $\alpha = 8.1$ and $\beta = 14.9$ values reported in Ref. [154] support this interpretation, since the increase of D due to higher Ge concentrations is larger

than the decrease due to lower misfit strain. Moreover, the experimental results show that the higher Ge content also compensate the reduction of vacancy diffusivity D due to the lower growth temperature (see Table 4.1 and equation 4.1).

Chapter 5

Nanofocused HR-XRD analysis of Ge/Si crystals

In this chapter it will be discussed the nanofocused HR-XRD analysis of $\text{Si}_{1-x}\text{Ge}_x/\text{Si}$ crystals performed at the European Synchrotron Radiation Facility (ESRF) of Grenoble during the experiments HS-4674 and HS-4277 at the beamline ID-01. In particular, the attention will be devoted to: studying the lattice bending of the Ge crystals due to the relaxation of thermal tensile strain, evaluating the net tilt of individual crystals after plastic relaxation, and finally, mapping the crystal quality at the nanometric scale showing that a nearly perfect single crystal structure has been obtained despite the

heavily dislocated interface [130].

In section 3.4 and in Refs. [102] and [98], have been presented an HR-XRD analysis of arrays of closely spaced Ge crystals deposited on patterned Si substrates. However, the informations, about strain and crystal quality, which can be extrapolated from these measurements are averaged over thousands of different crystals, since the spot size of the laboratory X-Ray source is ~ 1 mm.

In this chapter, we discuss the crystal quality and strain mapping at a nanometric scale, of isolated Ge crystals, using a nanofocused synchrotron X-Ray beam, with the scattering geometry reported in Figure 5.1. The incident and scattered wave vectors, respectively K_0 and K_s , define the scattering plane with reciprocal space directions (Q_x, Q_z) . Thanks to the incident beam focusing and the use of a two dimensional (2D) detector, the scattered X-ray signal simultaneously give informations in the whole reciprocal space (Q_x, Q_y, Q_z) .

Ge crystals have been individuated by recording the total diffracted intensity for the asymmetric Ge(115) Bragg reflection, moving the sample in the real space (x, y) plane defined in Figure 5.1. In Figure 5.2 are reported the (x, y) intensity scans together with SEM images of Ge crystals with differ-

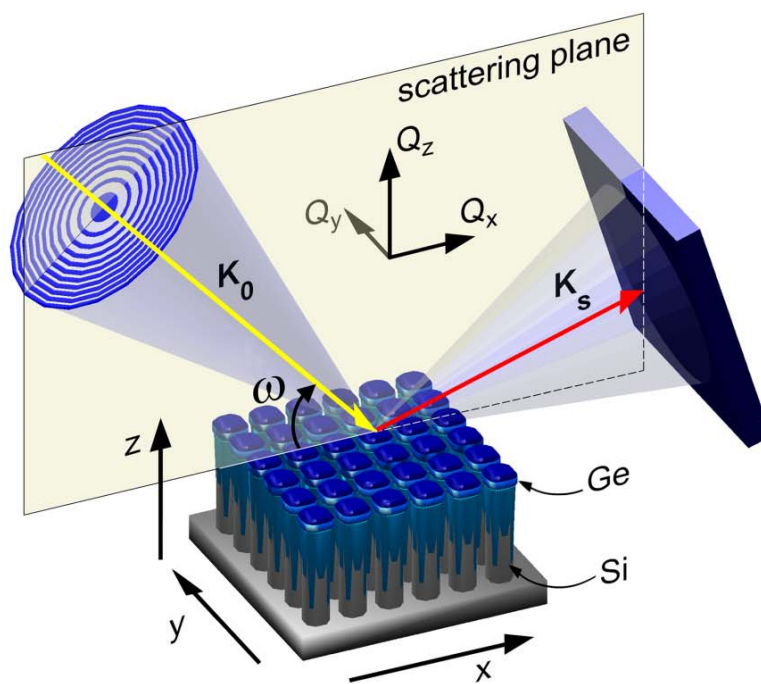


Figure 5.1: Schematic representation of the experimental setup used at the ESRF beamline ID-01. The incident beam (angle ω and wave vector K_0) is focused down to a spot size of $\sim 500 \times 300 \text{ nm}^2$ by means of Fresnel zone plates and it scans across the sample by a high-precision piezo-stage [130].

ent height deposited on Si pillars with side $d = 2 \mu\text{m}$ and separated by $1 \mu\text{m}$ wide trenches. It is evident that increasing the amount of deposited material, Ge crystals get closer and more difficult to spatially resolve due to the scattering geometry and penetration depth of X-Rays.

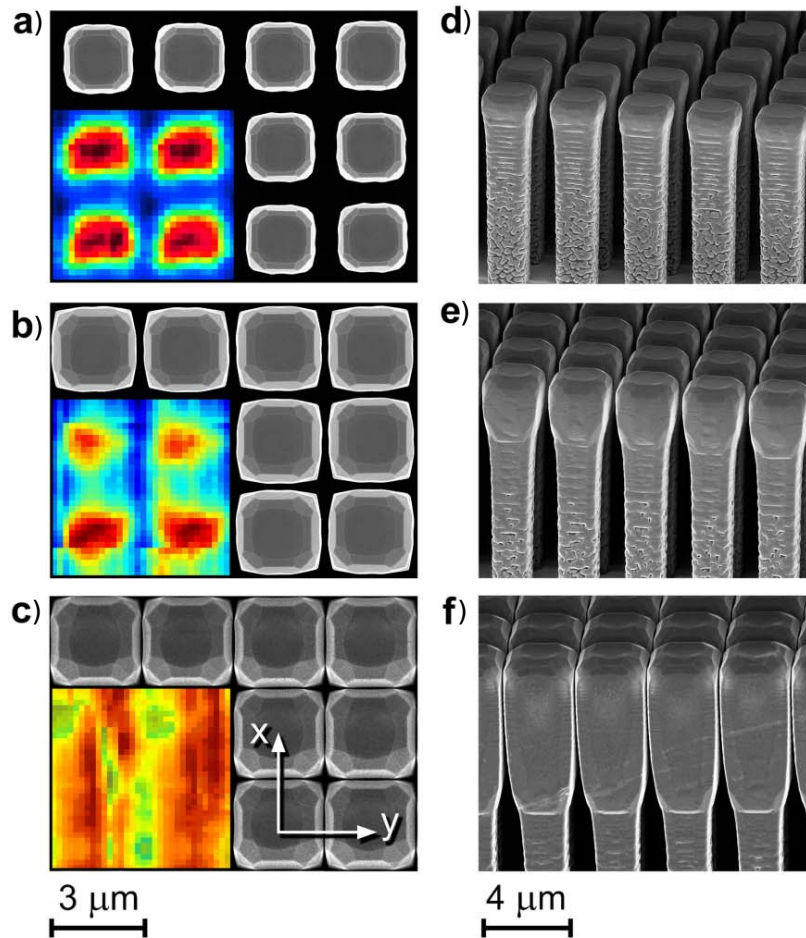


Figure 5.2: Top and perspective view SEM images of Ge crystals with height $1,2 \mu\text{m}$ (a), d)), $3,1 \mu\text{m}$ (b), e)), $7,3 \mu\text{m}$ (c), f)) deposited on Si pillars with side $d = 2 \mu\text{m}$ and separated by $1 \mu\text{m}$ wide trenches. The insets in a), b) and c) show the total intensity scans in the (x, y) plane for the Ge(115) Bragg reflection [130].

5.0.1 Lattice bending at the Ge/Si interface

In this section the lattice bending of Ge crystals with height $1,2 \mu\text{m}$, deposited on Si pillars with side $d = 2 \mu\text{m}$ and separated by $1 \mu\text{m}$ wide trenches, will be treated.

Figure 5.3 reports the 3D reciprocal space maps (RSMs) for the Si and Ge(115) Bragg reflections, projected on to the (Q_x, Q_y) plane parallel to the Ge/Si interface (see Figure 5.1). The Si(115) diffraction peak position doesn't change by scanning the incident X-ray beam on different positions of the Ge crystal array. On the other hand, this is not the case for the Ge(115) peak, where the scattered intensity profile is correlated to the incident X-Ray beam position.

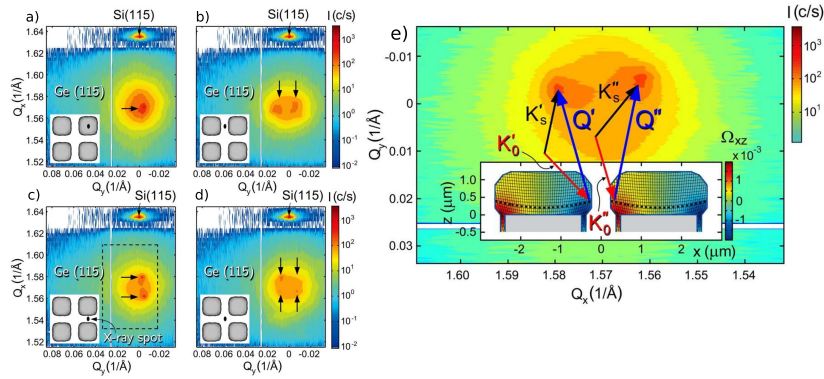


Figure 5.3: a)-d) projections of the (115) 3D RSM onto the (Q_x, Q_y) plane, taken at different (x, y) positions (indicated in the bottom left inset). The black arrows indicate the local diffraction intensity maxima coming from lattice planes with opposite bending in adjacent Ge crystals. e) magnification of the Ge RSM marked in c) by a dashed rectangle and rotated by 90° . The inset reveals how the lattice bending of adjacent Ge crystals give rise to multiple diffracted peaks. K'_0 and K''_0 , K'_s and K''_s , Q' and Q'' are respectively the incident wave vectors, diffracted wave vectors and scattering vectors arising from adjacent Ge crystals with opposite lattice bending fulfilling the Bragg reflection condition. The Ge lattice bending is displayed by black curves extracted from the rotation tensor obtained by FEM simulations. The FEM color map is extracted by cutting in the middle a Ge crystal along the $[110]$ direction ($y = 0$). The thick black dashed line represents the experimental curvature obtained by nanofocused XRD and its position along the z -axis has been chosen to match the FEM value. The scale of the lattice bending has been increased by a factor $\times 200$ to make it more visible [130].

Indeed, the bottom left insets of panels a), b), c) and d), show different positions of the incident X-Ray beam and correspondingly, one, two or four Ge(115) diffraction peak maxima are detected. In particular, one, two or four peaks are detected when the X-Ray beam is respectively centered on one pillar (panel a)), on the trench between two pillars (panels b), c)), on the crossing point between two perpendicular trenches (panel d)).

To study the origin of multiple intensity maxima diffracted peaks, we recorded their shift in the reciprocal (Q_x, Q_y) plane, while scanning the (x, y) position of the sample with 200 nm steps in the y direction and 400 nm in the x direction. The data analysis reveals that the shift of the Ge(115) diffraction peak is related to the concave bending of the Ge lattice planes with a curvature radius $R=[(\partial Q_\zeta/\partial \zeta)(1/Q_z)]$, where ζ is an arbitrary direction in the (x, y) plane [156]. By averaging the radius of curvature over 4 different crystals $R=770 \pm 20 \mu\text{m}$ has been obtained for the Ge crystals reported in Figure 5.2 a) and d), corresponding to a net bending of (001) planes towards the lateral sidewalls of $\sim \pm 0.1^\circ$.

The bending of the lattice planes explains the appear-

ance of several diffracted intensity maxima for the Ge(115) Bragg reflection depending on the incident position of the X-Ray beam. Indeed, as reported in Figure 5.3 e), close to the trenches, the lattice planes of adjacent Ge crystals are bent in opposite directions due to the bending. Thus, when the X-Ray beam hits close to a trench, the Bragg condition is satisfied for two different values of the Q_x component of the scattering vector, stemming from lattice planes belonging to two different Ge crystals on both sides of the trench. The X-Ray data have been compared by 3D FEM simulations of Ge/Si crystals (the geometry has been taken from SEM images), revealing that the observed lattice bending of Ge crystals is related to the elastic relaxation of the tensile thermal strain (see section 3.4, [97]) accumulated during the cooling process from the growth to room temperature. Figure 5.3 e) shows cross-section FEM simulations for the Ge crystals reporting the bending of the (001) lattice planes by black dashed lines and the color code map represents the xz component of the calculated rotational tensor. The curvature has been increased by a factor 200 to make it more readable. The calculations reveal a decrease of the lattice bending with the increase of the height of the Ge crystals,

while the X-Ray data give informations which are averaged on the whole structure.

An analogous analysis has been performed also on taller Ge crystals. In the case of 3.1 μm tall Ge crystals, a curvature radius of $R = 10 \pm 8$ mm has been measured and according to the respective FEM simulations the lattice bending at the top of the crystal is negligible. This finding explains why the measured lattice bending is smaller than 1.2 μm tall Ge crystals case, since now the volume contribution with small lattice bending is larger than the former case. Finally for the 7.3 μm tall Ge crystal case, the measured lattice bending becomes negligible.

5.0.2 Random net tilt of Ge/Si crystals induced by misfit dislocations

The analysis of the RSMs reported in Figure 5.3 a)-d), reveals that apart from the lattice bending of the Ge crystals, due to the elastic relaxation of the thermal strain, a net tilt of each Ge crystal as a whole, is also present. This net tilt is typically attributed to the presence of misfit dislocations at the Ge/Si interface with different Burger’s vectors [157, 158]. For 1.2 μm tall Ge crystals, the effect of the lattice bending is preponderant over the net tilt, thus only for taller crystals the latter one predominates. Unfortunately, as reported in Figure 5.2 c), it is impossible to resolve taller Ge crystals, since the trench width is comparable with the measurement resolution.

In order to measure the net tilt of one isolated Ge crystal, we firstly performed an etching of the Ge crystal array in hydrogen peroxide to increase their separation. Secondly we removed the majority of the Ge crystals by a micro-manipulator placed in a SEM, leaving only few of them separated by several micrometers.

Once the isolated Ge crystals are fabricated, RSMs

around the Ge(115) and Si(115) Bragg reflections have been recorded by scanning the Ge/Si crystal in the whole height, as reported in Figure 5.4 a).

By comparing for each RSM, the Ge(115) peak position, with respect to the nominal value and normalized with that of the silicon substrate, the net tilt χ of three different isolated crystal can be accurately determined (see section S5 of reference [156]) both along the x (χ_x) and y direction (χ_y). Indeed, net tilts of $\chi_x = -0.023^\circ \pm 0.006^\circ$ and $\chi_y = 0.033^\circ \pm 0.005^\circ$, $\chi_x = -0.006^\circ \pm 0.001^\circ$ and $\chi_y = 0.068^\circ \pm 0.001^\circ$, $\chi_x = 0.012^\circ \pm 0.001^\circ$ and $\chi_y = 0.023^\circ \pm 0.001^\circ$ have been respectively found for Ge crystal #1, #2 and #3 (see Figure 5.4 b)).

Nevertheless the statistics is not very large, the discrepancy of tilt for each crystal, explains the large peak broadening of $\sim 0.1^\circ$ along Q_x observed by laboratory HR-XRD presented in [97], where the diffracted signal is a convolution of thousands of pillars.

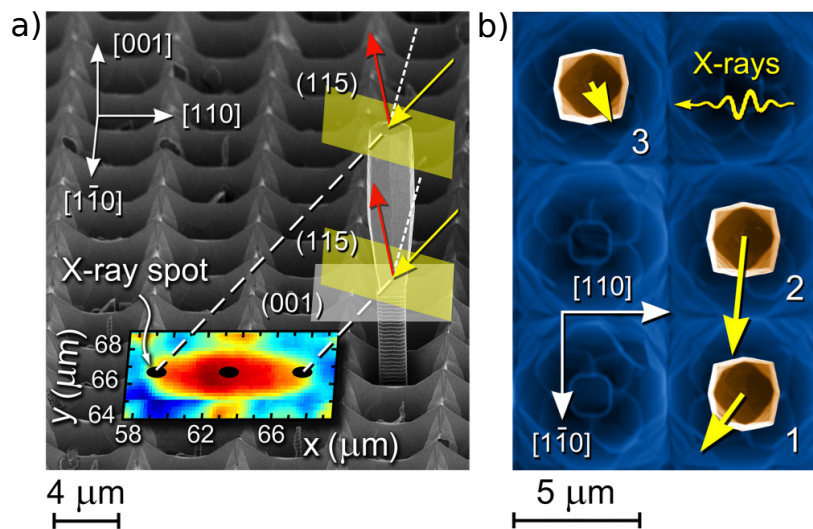


Figure 5.4: a) scattering geometry for the (115) Bragg reflection for isolated $8 \mu\text{m}$ tall Ge crystals, with $\{113\}$ top facets, deposited on Si pillars with side $d = 2 \mu\text{m}$ and $4 \mu\text{m}$ wide trenches. (001) and (115) planes are drawn respectively in gray and green. Yellow arrows indicate the incident X-Ray beam at the top and bottom of the Ge crystal, while the red ones depict the diffracted beams. The color map represents the total scattered intensity for the Ge(115) Bragg reflection scanning along the crystal height. b) top-view SEM image of three isolated Ge crystals, each yellow arrow indicates the net tilt of the Ge crystals (magnified by a factor 500) [130].

5.0.3 High quality Ge crystals from dislocated Ge/Si interface

The ability of addressing one isolated Ge crystal by X-Ray nanodiffraction, gives us the unique possibility to measure the crystal quality at a nanometric scale.

The Ge crystals reported in Figure 5.4 a), and here analyzed, are deposited at 610° on Si pillars with side $d = 2 \mu\text{m}$ and $4 \mu\text{m}$ wide trenches, presenting a pyramidal top surface morphology with $\{113\}$ facets. As already described, in section 4.1, the slanted $\{113\}$ guarantee the complete expulsion of all TDs at the lateral crystal sidewalls few micrometers far from the Ge/Si interface.

The 3D RSM of an isolated TD-free Ge crystal, and the diffracted peak projections on the (Q_x, Q_z) , (Q_y, Q_z) and (Q_x, Q_y) planes for the Si(115) and Ge(115) Bragg reflections, are reported in Figure 5.5. From these measurements, it is possible to appreciate the extraordinary quality of the Ge/Si crystals, despite the heavily dislocated interface due to the 4.2 % lattice mismatch. Indeed, the FWHM of the diffracted Ge(115) peak, both along the Q_x and Q_z is analogous to that of the Si(115) substrate, being the peak widths

limited by the instrument resolution (see [156]).

Moreover, we have recorded the RSMs along the whole isolated Ge crystal, from the dislocated Ge/Si interface to the TD-free faceted top surface.

Figure 5.6 a), shows the evolution of the Ge(115) diffracted peak FWHM (ΔQ_x) as a function of the crystal height. As shown by the dashed black curve, ΔQ_x exponentially decays from the Ge/Si interface towards the top crystal surface. The peak width is $\sim 0.0048 \text{ 1/\AA}$ at $\sim 200 \text{ nm}$ from the heterointerface and it drops by a factor $1/e$ at the crystal height of $\sim 2.9 \text{ }\mu\text{m}$, reaching the resolution limit for height of $\sim 4 \text{ }\mu\text{m}$.

In Figure 5.6 b), c), d) are displayed three representative RSM cross-sections with their respective Gaussian fits to measure the FWHM. They have been recorded at three different heights of the Ge crystal, indicated by the roman numbers I, II and III in Figure 5.6 a). The decay of the diffracted Ge(115) peak with the increase of the crystal height (i.e. distance from the dislocated interface) is a clear manifestation of the reduction of strain fields and of the expulsion of TDs at the lateral sidewalls. To our knowledge, this is the first example of a perfect, strain free, heterostructure

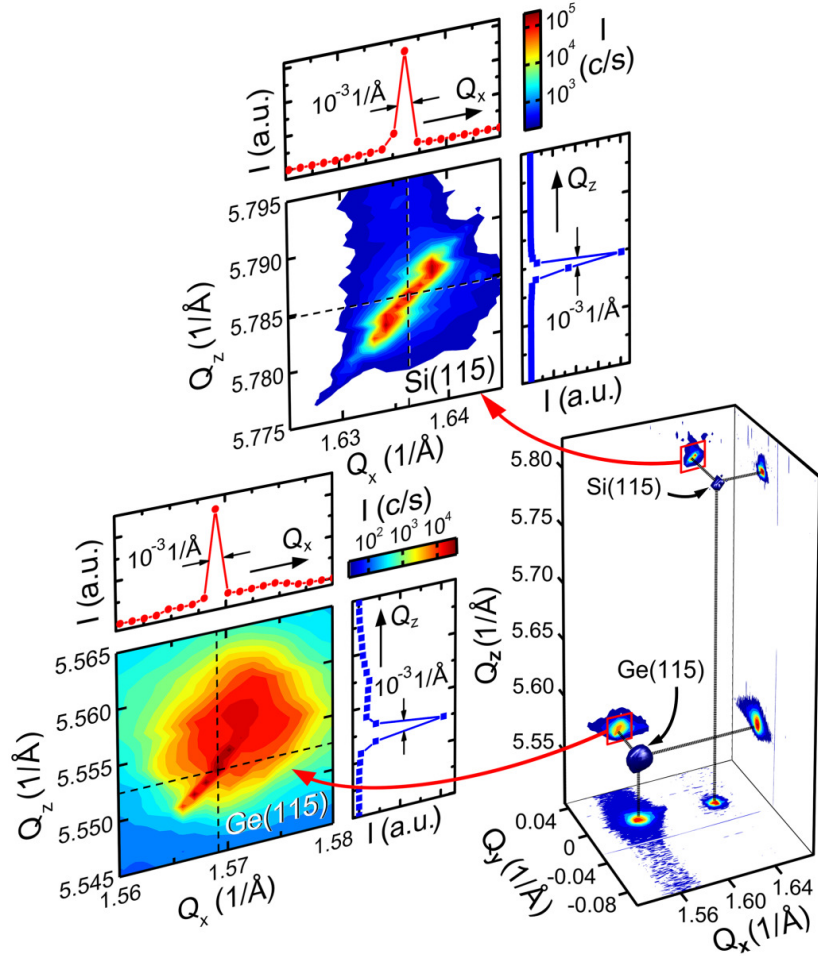
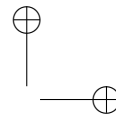
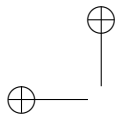
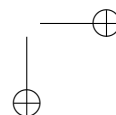
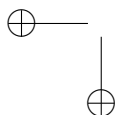


Figure 5.5: 3D RSMs around Si(115) and Ge(115) Bragg reflections, and the corresponding projections on the (Q_x, Q_z) , (Q_y, Q_z) and (Q_x, Q_y) planes, recorded at the top of a Ge crystal reported in Figure 5.4 a) (Ge crystal is TD-free thanks to the top surface faceting) [130].



evolving from an highly mismatched interface. Interestingly, the Ge(115) peak position measured at three different crystal height doesn't coincide. This is in agreement with the analysis described before about the bending and tilt of the lattice planes which strongly depends on the crystal height.



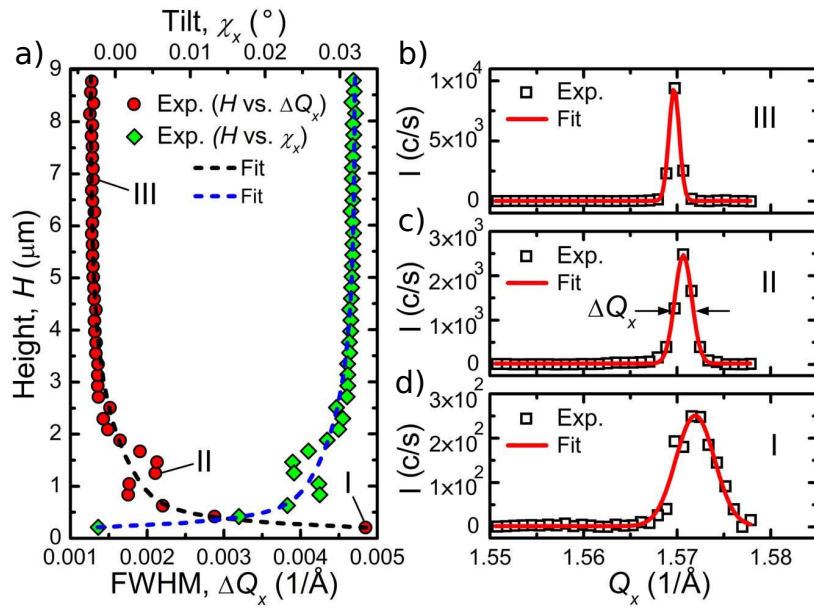


Figure 5.6: a) FWHM (ΔQ_x) and tilt (χ_x) of the Ge(115) diffraction peak versus the Ge crystal height H . The experimental data are fitted with asymptotic exponential functions $y(x) = y_0 + a \times \exp(-bx)$, where a is respectively negative and positive for $y = \chi_x$ and $y = \Delta Q_x$ (dashed blue and black lines). b), c), d) Q_x cross-section of the Ge(115) diffraction peak at 3 different crystal heights (I,II and III) shown in a). The experimental data are here fitted to single Gaussians [130].

Chapter 6

Optical properties of Ge/Si crystals

In this chapter the impact of the threading dislocation density (TDD) on the optical properties of Ge/Si crystals, as measured by photoluminescence (PL) spectroscopy, is presented. In particular great attention has been devoted to study the interplay between the TDD and the internal quantum efficiency, presenting an innovative approach, based on the insertion of $\text{Si}_{0.25}\text{Ge}_{0.75}$ barriers, to address the location of non radiative centers. Finally, the PL quality of TD free Ge multiple quantum wells (MQWs) deposited on Si pillars will be treated and compared with a standard reference sam-

ple [159]. The PL measurements have been performed under the supervision of Dr. F. Pezzoli at the Università degli studi di Milano Bicocca.

6.1 PL intensity *vs* TDD

In order to study the impact of the TDD in Ge/Si crystals on the PL intensity, three different arrays of Ge crystals and a planar layer have been studied. As already described in chapter 3, depending on the lateral side d of the Si pillars and on the growth temperature, different morphologies can be achieved: fully $\{113\}$ faceted crystals or truncated pyramids with large (001) central surface. In particular, as described in chapter 4, slanted $\{113\}$ facets attracts and expel at the crystal sidewalls the TDs, thus leaving the upper part of the Ge crystal free from defects. This expulsion mechanism doesn't work for the (001) surface, since vertical TDs can run within the entire crystal volume reaching the top surface. The TDD both in a planar Ge layer and on the (001) surface of the Ge crystals has been measured, being $3.5 \pm 0.9 \times 10^8 \text{ cm}^{-2}$.

The Ge crystals which have been investigated by PL spec-

troscopy are reported in Figure 6.1. Depending on the Si pillar size $d = 2, 5$ or $9 \mu\text{m}$, the extension of the central (001) area changes, thus influencing the overall TDD on the entire crystal volume, as displayed by the AFM scans after defect etching (see dashed insets in a), b), c)) and panel d).

In Figure 6.2 a) the room temperature (RT) PL spectra of Ge crystals deposited on Si pillars with different size $d = 2 \mu\text{m}$ (blue line), $d = 5 \mu\text{m}$ (red line) and $d = 9 \mu\text{m}$ (orange line) are reported, comparing also the PL spectrum of the Ge layer deposited on the unpatterned Si (001) planar region. The different Ge crystal arrays and planar layer have been deposited on the same substrate and the PL measuring conditions are equivalent.

The Ge layer deposited on the planar unpatterned Si (001) region shows almost not detectable PL intensity, mostly for two reasons. First, due to the total internal reflection, the light generated within the crystal remains trapped and absorbed, thus limiting the emitting efficiency. Second, the large number of dislocations which are non-radiative channels, severely alters the carrier dynamic. Indeed, the time scale for these processes is much shorter than that one of

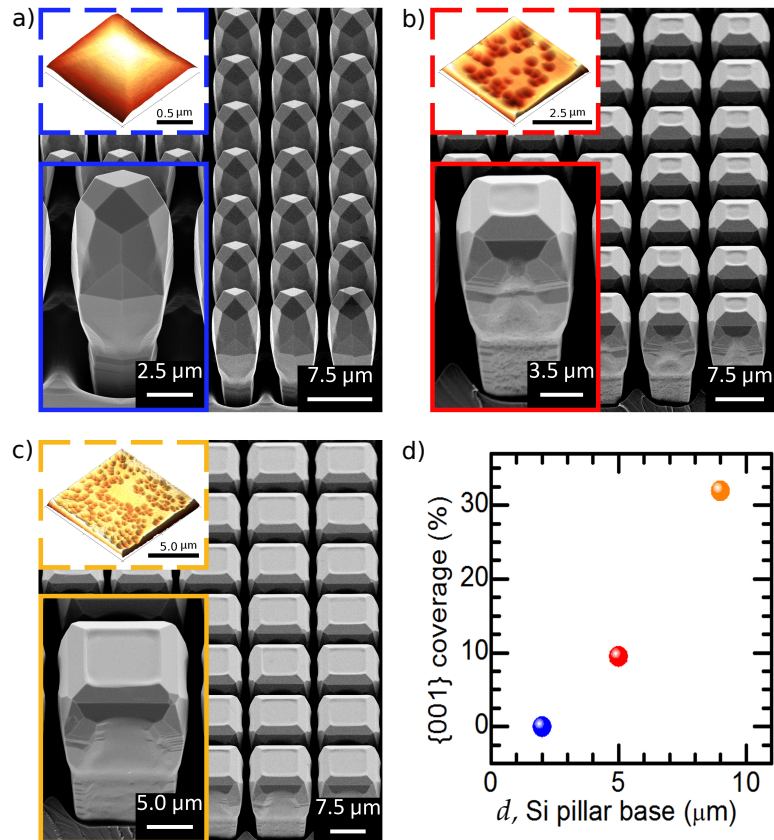


Figure 6.1: SEM perspective view images of 8 μm tall Ge crystals array deposited at 610°C and 4.2 nm/s on Si pillars with side a) $d = 2 \mu\text{m}$, b) $d = 5 \mu\text{m}$ and c) $d = 9 \mu\text{m}$. The dashed insets display AFM scans of the top crystal surface after defect etching in *Iodine* solution, emerging TDs are visible as dark spots. d) Top surface coverage of the (001) area as a function of the Si pillar size.

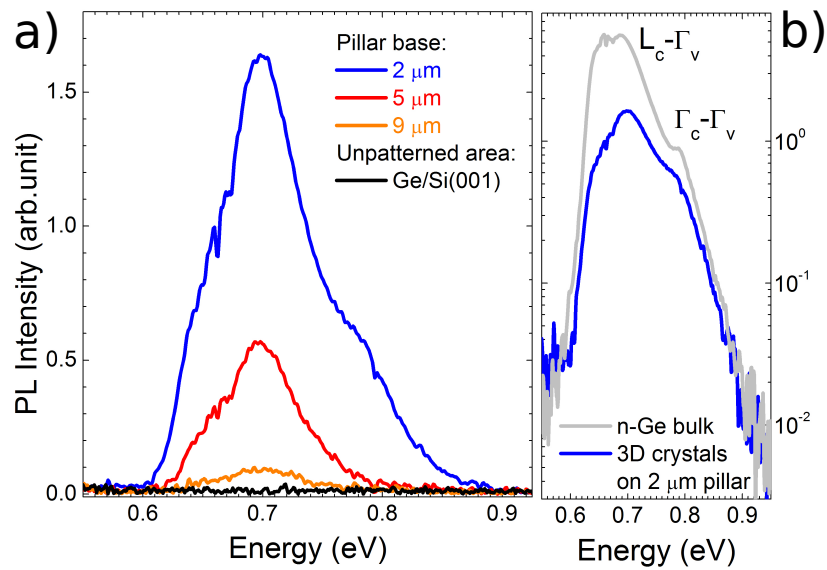


Figure 6.2: a) room temperature PL spectra of Ge crystals deposited on Si pillars with different size $d = 2 \mu\text{m}$ (blue line), $d = 5 \mu\text{m}$ (red line) and $d = 9 \mu\text{m}$ (orange line) and Ge planar layer on Si(001) (black line). b) comparison of the RT PL spectra of a Ge bulk reference (grey line) with TD-free Ge crystals (blue line). The transition between the conduction band (CB) minima at the points L_c or Γ_c and the valence band (VB) Γ_v point are indicated [159].

radiative inter-band recombination, resulting in a drastic reduction (comparable with the noise level) of the PL signal. This is in agreement with literature results [160] which show no PL signal for as-grown (no annealing processes) Ge/Si layers with high TDD.

On the other hand, Figure 6.2 a) shows that the PL intensity dramatically increases by reducing the lateral size of the Si pillars, i.e. decreasing the fraction of the crystal volume with high TDD. Indeed, in the case of Ge crystals deposited on Si pillars with side $d = 2 \mu\text{m}$, the inter-band integrated PL intensity is ~ 300 times the noise level measured for the planar Ge layer. Despite the large surface to volume ratio of the 3D Ge crystals, this remarkable result has been achieved without any post growth annealing process or surface passivation treatment, thus confirming a slow surface recombination process.

In the Ge layer deposited on the planar region, the emitted light outside the critical angle of 14° experiences full internal reflection, thus preventing its collection from the top surface of the sample. On the other hand, for Ge crystals, the lateral sidewalls bounce off most of the emitted light outside the critical angle, being guided to the top surface. Here

it can out couple with the air, thus enhancing the light extraction efficiency compared to the planar layer case. Finite difference time domain calculations show that in the case of Ge crystals on Si pillars with side $d = 2 \mu\text{m}$, the extraction efficiency of the emitted power into the detection solid angle is 3 times larger than the planar layer case. Still, the enhancement of the PL intensity by a factor 300 has to be explained by the reduction of defects.

According to Figure 6.2 b), the RT PL emission of Ge crystals (unintentionally doped with a B concentration of $4.2 \pm 0.8 \cdot 10^{15} \text{ cm}^3$) deposited on Si pillars with side $d = 2 \mu\text{m}$ (blue line), have been compared with a Ge bulk reference (gray line) with an As doping of $8.3 \cdot 10^{16} \text{ cm}^3$. Two main spectral features are labeled: $L_c - \Gamma_v$ at $\sim 0.7 \text{ eV}$ and $\Gamma_c - \Gamma_v$ at $\sim 0.77 \text{ eV}$ which respectively correspond to the fundamental indirect band gap and the direct one. The two PL signals have the same spectral shape: the intensity I^d related to the direct recombination is weaker than the intensity I^i of the indirect one, i.e. $I^d < I^i$. By contrast, all previously reported literature data [160–168] show exactly the opposite behavior: $I^d > I^i$.

The relative intensity ratio between the direct-to-indirect

gap emissions in a PL experiment is determined by the quasi-equilibrium conditions in the conduction band [160]. Apart from excitation conditions, the ratio between the L and Γ valleys electron population is determined by the presence of non-radiative recombination centers. Indeed, a high density of defects, besides reducing the internal quantum efficiency, can modify the electron distribution in the conduction band and reduce the PL spectral weight of the indirect recombination, thus favoring $I^d > I^i$. Note that for Ge/Si layers with comparable thickness [163], and for 8 μm thick (same thickness of the Ge crystals) Ge planar layers deposited by LEPECVD and annealed to reduce the TDD to $7.9 \pm 0.9 \times 10^6 \text{ cm}^{-2}$, the PL spectra always present $I^d > I^i$, as reported in Figure 6.3.

Although the Ge crystals deposited on Si pillars with $d = 2 \mu\text{m}$ display a PL spectrum resembling a defect-free bulk reference, still TDs are not eliminated at all, but buried in the first micrometers far from the Ge/Si interface, affecting the overall emission efficiency. In order to analyze the role of TDs on the band carrier population, temperature-dependent PL measurements have been performed on fully {113} faceted Ge crystals. PL spectra have been recorded in a

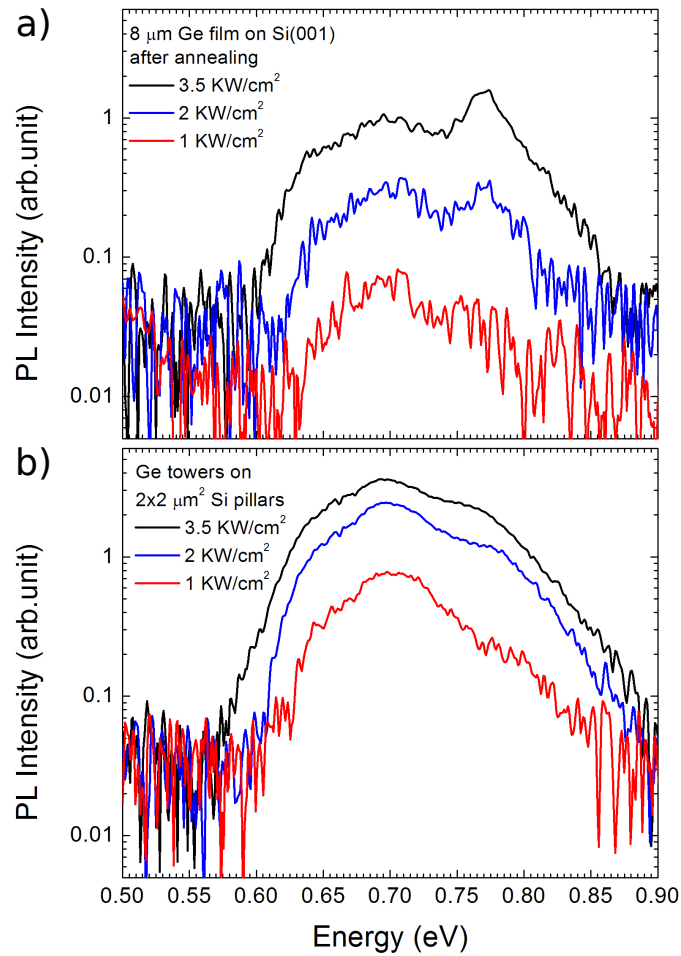


Figure 6.3: Room temperature PL spectra of 8 μm thick Ge/Si planar layer with $\text{TDD} = 7.9 \pm 0.9 \times 10^6 \text{ cm}^{-2}$ a) and 8 μm tall, TD-free Ge crystals on Si pillars with $d = 2 \mu\text{m}$ b) at different excitation powers.

broader spectral region in order to collect both the inter-band and dislocation PL signals.

As reported in Figure 6.4 a), at low temperature (6 K) the PL spectrum is characterized by direct gap recombination at 0.882 eV, indirect gap recombination assisted by emission of longitudinal acoustic phonons at 0.712 eV and no-phonon transition at 0.736 eV [169]. The additional broad band in the spectral range 0.45 - 0.67 eV is attributed to recombination at dislocations [170]. The broadening of the dislocation recombination spectrum may depend on their dissociation into Shockley partial ones [170–172]. By increasing the temperature, the PL spectral features become weaker and broader. In particular, the low energy edge of the indirect gap emission and the direct one, follow the Varshni law dependence on temperature [173]. Moreover, the high energy side of the indirect gap PL emission gets broader and its amplitude modified by the activation of transitions mediated by phonon absorption [169].

Figure 6.4 b), reports the inter-band (direct + indirect) and dislocation PL integrated intensities as a function of temperature. Interestingly, the inter-band integrated PL intensity exhibits two temperature regimes: below and above

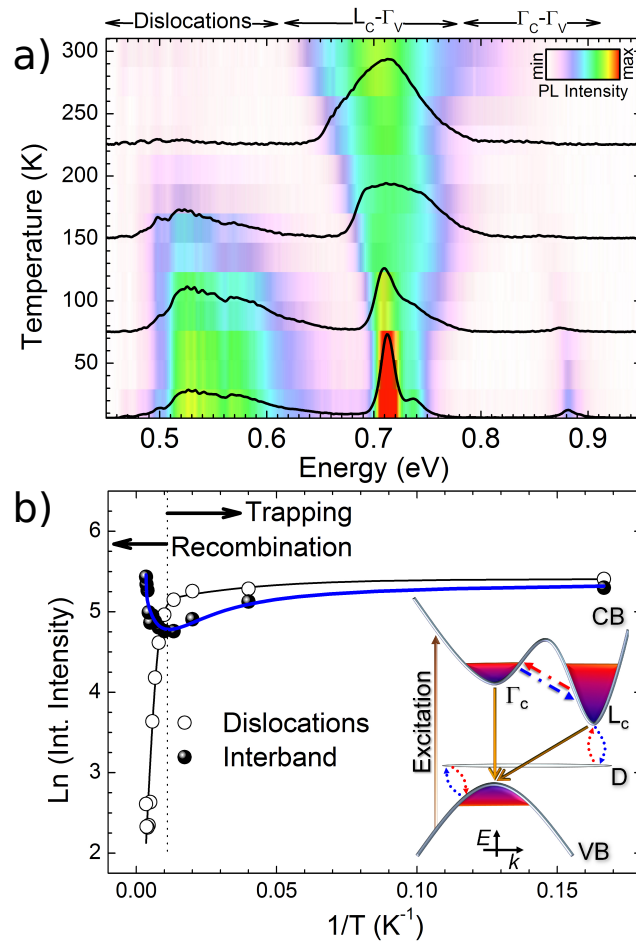


Figure 6.4: a) contour-plot of the temperature dependent PL emission of $8 \mu\text{m}$ tall Ge crystals on Si pillars with $d = 2 \mu\text{m}$. Spectra recorded at 6, 75, 150 and 225 K are superimposed as references. b) integrated PL intensity for inter-band (direct + indirect) and dislocation band as a function of temperature. The inset is a scheme showing the PL processes taking place in the Ge crystals [159].

a critical temperature $T_c = 125$ K. Above T_c the inter-band integrated PL intensity rises sharply, whereas below T_c it increase gradually, thus presenting a minimum for $T = T_c$. Simultaneously, above T_c , the dislocation PL integrated intensity drastically decreases.

In order to explain the observed inter-band and dislocation PL integrated intensities behavior as a function of temperature, we adopted the charge-dependent potential barrier model described in references [174–176]. At a certain temperature T , carriers trapped at the dislocations can either recombine radiatively, thus contributing to the dislocation PL emission, or non radiatively or be released to the bands and there recombining radiatively increasing the inter-band PL emission. The inset of Figure 6.4 b) schematically describes all these processes. According to the model, at low temperatures, carriers leak out from the bands and get trapped on the dislocations, thereby enhancing the dislocation PL emission. When the temperature is increased, carriers trapped at the dislocations can be thermally activated to the bands, thus favoring the inter-band PL emission which becomes predominant. Indeed, as shown in Figure 6.4 b), the critical temperature T_c , representing the border between the trapping

*Inter-band PL intensity
enhancement via band gap engineering* 217

and recombination regimes at the dislocation sites, coincides with the temperature in which the inter-band PL emission has a minimum and for higher T increases very sharply [175].

6.2 Inter-band PL intensity enhancement via band gap engineering

In the previous section 6.1, the optical activity of dislocations located close to the Ge/Si interface of 3D Ge crystals has been analyzed. In this section we propose an innovative approach to reduce the carrier recombination at the dislocation site by inserting fully strained $\text{Si}_{1-x}\text{Ge}_x$ barriers to reduce the carrier diffusion towards the dislocated Ge/Si interface.

The transmission coefficients for both carriers in Ge through the Ge-rich $\text{Si}_{1-x}\text{Ge}_x$ barriers, have been calculated within the transfer matrix formalism [177] using the band alignments and effective masses values reported in Refs. [178] and [179]. Figure 6.5 shows the transmitted fraction of carriers as a function of the Ge content x for 10 nm thick $\text{Si}_{1-x}\text{Ge}_x$ barrier by considering at room temperature an optically ex-

cited carrier density of $1 \times 10^{19} \text{ cm}^{-3}$ on the upper side of the barrier. The fraction of transmitted holes increases mono-

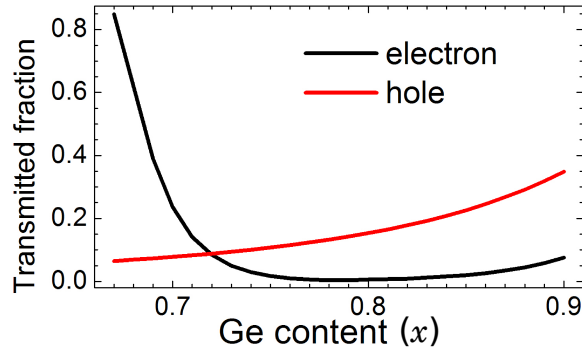


Figure 6.5: Fraction of transmitted electrons (black curve) and holes (red curve) in Ge through a 10 nm thick $\text{Si}_{1-x}\text{Ge}_x$ barrier as a function of the Ge content x [159].

tonically with the Ge content x since the valence band offset gets reduced. Surprisingly, the fraction of transmitted electrons through the barrier has a minimum for a Ge content $x \sim 0.75$ due to the cross-over between the Δ and L valleys of the $\text{Si}_{1-x}\text{Ge}_x$ band structure under tensile strain.

Considering the transmitted carrier fractions calculated in Figure 6.5, and taking into account that plastic relaxation at the Ge/ $\text{Si}_{1-x}\text{Ge}_x$ interface has to be avoided to prevent additional dislocations, a Ge content of $x = 0.25$ has been chosen for 10 nm thick barriers.

*Inter-band PL intensity
enhancement via band gap engineering* 219

Three different Ge samples with barriers have been grown on Si pillars with side $d = 2 \mu\text{m}$ in conditions analogous to those used for the Ge crystals reported in Figure 6.1 a). $\text{Si}_{0.25}\text{Ge}_{0.75}$ barriers have been introduced after $6 \mu\text{m}$ (A), $4 \mu\text{m}$ (B) and $2 \mu\text{m}$ (C) from the dislocated Ge/Si interface. A fourth sample with all A+B+C barriers has been also grown. Its cross-section SEM image is reported in Figure 6.6, $\text{Si}_{0.25}\text{Ge}_{0.75}$ barriers, spaced by $2 \mu\text{m}$ are clearly visible following the entire crystal shape.

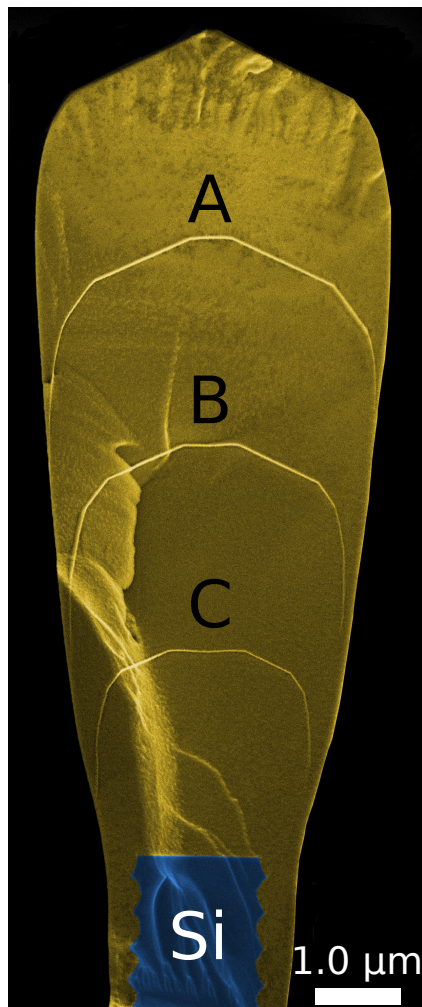


Figure 6.6: SEM cross-section image of 8 μm tall Ge crystal deposited at 610°C and 4.2 nm/s on Si pillars with side a) $d = 2 \mu\text{m}$ with embedded 3 $\text{Si}_{0.25}\text{Ge}_{0.75}$: after 6 μm (A), 4 μm (B) and 2 μm (C) from the dislocated Ge/Si interface.

*Inter-band PL intensity
enhancement via band gap engineering* 221

Figure 6.7 a) reports the inter-band PL emission, normalized to the dislocation one, of the Ge crystals with embedded $\text{Si}_{0.25}\text{Ge}_{0.75}$ barriers, together with the pure Ge crystal reference. It is evident that the presence of 3 $\text{Si}_{0.25}\text{Ge}_{0.75}$ barriers (A+B+C) largely enhances the inter-band radiative recombination, thus confirming that dislocations situated in the Ge/Si interface region are responsible for the direct and indirect gap PL quenching.

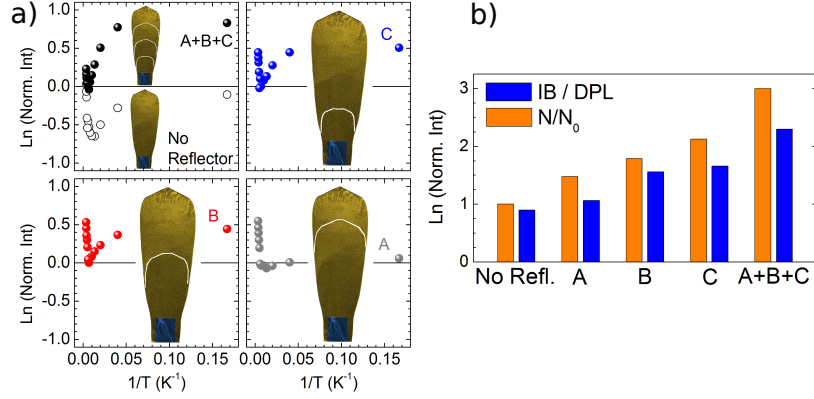


Figure 6.7: a) integrated PL intensity, as a function of temperature, of the inter-band emission for Ge crystals without and with Si_{0.25}Ge_{0.75} embedded after 6 μm (A), 4 μm (B) and 2 μm (C) from the dislocated Ge/Si interface. For each sample the inter-band PL emission is normalized to its respective dislocation PL signal. b) calculated number of carriers N (orange bars), normalized to the N₀ value of the Ge crystal without barriers. Blue bars are the inter-band/dislocation PL intensity ratio measured at 6 K. The data are reported as a function of Si_{0.25}Ge_{0.75} reflectors [159].

The role of the Si_{0.25}Ge_{0.75} barriers and the rate of recombination at the dislocations, are further explained by calculations [159] of carrier diffusion summarized in Figure 6.7 b). In the calculations, unipolar diffusion has been assumed and the local excess of electron density n is determined by one dimensional continuity equation: $\frac{\partial n}{\partial t} = D \frac{\partial^2 n}{\partial z^2} - \frac{n}{\tau} + G$ where

*Inter-band PL intensity
enhancement via band gap engineering* 223

G is the carrier generation rate per unit volume, z is the [001] direction and τ is the total carrier lifetime. The role of the $\text{Si}_{0.25}\text{Ge}_{0.75}$ barriers has been modeled by assuming the two regions on both sides of the barrier as independent integrating domains. The boundary condition for the transmitted current is given by: $J_n = -Pv_F\Delta n$ where P is the transmission probability reported in Figure 6.5, Δn is the carrier density difference between the two sides of the barrier and v_F the Fermi velocity.

Considering one $\text{Si}_{0.25}\text{Ge}_{0.75}$ barrier, by pushing it towards the Ge/Si interface, the numbers of carriers N within the whole Ge crystal volume increases, in turn enhancing the inter-band PL emission. Finally, the largest improvement of the inter-band/dislocation PL emission ratio, has been achieved by inserting three $\text{Si}_{0.25}\text{Ge}_{0.75}$ barriers, since this configuration is the most efficient to prevent carrier depletion by the dislocations located at the Ge/Si interface.

6.3 PL properties of Ge quantum wells crystals

In order to pursue the analysis of the impact of dislocations on the PL emission, keeping the active optical material separated from the defected area, 50 strain symmetrized Ge multiple quantum wells (MQWs) with nominally $\text{Si}_{0.15}\text{Ge}_{0.85}$ barriers have been deposited on top of TD-free $\text{Si}_{0.10}\text{Ge}_{0.90}$ crystals. This structure is known to have type-I band alignment with both holes and electrons in the L and Γ valleys confined in the Ge well.

In Figure 6.8 a) and b) are respectively reported SEM images of arrays of $\text{Si}_{0.10}\text{Ge}_{0.90}$ crystals and crystals composed by $\text{Si}_{0.10}\text{Ge}_{0.90}$ buffer + 50 Ge MQWs with $\text{Si}_{0.15}\text{Ge}_{0.85}$ barriers. In both cases the deposition has been performed on Si pillars with side $d = 2 \mu\text{m}$ and the growth temperature of the $\text{Si}_{0.10}\text{Ge}_{0.90}$ buffer optimized to 690°C in order to ensure full $\{113\}$ faceting and complete elimination of TDs. Subsequently, the MQWs structure has been deposited at lower temperature (535°C) to maintain sharp heterointerfaces, still the $\{113\}$ morphology is kept, as shown by the insets in Figure 6.8.

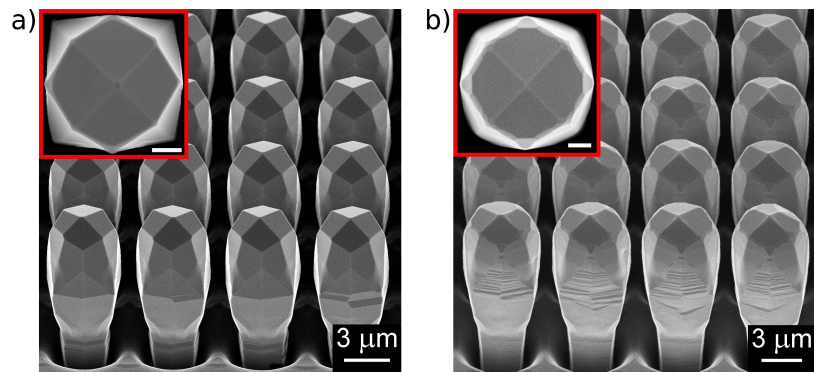


Figure 6.8: Perspective SEM images of a) array of 8 μm tall $\text{Si}_{0.10}\text{Ge}_{0.90}$ crystals deposited at 690°C and 4.9 nm/s, b) same of a) with on top 50 Ge MQWs 10 nm thick and $\text{Si}_{0.15}\text{Ge}_{0.85}$ 21 nm thick quantum barriers, deposited at 535°C on Si pillars with side $d = 2 \mu\text{m}$. Insets show top-view SEM images of a single crystal. The white size bar is 1 μm .

As already mentioned in chapter 4, in the unpatterned planar area, an high TDD ($\sim 10^8 \text{ cm}^{-2}$) is expected for the MQWs sample. Indeed the TEM and AFM scan after defect etching, reported in Figure 6.9, confirm that in the unpatterned planar area, a large number of vertical TDs is present and the total TDD is $2.8 \pm 0.9 \times 10^8 \text{ cm}^{-2}$.

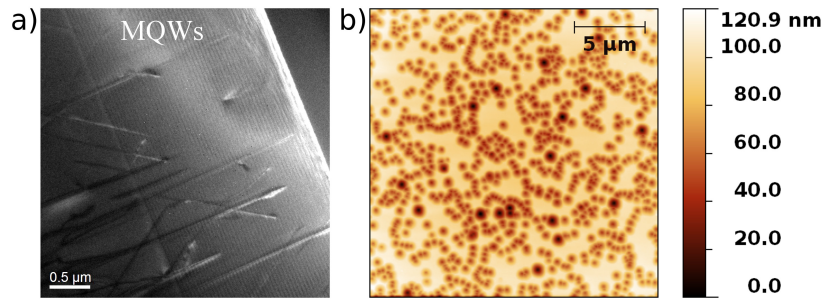


Figure 6.9: a) (004) dark field TEM image of the unpatterned planar area taken at the interface between the $\text{Si}_{0.10}\text{Ge}_{0.90}$ buffer and the MQWs. A large number of slanted and vertical TDs is present running through the MQWs stack. b) AFM scan after defect etching of the top surface of MQWs deposited in the unpatterned planar area, emerging TDs are visible as dark spots.

On the other hand, for the MQWs crystals deposited on Si pillars, the TDD is zero in the active region, thanks to the $\{113\}$ faceted growth front of the $\text{Si}_{0.10}\text{Ge}_{0.90}$ buffer. Indeed the TEM images of Figure 6.10 shows that at the $\text{Si}_{0.10}\text{Ge}_{0.90}/\text{Si}$ interface a large number of dislocation is

present (panel a)), while after $\sim 2 \mu\text{m}$ far from it (panel b)), TDs are absent and the active MQW region is completely TD-free (panel c)).

From the TEM image of Figure 6.10 a), the thicknesses of the Ge QW and the $\text{Si}_{0.15}\text{Ge}_{0.85}$ barrier have been extrapolated, respectively with the value of $16 \pm 2 \text{ nm}$ and $22 \pm 2 \text{ nm}$ on the $\{113\}$ facets.

The X-Ray data reported in Figure 6.11, confirm that the $\text{Si}_{0.10}\text{Ge}_{0.90}$ buffer is fully relaxed with a Ge content of $91 \pm 1 \%$ and from the spacing of the superlattice satellite peaks along the $\langle 113 \rangle$ directions, the thicknesses of the Ge QW and the $\text{Si}_{0.15}\text{Ge}_{0.85}$ barrier have been measured respectively $17 \pm 1 \text{ nm}$ and $20 \pm 1 \text{ nm}$, in good agreement with the TEM results.

The huge impact of the absence of TDs in MQWs deposited on Si pillars, compared to the unpatterned case, is shown in Figure 6.12. Indeed, in the unpatterned planar region, only dislocation related PL has been detected, on the other hand for the MQWs on Si pillars, it is strongly suppressed and intense quantum confined inter-band transitions, both at the direct and indirect points, are present. The PL peak at 0.959 eV has been attributed to the fundamental di-

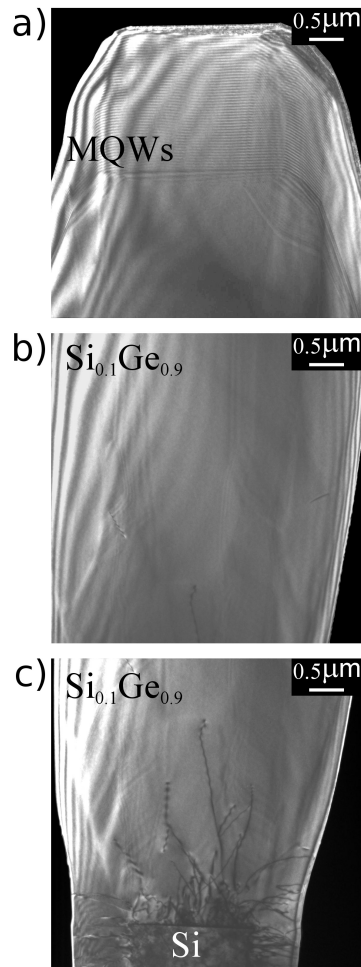


Figure 6.10: (220) dark field TEM images of MQWs on $\text{Si}_{0.10}\text{Ge}_{0.90}$ crystal deposited on Si pillar with side $d = 2 \mu\text{m}$. a) the MQWs/ $\text{Si}_{0.10}\text{Ge}_{0.90}$ interface, b) $\text{Si}_{0.10}\text{Ge}_{0.90}$ buffer and c) the $\text{Si}_{0.10}\text{Ge}_{0.90}$ /Si interface. TDs are clearly visible in c) as dark lines. In a) the crystal has a flat top surface because the TEM lamella was not cut exactly through the middle of the pillar.

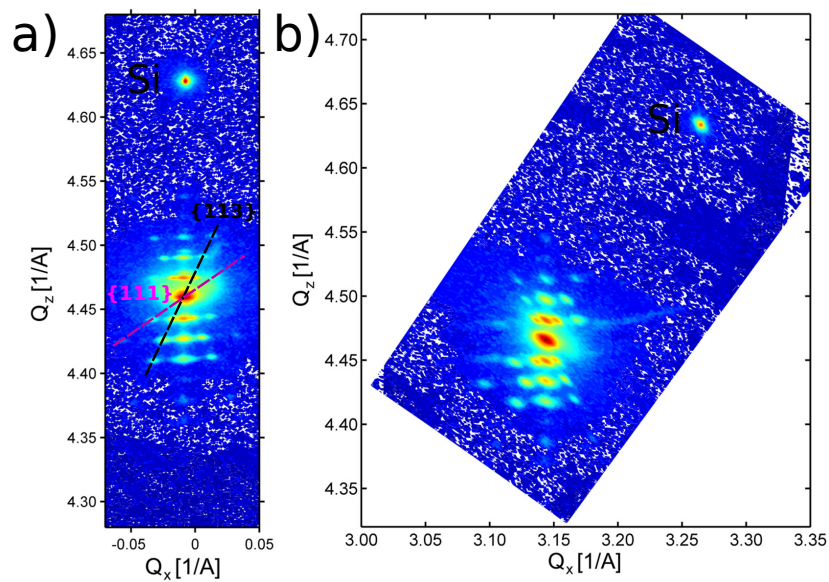


Figure 6.11: HR-XRD RSMs around a) (004) and b) (224) Bragg reflections for the MQWs/ $\text{Si}_{0.10}\text{Ge}_{0.90}$ crystals deposited on Si pillars with side $d = 2 \mu\text{m}$. The black and purple dashed lines refer respectively for the $\{113\}$ and $\{111\}$ diffraction peaks of the MQW superlattice.

rect transition at the conduction Γ point with the heavy-hole subband, called $c\Gamma$ 1-HH1. The low energy PL doublet is related to the indirect recombination: the peak at 0.745 eV is due to the cL 1-HH1 confined transition, while the one at 0.722 eV is the phonon assisted transition. These values are in agreement with transition energies of comparable MQWs deposited on graded buffer on Si(001) [180].

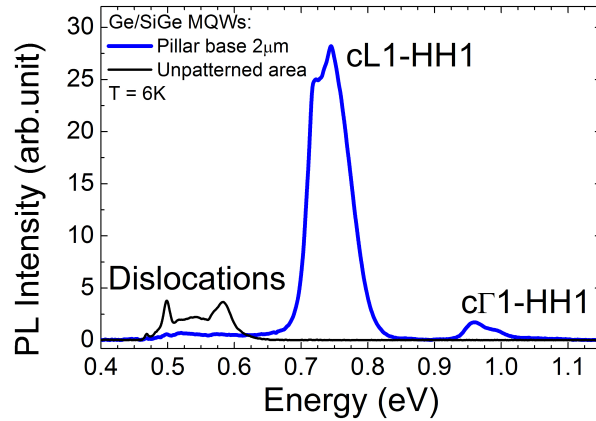


Figure 6.12: Low temperature PL spectra of MQWs deposited on Si pillars (blue curve) and on unpatterned planar region (black curve). Quantum confined inter-band transitions are also labeled [159].

In order to proof that the optical quality of the MQWs grown on Si pillars is by far better than other results reported in literature [180, 181] for Ge MQWs deposited on graded buffer ($TDD \sim 3 \times 10^6 \text{ cm}^{-2}$) on Si (001), PL spectra at low

excitation power have been measured and the results are displayed in Figure 6.13. In the MQW sample deposited on planar graded buffer the inter-band quantum well emission is quenched whereas the defect emission below 0.7 eV is visible. On the other hand, in the MQWs deposited on Si pillars, PL spectrum is dominated by the indirect gap recombination, thus confirming that QW crystals by far outperform high quality QW emitters grown on thick graded buffer with low TDD ($\sim 3 \times 10^6 \text{ cm}^{-2}$).

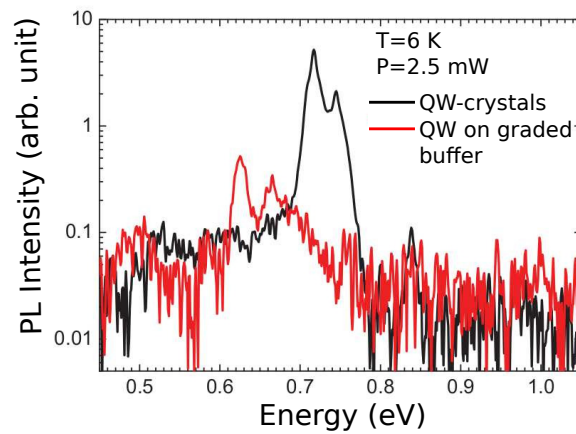


Figure 6.13: Low temperature and low excitation power ($P=2.5 \text{ mW}$) PL spectra of analogous Ge MQWs deposited on Si pillars with side $d = 2 \mu\text{m}$ (black curve) and on a graded buffer [180, 181] on planar Si(001) substrate.

Chapter 7

GaN/Si crystals by PA-MBE

In this chapter will be discussed the integration of high quality GaN micro-crystals on patterned (001) Si substrates. Their morphology has been analyzed and the optical properties studied by cathodoluminescence (CL) and micro-photoluminescence (micro-PL) measurements. The epitaxial growth by PA-MBE has been performed during my Ph.D. internship at the Paul-Drude-Institut in Berlin under the guidance of Dr. R. Calarco.

7.1 Growth and morphology

The crystalline quality of GaN/AlN crystals on silicon strongly depends on the crystallographic orientation of the Si substrate. Indeed, due to the fourfold symmetry of the Si(001) surface, the deposition of GaN results in the formation of poly-crystalline or very rough material [182, 183], while it is favorite on the threefold symmetry Si(111) surface [184]. In the latter case the GaN and AlN layers, grow with the in plane orientations $\langle 10\bar{1}0 \rangle$, $\langle \bar{1}\bar{1}20 \rangle$ respectively parallel to $\langle \bar{1}12 \rangle$ and $\langle \bar{1}10 \rangle$ Si directions (see Figure 7.1 b)). On the other hand in the former case, the sixfold symmetry of the GaN and AlN c-plane makes possible the formation of two preferential rotational alignments: $[10\bar{1}0] \parallel [\text{Si}0\bar{1}0]$ or $[10\bar{1}0] \parallel [\text{Si}\bar{1}00]$ (see Figure 7.1 a)). The deposition of an AlN buffer layer on the Si surface before the growth of the GaN crystal has been adopted in order to prevent the formation of amorphous silicon nitride and Ga etching of the Si surface [185].

In our innovative approach the deposition of GaN crystals by PA-MBE has been performed using (001) patterned Si substrates (see section 2.2) on which $2.5 \mu\text{m}$ of Si have been

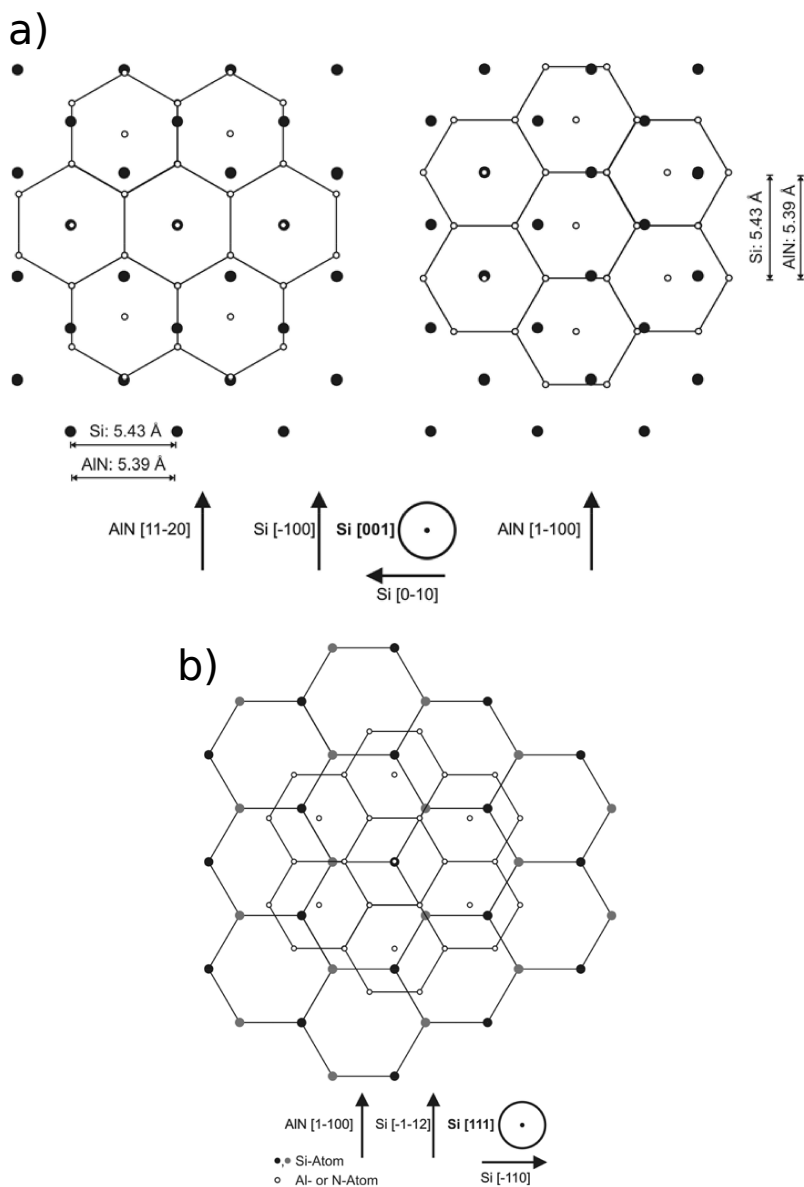


Figure 7.1: Schematic of the AlN atomic arrangement on Si surface with different orientations: (001) a) and (111) b) [184].

homoepitaxially deposited by LEPECVD. Indeed, as shown in Figure 7.2, by depositing $2.5 \mu\text{m}$ of Si at 750°C and 0.27 nm/s on Si pillars with side $d = 2 \mu\text{m}$, faceted crystals have been obtained. The top part of the Si crystals shows $\{113\}$ facets which are surrounded by four large $\{111\}$ facets.

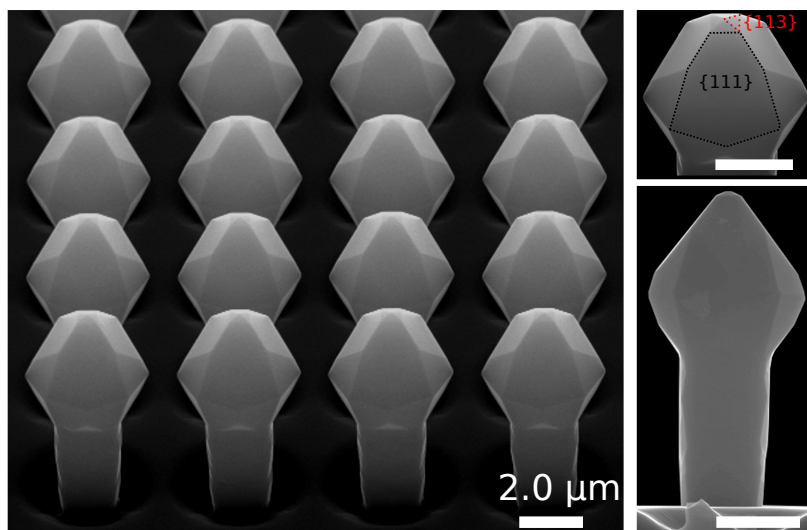


Figure 7.2: Perspective SEM images of $2.5 \mu\text{m}$ tall Si crystals deposited at 750°C and 0.27 nm/s on Si pillars with side $d = 2 \mu\text{m}$. $\{111\}$ and $\{113\}$ facets are also labeled respectively by black and red dashed lines.

Before the epitaxial deposition by PA-MBE, $1 \times 1 \text{ cm}^2$ chips containing the Si crystals have been diced from the original 4" wafer and have been cleaned by oxygen plasma, RCA, HF and finally loaded into the reactor and heated

up to the maximum temperature for 15 minutes ($\sim 815^\circ\text{C}$). Subsequently the substrate temperature has been lowered to 580°C for the deposition of the AlN buffer.

The AlN buffer has been deposited adopting a two temperature steps procedure with equivalent fluxes of Al and N respectively of $\phi_{\text{Al}} = 4.3 \text{ nm/min}$ and $\phi_{\text{N}} = 2.34 \text{ nm/min}$. In the first step at low temperature (580°C), 4.3 nm of Al have been deposited in order to cover homogeneously the Si surface, then the substrate temperature has been increased with a ramp rate of 40°C/min to the maximum achievable ($\sim 815^\circ\text{C}$) opening the nitrogen shutter for 180 seconds. Finally, at the maximum temperature, AlN buffer has been deposited with different thickness ranging from 50 to 200 nm. In Figure 7.3 are reported SEM images and the RHEED pattern (white inset) of 100 nm thick AlN buffer deposited on Si crystals. Despite the visible roughness of the AlN layer, confirmed also by the spotty RHEED pattern, it covers completely the Si surface.

After the deposition of the AlN buffer, the substrate temperature has been set to $\sim 610^\circ\text{C}$ to grow the GaN layer. In order to finely tune the surface temperature to match the Ga *intermediate growth regime*, (see section 1.5) which enables

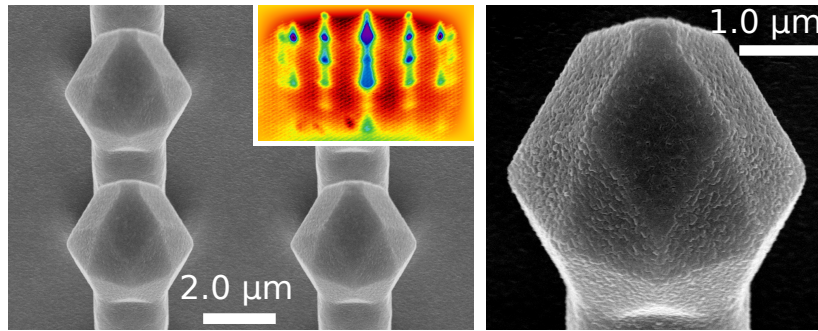


Figure 7.3: SEM perspective view of 100 nm thick AlN buffer layer deposited on Si crystals. The white inset shows the spotty RHEED pattern.

to stabilize ~ 2 MLs of liquid Ga on the sample surface, the desorption time of Ga has been measured and optimized by laser reflectometry [90]. Indeed, for the equivalent Ga flux $\phi_{Ga} = 6.34$ nm/min, which has been used to grow the GaN/Si crystals, the Ga desorption time has been optimized by depositing a smooth GaN film (surface roughness with $RMS < 1$ nm) on a template. In Figure 7.4 is shown the intensity of the laser reflectometry signal during the tuning of the substrate temperature. From t_0 to t_1 Ga is deposited for 30 seconds on the sample surface, then the Ga shutter has been closed and the Ga desorption time measured from t_1 to t_2 . The substrate temperature has been finely optimized to get a Ga desorption time of 23 -25 s, which ensures the

deposition of a smooth GaN layer, as confirmed by growing on a template.

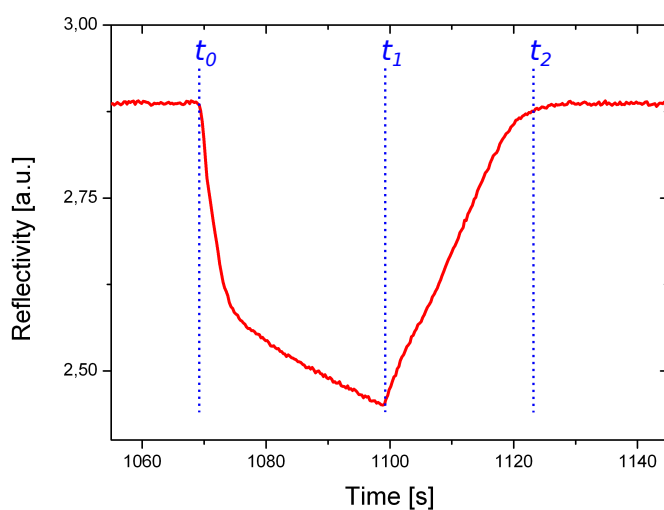


Figure 7.4: Intensity of the laser reflectometry signal during the tuning of the substrate temperature. From t_0 to t_1 Ga is deposited for 30 seconds on the sample surface, then the Ga shutter is closed and the desorption time is measured from t_1 to t_2 . The substrate temperature is finely tuned in order to get 23 - 25 s of Ga desorption time.

The morphology of 410 nm thick GaN crystals deposited on Si pillars with side $d = 2 \mu\text{m}$ is displayed in Figure 7.5 a). Several GaN micro-crystals have been nucleated on each Si facet but still without coalescing and forming a continu-

ous layer. The spotty RHEED pattern reported in panel c) confirms the formation of 3D micro-crystals also on $\{111\}$ Si facets. Indeed, spotty diffraction features inclined by $\alpha = 54.7^\circ$, which is the angle between (001) and $\{111\}$ planes, are present. The SEM cross section image of 300 nm thick GaN crystals with embedded 5 AlGaN markers, reported in Figure 7.5 b), reveals that despite the initial large roughness of the AlN buffer, after few hundreds of nanometers, the GaN micro-crystals recover a smooth growth front.

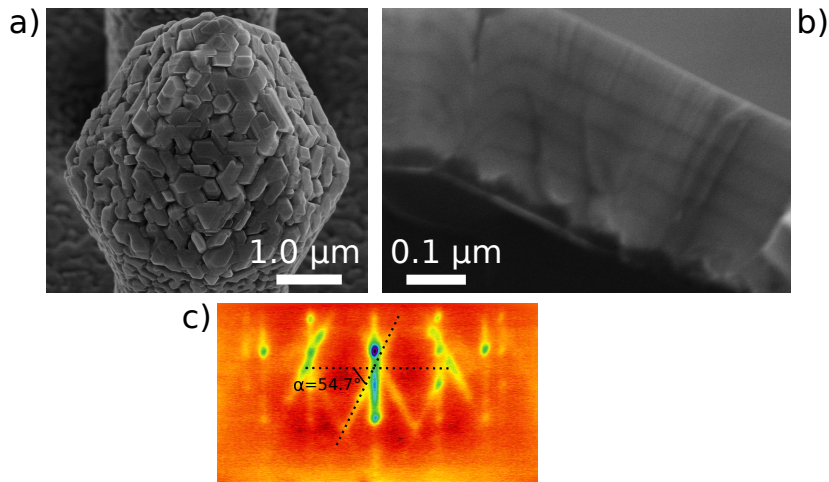


Figure 7.5: a) perspective view SEM image of 410 nm tall GaN crystal deposited on Si pillar with side $d = 2 \mu\text{m}$. b) cross-section SEM image of 300 nm tall GaN crystals with embedded 5 AlGaN barriers 10 nm thick. c) RHEED pattern of the crystals reported in a), $\alpha = 54.7^\circ$ is the angle between the (001) and $\{111\}$ planes.

The GaN micro-crystal orientation of the 410 nm thick sample reported in Figure 7.5 a), has been studied by means of electron back scattered diffraction (EBSD). The orientation maps displayed in Figure 7.6 a) and b), respectively for GaN micro-crystals deposited on Si {111}, {113} and {15 3 23} facets, show that in the central part of each crystalline facet, (0001) GaN planes are predominantly parallel to the Si surface (large area colored in red), irrespective of its orientation.

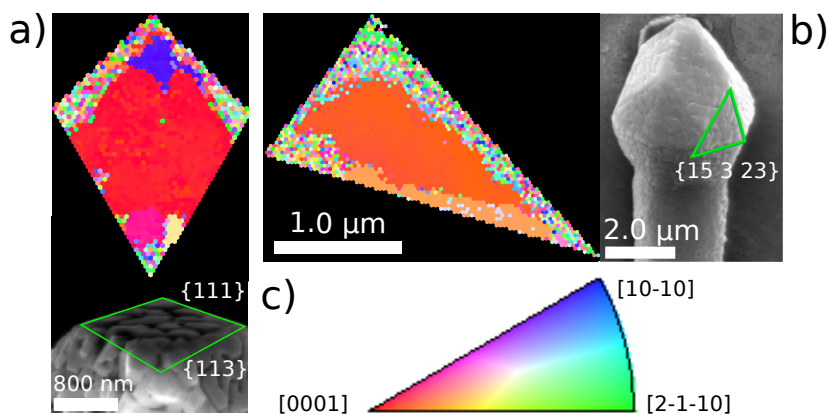


Figure 7.6: EBSD measurements of 410 nm thick GaN crystals reported in Figure 7.5 a). Panels a) and b) show SEM images of the analyzed area, marked in green, and the respective orientation map for GaN crystals deposited respectively on Si {111}, {113} and {15 3 23} facets. c) is the pole figure of the GaN crystal orientation.

In order to promote the coalescence of the GaN microcrystals deposited on the Si pillars, getting a continuous smooth layer, the thickness h of the deposited material has been increased from 0.41 to 3 μm . In Figure 7.7 perspective view SEM images of GaN crystals deposited on Si pillars with side $d = 2 \mu\text{m}$ and separated by 5 μm wide trenches are reported. The morphology of the GaN crystals is strongly influenced by increasing the thickness of the deposited material. Indeed, for GaN thickness larger than 1 μm , smooth, fully coalesced crystals start to form on Si {111} facets. In the case of 3 μm thick GaN deposition, crystals with smooth surfaces, RMS = 0.7 nm on Si {111} facets have been obtained, as reported in the AFM scan of Figure 7.8.

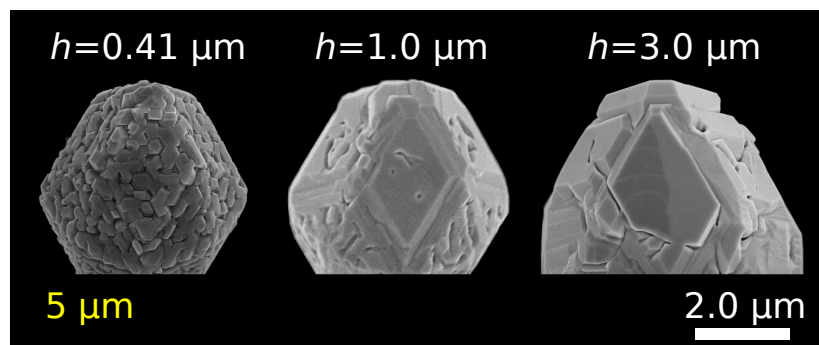


Figure 7.7: Perspective SEM images of GaN crystals with different thickness $h = 0.41, 1$ and $3 \mu\text{m}$ deposited on Si pillars with side $d = 2 \mu\text{m}$ and separated by $5 \mu\text{m}$ wide trenches (labeled in yellow).

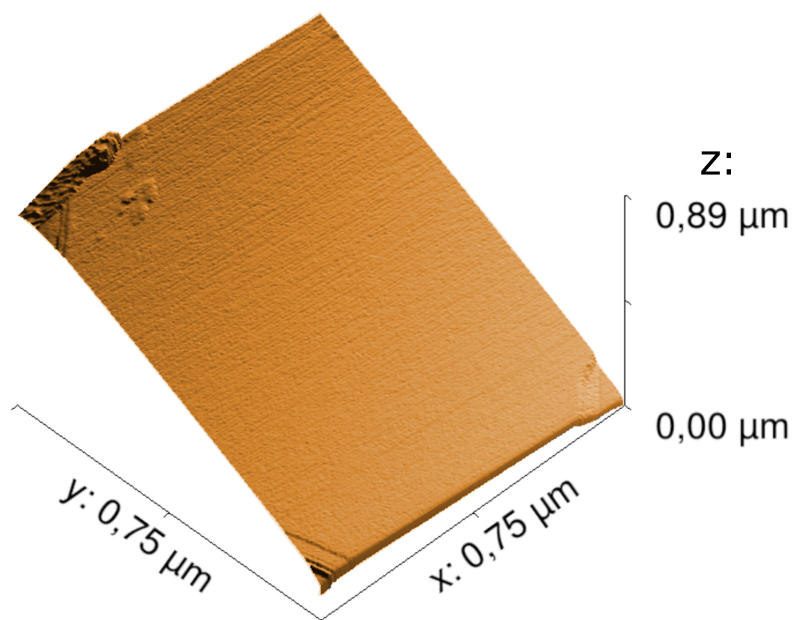


Figure 7.8: 3D AFM image of 3 μm thick GaN crystal deposited on the $\{111\}$ Si facets of pillars with side $d = 2 \mu\text{m}$ and separated by 5 μm wide trenches.

We now focus on the 3 μm thick GaN crystals deposited on Si pillars with side $d = 2 \mu\text{m}$ which show the best morphology in terms of crystal coalescence and surface roughness. In Figure 7.9, top-view SEM images of GaN crystals deposited on Si pillars separated by 5 or 50 μm and on the unpatterned planar Si (001) region (white inset) are displayed. In the unpatterned (001) area, the GaN surface quality is poor with high surface roughness (RMS $\sim 15 \text{ nm}$). Moreover, due to the large thermal expansion coefficient mismatch between Si and GaN, cracks are also present to relax the thermal stress. On the other hand, GaN crystals deposited both on Si pillars separated by 5 and 50 μm wide trenches, present similar morphologies: smooth and large crystalline facets on Si $\{111\}$ surfaces.

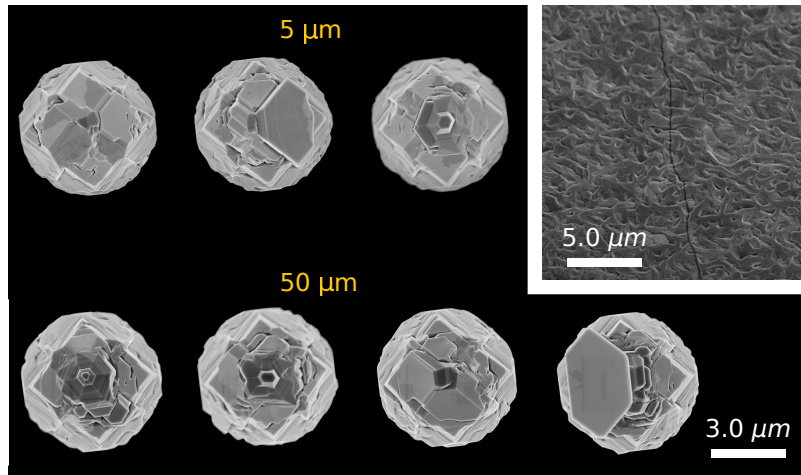


Figure 7.9: Top view SEM images of different $3 \mu\text{m}$ tall GaN crystals deposited on Si pillars with side $d = 2 \mu\text{m}$ and separated by 5 or $50 \mu\text{m}$ wide trenches (marked in yellow). The inset shows a SEM image of the GaN surface deposited in the unpatterned (001) Si planar region, a thermal crack is visible as a dark line.

By looking at the top and perspective view SEM images, reported respectively in Figure 7.9 and 7.10, it is possible to distinguish two kinds of GaN crystals deposited on the $\{111\}$ Si facets. The first one, where large hexagonal platelets are not completely attached to the pillar structure (e.g. top right corner of Figure 7.10), and the second one characterized by a compact structure (e.g. top left corner of Figure 7.10). A crystal morphology similar to the former case, has been already observed for pendeoepitaxial over-

growth of GaN nanowires on Si (111) [186]. TEM analysis will be performed in order to study the formation process of the large hexagonal platelets. GaN has been deposited also on the top $\{113\}$ and steep lateral $\{15\ 3\ 23\}$ Si facets. The deposition on $\{113\}$ Si facets results in the formation of hexagonal-shaped GaN top crystals, while on $\{15\ 3\ 23\}$ Si surfaces, highly stepped GaN layers are formed.

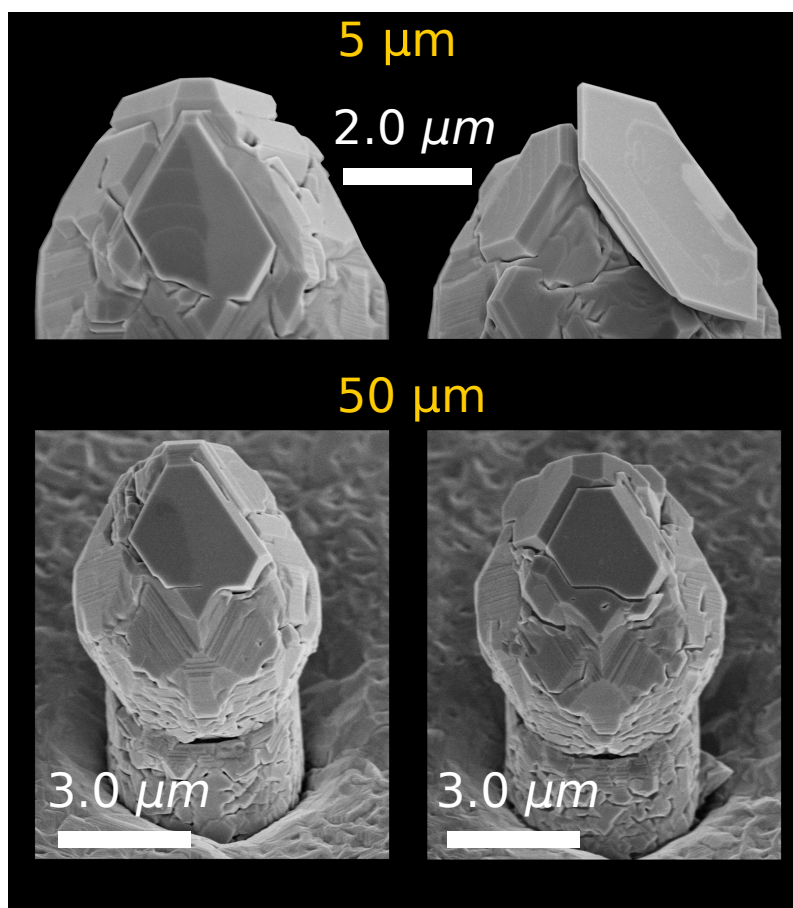


Figure 7.10: Perspective SEM images of different 3 μm tall GaN crystals deposited on Si pillars with side $d = 2$ μm and separated by 5 or 50 μm wide trenches (marked in yellow).

7.2 Optical properties

The optical quality of the 3 μm tall GaN crystals deposited on Si pillars has been also investigated by means of micro-photoluminescence (micro-PL) and cathodoluminescence (CL).

In Figure 7.11 a), is reported the room temperature micro-PL spectrum, in the 340 - 600 nm range, of a compact GaN/Si crystal. The D^0X exciton peak is located at 363 nm (3.42 eV), the shoulders at higher wavelengths are associated to LO-phonon replica spaced by 92 meV [187, 188]. The good crystal quality is confirmed by the absence of any feature in the yellow spectral range up to ~ 600 nm. Indeed, the presence of yellow luminescence has been attributed to point defects, especially gallium vacancies and their complexes, acting as deep acceptors [189, 190].

Figure 7.11 b) reports the comparison of the low temperature (10 K) micro-PL spectra of two different GaN/Si crystals: the first one with a compact morphology (green line) and the second one characterized by a large hexagonal platelet not completely attached to the structure (black line). The D^0X exciton emission is located at 357.4 nm (3.470 eV)

with a FWHM of 9.8 meV and at 357.2 nm (3.471 eV) with FWHM of 6.3 meV, respectively in the case of compact and hexagonal platelet crystals. The spectral position of the exciton peak is fully compatible with that one of fully relaxed GaN. In both cases, the FWHM of the exciton peaks are comparable, or even smaller, than literature results for GaN layers grown on Si (111) substrates by MBE [191, 192] and CVD [193] techniques. GaN micro-crystals grown by pendeo-epitaxy, starting from GaN nanowires on Si (111) and bulk GaN, grown by hydride vapor phase epitaxy, show respectively exciton peak FWHM of 1 and 0.6 meV [186]. It is worth to notice that in our case, the innovative approach of depositing GaN on faceted Si pillars, allows to deposit good quality crystals starting from (001) Si substrate.

At longer wavelengths, PL peaks related to recombination at defect sites, in particular stacking faults, are present [194]. In the case of the hexagonal platelet (black line), a strong PL peak, named I_1 , related to stacking fault with translational vector $\frac{1}{6}[\bar{2}02\bar{3}]$ [194, 195] is present at 363.7 nm, while it is absent for the compact GaN crystal (green line).

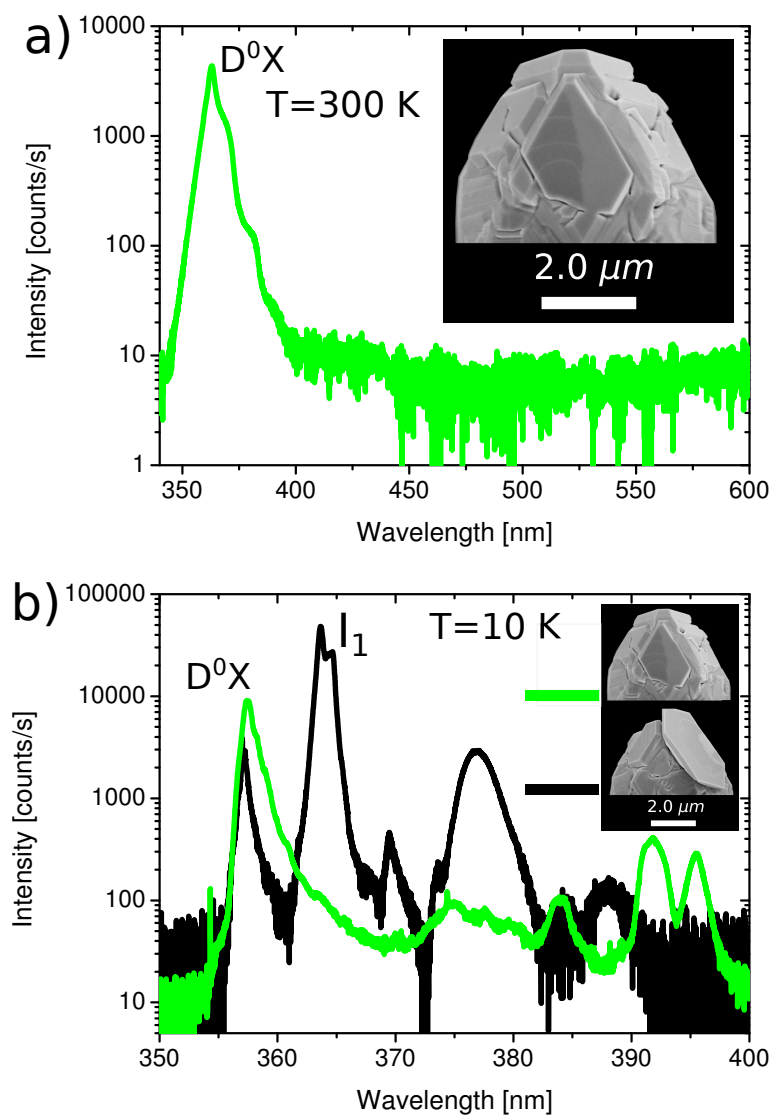


Figure 7.11: Micro-PL measurements of $3\ \mu\text{m}$ thick GaN crystals on Si pillars with side $d = 2\ \mu\text{m}$ and separated by $5\ \mu\text{m}$ wide trenches. a) Micro-PL spectrum at room temperature of a compact GaN crystal. b) micro-PL spectra comparison of different kinds of GaN crystals: compact (green line) and hexagonal platelet (black line) at 10 K. D^0X labels the donor bound exciton emission and I_1 the particular stacking fault recombination.

The low temperature micro-PL map of the GaN D^0X exciton peak, reported in Figure 7.12 for an area of $961 \mu\text{m}^2$, shows that a good uniformity of PL emission has been achieved despite the different morphology of each GaN/Si crystal. Indeed, the red bright peaks, which are spaced by $\sim 7 \mu\text{m}$, are associated to the PL exciton emission of the high quality GaN layer grown on the Si $\{111\}$ facets.

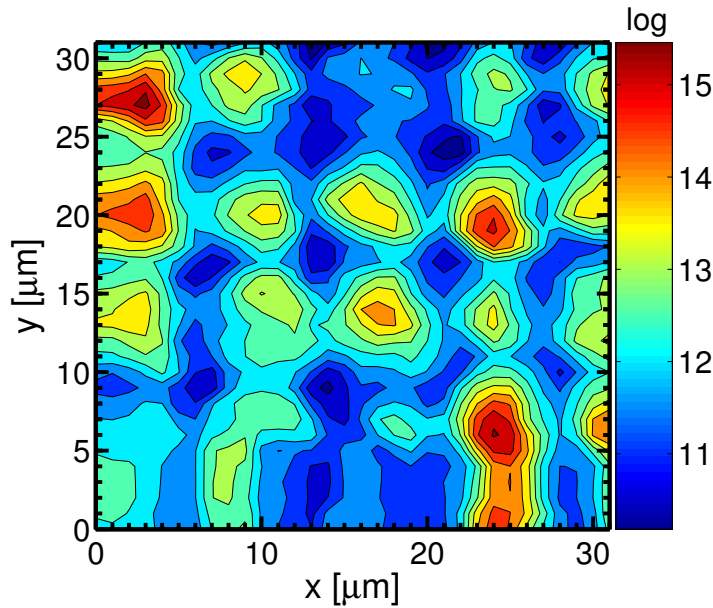


Figure 7.12: 2D intensity map of the GaN D^0X exciton peak emission for an area of $961 \mu\text{m}^2$, measured at 10 K. GaN crystal are $3 \mu\text{m}$ thick and deposited on Si pillars with side $d = 2 \mu\text{m}$ and separated by $5 \mu\text{m}$ wide trenches.

The high optical quality of the GaN/Si crystals is also confirmed by room temperature CL measurements reported in Figure 7.13. Panel c) shows the CL spectra of GaN crystals deposited on two different regions: Si {111} facet (green line, shown in panel b)) and ensemble of many crystals with Si (001) surface included (red line, shown in panel a)). Both CL spectra show exciton recombination at 363.4 nm, but in the case of GaN crystal deposited on Si {111}, recombination at wavelengths longer than 390 nm is not present (green line). On the other hand, a broad defect-related CL peak around 400 nm is detected for material deposited on different Si facets (red line). The image shown in panel d) confirms that exciton recombination (marked in blue) takes place homogeneously in GaN deposited on {111} Si facets of pillars with slightly different morphology and facet expansion. Stacking fault recombination at $\lambda = 385$ nm (marked in red) is mostly present at the border between different facets. Indeed, as also confirmed by the EBSD measurements reported in Figure 7.6, at the borders between different facets, GaN crystals are not perfectly c-oriented, probably due to the presence of stacking faults. Moreover, a large density of stacking faults is also expected on the highly stepped lateral

surfaces (e.g. on Si $\{15\ 3\ 23\}$).

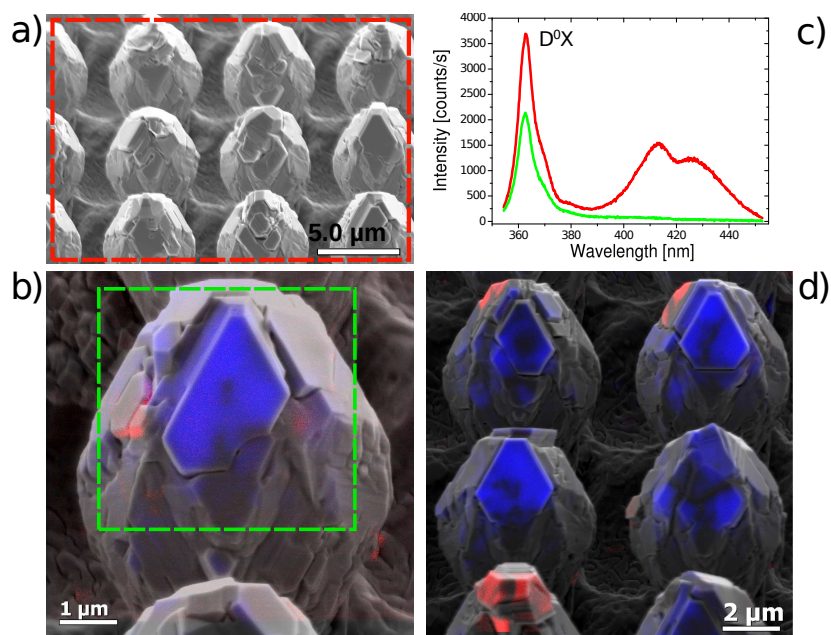


Figure 7.13: CL measurements of $3\ \mu\text{m}$ thick GaN crystals on Si pillars with side $d = 2\ \mu\text{m}$ and separated by $5\ \mu\text{m}$ wide trenches. a) and b) SEM perspective view of the areas (marked respectively in red and green) analyzed in c). c) CL spectra of the areas reported in a) (red line) and b) (green area). In b) and d) blue and red colors refer respectively to the $\lambda = 364\ \text{nm}$ and $\lambda = 385\ \text{nm}$ CL emissions.

In conclusion we have shown an innovative approach to deposit high quality GaN crystals on patterned Si (001) substrates by means of regular arrays of micrometer-sized Si pillars. Each Si pillar is constituted by large $\{111\}$ facets,

enabling the epitaxial deposition of GaN crystals with high optical quality (FWHM of the exciton peak at 10K of 9.8 meV) and good uniformity. EBSD and CL measurements reveal that most of the defect-related optical recombination processes happen at the borders between different crystalline facets and on highly stepped surfaces. This innovative approach, after future refinement of the growth procedure and device engineering, could pave the way to realize regular arrays of light emitting diodes based on In(Al)GaN nanostructures, integrated on Si (001) substrates with intrinsic pixelated geometry.

Conclusions

In this work we faced the problem of depositing on silicon substrates $\text{Si}_{1-x}\text{Ge}_x$ alloys, several micrometers thick, fulfilling the requirements of complete lattice relaxation, low threading dislocation density and absence of thermal cracks. In particular, our innovative epitaxial growth approach was based on depositing $\text{Si}_{1-x}\text{Ge}_x$ alloys on deeply patterned arrays of square micrometer-sized Si pillars.

The epitaxial growth was performed by LEPECVD. Thanks to its out-of-equilibrium growth conditions: high deposition rate (up to ~ 10 nm/s), low growth temperature ($\sim 500^\circ\text{C}$ for Ge) and partially isotropic distribution of the reactive impinging species, highly non conformal growth of Ge crystals, up to $50\ \mu\text{m}$ tall and separated by few tens of nanometers, has been obtained.

We called this novel growth approach *3D heteroepitaxy*,

which is based on self-limited lateral growth of the crystals. Firstly, the high deposition rate and low growth temperature ensure the surface adatom diffusion length being smaller than the Si pillar size and height, thus preventing material flow from the top to the bottom of the crystals. Secondly, steeper crystalline facets, close to the borders of the crystals, receive smaller reactive gas flux compared to the top ones, therefore having lower growth rate. Furthermore, in the case of closely spaced crystals, lateral steeper facets also suffer from reactive gas flux reduction due to shielding of neighboring pillars, thus further limiting their growth rate and lateral expansion.

The morphology and facet distribution of the crystals strongly depends on the competing growth velocities of each facet which can be finely tuned by changing the growth conditions. Indeed, by increasing the Ge growth temperature from 415 to 585°C, the top morphology can be switched from a flat (001) surface to pyramidal shape made by {113} facets.

The finite dimensions and the control of the top faceting of the crystals, allow to eliminate completely all threading dislocations at the lateral sidewalls, leaving the upper part of the crystals dislocation-free. Indeed, if slanted thread-

ing dislocations gliding in the $\{111\}$ planes are naturally eliminated at the sidewalls, vertical threading dislocations need to be bent and expelled by inclined $\{113\}$ facets. We demonstrated also the possibility to have flat topped (001) Ge crystals with no emerging dislocations by reducing the growth temperature after their complete elimination.

Photoluminescence measurements performed on Ge crystals with different threading dislocation densities revealed that, in the case of dislocation-free $8\ \mu\text{m}$ tall crystals, the inter-band PL signal is ~ 0.5 times that of a bulk Ge reference with fully comparable spectral shape. This result has been achieved for unintentionally doped Ge crystals without any annealing treatment. We also proposed a strategy to inhibit recombination of carriers at the defect sites by introducing fully strained $\text{Si}_{0.25}\text{Ge}_{0.75}$ reflectors within the Ge crystals, enhancing the ratio between the inter-band/dislocation PL recombination rate. We finally demonstrated the superior optical quality of dislocation-free Ge multiple quantum wells deposited on Si pillars compared to the best literature reference grown on graded buffer with threading dislocation density of $\sim 10^6\ \text{cm}^{-2}$.

High resolution X-ray diffraction measurements,

performed at the ESRF synchrotron, showed that Ge crystals are completely strain free, even from the tensile strain accumulated during the cooling from the growth to room temperature. Indeed, finite element method simulations confirm that the tensile thermal strain is elastically released for Ge crystals with aspect ratio larger than ~ 1 . While wafer bowing and thermal cracks are observed for thick Ge layers deposited on planar Si substrates, they are absent in the case of Ge crystals grown on micrometer-sized Si pillars. Moreover, in the case of dislocation-free Ge crystals, their excellent crystal quality is confirmed by the FWHM of the (115) Bragg reflection peak which is comparable to that one of the silicon substrate.

Inspired by the relevant results we obtained in the case of $\text{Si}_{1-x}\text{Ge}_x$ epitaxy on patterned Si substrates, during my Ph.D. internship at the Paul-Drude-Institut in Berlin, we tried to pursue a similar approach for another technologically relevant system: integration of high quality GaN crystals on (001) silicon substrates by plasma-assisted MBE.

The novelty of our approach consists in depositing $2.5\ \mu\text{m}$ of Si by LEPECVD on deeply patterned (001) silicon substrates, in this way crystals with large $\{111\}$ facets were

obtained. The threefold symmetry of the $\{111\}$ Si facets favors the deposition of the AlN buffer and GaN crystals. Indeed, after $\sim 1 \mu\text{m}$ of deposition, GaN micro-crystals on $\{111\}$ Si facets start to coalesce forming a continuous smooth layer, and after $3 \mu\text{m}$ the surface roughness has a RMS of 0.7 nm. Micro-photoluminescence and cathodoluminescence measurements confirm the high optical quality of the $3 \mu\text{m}$ thick GaN/Si crystals. Indeed, no yellow emission is detectable, while intense GaN bound exciton recombination, with a FWHM of 9.8 meV, takes place on the material deposited on the $\{111\}$ Si facets. Moreover, most of the stacking faults recombination processes are located at the borders between different facets and in highly stepped surfaces.

In conclusion we demonstrated a viable approach to deposit strain and dislocation-free Ge crystals on deeply patterned Si substrates with excellent optical and structural quality. We already have robust evidences that Ge crystals can be used to realize high efficiency IR light emitters and photodetectors, X-ray imaging detectors monolithically integrated onto a Si CMOS substrate and can act as virtual substrates for the deposition of III-As photovoltaic cells. Moreover, as already demonstrated here with the epitaxial

integration of GaN/Si (001) and from unpublished results on SiC/Si, we strongly believe that once the conditions to have self-limited lateral growth are fulfilled, i.e. large out-of-equilibrium growth conditions and shielding of the impinging species between neighboring crystals, the use of micrometer-sized patterned Si substrates can be useful for the integration of several semiconductors on silicon, irrespective of lattice and thermal expansion coefficients mismatch, different polarity and crystal symmetry.

Cover Gallery

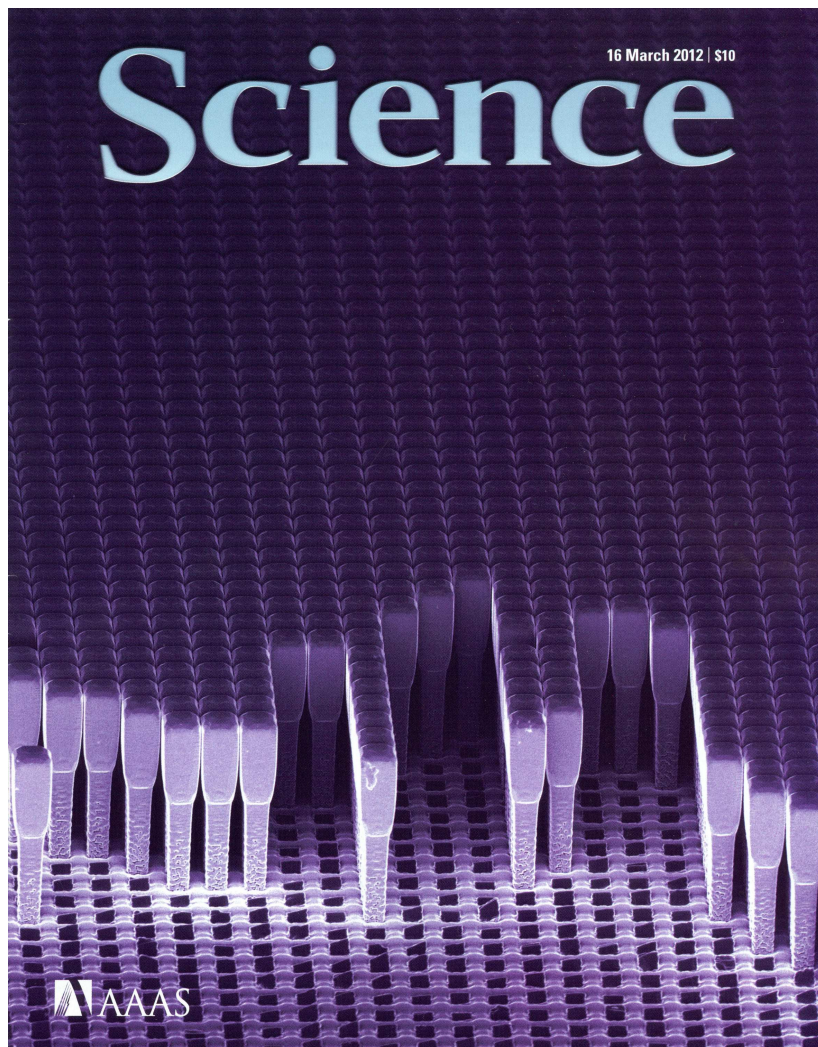


Figure 7.14: Cover *Science* Vol. **335**, Issue 6074 (2012)

An innovative strategy in dislocation analysis is described by Anna Marzegalli et al. on page 4408 demonstrating that vertical dislocations dominate in thick Ge layers on silicon substrates.

ADVANCED MATERIALS

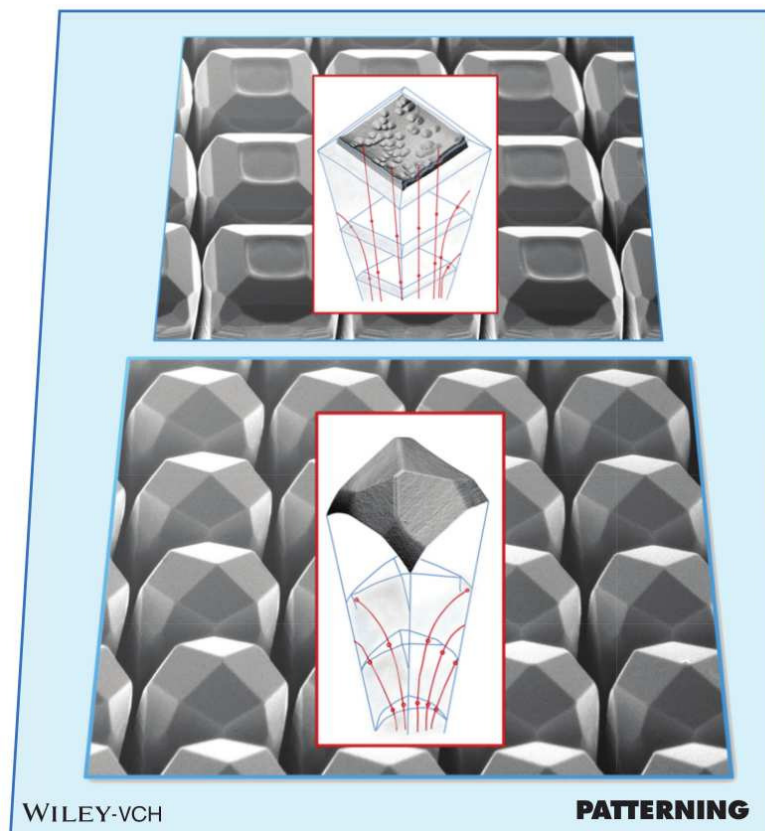


Figure 7.15: Frontispiece *Advanced Materials* Vol. 25, Issue 32 (2013)



Figure 7.16: Back cover *Physica Status Solidi a* Vol. 211, Issue 1 (2014)



Figure 7.17: Cover *Il Nuovo Saggiatore* Vol. **29**, Issue 3-4 (2013)

Acknowledgements

I'm gratefully to Dr. Giovanni Isella for his constant supervision, example and teaching during my Ph.D. thesis, to Prof. L. Miglio and Prof. H. von Känel, respectively from Università degli studi di Milano Bicocca and ETH Zürich, for their guide, advices and support. I would like to thank all the co-workers, especially Dr. C. V. Falub, Dr. A. G. Taboada, T. Kreiliger and Dr. E. Müller from ETH Zürich for structural and electrical characterizations, Dr. F. Pezzoli, Dr. A. Marzegalli, Prof. F. Montalenti, Dr. R. Bergamaschini, M. Salvalaglio, Prof. E. Grilli and Prof. M. Guzzi from Università degli studi di Milano Bicocca for PL measurements, dislocation analysis and epitaxial growth modelling, Dr. D. Chrastina from Politecnico di Milano and Dr. M. Meduňa from Masaryk University of Brno for X-ray diffraction measurements, Dr. H. Groiss and Prof. F. Schäffler

from Johannes Kepler University of Linz for TEM analysis, A. Pezous and Dr. P. Niedermann from CSEM Neuchâtel for the patterning of Si substrates.

I'm also gratefully to Dr. Raffaella Calarco who gave me the possibility to spend 7 months at the Paul-Drude-Institut in Berlin and for her constant constructive supervision. I acknowledge all the people who helped me at PDI, particularly Dr. C. Chèze, Dr. M. Siekacz and Dr. S. Garrido for teaching me the use of PA-MBE, C. Hauswald, Dr. J. Lähmann and Dr. O. Brandt for PL and CL measurements, Dr. M. Ramsteiner for Raman measurements.

I would like to acknowledge also all the people who contributed to my Ph.D. thesis with valuable discussions, suggestions and support: Dr. S. C. Cecchi, J. Frigerio, Dr. S. Bietti, Dr. A. Scaccabarozzi, Prof. S. Sanguinetti, M. Bianchi, Dr. J. Grandal, Dr. V. Kopp, M. Musolino, Dr. A. Fedorov, M. Leone, L. Martinelli, R. Wang and V. Bragaglia.

Bibliography

- [1] H. L. Stormer and D. C. Tsui, “The quantized Hall effect,” *Science*, vol. 220, no. 4603, pp. 1241–1246, 1983.
- [2] J. Faist, F. Capasso, D. L. Sivco, C. Sirtori, A. L. Hutchinson, and A. Y. Cho, “Quantum cascade laser,” *Science*, vol. 264, no. 5158, pp. 553–556, 1994.
- [3] T. Ghani, M. Armstrong, C. Auth, M. Bost, P. Charvat, G. Glass, T. Hoffmann, K. Johnson, C. Kenyon, J. Klaus, B. McIntyre, K. Mistry, A. Murthy, J. Sandford, M. Silberstein, S. Sivakumar, P. Smith, K. Zawadzki, S. Thompson, and M. Bohr, “A 90 nm high volume manufacturing logic technology featuring novel 45 nm gate length strained silicon CMOS transistors,” *IEDM Tech. Dig.*, pp. 11.6.1–11.6.3, 2003.
- [4] F. Schäffler, “High-mobility Si and Ge structures,”

-
- Semicond. Sci. Technol.*, vol. 12, no. 12, pp. 1515–1549, 1997.
- [5] D. J. Paul, “Silicon-Germanium Strained Layer Materials in Microelectronics,” *Adv. Mater.*, vol. 11, no. 3, pp. 191–204, 1999.
- [6] D. J. Paul, “Silicon germanium heterostructures in electronics: the present and the future,” *Thin Solid Films*, vol. 321, no. 1–2, pp. 172–180, 1998.
- [7] D. J. Paul, “Si/SiGe heterostructures: from material and physics to devices and circuits,” *Semicond. Sci. Technol.*, vol. 19, no. 10, pp. R75–R108, 2004.
- [8] F. C. Frank and J. H. van der Merwe, “One-dimensional dislocations. I. Static theory,” *Proc. R. Soc. (London)*, vol. A 198, no. 1053, pp. 205–216, 1949.
- [9] F. C. Frank and J. H. van der Merwe, “One-dimensional dislocations. II. Misfitting monolayers and oriented overgrowth,” *Proc. R. Soc. (London)*, vol. A 198, no. 1053, pp. 216–225, 1949.
- [10] J. W. Matthews, S. Mader, and T. B. Light, “Accommodation of misfit across the interface between crystals

- of semiconducting elements of compounds,” *J. Appl. Phys.*, vol. 41, no. 9, pp. 3800–3804, 1970.
- [11] L. M. Giovane, H.-C. Luan, A. M. Agarwal, and L. C. Kimerling, “Correlation between leakage current density and threading dislocation density in SiGe $p-i-n$ diodes grown on relaxed graded buffer layers,” *Appl. Phys. Lett.*, vol. 78, no. 4, pp. 541–543, 2001.
- [12] E. A. Fitzgerald, Y.-H. Xie, M. L. Green, D. Brasen, A. R. Kortan, J. Michel, Y.-J. Mii, and B. E. Weir, “Totally relaxed $\text{Ge}_x\text{Si}_{1-x}$ layers with low threading dislocation densities grown on Si substrates,” *Appl. Phys. Lett.*, vol. 59, no. 7, pp. 811–813, 1991.
- [13] J.-S. Park, J. Bai, M. Curtin, B. Adekore, M. Carroll, and A. Lochtefeld, “Defect reduction of selective Ge epitaxy in trenches on Si(001) substrates,” *Appl. Phys. Lett.*, vol. 90, no. 5, p. 052113, 2007.
- [14] D. Zubia and S. D. Hersee, “Nanoheteroepitaxy: The application of nanostructuring and substrate compliance to the heteroepitaxy of mismatched semiconduc-

- tor materials,” *J. Appl. Phys.*, vol. 85, no. 9, pp. 6492–6496, 1999.
- [15] P. Zaumseil, G. Kozlowski, Y. Yamamoto, J. Bauer, M. A. Schubert, T. U. Schüllli, B. Tillack, and T. Schroeder, “Compliant Si nanostructures on SOI for Ge nanoheteroepitaxy—a case study for lattice mismatched semiconductor integration on Si(001),” *J. Appl. Phys.*, vol. 112, no. 4, p. 043506, 2012.
- [16] M. Yamaguchi, M. Tachikawa, Y. Itoh, M. Sugo, and S. Kondo, “Thermal annealing effects of defect reduction in GaAs on Si substrates,” *J. Appl. Phys.*, vol. 68, no. 9, pp. 4518–4522, 1990.
- [17] S. Harada, J. Kikkawa, Y. Nakamura, G. Wang, M. Caymax, and A. Sakai, “Vertical dislocations in Ge films selectively grown in submicron Si windows of patterned substrates,” *Thin Solid Films*, vol. 520, no. 8, pp. 3245–3248, 2012.
- [18] J. Bai, J.-S. Park, Z. Cheng, M. Curtin, B. Adekore, M. Carroll, A. Lochtefeld, and M. Dudley, “Study of the defect elimination mechanisms in aspect ratio trap-

- ping Ge growth,” *Appl. Phys. Lett.*, vol. 90, no. 10, p. 101902, 2007.
- [19] A. Marzegalli, F. Isa, H. Groiss, E. Müller, C. V. Falub, A. G. Taboada, P. Niedermann, G. Isella, F. Schäffler, F. Montalenti, H. von Känel, and L. Miglio, “Unexpected dominance of vertical dislocations in high-misfit Ge/Si(001) films and their elimination by deep substrate patterning,” *Adv. Mater.*, vol. 25, no. 32, pp. 4408–4412, 2013.
- [20] Y. Ishikawa, K. Wada, J. Liu, D. D. Cannon, H.-C. Luan, J. Michel, and L. C. Kimerling, “Strain-induced enhancement of near-infrared absorption in Ge epitaxial layers grown on Si substrate,” *J. Appl. Phys.*, vol. 98, no. 1, p. 013501, 2005.
- [21] J. P. Dismukes, L. Ekstrom, and R. J. Paff, “Lattice Parameter and Density in Germanium-Silicon Alloys,” *J. Phys. Chem.*, vol. 68, no. 10, pp. 3021–3027, 1964.
- [22] M. A. Biot, “Theory of elasticity and consolidation for a porous anisotropic solid,” *J. Appl. Phys.*, vol. 26, no. 2, pp. 182–185, 1955.

-
- [23] J. J. Wortman and R. A. Evans, “Young’s modulus, shear modulus, and Poisson’s ratio in silicon and germanium,” *J. Appl. Phys.*, vol. 36, no. 1, pp. 153–156, 1965.
- [24] H. Kroemer *Proc. IRE*, vol. 45, p. 1535, 1957.
- [25] Z. Zhou, C. Li, H. Lai, S. Chen, and J. Yu, “The influence of low-temperature Ge seed layer on growth of high-quality Ge epilayer on Si(100) by ultrahigh vacuum chemical vapor deposition,” *J. Cryst. Growth*, vol. 310, no. 10, pp. 2508–2513, 2008.
- [26] T. F. Wietler, E. Bugiel, and K. R. Hofmann, “Surfactant-mediated epitaxy of relaxed low-doped Ge films on Si(001) with low defect densities,” *Appl. Phys. Lett.*, vol. 87, no. 18, p. 182102, 2005.
- [27] A. Marzegalli, V. A. Zinovyev, F. Montalenti, A. Rastelli, M. Stoffel, T. Merdzhanova, O. G. Schmidt, and L. Miglio, “Critical shape and size for dislocation nucleation in $\text{Si}_{1-x}\text{Ge}_x$ islands on Si(001),” *Phys. Rev. Lett.*, vol. 99, no. 23, p. 235505, 2007.
- [28] A. Rastelli and H. von Känel, “Island formation

- and faceting in the SiGe/Si(001) system,” *Surf. Sci.*, vol. 532–535, pp. 769–773, 2003.
- [29] J. H. van der Merwe, “Crystal interface. Part I. Semi-infinite crystals,” *J. Appl. Phys.*, vol. 34, no. 1, pp. 117–122, 1963.
- [30] J. H. van der Merwe, “Crystal interface. Part II. Finite overgrowth,” *J. Appl. Phys.*, vol. 34, pp. 123–127, 1963.
- [31] J. W. Matthews and A. E. Blakeslee, “Defects in epitaxial multilayers — I. Misfit dislocations,” *J. Cryst. Growth*, vol. 27, pp. 118–125, 1974.
- [32] J. W. Matthews, “Defects associated with the accommodation of misfit between crystals,” *J. Vac. Sci. Technol.*, vol. 12, no. 1, pp. 126–133, 1975.
- [33] R. People and J. C. Bean, “Calculation of critical layer thickness versus lattice mismatch for $\text{Ge}_x\text{Si}_{1-x}/\text{Si}$ strained-layer heterostructures,” *Appl. Phys. Lett.*, vol. 47, no. 3, pp. 322–324, 1985.
- [34] R. People and J. C. Bean, “Erratum: Calculation of critical layer thickness versus lattice mismatch

- for $\text{Ge}_x\text{Si}_{1-x}/\text{Si}$ strained-layer heterostructures [appl. phys. lett. 47. 322 (1985)][33],” *Appl. Phys. Lett.*, vol. 49, no. 4, p. 229, 1986.
- [35] J. Bevk, J. P. Mannaerts, B. A. Davidson, L. C. Feldman, and A. Qurmazd *Bull. Am. Phys. Soc.*, 1986.
- [36] F. R. N. Nabarro, “Theory of crystal dislocations,” *Clarendon, Oxford*, 1967.
- [37] R. Hull, J. C. Bean, and C. Buescher, “A phenomenological description of strain relaxation in $\text{Ge}_x\text{Si}_{1-x}/\text{Si}(100)$ heterostructures,” *J. Appl. Phys.*, vol. 66, no. 12, pp. 5837–5843, 1989.
- [38] B. W. Dodson and J. Y. Tsao, “Relaxation of strained-layer semiconductor structures via plastic flow,” *Appl. Phys. Lett.*, vol. 51, no. 17, pp. 1325–1327, 1987.
- [39] H. Alexander and P. Haasen, “Solid state physics,” *Academic, New York*, 1968.
- [40] W. Hagen and H. Strunk, “A new type of source generating misfit dislocations,” *Appl. Phys.*, vol. 17, no. 1, pp. 85–87, 1978.

- [41] E. A. Fitzgerald, “The effect of substrate growth area on misfit and threading dislocation densities in mismatched heterostructures,” *J. Vac. Sci. Technol. B*, vol. 7, no. 4, pp. 782–788, 1989.
- [42] E. P. Kvam, D. M. Maher, and C. J. Humphreys, “Variation of dislocation morphology with strain in $\text{Ge}_x\text{Si}_{1-x}$ epilayers on (001)Si,” *J. Mater. Res.*, vol. 5, no. 9, pp. 1900–1907, 1990.
- [43] E. A. Fitzgerald, G. P. Watson, R. E. Proano, D. G. Ast, P. D. Kirchner, G. D. Pettit, and J. M. Woodall, “Nucleation mechanisms and the elimination of misfit dislocations at mismatched interfaces by reduction in growth area,” *J. Appl. Phys.*, vol. 65, no. 6, pp. 2220–2237, 1989.
- [44] P. Hirth and J. Lothe, *Theory of Dislocations*. McGraw-Hill, New York, 1985.
- [45] D. J. Bacon and A. G. Crocker, “The elastic energies of symmetrical dislocation loops,” *Phil. Mag.*, vol. 12, no. 1, pp. 195–198, 1965.
- [46] R. Hull and J. C. Bean, “Nucleation of misfit disloca-

- tions in strained-layer epitaxy in the $\text{Ge}_x\text{Si}_{1-x}/\text{Si}$ system," *J. Vac. Sci. Technol. A*, vol. 7, no. 4, pp. 2580–2585, 1989.
- [47] P. M. J. Marée, J. C. Barbour, J. F. van der Veen, K. L. Kavanagh, C. W. T. Bulle-Lieuwma, and M. P. A. Vieggers, "Generation of misfit dislocations in semiconductors," *J. Appl. Phys.*, vol. 62, no. 11, pp. 4413–4420, 2006.
- [48] S. A. Dregia and J. Hirth, "A rebound mechanism for lomer dislocation formation in strained structures," *J. Appl. Phys.*, vol. 69, no. 4, p. 2169, 1991.
- [49] J. Narayan and S. Sharan, "Mechanism of formation of 60° and 90° misfit dislocations in semiconductor heterostructures," *Mat. Sci. Eng. B*, vol. 10, no. 5107, pp. 261–267, 1991.
- [50] V. I. Vdovin, "Nature and origin of pure edge dislocations in low mismatched epitaxial structures," *J. Cryst. Growth*, vol. 22F, p. 58, 1997.
- [51] A. Sakai, T. Tatsumi, and K. Aoyama, "Growth of

- strain-relaxed Ge films on Si(001) surfaces,” *Appl. Phys. Lett.*, vol. 71, no. 24, pp. 3510–3512, 1997.
- [52] Y. B. Bolkhovityanov, A. S. Deryabin, A. K. Gutakovskii, and L. V. Sokolov, “Mechanisms of edge-dislocation formation in strained films of zinc blende and diamond cubic semiconductors epitaxially grown on (001)-oriented substrates,” *J. Appl. Phys.*, vol. 109, no. 12, p. 123519, 2011.
- [53] G. A. Slack and S. F. Bartram, “Thermal expansion of some diamondlike crystals,” *J. Appl. Phys.*, vol. 46, no. 1, pp. 89–98, 1975.
- [54] H. P. Singh, “Determination of thermal expansion of germanium, rhodium, and iridium by x-rays,” *Acta Crystallogr. A*, vol. 24, no. 4, pp. 469–471, 1968.
- [55] Y. Okada and Y. Tokumaru, “Precise determination of lattice parameter and thermal expansion coefficient of silicon between 300 and 1500 K,” *J. Appl. Phys.*, vol. 56, no. 2, pp. 314–320, 1984.
- [56] G. Capellini, M. De Seta, P. Zaumseil, G. Kozlowski, and T. Schroeder, “High temperature x ray diffrac-

- tion measurements on Ge/Si(001) heterostructures: A study on the residual tensile strain,” *J. Appl. Phys.*, vol. 111, no. 7, p. 073518, 2012.
- [57] D. Colombo, E. Grilli, M. Guzzi, S. Sanguinetti, S. Marchionna, M. Bonfanti, A. Fedorov, H. von Känel, G. Isella, and E. Müller, “Analysis of strain relaxation by microcracks in epitaxial GaAs grown on Ge/Si substrates,” *J. Appl. Phys.*, vol. 101, no. 10, p. 103519, 2007.
- [58] O. Moutanabbir and U. Gösele, “Heterogeneous integration of compound semiconductor,” *Annu. Rev. Mater. res.*, vol. 40, p. 469, 2010.
- [59] H. Morkoç, *Handbook of nitride semiconductors and devices, Volume 1, materials properties, physics and growth*. Wiley-vch, 2008.
- [60] M. Musolino, “Growth and investigation of Al-GaN/GaN heterostructures for applications in solid state electronics,” master thesis, Università degli Studi di Roma Tor Vergata, 2010/2011.
- [61] S. F. Garrido, X. Kong, T. Gotschke, R. Calarco,

- L. Geelhaar, A. Trampert, and O. Brandt, “Spontaneous nucleation and growth of GaN nanowires: The fundamental role of crystal polarity,” *Nano Lett.*, vol. 12, pp. 6119–6125, 2012.
- [62] O. Ambacher, “Growth and applications of group III-nitrides,” *Journal of Physics D: Applied Physics*, vol. 31, p. 2653, 1998.
- [63] S. Guha, N. A. Bojarczuk, and D. W. Kisker, “Surface lifetimes of Ga and growth behavior on GaN (0001) surfaces during molecular beam epitaxy,” *Appl. Phys. Lett.*, vol. 69, p. 2879, 1996.
- [64] C. Adelman, J. Brault, D. Jalabert, P. Gentile, H. Mariette, G. Mula, and B. Daudin, “Dynamically stable gallium surface coverages during plasma-assisted molecular-beam epitaxy of (0001) GaN,” *J. Appl. Phys.*, vol. 91, no. 12, pp. 9638–9645, 2002.
- [65] C. Kruse, S. Einfeldt, T. Bottcher, D. Hommel, D. Rudloff, and J. Christien, “Spatially modified layer properties related to the formation of gallium droplets on GaN(0001) surfaces during plasma-assisted

- molecular-beam epitaxy,” *Appl. Phys. Lett.*, vol. 78, no. 24, pp. 3827–3829, 2001.
- [66] G. Koblmüller, R. Averbeck, H. Riechert, and P. Pongratz, “Direct observation of different equilibrium Ga adlayer coverages and their desorption kinetics on GaN (0001) and (000 $\bar{1}$) surfaces,” *Phys. Rev. B*, vol. 69, no. 3, p. 035325, 2004.
- [67] T. Zywietz, J. Neugebauer, and M. Sceffler, “Adatom diffusion at GaN (0001) and (000 $\bar{1}$) surfaces,” *Appl. Phys. Lett.*, vol. 73, p. 487, 1998.
- [68] N. Newman, “The energetics of the GaN MBE reaction: a case study of meta-stable growth,” *J. Cryst. Growth*, vol. 178, p. 102, 1997.
- [69] B. Heying, R. Averback, L. F. Chen, E. Haus, H. Riechert, and J. S. Speck, “Control of GaN surface morphologies using plasma-assisted molecular beam epitaxy,” *J. Appl. Phys.*, vol. 88, no. 4, p. 1855, 2000.
- [70] R. Calarco, R. J. Meijers, R. K. Debnath, T. Stoica, E. Sutter, and H. Lüth, “Nucleation and growth of GaN

nanowires on Si(111) performed by MBE,” *J. Appl. Phys.*, vol. 88, no. 4, p. 1855, 2000.

- [71] C. Adelman, J. Brault, G. Mula, B. Daudin, L. Lymperakis, and J. Neugebauer, “Gallium adsorption on (0001) GaN surfaces,” *Phys. rev. B*, vol. 67, no. 16, p. 165419, 2003.
- [72] G. Koblmüller, J. Brown, R. Averbeck, H. Riechert, P. Pongratz, and J. S. Speck, “Continuous evolution of Ga adlayer coverages during plasma-assisted molecular beam epitaxy of (0001)GaN,” *Appl. Phys. Lett.*, vol. 86, no. 4, p. 041908, 2005.
- [73] O. Brandt, R. Muralidharan, P. Waltereit, A. Thamm, A. Trampert, H. von Kiedrowski, and K. H. Plog, “Critical issues for the growth of high-quality (Al,Ga)N/GaN and GaN/(In,Ga)N heterostructures on SiC(0001) by molecular beam epitaxy,” *Appl. Phys. Lett.*, vol. 75, p. 4019, 1999.
- [74] N. Grandjean, J. Massies, F. Semond, S. Y. Karpov, and R. A. Talalaev, “GaN evaporation in molecular-

- beam epitaxy environment,” *Appl. Phys. Lett.*, vol. 74, no. 13, pp. 1854–1856, 1999.
- [75] Z. A. Munir and A. Searcy, “Activation energy for sublimation of gallium nitride,” *J. Chem. Phys.*, vol. 42, p. 4223, 1965.
- [76] G. Isella, D. Chrastina, B. Rössner, T. Hackbarth, H.-J. Herzog, U. König, and H. von Känel, “Low-energy plasma-enhanced chemical vapor deposition for strained Si and Ge heterostructures and devices,” *Solid State Electron.*, vol. 48, no. 8, pp. 1317–1323, 2004.
- [77] C. Rosenblad, H. R. Deller, A. Dommann, T. Meyer, P. Schroeter, and H. von Känel, “Silicon epitaxy by low-energy plasma enhanced chemical vapor deposition,” *J. Vac. Sci. Technol. A*, vol. 16, no. 5, pp. 2785–2790, 1998.
- [78] R. Kaufmann, G. Isella, A. Sanchez-Amores, S. Neukom, A. Neels, L. Neumann, A. Brenzikofer, A. Dommann, C. Urban, and H. von Känel, “Near infrared image sensor with integrated germanium pho-

- todiodes,” *J. Appl. Phys.*, vol. 110, no. 2, p. 023107, 2011.
- [79] M. Bonfanti, *Ge Multiple Quantum Wells: Electronic States and Optical Properties*. PhD thesis, Università degli Studi di Milano-Bicocca, 2008.
- [80] P. Chaisakul, D. Marris-Morini, M.-S. Rouifed, G. Isella, D. Chrastina, J. Frigerio, X. Le Roux, S. Edmond, J.-R. Coudevylle, and L. Vivien, “23 GHz Ge/SiGe multiple quantum well electro-absorption modulator,” *Opt. Express*, vol. 20, no. 3, pp. 3219–3224, 2012.
- [81] J. Osmond, G. Isella, D. Chrastina, R. Kaufmann, M. Acciarri, and H. von Känel, “Ultra low dark current Ge/Si(100) photodiodes with low thermal budget,” *Appl. Phys. Lett.*, vol. 94, no. 20, p. 201106, 2009.
- [82] U. Kafader, H. Siringhaus, and H. von Känel, “In situ DC-plasma cleaning of silicon surfaces,” *Appl. Surf. Sci.*, vol. 90, no. 3, pp. 297–302, 1995.
- [83] C. Rosenblad, H. R. Deller, M. Döbeli, E. Müller, and H. von Känel, “Low-temperature heteroepitaxy

- by LEPECVD,” *Thin Solid Films*, vol. 318, no. 1–2, pp. 11–14, 1998.
- [84] M. Kummer, C. Rosenblad, A. Dommann, T. Hackbarth, G. Höck, M. Zeuner, E. Müller, and H. von Känel, “Low energy plasma enhanced chemical vapor deposition,” *Mat. Sci. Eng. B*, vol. 89, no. 1–3, pp. 288–295, 2002.
- [85] M. Kummer, “LEPECVD provides high-quality virtual substrates,” *Chip*, vol. January 2002, no. 6, pp. 24–26, 2002.
- [86] M. Bollani, E. Müller, G. Isella, S. Signoretti, D. Chrastina, and H. von Känel, “Dislocation density and structure in $\text{Si}_{1-x}\text{Ge}_x$ buffer layers deposited by LEPECVD,” *Inst. Phys. Conf. Ser.*, vol. 180, pp. 247–250, 2004.
- [87] M. Rondanini, S. Cereda, F. Montalenti, L. Miglio, and C. Cavallotti, “A multiscale model of the plasma assisted deposition of crystalline silicon,” *Surf. Coat. Technol.*, vol. 201, no. 22–23, pp. 8863–8867, 2007.
- [88] M. Rondanini, C. Cavallotti, D. Ricci, D. Chrastina,

- G. Isella, T. Moiseev, and H. von Känel, “An experimental and theoretical investigation of a magnetically confined dc plasma discharge,” *J. Appl. Phys.*, vol. 104, no. 1, p. 013304, 2008.
- [89] W. E. Hoke, P. J. Lemonias, and D. G. Weir, “Evaluation of a new plasma source for molecular beam epitaxial growth of inn and gan films,” *J. Cryst. Growth*, vol. 111, p. 1024, 1991.
- [90] M. Siekacz, A. Feduniewicz-Żmuda, G. Cywiński, M. Kryśko, I. Grzegory, S. Krukowski, K. E. Waldrip, W. Jantsch, Z. R. Wasilevski, S. Porowski, and C. Skierbiszewski, “Growth of InGaN and InGaN/InGaN quantum wells by plasma-assisted molecular beam epitaxy,” *J. Cryst. Growth*, vol. 310, pp. 3983–3986, 2008.
- [91] C. Chang, Y. F. Wang, Y. Kanamori, J. J. Shih, Y. Kawai, C. K. Lee, K. C. Wu, and M. Esashi, “Etching submicrometer trenches by using the bosch process and its application to the fabrication of antireflection structures,” *J. Micromech. Microeng.*, vol. 15, no. 1, pp. 580–585, 2005.

-
- [92] S. Tachi, K. Tsujimoto, and S. Okudaira, “Low-temperature reactive ion etching and microwave plasma etching of silicon,” *Appl. Phys. Lett.*, vol. 52, no. 8, pp. 616–618, 1988.
- [93] S. Marchionna, A. Virtuani, M. Acciarri, G. Isella, and H. von Känel, “Defect imaging of SiGe strain relaxed buffers grown by LEPECVD,” *Mat. Sci. Semicond. Process.*, vol. 9, no. 4–5, pp. 802–805, 2006.
- [94] C. Pfüller, *Optical properties of single semiconductor nanowires and nanowire ensembles*. PhD thesis, Humboldt-Universität zu Berlin, 2011.
- [95] J. Lähnemann, *Luminescence of group-III-V nanowires containing heterostructures*. Ph.d. thesis, Humboldt-Universität zu Berlin, 2013.
- [96] E. Gatti, E. Grilli, M. Guzzi, D. Chrastina, G. Isella, and H. von Känel, “Room temperature photoluminescence of Ge multiple quantum wells with Ge-rich barriers,” *Appl. Phys. Lett.*, vol. 98, no. 3, p. 031106, 2011.
- [97] C. V. Falub, H. von Känel, F. Isa, R. Bergamaschini, A. Marzegalli, D. Chrastina, G. Isella, E. Müller,

- P. Niedermann, and L. Miglio, “Scaling hetero-epitaxy from layers to three-dimensional crystals,” *Science*, vol. 335, no. 6074, pp. 1330–1334, 2012.
- [98] R. Bergamaschini, F. Isa, C. V. Falub, P. Niedermann, E. Müller, G. Isella, H. von Känel, and L. Miglio, “Self-aligned Ge and SiGe three-dimensional epitaxy on dense Si pillar arrays,” *Surf. Sci. Rep.*, vol. 68, p. 390, 2013.
- [99] D. Chrastina, B. Rössner, G. Isella, H. von Känel, J. P. Hague, T. Hackbarth, H.-J. Herzog, K.-H. Hieber, and U. König, “LEPECVD – a production technique for SiGe MOSFETs and MODFETs,” in *Materials for Information Technology* (E. Zschech, C. Whelan, and T. Mikolajick, eds.), pp. 17–29, Springer, 2005.
- [100] J. T. Robinson, A. Rastelli, O. Schmidt, and O. D. Dubon, “Global faceting behavior of strained Ge islands on Si,” *Nanotechnology*, vol. 20, no. 8, p. 085708, 2009.
- [101] D. B. Migas, S. Cereda, F. Montalenti, and L. Miglio *Surf. Sci.*, vol. 556, p. 121, 2004.

-
- [102] C. V. Falub, H. von Känel, F. Isa, R. Bergamaschini, A. Marzegalli, D. Chrastina, G. Isella, E. Müller, P. Niedermann, and L. Miglio, “Scaling hetero-epitaxy from layers to three-dimensional crystals - *supporting information*,” *Science*, vol. 335, no. 6074, pp. 1330–1334, 2012.
- [103] B. J. Spencer, P. W. Voorhees, and S. H. Davis, “Morphological Instability in Epitaxially Strained Dislocation-Free Solid Films,” *Phys. Rev. Lett.*, vol. 67, no. 26, pp. 3696–3699, 1991.
- [104] W. W. Mullins *J. Appl. Phys.*, vol. 28, p. 333, 1957.
- [105] G. Biasol and E. Kapon *Phys. rev. Lett.*, vol. 81, p. 2962, 1998.
- [106] Y. W. Zhang *Phys. Rev. B*, vol. 61, p. 10388, 2000.
- [107] J. Tersoff *Appl. Phys. Lett.*, vol. 83, p. 353, 2003.
- [108] R. Bergamaschini, J. Tersoff, Y. Tu, J. Zhang, G. Bauer, and F. Montalenti *Phys. Rev. Lett.*, vol. 109, p. 156101, 2012.

- [109] A. Madhukar, “Growth of semiconductor heterostructures on patterned substrates: defect reduction and nanostructures,” *Thin Solid Films*, vol. 231, no. 1–2, pp. 8–42, 1993.
- [110] Q. Xiang, S. Li, D. Wang, K. L. Wang, J. G. Couillard, and H. G. Craighead, “Interfacet mass transport and facet evolution in selective epitaxial growth of Si by gas source molecular beam epitaxy,” *J. Vac. Sci. Technol. B*, vol. 14, no. 3, pp. 2381–2386, 1996.
- [111] S. Li, Q. Xiang, D. Wang, and K. L. Wang *J. Cryst. Growth*, vol. 157, p. 185, 1995.
- [112] M. Ohtsuka and S. Miyazawa *J. Appl. Phys.*, vol. 64, p. 3522, 1988.
- [113] M. Ohtsuka and A. Suzuki *J. Cryst. Growth*, vol. 95, p. 55, 1989.
- [114] M. Ohtsuka and A. Suzuki *J. Appl. Phys.*, vol. 73, p. 7358, 1993.
- [115] P. Atkinson and D. A. Ritchie *J. Cryst. Growth*, vol. 278, p. 482, 2005.

-
- [116] S. Jones, L. K. Siedel, and K. M. Lau *J. Cryst. Growth*, vol. 108, p. 73, 1991.
- [117] A. Pimpinelli and J. Villain, *Physics of crystal growth*. Cambridge University Press, 1998.
- [118] D. W. Shaw *J. Cryst. Growth*, vol. 47, p. 509, 1979.
- [119] G. M. Vanacore, M. Zani, G. Isella, J. Osmond, M. Bolani, and A. Tagliaferri, “Quantitative investigation of the influence of carbon surfactant on Ge surface diffusion and island nucleation on Si(100),” *Phys. Rev. B*, vol. 82, no. 12, p. 125456, 2010.
- [120] G. M. Vanacore, *Investigation of Ge surface diffusion and SiGe nanostructures by spectro-microscopy techniques*. PhD thesis, Politecnico di Milano, 2011.
- [121] D. J. Godbey, J. V. Lill, J. Deppe, and K. D. Hobart *Appl. Phys. Lett.*, vol. 65, p. 711, 1994.
- [122] A. Oshiyama *Phys. Rev. Lett.*, vol. 74, p. 130, 1995.
- [123] L. Vescan, K. Grimm, and C. Dieker *J. Vac. Sci. Technol. B*, vol. 16, p. 1549, 1998.

- [124] J.-S. Park, J. Bai, M. Curtin, M. Carroll, and A. Lochtefeld, “Facet formation and lateral overgrowth of selective Ge epitaxy on SiO₂-patterned Si(001) substrates,” *J. Vac. Sci. Technol. B*, vol. 26, no. 1, pp. 117–121, 2008.
- [125] S.-H. Lim, S. Song, E. Yoon, and J.-H. Lee, “Isotropic/anisotropic growth behavior and faceting morphology of Si epitaxial layer selectively grown by cold wall ultrahigh vacuum chemical vapor deposition,” *J. Vac. Sci. Technol. B*, vol. 22, no. 1, pp. 275–282, 2004.
- [126] M. Ohtsuka *J. Cryst. Growth*, vol. 205, p. 112, 1999.
- [127] K. Shiraishi, Y. Y. Suzuki, and H. K. T. Ito *Appl. Surf. Sci.*, vol. 130-132, p. 431, 1998.
- [128] T. Nishinaga *Prog. Cryst. Growth Charact. Mater.*, vol. 48-49, p. 104, 2004.
- [129] R. L. Schwoebel and E. J. Shipsey, “Step Motion on Crystal Surfaces,” *J. Appl. Phys.*, vol. 37, no. 10, p. 3682, 1966.

- [130] C. V. Falub, M. Meduňa, D. Chrastina, F. Isa, A. Marzegalli, T. Kreiliger, A. G. Taboada, G. Isella, L. Miglio, A. Dommann, and H. von Känel, “Perfect crystals grown from imperfect interfaces,” *Sci. Reports*, vol. 3, p. 2276, 2013.
- [131] Y. Ashizawa, S. Akbar, W. J. Schaff, L. F. Eastman, E. A. Fitzgerald, and D. G. Ast, “Influence of lattice misfit on heterojunction bipolar transistors with lattice-mismatched InGaAs bases,” *J. Appl. Phys.*, vol. 64, p. 4065, 1998.
- [132] Y. B. Bolkhovityanov, O. P. Pchelyakov, M. A. Revenko, L. V. Sokolov, and S. I. Chikichev, “Artificial GeSi substrates for heteroepitaxy: Achievements and problems,” *Semiconductors*, vol. 37, no. 5, pp. 493–518, 2003.
- [133] F. Isa, A. Marzegalli, A. G. Taboada, C. V. Falub, G. Isella, F. Montalenti, H. von Känel, and L. Miglio, “Onset of vertical threading dislocations in $\text{Si}_{1-x}\text{Ge}_x/\text{Si}(001)$ at a critical Ge concentration,” *APL Mater.*, vol. 1, p. 052109, 2013.

- [134] J. W. P. Hsu, E. A. Fitzgerald, Y. H. Xie, P. J. Silverman, and M. J. Cardillo, “Surface morphology of related $\text{Ge}_x\text{Si}_{1-x}$ films,” *Appl. Phys. Lett.*, vol. 61, no. 11, pp. 1293–1295, 1992.
- [135] M. A. Lutz, R. M. Feenstra, F. K. LeGoues, P. M. Mooney, and J. O. Chu, “Influence of misfit dislocations on the surface morphology of $\text{Si}_{1-x}\text{Ge}_x$ films,” *Appl. Phys. Lett.*, vol. 66, no. 6, pp. 724–726, 1995.
- [136] L. Souriau, T. Atanasova, V. Terzieva, A. Moussa, M. Caymax, R. Loo, M. Meuris, and W. Vandervorst, “Characterization of threading dislocations in thin germanium layers by defect etching: Toward chromium and HF-free solution,” *J. Electrochem. Soc.*, vol. 155, no. 9, pp. H677–H681, 2008.
- [137] J. P. Morniroli *Ultramicroscopy*, vol. 83, pp. 227–243, 2000.
- [138] J. P. Morniroli *Journal of Microscopy*, vol. 223, pp. 240–245, 2006.
- [139] A. Marzegalli, F. Isa, H. Groiss, E. Müller, C. V. Falub, A. G. Taboada, P. Niedermann, G. Isella, F. Schäf-

- fler, F. Montalenti, H. von Känel, and L. Miglio, “Unexpected dominance of vertical dislocations in high-misfit Ge/Si(001) films and their elimination by deep substrate patterning - *supporting information*,” *Adv. Mater.*, vol. 25, no. 32, pp. 4408–4412, 2013.
- [140] A. Marzegalli, M. Brunetto, M. Salvalaglio, F. Montalenti, G. Nicotra, M. Scuderi, C. Spinella, M. D. Seta, and G. Capellini *Phys. Rev. B*, vol. 88, p. 165418, 2013.
- [141] C. S. Peng, Y. K. Li, Q. Huang, and J. M. Zhou, “The formation of dislocations in the interface of GeSi/low-temperature Si buffer grown on Si (001),” *Appl. Phys. Lett.*, vol. 73, p. 487, 1998.
- [142] J. S. Speck, M. A. Brewer, G. Beltz, A. E. Romanov, and W. Pompe, “Scaling laws for the reduction of threading dislocation densities in homogeneous buffer layers,” *J. Appl. Phys.*, vol. 80, no. 7, pp. 3808–3816, 1996.
- [143] M. Yamaguchi, A. Yamamoto, M. Tachikawa, Y. Itoh, and M. Sugo, “Defect reduction effects in GaAs on Si

- substrates by thermal annealing,” *Appl. Phys. Lett.*, vol. 53, no. 23, pp. 2293–2295, 1988.
- [144] H.-C. Luan, D. R. Lim, K. K. Lee, K. M. Chen, J. G. Sandland, K. Wada, and L. C. Kimerling, “High quality Ge epilayers on Si with low threading-dislocation densities,” *Appl. Phys. Lett.*, vol. 75, no. 19, pp. 2909–2911, 1999.
- [145] H.-C. Luan, *Ge Photodetectors for Si Microphotonics*. PhD thesis, Massachusetts Institute of Technology, 2001.
- [146] Y. Yamamoto, G. Kozlowski, P. Zaumseil, and B. Tillack, “Low threading dislocation Ge on Si by combining deposition and etching,” *Thin Solid Films*, vol. 520, no. 8, pp. 3216–3221, 2012.
- [147] G. Capellini, M. De Seta, Y. Busby, M. Pea, F. Evangelisti, G. Nicotra, C. Spinella, M. Nardone, and C. Ferrari, “Strain relaxation in high Ge content SiGe layers deposited on Si,” *J. Appl. Phys.*, vol. 107, no. 6, p. 063504, 2010.
- [148] H. Klapper, “Generation and propagation of disloca-

- tions during crystal growth,” *Mater. Chem. Phys.*, vol. 66, no. 2–3, pp. 101–109, 2000.
- [149] L. Miglio, R. Bergamaschini, A. Marzegalli, F. Isa, D. Chrastina, G. Isella, P. Niedermann, A. Dommann, C. V. Falub, E. Müller, and H. von Känel, ““divide et impera” in detector technology,” *Il Nuovo Saggiatore*, vol. 29, no. 3–4, pp. 7–14, 2013.
- [150] B. Cunningham, J. O. Chu, and S. Akbar *Appl. Phys. Lett.*, vol. 59, p. 3574, 1991.
- [151] Y. B. Bolkhovityanov, A. S. Deryabin, A. K. Gutakovskii, and L. V. Sokolov, “Formation of edge misfit dislocations in $\text{Ge}_x\text{Si}_{1-x}$ ($x \sim 0.4\text{--}0.8$) films grown on misoriented (001) \rightarrow (111) Si substrates: Features before and after film annealing,” *J. Appl. Phys.*, vol. 107, no. 12, p. 123521, 2010.
- [152] R. Hull and J. C. Bean, “Variation in misfit dislocation behavior as a function of strain in the GeSi/Si system,” *Appl. Phys. Lett.*, vol. 54, p. 925, 1989.
- [153] A. E. Blakeslee, “The use of superlattices to block the

propagation of dislocations in semiconductors,” *Mater. Res. Soc. Symp. Proc.*, vol. 148, p. 217, 1989.

- [154] G. M. Xia, J. L. Hoyt, and M. Canonico, “Si–Ge interdiffusion in strained Si/strained SiGe heterostructures and implications for enhanced mobility metal-oxide-semiconductor field-effect transistors,” *J. Appl. Phys.*, vol. 101, no. 4, p. 044901, 2007.
- [155] P. Ramanarayanan, K. Cho, and B. M. Clemens, “Effect of composition on vacancy mediated diffusion in random binary alloys: First principles study of the $\text{Si}_{1-x}\text{Ge}_x$ system,” *J. Appl. Phys.*, vol. 94, p. 174, 2003.
- [156] C. V. Falub, M. Meduňa, D. Chrastina, F. Isa, A. Marzegalli, T. Kreiliger, A. G. Taboada, G. Isella, L. Miglio, A. Dommann, and H. von Känel, “Perfect crystals grown from imperfect interfaces - supporting online informations,” *Sci. Reports*, vol. 3, p. 2276, 2013.
- [157] B. W. Dodson, D. R. Myers, A. K. Datye, V. S. Kaushik, D. L. Kendall, and B-Martinez-Tovar, “Asymmetric tilt boundaries and generalized het-

- eroepitaxy,” *Phys. Rev. Lett.*, vol. 61, pp. 2681–2684, 1988.
- [158] E. C. Young, F. Wu, A. E. Romanov, A. Tyagi, C. S. Gallinat, S. P. DenBaars, S. Nakamura, and J. S. Speck, “Lattice tilt and misfit dislocations (1122) in semipolar GaN heteroepitaxy,” *Appl. Phys. Express*, vol. 3, p. 011004, 2010.
- [159] F. Pezzoli, F. Isa, G. Isella, C. V. Falub, T. Kreiliger, M. Salvalaglio, R. Bergamaschini, E. Grilli, M. Guzzi, H. von Känel, and L. Miglio, “Germanium crystals on silicon show their light,” *arXiv.org e-Print archive*, vol. cond-mat, p. arXiv:1306.5270, 2013.
- [160] G. Grzybowski, R. Roucka, J. Matthews, L. Jiang, R. T. Beeler, J. Kouvetakis, and J. Menéndez, “Direct versus indirect optical recombination in Ge films grown on Si substrates,” *Phys. Rev. B*, vol. 84, no. 20, p. 205307, 2011.
- [161] M. Kittler, T. Arguirov, M. Oehme, Y. Yamamoto, B. Tillack, and N. V. Abrosimov, “Photoluminescence study of Ge containing crystal defects,” *Physica Status*

Solids A-Applications and Materials Science, vol. 208, pp. 754–759, 2011.

- [162] M. E. Kurdi, S. David, X. Checoury, G. Fishman, P. Bokaud, O. Kermarrec, D. Bensahel, and B. Ghysselen, “Two-dimensional photonic crystals with pure germanium-on-insulator,” *Optics Comm.*, vol. 281, pp. 846–850, 2008.
- [163] T. Arguirov, M. Kittler, and N. V. Abrosimov, “Room temperature luminescence from germanium,” *Journal of Physics: Conference Series*, vol. 281, p. 012021, 2011.
- [164] S.-R. Jan, C.-Y. Chen, C.-H. Lee, S.-T. Chan, K.-L. Peng, C. W. Liu, Y. Yamamoto, and B. Tillack, “Influence of defects and interface on radiative transition of Ge,” *Appl. Phys. Lett.*, vol. 98, no. 14, p. 141105, 2011.
- [165] D. Nam, D. Sukhdeo, S.-L. Cheng, A. Roy, K. C.-Y. Huang, M. Brongersma, Y. Nishi, and K. Saraswat, “Electroluminescence from strained germanium membranes and implications for an efficient Si-compatible

- laser,” *Appl. Phys. Lett.*, vol. 100, no. 13, p. 131112, 2012.
- [166] L. Carroll, P. Friedli, S. Neuenschwander, H. Sigg, S. Cecchi, F. Isa, D. Chrastina, G. Isella, Y. Fedoryshyn, and J. Faist, “Direct-gap gain and optical absorption in germanium correlated to the density of photoexcited carriers, doping, and strain,” *Phys. Rev. Lett.*, vol. 109, no. 5, p. 057402, 2012.
- [167] J. R. Haynes, “New radiation resulting from recombination of holes and electrons in germanium,” *Phys. Rev.*, vol. 98, no. 6, pp. 1866–1868, 1955.
- [168] M. E. Kurdi, T. Kociniewski, T.-P. Ngo, J. Boulmer, D. Débarre, P. Boucaud, J. F. Damlencourt, O. Kermarrec, and D. Bensahel, “Enhanced photoluminescence of heavily n -doped germanium,” *Appl. Phys. Lett.*, vol. 94, no. 19, p. 191107, 2009.
- [169] R. R. Lieten, K. Bustillo, T. Smets, E. Simoen, J. W. Ager, E. E. Haller, and J.-P. Locquet, “Photoluminescence of bulk germanium,” *Phys. rev. B*, vol. 86, p. 035204, 2012.

- [170] A. N. Izotov, A. I. Kolyubakin, S. A. Shevchenko, and E. A. Steinman, “Photoluminescence and splitting of dislocations in germanium,” *phys. stat. sol. (a)*, vol. 130, no. 1, pp. 193–198, 1995.
- [171] R. Sauer, C. Kieselowskikemmerich, and H. Alexander, “Dissociation-width dependent radiative recombination of electrons and holes at widely split dislocations in silicon,” *Phys. Rev. Lett.*, vol. 57, pp. 1472–1475, 1986.
- [172] S. A. Shevchenko and A. N. Tereschenko, “Photoluminescence in germanium with a quasi-equilibrium dislocation structure,” *Physics of the solid State*, vol. 49, pp. 28–33, 2007.
- [173] Y. P. Varshni, “Band-to-band radiative recombination in groups IV, VI, and III-V semiconductors (I),” *phys. stat. sol. (b)*, vol. 19, no. 2, pp. 459–514, 1967.
- [174] S. R. Morris, “Recombination of electrons and holes at dislocations,” *Phys. Rev.*, vol. 104, no. 3, pp. 619–623, 1956.

- [175] T. Figielski, “Recombination at dislocations,” *Solid State Electron.*, vol. 21, pp. 1403–1412, 1978.
- [176] T. Figielski, “Theory of carrier recombination at dislocations in germanium,” *phys. stat. sol. (b)*, vol. 6, no. 2, pp. 429–440, 1964.
- [177] R. Tsu and L. Esaki, “Tunneling in a finite superlattice,” *Appl. Phys. Lett.*, vol. 22, p. 562, 1973.
- [178] M. M. Rieger and P. Vogl, “Electronic-band parameters in strained $\text{Si}_{1-x}\text{Ge}_x$ alloys on $\text{Si}_{1-y}\text{Ge}_y$ substrates,” *Phys. Rev. B*, vol. 48, no. 19, pp. 14276–14287, 1993.
- [179] M. M. Rieger and P. Vogl, “Erratum: Electronic-band parameters in strained $\text{Si}_{1-x}\text{Ge}_x$ alloys on $\text{Si}_{1-y}\text{Ge}_y$ substrates [178],” *Phys. Rev. B*, vol. 50, no. 11, p. 8138, 1994.
- [180] M. Bonfanti, E. Grilli, M. Guzzi, M. Virgilio, G. Grosso, D. Chrastina, G. Isella, H. von Känel, and A. Neels, “Optical transitions in Ge/SiGe multiple quantum wells with Ge-rich barriers,” *Phys. Rev. B*, vol. 78, no. 4, p. 041407(R), 2008.

- [181] A. Giorgioni, E. Gatti, E. Grilli, A. Chernikov, S. Chatterjee, D. Chrastina, G. Isella, and M. Guzzi, “Photoluminescence decay of direct and indirect transitions in Ge/SiGe multiple quantum wells,” *J. Appl. Phys.*, vol. 111, no. 1, p. 013501, 2012.
- [182] P. Kung, A. Saxler, X. Zhang, D. Walker, T. C. Wang, I. Ferguson, and M. Razeghi, “High quality AlN and GaN epilayers grown on (00-1) sapphire, (100), and (111) silicon substrates,” *Appl. Phys. Lett.*, vol. 66, p. 2958, 1995.
- [183] X. Zhang, S. J. Chua, P. Li, K. B. Chong, and Z. C. Feng, “Enhanced optical emission from GaN films grown on a silicon substrate,” *Appl. Phys. Lett.*, vol. 74, p. 1984, 1999.
- [184] A. Dadgar, F. Schulze, M. Wienecke, A. Gadanez, J. Bläsing, P. Veit, T. Hempel, A. Diez, J. Christen, and A. Krost, “Epitaxy of GaN on silicon-impact of symmetry and surface reconstruction,” *New Journal of Physics*, vol. 9, p. 389, 2007.
- [185] A. Watanabe, T. Takeuchi, K. Hirose, H. Amano,

- K. Hiramatsu, and I. Akasaki, "The growth of single crystalline GaN on a Si substrate using AlN as an intermediate layer," *J. Crystal Growth*, vol. 128, p. 391, 1993.
- [186] P. Dogan, O. Brandt, C. Pfüller, J. Lähnemann, U. Jahn, C. Roder, A. Trampert, L. Geelhaar, and H. Riechert, "Formation of high-quality GaN microcrystals by pendeoepitaxial overgrowth of GaN nanowires on Si(111) by molecular beam epitaxy," *Cryst. Growth Des.*, vol. 11, p. 4257, 2011.
- [187] D. K. Kim and C. B. Park, "Photoluminescence studies of GaN films on Si(111) substrate by using an AlN buffer control," *J. Korean Phys. Soc.*, vol. 47, p. 1006, 2005.
- [188] W. Liu, M. F. Li, S. J. Xu, K. Uchida, and K. Matsumoto, "Phonon-assisted photoluminescence in wurtzite GaN epilayer," *Semicond. Sci. Technol.*, vol. 13, pp. 769–772, 1998.
- [189] J. Neugebauer and C. G. V. de Walle, "Gallium vacan-

cies and the yellow luminescence in GaN,” *Appl. Phys. Lett.*, vol. 69, p. 503, 1996.

- [190] E. Calleja, F. J. Sánchez, D. Basak, M. A. Sánchez-García, E. M. noz, I. Izpura, F. calle, J. M. G. Tijero, J. L. Sánchez-Rojas, B. Beaumont, P. Lorenzini, and P. Gibart, “Yellow luminescence and related deep states in undoped GaN,” *Phys. Rev. B*, vol. 55, no. 7, p. 4689, 1997.
- [191] F. Semon, B. Damilano, S. VÃfzian, N. Grandjean, M. Leroux, and J. Massies, “GaN grown on si(111) substrate: From two-dimensional growth to quantum well assessment,” *Appl. Phys. Lett.*, vol. 75, p. 82, 1999.
- [192] A. Ohtani, K. S. Stevens, and R. Beresford, “Microstructure and photoluminescence of GaN grown on Si(111) by plasma assisted molecular beam epitaxy,” *Appl. Phys. Lett.*, vol. 65, p. 61, 1994.
- [193] M.-H. Kim, Y.-C. Bang, N.-M. Park, C.-J. Choi, T.-Y. Seong, , and S.-J. Park, “Growth of high-quality GaN on si(111) substrate by ultrahigh vacuum chemical va-

- por deposition,” *Appl. Phys. Lett.*, vol. 78, p. 2858, 2001.
- [194] R. Liu, A. Bell, F. A. Ponce, C. Q. Chen, J. W. Yang, and M. A. Khan, “Luminescence from stacking faults in gallium nitride,” *Appl. Phys. Lett.*, vol. 86, p. 021908, 2005.
- [195] Y. T. Rebane, Y. G. Shreter, and M. Albrecht, “Stacking faults as quantum wells for excitons in wurtzite GaN,” *Phys. Stat. Sol. (a)*, vol. 164, p. 141, 1997.

Publications

1. A. G. Taboada, T. Kreiliger, C. V. Falub, F. Isa, M. Salvalaglio, L. Wewior, D. Fuster, M. Richter, E. Uccelli, P. Niedermann, A. Neels, F. Mancarella, B. Alén, L. Miglio, A. Dommann, G. Isella and H. von Känel, [Strain relaxation on GaAs/Ge crystals on patterned Si substrates](#), *Appl. Phys. Lett.* **104**, 022112 (2014)
2. T. Kreiliger, C.V. Falub, F. Isa, G. Isella, D. Chrastina, R. Bergamaschini, A. Marzegalli, R. Kaufmann, P. Niedermann, A. Neels, E. Müller, M. Meduña, A. Dommann, L. Miglio and H. von Känel: [Epitaxial Ge-crystal arrays for X-ray detection](#), *J. Instrum.* in press (2014)
3. T. Kreiliger, C. V. Falub, A. G. Taboada, F. Isa, S. Cecchi, R. Kaufmann, P. Niedermann, A. Pezous, S.

- Mouaziz, A. Dommann, G. Isella, and H. von Känel: [Individual heterojunctions of 3D germanium crystals on silicon CMOS for monolithically integrated X-ray detector](#), *phys. stat. sol. (a)* **211**, 131 (2014)
4. F. Isa, A. Marzegalli, A. G. Taboada, C. V. Falub, G. Isella, F. Montalenti, H. von Känel, and L. Miglio: [Onset of vertical threading dislocations in \$\text{Si}_{1-x}\text{Ge}_x/\text{Si}\$ \(001\) at a critical Ge concentration](#), *APL Materials* **1**, 052109 (2013)
5. A. G. Taboada, T. Kreiliger, C. V. Falub, M. Richter, F. Isa, E. Müller, E. Uccelli, P. Niedermann, A. Neels, G. Isella, J. Fompeyrine, A. Dommann, and H. von Känel: [Integration of GaAs on Ge/Si towers by MOVPE](#), *MRS Proceedings* **1538**, 283 (2013)
6. C. V. Falub, T. Kreiliger, F. Isa, A. G. Taboada, M. Meduňa, F. Pezzoli, R. Bergamaschini, A. Marzegalli, E. Müller, D. Chrastina, G. Isella, A. Neels, P. Niedermann, A. Dommann, L. Miglio, and H. von Känel: [3D heteroepitaxy of mismatched semiconductors on silicon](#), *Thin Solid Films*
DOI:<http://dx.doi.org/10.1016/j.tsf.2013.10.094> (2013)

7. R. Bergamaschini, F. Isa, C. V. Falub, P. Niedermann, E. Müller, G. Isella, H. von Känel, and L. Miglio: [Self-aligned Ge and SiGe three-dimensional epitaxy on dense Si pillar arrays](#), *Surf. Sci. Rep.* **68**, 390 (2013)
8. C. V. Falub, M. Meduña, D. Chrastina, F. Isa, A. Marzegalli, T. Kreiliger, A. G. Taboada, G. Isella, L. Miglio, A. Dommann, and H. von Känel: [Perfect crystals grown from imperfect interfaces](#), *Sci. Reports* **3**, 2276 (2013)
9. F. Pezzoli, F. Isa, G. Isella, C. V. Falub, T. Kreiliger, M. Salvalaglio, R. Bergamaschini, E. Grilli, M. Guzzi, H. von Känel, and L. Miglio: [Germanium crystals on silicon show their light](#), *arXiv.org e-Print archive cond-mat*, arXiv:1306.5270 (2013)
10. A. Marzegalli, F. Isa, H. Groiss, E. Müller, C. V. Falub, A. G. Taboada, P. Niedermann, G. Isella, F. Schäffler, F. Montalenti, H. von Känel, and L. Miglio: [Unexpected dominance of vertical dislocations in high-misfit Ge/Si\(001\) films and their elimination by deep substrate patterning](#), *Adv. Mater.* **25**, 4408 (2013)

11. L. Miglio, R. Bergamaschini, A. Marzegalli, F. Isa, D. Chrastina, G. Isella, P. Niedermann, A. Dommann, C. V. Falub, E. Müller, and H. von Känel: [“divide et impera” in detector technology](#), *Il Nuovo Saggiatore* **29**, 7 (2013)
12. M. Richter, E. Uccelli, A. G. Taboada, D. Caimi, N. Daix, M. Sousa, C. Marchiori, H. Siegwart, C. V. Falub, H. von Känel, F. Isa, G. Isella, A. Pezous, A. Dommann, P. Niedermann, and J. Fompeyrine: [Heterointegration by molecular beam epitaxy: \(In,Ga\)As/GaAs quantum wells on GaAs, Ge, Ge/Si and Ge/Si pillars](#), *J. Cryst. Growth* **378**, 109 (2013)
13. C. V. Falub, T. Kreiliger, A. G. Taboada, F. Isa, D. Chrastina, G. Isella, E. Müller, M. Meduña, R. Bergamaschini, A. Marzegalli, E. Bonera, F. Pezzoli, L. Miglio, P. Niedermann, A. Neels, A. Pezous, R. Kaufmann, A. Dommann, and H. von Känel: [Three dimensional heteroepitaxy: A new path for monolithically integrating mismatched materials with silicon](#), *2012 International Semiconductor Conference (CAS)*, 45-50 (2012)

14. C. V. Falub, F. Isa, T. Kreiliger, R. Bergamaschini, A. Marzegalli, A. G. Taboada, D. Chrastina, G. Isella, E. Müller, P. Niedermann, A. Dommann, A. Neels, A. Pezous, M. Meduña, L. Miglio, and H. von Känel: [Space-filling arrays of three-dimensional epitaxial Ge and Si_{1-x}Ge_x crystals](#), *SiGe Technology and Device Meeting, 2012. ISTDM 2012* (2012)
15. A. Picco, E. Bonera, F. Pezzoli, E. Grilli, O. G. Schmidt, F. Isa, S. Cecchi, and M. Guzzi: [Composition profiling of inhomogeneous SiGe nanostructures by Raman spectroscopy](#), *Nanoscale Res. Lett.* **7**, 633 (2012)
16. L. Carroll, P. Friedli, S. Neuenschwander, H. Sigg, S. Cecchi, F. Isa, D. Chrastina, G. Isella, Y. Fedoryshyn, and J. Faist: [Direct-gap gain and optical absorption in germanium correlated to the density of photoexcited carriers, doping, and strain](#), *Phys. Rev. Lett.* **109**, 057402 (2012)
17. D. J. Paul, A. Samarelli, L. Ferre-Llin, J. R. Watling, Y. Zhang, J. M. R. Weaver, P. S. Dobson, S. Cecchi, J. Frigerio, F. Isa, D. Chrastina, G. Isella, T. Etzelstorfer, J. Stangl, and E. Müller Gubler: [Si/SiGe](#)

nanoscale engineered thermoelectric materials for energy harvesting, *Proceedings of the 12th IEEE International Conference on Nanotechnology (IEEE-NANO) 2012* 1-5 (2012)

18. C. V. Falub, H. von Känel, F. Isa, R. Bergamaschini, A. Marzegalli, D. Chrastina, G. Isella, E. Müller, P. Niedermann, and L. Miglio: [Scaling hetero-epitaxy from layers to three-dimensional crystals](#), *Science* **335**, 1330 (2012)
19. S. Bietti, L. Cavigli, M. Abbarchi, A. Vinattieri, M. Gurioli, A. Fedorov, S. Cecchi, F. Isa, G. Isella, and S. Sanguinetti: [High quality GaAs quantum nanostructures grown by droplet epitaxy on Ge and Ge-on-Si substrates](#), *phys. stat. sol. (c)* **9**, 202 (2012)